Dissertation
submitted to the
Combined Faculty of Mathematics, Engineering and Natural Sciences
of Heidelberg University, Germany
for the degree of
Doctor of Natural Sciences

Put forward by
Maximilian Kaiser
Born in: Kaiserslautern
Oral examination: 26.11.2025

Heidelberg Quantum Architecture:
A modular platform for quantum simulations

Referees:

Prof. Dr. Selim Jochim
Prof. Dr. Julian Schmitt

Maximilian Kaiser
Heidelberg Quantum Architecture: A modular platform for quantum simulations
Dissertation
Supervised by: Prof. Dr. Selim Jochim

Physikalisches Institut - Ruprecht-Karls-Universität Heidelberg
Research Group: Ultracold Quantum Gases

Physikalisches Institut
Im Neuenheimer Feld 226
69120 Heidelberg

Abstract

The presented thesis reports on the development of a broadly applicable, open-source, modular system architecture for quantum gas experiments, which has been named Heidelberg Quantum Architecture (HQA). In the ongoing rollover of quantum gas apparatuses from mere experiments to usable platforms for quantum simulation, similar to classical computing in the 1950s, such an architecture can be beneficial in the pursuit of improving the usability and raising the technology readiness level (TRL) of these systems.

An exemplary quantum gas apparatus for quantum simulation with ultracold ^{6}Li, following the guidelines of HQA, is constructed. It is named Heidelberg Quantum Architecture based experiment described in this thesis (HQA-ONE). The modular concept of Heidelberg Quantum Architecture (HQA), which disentangles the complexity of the quantum gas apparatus into subsystems that are attached to a common mechanical frame of reference (FOR), is demonstrated. A passive interfacing precision of the exchangeable modules mounted to the framework of around $\pm 10\,\mu$m is measured.

The reconfigurable apparatus HQA-ONE is equipped with modules for deterministic preparation of atom number states in the ground state of an optical tweezer to exemplarily demonstrate a core capability of quantum simulators, quantum state initialization, with the apparatus and indirectly with the platform.

Further modules to choose from when configuring the apparatus for quantum simulations in the future are developed, constructed, and presented in the thesis, underlining the reconfiguration character of the platform and its versatility.

Zusammenfassung

Die vorliegende Arbeit handelt von der Entwicklung einer vielseitig anwendbaren, modularen Systemarchitektur für Quantengas Experimente. Diese Architektur, genannt Heidelberg Quantum Architecture (HQA), ist dabei open-source. Im aktuellen Transit in der Nutzung von Maschinen zur Erzeugung von ultrakalten Quantengasen von rein akademischen Experimenten hin zu nutzbaren Platformen für Quantensimulation, analog zu frühen klassischen Computern in den 1950ern, kann solch eine Architektur helfen die Nutzbarkeit und den Technology Readiness Level (TRL) zu erhöhen.

Eine exemplarische Quantengas Maschine für Quantensimulationen mit ultrakaltem ^{6}Li wird gemäß der Konzeptionen von HQA errichtet. Diese Maschine wird im Folgenden HQA-ONE genannt. HQAs modulares Konzept zur Segmentierung der Maschine in Subsysteme, die an einem gemeinsamen mechanischen Zentralelement referenziert und befestigt werden, wird demonstriert. Dabei wird die passive Referenzierungspräzision der austauschbaren Module in ihrer Schnittstelle auf etwa 10 µm bestimmt.

Die rekonfigurierbare Maschine HQA-ONE wird mit Modulen zur deterministischen Präparation von Fock-Zuständen im Grundzustand einer optischen Dipolfalle ausgerüstet. Damit wird für HQA-ONE und exemplarisch für HQA, durch deterministische Zustandsinitialisierung, die Eignung zur Anwendung in Quaten Simulatoren demonstriert.

Weitere Module zur Bestückung von HQA-ONE wurden entwickelt, konstruiert und werden im Rahmen dieser Arbeit vorgestellt. Die Einsetzbarkeit solcher Module zur Erweiterung oder Änderung der zur Verfügung stehenden experimentellen Techniken unterstreicht dabei die Vielseitigkeit der Architektur und der Maschine.

Contents

1 Introduction

1.1 Modular technology architecture

In the early 1960s, after the advent of transistor-based computers at the end of the 1950s, IBM identified issues with its sales of mainframe computers. So far, different models have been sold as complete, yet unique, machines with individual hardware, operating systems, and user software. This was common practice for all mainframe computer manufacturers. However, this requires the manufacturer to develop new versions of all these components again for each new model. On the other hand, switching to newer, more powerful models commonly resulted in users having to rewrite their programs and potentially losing data during transfer between models, which led to the customers being hesitant to buy new equipment [1]. The story of IBM's solution is described in detail in [1], a summary of which will be given here.

IBM's solution was introduced in 1964, the IBM System/360, a family of cross-compatible mainframe computers based on identical instruction sets and upgradeable with common peripherals. Emulators ensured that machines could also run older software. The system became a success, enabling users to overcome their previous concerns and adapt the apparatus over time according to their needs. This marked a transformative switch in the design of mainframe computers, which made IBM the dominant company in this business segment. However, it also marked the beginning of the dynamic and specialized computer market we observe today. Other companies started developing and building peripherals[1] compatible with the IBM system, eventually surpassing IBM's offered peripherals in selection or quality, leading to a computer market with multiple subsystem-specialized companies as it is today [1].

What IBM essentially did was move from a fully integrated system to a modular one. While an integrated system describes a 'closed' system of tightly interconnected subsystems, modularity describes loose connections or independence of the subsystems, making the overall system more 'open' [2]. In more general terms, reference [1] defines modularity as a strategy for organizing systems and processes in independent units, called modules, that work together forming the full system. The key for this strategy, following [1], is to develop and to disentangle visible design rules from hidden design parameters.

These visible design rules are based on design choices that apply to all modules, dictating further design boundaries for individual modules to ensure compatibility. Visible design rules can be grouped into three categories: architecture-based, which dictate the types of modules and core functionalities that the system supports; interface-based, which define the standards with which modules must comply for integration; and standardized performance validation-based, which determine the testing capabilities required for performance verification and inter-module performance comparison. These rules, determined by the modular framework, have to be set up front as they govern the boundaries of the

[1] e.g., printer, memory, or software

development process of all subsequent modules [1].

Hidden design parameters describe the detailed design choices made on each local module to realize the desired functionality within the boundaries set by the visible rules. These choices do not affect other modules and therefore allow for specialized development, design experimentation, and frequent change of the parameter during development [1].

Staying within the computer example [1], developers for components like hard drives in modern computers have to comply with preset constraints like maximum physical size, mechanical mounting, and communication protocols. These are the visible design rules for these components, or in other words, modules. The exact realization of the hard drive, for example, pursuing solid state drives or hard disk drives and their detailed structure, sets the hidden design parameters that are solely driven by their development and not of relevance for the system as a whole.

The art in developing modular systems is to identify suitable visible design rules that maximize the system's modular usability while limiting constraints on hidden design parameters for both currently envisioned and future modules, ensuring they can perform as expected.

Today, in product engineering and system development, modularity is desired for ensuring three distinct features for the developed system [3]:

First, it allows breaking down the complexity of the full system into smaller pieces. If necessary for users or developers, in-depth knowledge about these smaller systems can be more easily acquired, managed, and transferred than for the system as a whole. For this reason, modular systems can be considered cognitively economic [3].

Second, it enables parallel, decoupled development, assembly, and integration of different subsystems as respective modules by independent teams, resulting in shorter overall development and construction times for the complete system. For this reason, modular systems can be considered temporally economic [3].

Third, it allows for change, upgrades, and user flexibility [4], which ensures on the user side adaptability to changing requirements and on the developer side possibility for upgrades and experimentation within the modules. For this reason, modular systems can be considered tolerant of uncertainty [3].

The widespread use of modular system design led to various studies on modularity and its implications in different contexts [4]. These include, on the engineering side, factors like impacts on innovation [5–7] as well as user innovation [8, 9], knowledge management [10], and the process of technological search [11]. The latter also applies to systems where the exact technological realization of a system is not clear during initial development. [12] discusses this for product modularity upon market entry in emerging markets. They conclude that modular systems, supporting several standards and therefore applying few visible design rules, can be beneficial to react initially to unpredictable industry dynamics. In later product cycles and development, it is suggested to reduce the supported standards to one, thereby reducing the visible design rules and allowing for increased performance.

1.2 Outline of the thesis

This thesis presents an approach suitable for the incorporation of a modularity concept in the next generation of ultracold quantum gas experiments and related quantum techno-

logical setups, largely independent of the used atomic species. The concept, called HQA, breaks down the complex optical, mechanical, and electrical setups of such apparatuses into functional groups, with suitable, well-defined interfaces, which provide the basis for disentangled subsystems, the modules. An exemplary realization of a HQA-based quantum gas apparatus for experiments with ultracold ^{6}Li, HQA-ONE, has been built and is accordingly described in the thesis.

Chapter 1 introduced the concept of modularity in general and its role across natural sciences and technology. Additionally, it provides references for further reading. These include the publication corresponding to the developed platform architecture and exemplary apparatus, as well as multiple Bachelor's and Master's theses, that detail the development of specific subsystems of HQA-ONE.

Chapter 2 briefly discusses programmable quantum simulations with ultracold atoms, with their rise in complexity, yet pursuit of near-future real-world applications and usability, providing a field highly relevant for the implementation of modularity concepts. Such concepts could, in principle, allow for further improvement of the technological readiness of these systems.

Chapter 3 presents one possible solution, HQA. This architecture does not claim to set new standards or general visible design rules that have to be followed for building quantum gas apparatuses; however, it presents a complete and tested solution to incorporate modularity in a platform architecture that differs from traditional quantum gas experiments. This chapter focuses on HQA as a broadly applicable concept, its visible design rules, which are essentially independent of the used atomic species, and tests of the architecture in its exemplary realization with HQA-ONE.

Chapter 4 on the other hand focuses on the specifics of HQA-ONE beyond the concepts of HQA. These include the systems relevant for operation of the Lithium-based apparatus, such as magnetic field coils, thermal management, and laboratory automation.

Chapter 5 demonstrates that HQA-ONE, and therefore HQA as a whole, has the potential for use in quantum simulation, by demonstrating high-fidelity, deterministic preparation of few-fermion states in an optical tweezer with the HQA-ONE.

To conclude the thesis, Chapter 6 concludes the presented results and provides an outlook on the near future of HQA-ONE with expansions of its toolbox, partially already developed, constructed, and awaiting implementation.

1.3 Further Reading in supervised theses

Development and construction of a quantum gas experiment is generally speaking a work intensive endeavour and requires a significant workforce. The construction of HQA-ONE was supported by numerous students within the scope of their respective Bachelor- or Masterthesis. These theses are recommended for further reading about specific details of the described subsystems and topics beyond the description within this dissertation. An overview of these references and their focus is given in Table 1.1. Unless stated differently, the listed students were jointly supervised by the PhD students working on HQA-ONE, among them the author of this thesis.

Table 1.1: Overview of student theses and their contributions to the development of HQA and the construction of HQA-ONE during the time of this dissertation.

Student	Thesis	Main Contribution	Reference
Tobias Hammel[a]	Master thesis 2021	First concepts for HQA and design of the vacuum apparatus, the 2D-MOT and magnetic field coils	[13]
Leo Walz	Bachelor thesis 2021	Spectroscopy Cell	[14]
Malaika Görtz	Bachelor thesis 2022	2D-MOT Optics	[15]
Marlene Matzke	Bachelor thesis 2022	AOM double pass module	[16]
Micha Bunjes	Master thesis 2022	Objective design and characterization	[17]
Hüseyin Yildiz	Bachelor thesis 2022	RF-coil planning and prototyping	[18]
Vivienne Leidel	Master thesis 2023	MOT light distribution and optical accordion planning	[19]
Jan Ricken	Bachelor thesis 2023	Development of an optical accordion module	[20]
Marta Pastori	Bachelor thesis 2023	Proof of concept spin resolved imaging	[21]
Juan Provencio	Bachelor thesis 2024	Development of a DMD module	[22]
Sofia Barth[b]	Bachelor thesis 2024	Prototype implementation digital laserlock	[23]
Johanna Schulz	Master thesis 2024	Characterization RF-coils and optical accordion	[24]
Suraj Iyer	Master thesis 2024	Magnetic field switching and stabilization	[25]
Finn Lubenau	Master thesis 2025	Development of a SLM module	in preparation
Jonathan Weiß	Bachelor thesis 2025	Automation of on-module optomechanical components and enclosed mPoCs for in-vacuum optics	in preparation

[a] Tobias was the first student to work on HQA supervised by Dr. Philipp Preiss as a postdoctoral researcher. I joined the project as a PhD student in the last quarter of his Master thesis, hence no significant contribution to the supervision was held from my side.

[b] Sofia was primarily supervised by Paul Hill.

1.4 List of Publications

The concepts behind HQA and the technical details of HQA-ONE have been published and can also be found in the following reference:

> **Modular quantum gas platform**
> Tobias Hammel*, Maximilian Kaiser*, Daniel Dux, Philipp M. Preiss, Matthias Weidemüller, Selim Jochim
> doi: 10.1103/PhysRevA.111.033314 (2025), arXiv: 2501.08211 (2025)

Authors marked with * contributed equally to the publication.

1.5 Writing tools

The artificial intelligence (AI)-based writing assistant *Grammarly*[2] has been used in this thesis as a spell-check software and helped in grammatically refining the provided text after it had been written. The tool has not been used to generate new content.

[2] www.grammarly.com

2 Quantum simulation with ultracold atoms

The year 2025, recognized by UNESCO as the International Year of quantum science and technology[1,2], is in the middle of a time by many referred to as a quantum revolution [26]. While the initial development of quantum mechanics and its role in describing nature and physical reality during the last century is commonly called the first quantum revolution, the second quantum revolution refers to the rollover of quantum mechanics from a mere description of observations to the fundamental rules for development of new technologies, which led to the term quantum engineering [27]. The large-scale rollout and practical use of quantum technologies, commonly referred to as the third quantum revolution [28], is expected to be technologically and economically transformative. While we are arguably still at the beginning of the third quantum revolution, the anticipated prospects led to a quantum hype [26] and geopolitically to both significant financial and organizational efforts by most countries in order to try to utilize the expected technological advantages first[3] [26, 29, 30].

In this context, the most discussed and promising applications are quantum sensing, quantum communications, and quantum computation.

Within the field of quantum sensing, various quantum systems have been realized as quantum sensors, demonstrating unprecedented metrological capabilities [31–33]. First quantum sensors, like superconducting quantum interference devices (SQUIDs), are already commercially available today[4].

Within the field of quantum communication, essential concepts like quantum key distribution have been demonstrated on relevant scales [34], leading now to larger rollouts of these technologies towards real-world use [35, 36].

While these technologies are therefore arguably en route towards practical use, quantum computation, on the other hand, falls short so far. Advantages over classical computers have been demonstrated in tailored niche problems [37]; however, general use is for now out of reach [38]. It is estimated that it will take around 10-15 more years until a noise-resilient quantum computer usable for a broad application spectrum becomes available [26].

2.1 Quantum simulation

While general use quantum computing is expected to be at least a decade away, a subsection of quantum computing, so-called quantum simulation, is expected to yield practical results in the next few years, due to less demanding requirements [26]. The idea of a quantum

[1] celebrating the 100th anniversary of the original formulation of quantum mechanics
[2] www.quantum2025.org
[3] Unfortunately, this also led to countries becoming more restrictive in international collaborations and export of relevant technologies, as these are starting to be deemed strategically important [26, 29].
[4] Like for example the SQUID Magnetometer MPMS3 by Quantum Design, www.qdusa.com

simulator builds on the proposal, commonly attributed to Feynman [39], of using a well-controllable quantum system to mimic another complex quantum system which is to be studied [40]. While the size of the Hilbert space for many-body quantum systems scales exponentially with the particle number, putting exact calculations out of reach for classical computers, a quantum simulator would provide a controllable analog system, following for relevant properties identical physical rules on a controllable scale, comparable to a wind tunnel in aerodynamics [41].

On the one hand, a general-use quantum computer would be able to perform quantum simulations by encoding the system which is to be investigated into the computer's qubits and performing quantum circuit-based quantum[5] algorithms to evaluate the system. This is commonly referred to as digital quantum simulation [42]. Due to the necessary abstraction layer, in the above-mentioned aerodynamics analogy, this would correspond to an exact computer-based simulation of the system.

On the other hand, the wind tunnel testing, the direct implementation of a problem and its Hamiltonian in an analog quantum system[6] is commonly referred to as analogue quantum simulation. If these devices allow for the simulation of more than one specific Hamiltonian, but a class of Hamiltonians, these can be referred to as programmable quantum simulators[7] [43].

Growing programmability of analogue quantum simulators softens the distinction between analogue and digital quantum simulations. However, it directly leads to a stepping stone role, as it can be used to gather first experiences with quantum circuitry and quantum algorithms [43]. This pivotal role towards quantum computing, as well as expected scientific opportunities in fields like quantum materials simulation, quantum chemistry, and non-equilibrium quantum many-body dynamics, led to significant interest in the field and an ever-growing repertoire of publications and reviews. The manuscripts [40, 42–44] can be seen as a personal selection of relevant literature, providing a good starting point for an overview of the field at the time this thesis is being written.

2.2 Chances for modularity in atom-based quantum simulation

The enabling technological path towards quantum computation and digital quantum simulation is not yet clear; it is at the moment a contest, especially between superconducting qubit-based architectures and atom-based systems [45]. Here we will focus on atom-based approaches, which recently demonstrated significant technological progress [46–48], but are especially promising for quantum simulations [43].

The high degree of control, clean systems, and the possibility of sandbox-like assembly of physical systems made ultracold atoms an early system for first quantum simulations [49]. First analogue simulations used the atoms directly for experimental implementation of a specific scientifically interesting system, which was 'hardcoded' into the simulator. Investigated systems span across fields like high-energy physics [50], solid state physics [51], and astronomy [52, 53], as well as cosmology [54].

[5] I agree that the word 'quantum', can be considered to be a bit overused in the common terminology of quantum computation and simulation.

[6] These do not necessarily need a qubit structure but could also provide continous observables [43]

[7] Following this logic, digital quantum simulation is always programmable quantum simulation, assuming there is a mapping of the relevant physical problem to the qubit structure.

Today, in the pursuit of achieving programmable analogue quantum simulators and hybrid solutions towards digital quantum simulation, ultracold gases are typically trapped in optical lattices [55] or prepared in Rydberg states in optical tweezer arrays [46, 47], which are initialized and subsequently evolve under programmable (time-dependent) Hamiltonians to allow mapping of a class of physical problems onto the same realized quantum system instead of a single implemented Hamiltonian.

While these systems for analogue quantum simulations and new approaches for programmable analogue[8] quantum simulation are significantly different, they essentially both utilize techniques from the same physical toolbox: optical dipole trapping light [56] to form the underlying potential for the atoms; optical, RF, and microwave (MW) adressing, magnetic field control, and imaging techniques for individual atom readout.

This common toolbox is the starting point for modular architecture. With many people using the same tools and techniques, modularizing these tools and capabilities for the respective platform could provide similar benefits to those achieved over time in classical computers. With quantum simulation in mind, three important aspects are:

Firstly, traditional analogue quantum simulation, which implements one specific Hamiltonian without much programmability, could directly benefit from a modular structure, as modules would allow for easy exchange to reconfigure the apparatus for studies of a different system. This would not compare with the rapid timescales programmable quantum simulators can shift their realized Hamiltonian on, but it would allow for expanding the capabilities of versatile experiments that can be freely reconfigured when necessary. In that sense, it would enable reconfigurability for these platforms as a variation to programmability.

Secondly, a quantum simulator based on a modular platform allows for decoupled development of the individual modules, which can be pivotal in fields where the exact technological route for realization is not yet well understood. As long as the visible design rules do not restrain the general functionality, experimentation with the detailed realization of the modules and their hidden design parameter would allow easier, faster, and collaborative development. Allowing for both improved internal developments and synergetic developments between groups.

Moreover, once a technological path for realizing breakthrough quantum simulations has been found, a modular structure would allow to reconfigure the existing quantum simulators that were also built in pursuit of this goal, giving them identical or at least similar capabilities to allow for cutting-edge quantum simulator operation by all involved teams.

[8] or hybrid

3 A modular quantum gas platform

This chapter introduces the development of a broadly applicable, modular platform for quantum gas experiments, referred to as Heidelberg Quantum Architecture (HQA), along with its technical realization in a representative apparatus following these concepts, called HQA-ONE. While HQA-ONE was built for experiments with ultracold ^{6}Li, this chapter focuses on the general modularization of quantum gas experiments and our approach to achieving this. Specific details of HQA-ONE, beyond general relevance in the sense of HQA concepts, are deferred to Chapter 4. These developments and their technical realization have been previously published by our team in [57]; this chapter is based on this publication, yet provides a deeper insight into the development process.

We are happy that the approaches presented in the publication and subsequently in this chapter have been well received by the ultracold gases researcher community and that several experiments have already either adapted or considered adapting the platform or parts of it in joint meetings. These include, for example, the teams of Dr. Preiss (MPQ Garching), Prof. Chomaz (Heidelberg University), Prof. Roati (LENS Florence), Prof. Cornish (Durham University), and Prof. Ketterle (MIT Cambridge). Beyond that, the corresponding publication has been acknowledged by QuEra Computing Inc., one of the globally leading companies for atom-based quantum computing, by sharing the manuscript in a post [58].

In this chapter, Section 3.1 will introduce the general rationale of HQA and its approach towards modularization of quantum gas experiments. Essential building blocks of such systems are identified and their role in the pursuit of modularity elaborated. The general workflow of a modular quantum gas experiment is sketched out. Section 3.2 - Section 3.7 present the development of the essential building blocks identified in the first section, together forming the technical realization of HQA. Section 3.8 clarifies the availability of the design and its applicability to other atomic species.

3.1 Rationale of the architecture

The rationale of HQA's architecture has been carefully elaborated in our corresponding publication [57]. This section will therefore closely follow the argumentation presented in the paper. Paragraphs in this section, which have been directly duplicated from the publication, are marked with the citation mark [57] at the end of the paragraph.

In order to illustrate the design choices made on the path towards developing a modular quantum gas platform, let us start by specifying the goal system on an abstract level. Consider a typical, broadly applicable experimental setting, an experiment aiming to image single atoms in a cloud of ultracold, optically trapped atoms. In essence, these experiments require: An ultra-high vacuum (UHV) chamber including an atom source within to protect the cloud from collisions with background atoms. Multiple sets of near-resonant and off-resonant laser fields for cooling, trapping, and diagnostics. Magnetic fields for interaction control and magneto-optical trapping. As well as a large numerical aperture

(NA) microscope objective to gather a sufficient fluorescence signal to resolve individual atoms. [59]

3.1.1 Building blocks of a quantum gas platform

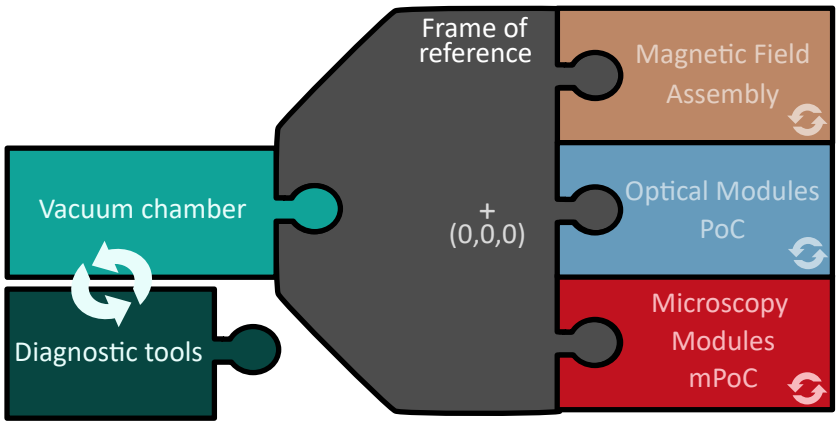

Figure 3.1: Schematic visualization of the concept behind HQA's modular layout. The experimental platform consists of a central mechanical structure introducing a common frame of reference with well-defined interfaces to which different modules can be attached. These exchangeable modules are passively positioned and provide different functionalities like magnetic- (brown), general optical- (blue), or high-numerical aperture optical (red) field generation at the designated center point. The vacuum chamber (turquoise) provides the UHV environment and atom source for using this platform for quantum gas experiments, but is retractable to allow placement of diagnostic tools (dark green) to probe fields at the mechanical center point. Figure adapted from [57].

Based on these necessary building blocks, Figure 3.1 schematically depicts the rationale of HQA where the fundamental concept is to disentangle the entire setup into segments, each devoted to a specific functional task (e.g. cooling light, optical trapping, magnetic fields, imaging, diagnostic tools, etc.). We distinguish between segments designed for regular exchange, so called *modules*, and semi-permanent segments that can be replaced but are not intended for regular exchange, referred to as *assemblies*. However, all of these are connected to the central frame of reference (FOR) (grey). This structure defines the mechanical connection of modules and assemblies with distinct functionalities, such as magnetic (brown) or optical (blue and red), to the platform. Introducing a common FOR with a respective mechanically designated center point provides a passive coarse alignment of all modules to one point. If this overlaps adequately with the later position of the atoms, it allows the modules to provide alignment of their optics to the atom position passively, sufficient to obtain a first signal.

Due to the modularity, each individual module can be tested and calibrated independently before attaching it to the central interface. For instance, an optical module could be a breadboard with optical elements, which has the task of generating a particular light field distribution, to interact with the cold atom cloud in a well-defined plane inside the experimental chamber. This light field distribution can be precisely pre-aligned by mapping it onto characterization tools outside of the experimental platform. Such a modular

approach takes advantage of the fact that, even for complex quantum gas experiments, tolerances for initial alignment of light or magnetic fields are on the same order of magnitude as tolerances achieved by computer numerical control (CNC) guided machining tools. By mechanically referencing the optics and possibly other modules to a common CNC machined frame of reference, each module can be pre-adjusted at an external test bench, with a mock-up of the interface, and then precisely integrated mechanically into the platform, thus preserving the absolute orientation to all other components of the setup. [57]

Further optimization can then be performed by fine-tuning the alignment of the *components* on the module once integrated in the apparatus. In analogy to the free space in-coupling of a laser beam into an optical fiber, this passive alignment can omit the tedious search for an initial signal and allow one to directly start with optimizing the signal, which is usually much more straightforward and can in principle even be automated.[1]

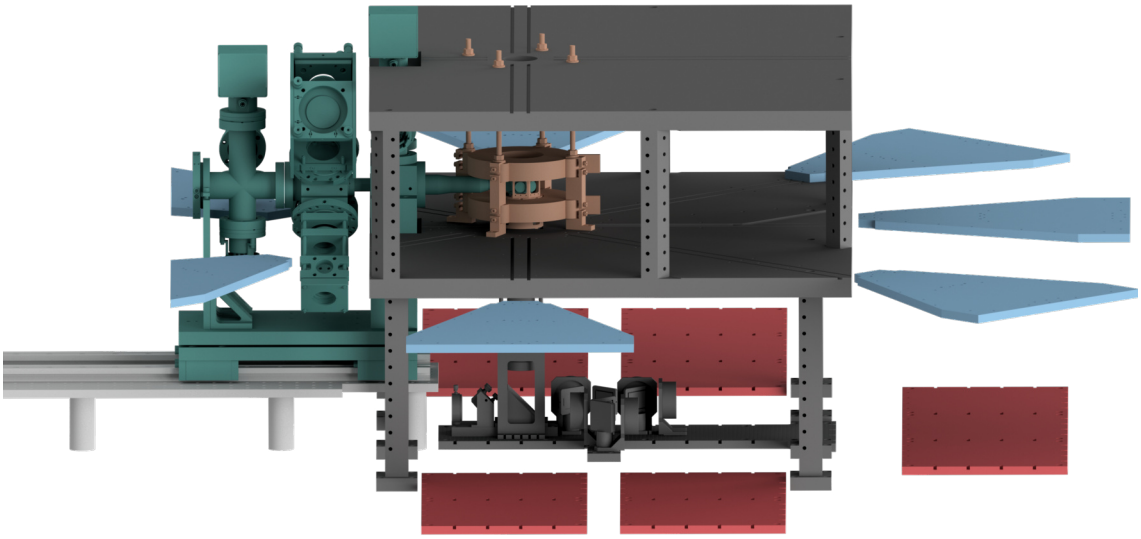

Figure 3.2: Simplified CAD model of the mechanical realization of HQA. The colors of the subsystems match Figure 3.1 for easier identification of their role within the platform. The design is centered around a common mechanical structure (grey), which serves as a frame of reference for all modules. The vacuum system with an octagonal glass cell as the main science chamber (turquoise) is mounted on a rail system. It can be repeatably inserted or retracted from the origin of the frame of reference. This origin, passively overlapping with the focal plane of the high-NA objective, is surrounded by an assembly of magnetic field coils (brown). Optical access to the center is provided via the optical modules. These exchangeable modules are passively aligned to the center of the interface with precision on the order of a few tens of micrometers. Optical modules perpendicular to the optical axis of the objective (blue) are referenced with stainless steel pins, and modules for propagation through the high-NA objective, so-called microscopy modules (red), are placed using stainless steel parallel keys. Possible diagnostic tools are not shown in the model. Figure and caption adapted from [57].

[1] At the time this thesis is being written, Jonathan Weiß, a Bachelor Student at HQA-ONE, is working on optomechanical components required for the automation of the hardware alignment of the modules.

Figure 3.2 shows a CAD model of the mechanical realization of this concept in an experimental platform. The color coding follows Figure 3.1 to identify the different modules.

The common frame of reference in our platform is provided by a custom-machined board with precision locating holes (see Section 3.3). We can position the horizontal optical modules (blue in Figure 3.1 and Figure 3.2) with a precision of typically a few tens of microns with respect to the origin of the frame of reference. We achieve this by utilizing precision positioning pins, which will be discussed in detail in Section 3.6. Due to their shape and the huge facilitation they provide in everyday work, we call the corresponding modules Piece of Cake (PoC).

In terms of sensitivity to misalignment, the most demanding piece of optics is the central high-NA objective. For all optics using the same high-NA objective, for example, to perform high-resolution manipulation, trapping, or imaging, we developed an adapted modularization strategy. For details, see Section 3.7. To summarize the idea, an appropriate optical setup introducing a magnification into the optical path can transform position requirements of tens of microns in the atom plane to hundreds of microns or even millimeters in the image plane. The modules used for this purpose, shown in red in Figure 3.1 and Figure 3.2, are called Microscopy Piece of Cake (mPoC).

These two types of optical modules (Piece of Cake (PoC) and Microscopy Piece of Cake (mPoC)) form the core of this modularization concept for optics arrangements in the context of quantum gas experiments. To interface horizontal and vertical optical modules, a precise pre-characterization of the objective and its optical axis is required, as it allows the positioning of the objective such that its field of view (FOV) is centered around the origin of the global coordinate system given by the mechanical frame of reference. Using the same positioning mechanism as for the PoC, the objective is mounted onto the frame of reference without adjustable degrees of freedom. The angular adjustment of the objective with the vacuum window is critical, as tilting the optical viewport introduces aberrations for high-NA objectives. Precise alignment of this degree of freedom is ensured by tilting the whole vacuum system, instead of the objective, using spacers, as outlined in Section 3.2.

The vacuum system, including the cold atom source, main science chamber, and pumping units, is disconnected from the frame of reference, but can readily be moved in and out using a rail system (see Figure 3.2). The absolute positioning of the science chamber compared to the frame of reference is not critical and is defined by placing a stop to the travel range of the rail system. The vacuum chamber can be moved in and out of the frame of reference, providing access to the origin of the reference coordinate system, where the atoms are approximately located, allowing one to place diagnostic tools like cameras or magnetic field sensors. This feature of interchangeability between the vacuum chamber and diagnostic tools is illustrated in Figure 3.1.

In addition, connected to the frame of reference are magnetic field and RF coils in the magnetic field assembly, shown in brown in Figure 3.1 and Figure 3.2. These can be removed or added to the platform, but are not designed for frequent exchange. Technical details of the magnetic field assemblies can be found in Section 3.4.

A combination of multiple of these modules defines the functionality of the experiment, and in the following will be called *configuration* of the platform. As modules can easily be exchanged, this makes the platform highly versatile and adaptable to other experimental requirements (see Section 3.8). [57]

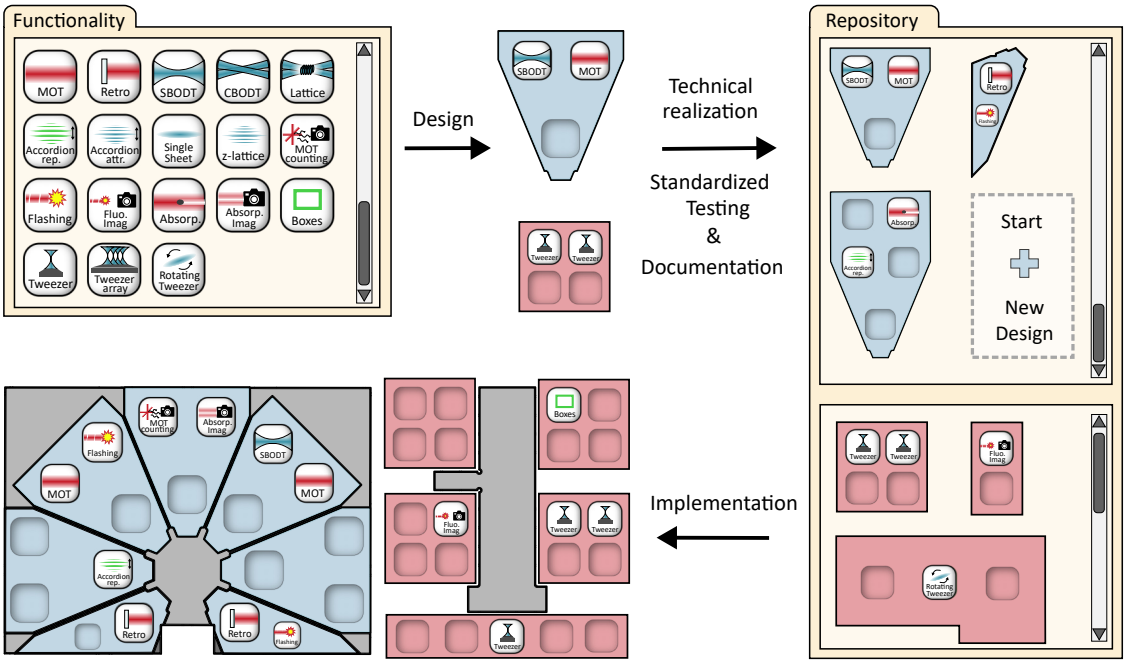

Figure 3.3: Typical workflow for configuring HQA's modular platform. The top-down path, starting from the idea of a functionality and going through design, realization, documentation, and implementation, is shown. The workflow starts in the upper left corner. There, one can select the desired functionalities (depicted as rectangular icons) for the new PoC or mPoC. All functionalities have internal DoFs, for example, a single beam optical dipole trap (SBODT) has as parameters the waist, trap frequencies, and depth of the required potential. These provide a clear framework for the design and subsequent technical realization of the components within the module. With standardized testing capabilities, it can be validated that the light field generated by the module meets the required performance. Afterwards, the design files are uploaded to a shared online repository, and the physical module is either prepared for implementation or stored in a hardware repository in the laboratory. The implementation of the PoC or mPoC is straightforward and follows the description in the respective sections. Figure and caption adapted from [57].

3.1.2 Configuring a modular platform

Once constructed, adding new hardware to the modular platform can follow a top-down approach, focused on the desired functionality and required light-field distribution in the atom plane rather than the technical generation. Analogous to the work with bought laser systems as a lab user. The precise internal arrangement of optical components on the module is not of general relevance for its use, effectively making it a black box for the user. A workflow we envisioned for HQA is schematically depicted in Figure 3.3.

If a new or different functionality is needed for the experiment at hand, the configuration of the platform has to be changed to provide the proper experimental toolbox. On a hardware level, this means that individual implemented modules may need to be exchanged for new ones. Building new modules starts by defining all the required functionalities it

has to provide, hence specifying the expected light field distribution in the atom plane. In Figure 3.3, this is depicted as selecting corresponding icons in the upper left. Such a functionality could be, for example, a single beam optical dipole trap (SBODT) with a given waist and maximum depth. After specifying the desired functionality and its fundamental parameters, paths to possible optical realizations on the module, e.g., selecting the right beam sizes and lenses, are identical to those in other laser laboratories.

Extra functionalities, such as additionally providing near resonant light for a MOT arm, can be added to the same module, e.g. by overlapping the beams with a dichroic mirror. Eventually, the maximum number of functionalities is limited by the available space to fit all necessary optical components onto the module.

In order to maximize the usable space on the modules, we use custom optomechanical mounts with a compact footprint and a 12.5 mm double-density grid of M3 threads as mounting points on the modules. This system is an adaption based on the optomechanical mounts used at the Max Planck Institute of Quantum Optics in Garching [60] and internally nicknamed *Optics-Lego* or *O-Lego*[2]. More information on the custom mounting system can be found in Section 3.6. However, it is essential to clarify that the use of HQA is not limited to these custom optomechanical mounts. It is perfectly possible to adapt individual or all modules to use, for example, a 25 mm M6 grid and optomechanical posts with clamping forks.

The technical realization of the module, so the actual building of the components onto the module, takes place on a testbench (see Section 3.6). It is a mockup of the FOR. It provides the same mechanical interface as the platform, along with the possibility to mount the module and place diagnostic tools, such as optical power meters, cameras, or wavefront sensors, in the equivalent of the later atom plane. This testbench approach provides complete diagnostics for the construction, testing, and performance validation before use of the module or during debugging. Furthermore, it is decoupled from the actual experimental apparatus, so development and initial testing of new modules does not disrupt the experiments' uptime. Development and data collection can be performed in parallel.

After completing development and performance validation, the construction plans and test data are documented in a repository. The physical module is either directly implemented on the platform or preliminarily stored in a local hardware storage in the lab. Details on the implementation of the modules are presented in the respective sections in this chapter. Over time, by utilizing modules from this storage, the experimental platform can be rapidly reconfigured to meet the toolbox requirements for the next major project.

Additionally, the repository opens up opportunities for collaboration between experimental groups with a common interface on their platforms. Sharing the repository between these groups allows to quickly replicate tools from their toolbox on each others machine, as the blueprints and testing data are available and directly applicable, the optical setup on the module can be identically replicated[3]. The more labs that use the same platform, the broader and more usable this module database gets. Following this, both individual labs and a community can benefit from modularization of their experimental platform.

[2] This nickname follows the naming of the system in Garching and is inspired by the user experience when working with it. As a colleague once phrased it: *"The difference in building with O-Lego versus regular optics with posts and clamping forks feels like the difference between Lego and Duplo."*

[3] It is also possible to share the physical modules between groups when not in use, but we expect that sharing the applicable blueprints will have more regular use cases.

The following sections will now focus on the technical realization of modularity as part of HQA and follow the presented building blocks in Figure 3.1.

3.2 Vacuum chamber

The first building block to look into will be the vacuum setup of the platform. Naturally, the specific requirements for the vacuum chamber for different atomic species can vary; therefore, this section will focus on the fundamental design choices made for integration as a building block in this architecture. The details of the vacuum chamber in our realization of HQA, optimized for using ^{6}Li atoms, are covered in Section 4.2.

The vacuum chamber and its integration into the modularization strategy were initially developed by Tobias Hammel and Dr. Philipp Preiss. More information, especially on the initial development phase, is presented in [13].

3.2.1 Science chamber

The first general design choice we want to discuss concerns the layout of the vacuum chamber, more specifically, the region in the chamber where later experiments are being conducted. If the vacuum chamber is split into several sections, e.g., in a section dedicated to loading and one for experiments, the latter is usually also referred to as the science chamber. Typically, this cell is either made from stainless steel with multiple viewports [61], or entirely out of glass [62–64]. While the material of the science chamber does not necessarily matter for the pursuit of our modularization approach, the geometry of the cell does. Following the rationale in Figure 3.1, the vacuum chamber must extend into the enclosing FOR, reaching the frameworks' designated centerpoint with its science chamber to perform experiments there. This means, in order not to block half of the available optical access with the attached vacuum chamber, the science cell has to extend out from the rest of the vacuum chamber on an arm-like structure. Such a feature is widely common for compact glass cells, but much harder to realize for heavier stainless steel chambers. Additional relevant aspects in which glass cells typically outperform stainless steel chambers include better optical access due to the compact size with less opaque interfaces, avoidance of Eddy currents induced magnetic stray field when rapidly switching exterior fields, and no screening effects for access with RF and MW fields.

An annotated photo of the glass cell used at HQA-ONE and recommended in general for use as part of HQA is provided in Figure 3.4. The cell, attached to the vacuum chamber via a stainless steel CF40 flange, consists of a 5.25" (133.4 mm) long neck with an attached compact octagonal prism shaped glass cell body. This body is fitted with two large viewports with an clear aperture of 1.5" (38.1 mm) on top and bottom and following the octagonal base symmetry seven smaller viewports on the sides each with a clear aperture of 0.5" (12.7 mm). In terms of optical access, this translates to the glass cell providing a NA of up to 0.9 for the top and bottom window and 0.3 for all seven sideward-facing windows. The viewports with the highest NA are typically reserved for applications requiring the use of custom-made objectives to utilize the available solid-angle as much as possible. These objectives are typically tailored to the window thickness and required working distances of the port they are later used on. However, in order to have the possibility to harness the full

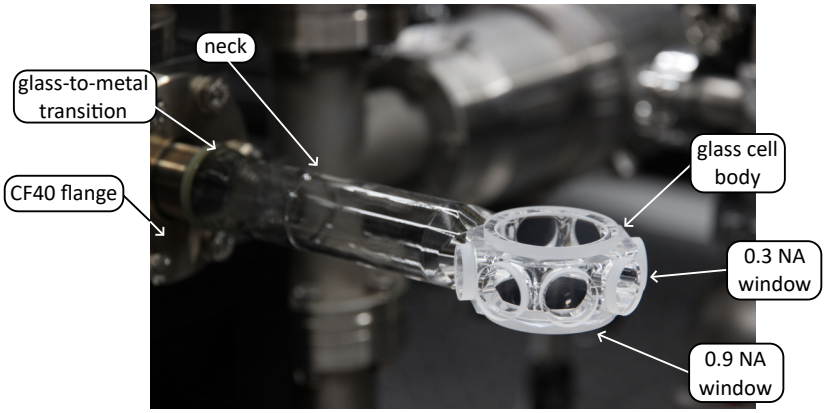

Figure 3.4: Annotated photo of the glass cell used at HQA-ONE. From left to right, one sees the flange attachment to the vacuum chamber, the 133.4 mm long neck of the glass cell, and the connected octagonal, 52.2 mm wide chamber body. It features a large 38.1 mm viewport on top and bottom and seven smaller 12.7 mm viewports on its side. The presented glass cell geometry is the recommended type for use as part of HQA.

optical access also from the side viewports, where expensive custom designed objectives are impractical, we chose the window thickness for these ports to be 3.5 mm to match the requirements of commercial off the shelf (COTS) available objectives with coverglass compensation[4]. This allows comparably simple, cheap, and readily available access to the full NA of the side windows.

A challenge of the high-NA provided by the glass cell, however, is the wide range of the beams angle of incidence (AOI) that has to be covered by the anti-reflection (AR) coating of the viewports. While the described glass cell was manufactured by *Precision Glassblowing*[5], the 'coating' of the windows was provided by *TelAztec*[6]. The windows are structured on both the inner and outer surface with a random anti-reflection (RAR) nano-texture (RAR-L2). Etched into these surfaces are randomly distributed cone-like structures with sub-wavelength diameter and distances creating an effective AR structure with extreme broadband optical performance ranging from the near ultraviolet (NUV) up into the short wavelength infrared (SWIR) and more importantly for the high-NA application, suited for AOI of up to 50° while still providing reflectivity of below 1 % [13]. Hence, this AR-structure allows for effective use of the entire solid angle of the glass cell with high-NA objectives, as even photons with a large AOI on the window can be collected without significant reflection losses.

However, these nano-textured windows come at the cost of requiring extra careful handling compared to standard optics with a dielectric coating. While removing dust from textured surfaces can be easily achieved with dry Nitrogen, wet-cleaning of the windows is not as easy as for dielectric coatings and potentially not possible with the glass cell attached to the vacuum chamber. Additionally, the reflections that still occur on the textured surfaces are not directional but diffuse. The reflections, as well as forward scattering, on the nano-structure can introduce a wide variety of possible wave vector pointings. A

[4] e.g. Mitutoyo G Plan Apo 20x (t3,5) (Part No: 378-847) providing an NA coverage of 0.28 while being compatible with the glass cell.
[5] www.precisionglassblowing.com
[6] www.telaztec.com

fraction of these lead to coupling into the glass cell body in which the windows are sitting (see Figure 3.4). Even for collimated beams passing through the windows without clipping, a faint glow of the glass cell body is visible. We attributed this effect to the injection of large wave vectors upon reflection on the windows, coupling light into whispering gallery-like modes of the glass cell body and leaking out on the the glass-to-air interface. This can lead to undesired background light in the experimental environment. We did, however, not observe crosstalk between the windows themselves. A potential solution to further suppress the background light from the glass cell body in new experiments could involve discussing with the manufacturer the possibility of blackening the body. It could minimize the leaking due to an added painting layer or reduce light propagation in general by adding dye to the quartz glass.

Besides the glass cell geometry used here, there are also other geometries available on the market. Most commonly used other glass cell types are rectangular ones [63, 64]. We originally chose the octagonal cell because we wanted to use the nano-texture AR coating, which was not available for both inside and outside surfaces on rectangular glass cells at the time we started developing HQA. Besides that, the octagonal glass cell geometry has the additional benefit of being especially suited for a modularization approach as it naturally segments the horizontal space around the cell into seven equal parts, each with access to the chamber via an orthogonal window. A rectangular glass cell also allows segmentation, but there one could either only have three segments, each with a horizontal module, or more segments but with non-perpendicular glass interfaces for some of them. This would, on the one hand, break exchange symmetry between the segments and, on the other hand, cause potential problems due to beam displacement of the beams and introduced astigmatism on non-collimated beams. That being said, it is still possible to use a rectangular glass cell, even for adapting the concepts of HQA, but it will introduce additional challenges beyond the approaches that are presented here.

3.2.2 Modularization of the vacuum chamber mounting

The second general design choice to discuss is how one can turn the vacuum chamber into a puzzle piece in the sense of Figure 3.1. In other words, how is it possible to build a vacuum chamber setup that can be inserted and removed from a central mechanical FOR instead of being the centerpiece itself with all other parts of the experiment tailored to the chamber? We concluded that the actual layout and design of the vacuum chamber do not play a role in achieving this; only its mechanical mounting and integration into the platform are relevant. The result is a sled-like vacuum chamber mounting with linear translation and controllable tilt capabilities, depicted in an annotated sketch in Figure 3.5. Due to its non-specific mounting points, it is widely adaptable to be used with other vacuum chamber designs.

At the heart of this mechanical system is a 1.2 m long rail system of Igus DryLin T linear translation stage. A total of four carriages are mounted on two compatible guiding rails, each carriage capable of holding up to 1000 kg and withstanding 50 N m of torque. The carriages do not contain any lubricants, which omits servicing them after some time and makes them temperature resistant up to 90 °C [13], a feature which is valuable during the bake-out of the attached vacuum chamber, where undesired heating of the mechanical mounting can happen. The four carriages are attached to a 20 cm x 36 cm stage baseplate

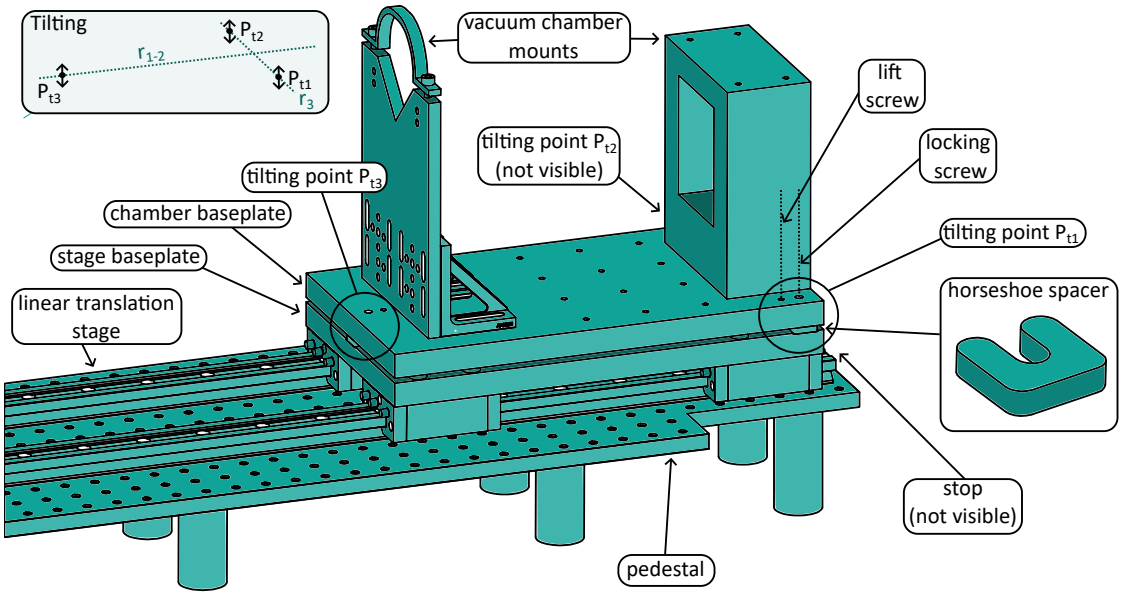

Figure 3.5: Annotated sketch of the vacuum chamber mounting, consisting of a pedestal on which a 1.2 m long rail system is placed. Guided by these rails, a cart with adjustable tilt provides the mounting points for the vacuum apparatus and linear translation to insert or respectively retract the vacuum chamber from the surrounding FOR. The exchangeable horseshoe spacers used for fine adjustment of the tilt of the vacuum chamber mounting are depicted. The inset shows how changing their height tilts the chamber baseplate and identifies two possible rotation axes for the tilt.

made from anodized aluminum. With the four narrow-tolerance carriages fixed to the stage baseplate and following the two parallel rails, the setup is prone to jamming if the rails are not perfectly parallel, i.e., if the rail distance deviates over the full length more than the tolerance of the carriages. With the respective tolerances of the carriages of down to 0.02 mm, this would make placing the rails a delicate task. In order to circumvent this problem for our setup, the carriages on one rail are set to be floating. Therefore, they provide support but cannot lead to jamming.

Mounted on top of the stage baseplate is the chamber baseplate, which is identical in size and houses the specific mounting points for the actual vacuum chamber. As depicted in Figure 3.5, they are connected at the three tilting points P_{t1}, P_{t2} and P_{t3}. At each of these points, an M6 locking screw connects the two baseplates via a through hole in the upper plate and a thread in the lower plate. A horseshoe-shaped spacer surrounding the locking screw (see Figure 3.5) sets the distance between the plates. All three spacers together therefore set the orientation of the chamber baseplate plane relative to the stage baseplate. As shown in the inset of Figure 3.5, exchanging the horseshoe spacers allows for precise tilting of the chamber baseplate and the attached vacuum chamber around the presented rotation axes. To achieve full decoupling, the rotation around r_{1-2} has to be generated by splitting the height adjustment between P_{t1} and P_{t2} increasing the spacer thickness on one side, for example by 20 µm, while decreasing the thickness on the other tilting point by the same amount. The thickness at P_{t3} can be changed independently, leading to the sketched rotation axis r_3. It is possible to shift r_3 parallel to its sketched

position by also equally counter-adjusting the thickness of P_{t1} and P_{t2}, but this is not needed to achieve decoupling of the rotation axes. In our lab, we have the horseshoe spacers available in thicknesses between 5.0 mm and 5.2 mm in steps of 20 µm leading to a tilt adjustment resolution of 0.06 mrad at a full tuning range of ±2.9 mrad [13]. However, smaller steps or other thicknesses are, in principle, easily adaptable if necessary.

To exchange the spacer on the tilting points, unscrew all locking screws and then turn down the lift screw on the desired tilting point. This M6 screw sits in a thread in the chamber baseplate and can push down on the stage baseplate, lifting the upper baseplate, like a mechanical jack. The spacer can be taken out and exchanged for a different one. A milled recess in both the stage baseplate and the chamber baseplate ensures that positioning the spacer is repeatable. After the exchange, the upper plate can be lowered again via the lift screws and secured with the locking screws.

When we first assembled the apparatus, we monitored the angle of the glass cell with a 3-axis acceleration sensor[7] on a custom mount to measure the angle of the upper window of the glass cell with respect to a reference point on the optical table. We matched them using the previously described horseshoe spacer mechanism.

The actual mounting of the vacuum chamber is placed on the chamber baseplate. The mounting used for HQA-ONE is shown in Figure 3.5, but for new implementations of HQA, this can be widely adapted to match the needs of other vacuum chambers without restricting the functionality of the rail system and the integration into the modular framework. A benefit of the compact mounts shown in Figure 3.5, which are less than 20 cm tall, is that they keep the moving mass on the rail system low and therefore minimize the stress on the four carriages. It is expected that this helps to maximize stability and precision of the vacuum chamber puzzle piece in the sense of Figure 3.1. While we did not perform tests with various masses mounted on the carriages, we can report that for our setup, we found angular repeatabilities of better than 0.25 mrad [13] and did not observe long-term degradation of the mounting system and the stage. We did not observe any influence on experimental performance parameters like MOT loading, optical dipole trap (ODT) loading, or optical few-body sample preparation (see Chapter 5) over the last years, despite regularly moving the vacuum chamber in and out of the FOR, for up to a year, even on a daily basis. These experiences comply with those of the former Jendrzejewski group [65, 66].

This low height of the vacuum mounting, however, might not comply with the dimensions of the FOR. It can be necessary to provide more space below the glass cell. This is achieved here by putting the entire translation system on a pedestal. The rails are supported by a total of ten cylindrical aluminum posts with a diameter of 1.5", five per rail. The posts are mounted onto the grid of the optical table with set screws, and the rails are mounted with screws from the top into the posts. A modified 1200 mm x 300 mm x 12.7 mm breadboard from Thorlabs[8], with some additional cutouts to fit into the FOR, is used as additional support and protection for the vacuum mounting system. To prevent the breadboard from influencing the translation system due to bending, the posts are positioned directly under the rail system. The breadboard is clamped between the rails and the posts, with screws from the rails extending into the posts through holes in the breadboard. Adapting the height of the pedestal for other experiments is possible by varying the height of the posts. The stop of the translation system is mounted on the pedestal as well. This L-

[7] 3-axis inclinometer Murata SCL3300
[8] MB30120/M

shaped CNC machined stop interfaces the baseplate on the rail system with two spherical contacts, ensuring that the two contact points well define the stop position of the cart moving parallel to the plane of the optical table.

Besides keeping the moving mass on the translation system low, the pedestal approach additionally minimizes the space on the optical table, which is effectively blocked by the rail system and the movement path of the vacuum chamber. We typically use the space under the pedestal as a cable duct, but in principle it can also be used to route beams below.

With these two design choices, it is possible to build the vacuum system compatible with Figure 3.1. A system that can be repeatably inserted and removed from the FOR while still being broadly adaptable to the needs of different atomic species. The design of the building block into which the vacuum system is inserted, the central frame of reference (FOR), is presented in the next section.

3.3 Central frame of reference

As introduced in Section 3.1, the function of the central frame of reference (FOR) within HQA is to provide interfaces and a common coordinate system for all modules and assemblies of the platform. The FOR has to provide the rigid framework for the pursued modularization approach. The mechanical realization of this structure will be discussed in this section.

3.3.1 General layout of the mechanical reference

The general design of our mechanical realization of the FOR is sketched in Figure 3.6. Figure 3.6 a) presents an overview and dimensions of the structure, consisting of three levels, of which two are provided by custom machined breadboards. A sketch of the top view of these two breadboards is shown in Figure 3.6 b) and c), respectively. In operation, the glass cell is placed between level 1 and level 2.

Level 2 provides the interface for optical access to the top 0.9 NA window of the glass cell via a central aperture in the breadboard. The breadboard features a 25 mm x 25 mm grid of M6 threads for mounting of standard optomechanical components. It is additionally equipped with a 100 mm x 100 mm grid of blind holes for 5 mm reference pins (see also Section 3.6) to position smaller breadboards as complete modules on level 2. However, at the time this thesis is being written, these referencing pin positions are not used at HQA-ONE. As we currently only send one beam, the vertical MOT beam, into the glass cell from level 2, we have integrated the modularization option for that interface but have not utilized it to date. This can change if more beams need to be fed into the glass cell from that direction in the future or if other realizations of HQA decide on using a second microscope objective from the top. Some remarks on this are given in Section 3.8.

Level 1 provides the sideward interface for the glass cell, houses the main high-NA objective, and defines the center point of the FOR. That means, unlike the breadboard for level 2, it has to follow the symmetry of the glass cell for optimal modularization (see Section 3.2). As depicted in Figure 3.6 c), it incorporates the octagonal symmetry of the glass cell by providing eight ports surrounding the central axis and the center point of the FOR. While ports 1-7 are dedicated to the PoCs, the modules of optical access of

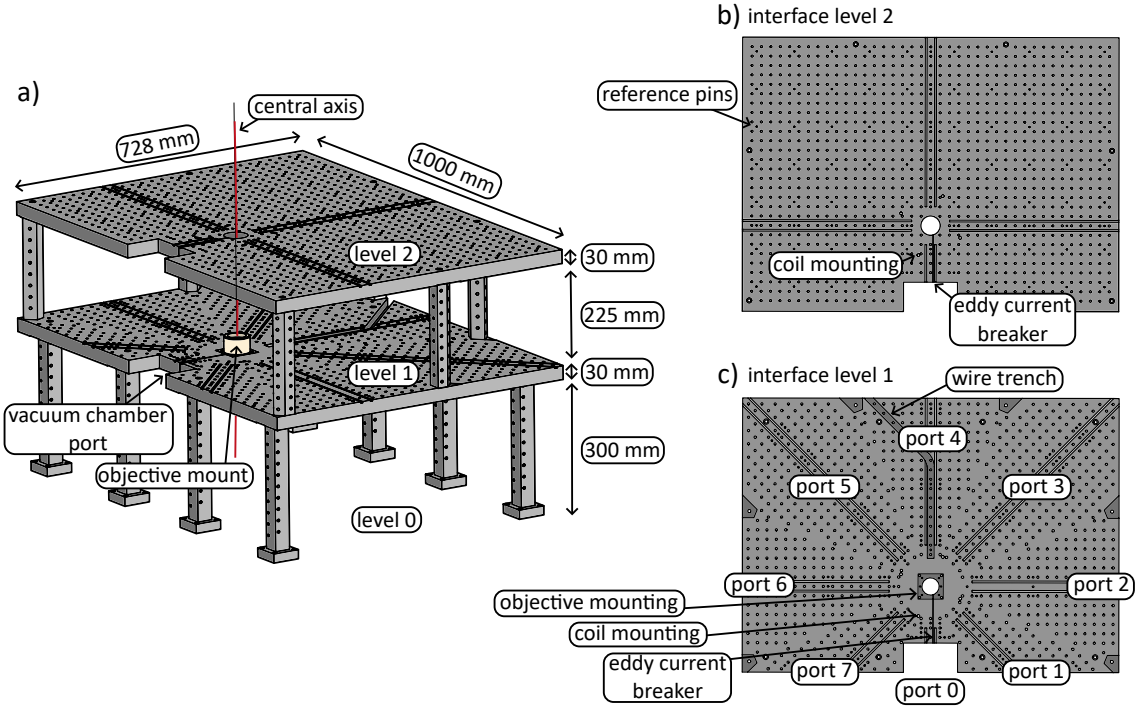

Figure 3.6: Annotated sketches of the mechanical FOR of the design. **a)** shows the general setup and dimensions of the mechanical superstructure on the optical table providing the FOR and interfaces for the different modules following Figure 3.1. The structure consists of three vertically stacked levels, of which level 0 is provided by the optical table, the FOR is mounted on, and two horizontal levels provided by the structure itself. When inserted, the glass cell sits between level 1 and level 2 above the objective mount. **b)** and **c)** depict the layout details of the two breadboards forming the horizontal level of the FOR. The octagonal symmetry of the glass cell is utilized on level 1 (c). The naming of the different spatial ports on this level is annotated. The vacuum chamber and hence the glass cell enter via Port 0.

the 0.3 NA side windows of the cell, port 0 is dedicated to be the port along which the vacuum chamber with the glass cell enters the structure. All eight ports follow the same hole pattern for mounting, providing equal mounting options for all ports. Only ports 0, 1, and 7 are shorter in length due to the general size requirements of the FOR. Each port of the ports features the mounting options for placing and fastening the PoC breadboards on top (details in Section 3.6) and an additional 25 mm x 25 mm grid of M6 threads following the triangular base shape of the ports. This is not necessary for the modularization, but was added at HQA-ONE as a general-purpose mounting option for regular optomechanical mounts and as a safety net in case the modularization strategy would not have worked to our satisfaction.

The central axis of the breadboard and the FOR can be identified in Figure 3.6 c) by the 52 mm wide aperture in the breadboard and the surrounding mounting points for the high-NA objective. The upward-facing objective is mounted in a separate polyetheretherketone (PEEK) mount and placed in a pocket of the breadboard to provide a flush surface around the objective. The ring-like surrounding of the central axis is the region on the breadboard

where the magnetic field coils can be mounted. More on that is presented in Section 3.4.

The feet between the breadboards of level 1 and level 2 encircle the central axis of the FOR and are mounted in dedicated recesses on level 1 and the lower side of the breadboard of level 2 for straightforward, yet precise assembly. A total of six feet are mounted. They are positioned such that they do not obstruct the optical access of the ports. Their pentagonal prism shape provides auxiliary M6 mounting points, e.g., for cable management or mounting of a panel, on the surfaces perpendicular and parallel to the line of sight of the respective port.

Level 0 provides the interface for all optics that have to pass through the high-NA objective of the setup. In the presented design, this level is provided by the optical table on which the FOR is mounted. To position the FOR with respect to the M6 hole pattern on the optical table, we used custom machined referencing pins (similar to the ones shown in Figure 3.19) which just fit on the lower end into the M6 threads of the optical table and on the upper part just into the through holes of the mounting points of the FOR. Using these pins, which effectively overlap the the central axis of the thread and the through hole, on two mounting points of the FOR, before bolting it down with M6 screws, allows it to be placed with respect to the optical table's hole pattern. Now, another mechanical structure can be mounted to the optical table with the same positioning approach. The modules for optics passing through the high-NA objective, the mPoCs, can be referenced to this additional structure and are therefore indirectly also referenced to the FOR. However, the critical optical components that require the least possible misalignment from the objective are mounted directly to the FOR. More details on the interface on level 0 for the mPoCs will be presented and discussed in Section 3.7.

In future realizations, one could also place a custom-machined breadboard on level 0, which is mechanically connected to the feet of the structure. This would omit the indirect referencing of the mPoC interface, e.g., by using recesses for the inner four feet below level 1 to align the interface on level 0 with level 1. However, this might make assembly more complicated and might not be needed as the indirect referencing is expected to produce only small offsets, well below 100 µm. Combined with the demagnification and layout of the high-NA path, it can be engineered that such an offset becomes negligible for the modularization strategy. This will be further discussed in Section 3.7.

The 35 mm x 35 mm feet are mounted in recesses on the lower side of the level 1 breadboard, but poses a square base shape to match the symmetry of the hole pattern of the optical table. Just like their counterparts between levels 1 and 2, they provide auxiliary M6 mounting points on each foot. The FOR is supported by a total of eight of these feet. The length of the feet and hence the clearance between the optical table and the breadboard of level 1 is chosen such that larger components that require access through the high-NA objective, like DMDs, SLMs or large scientific cameras, can be placed there.

The general size of the structure started with a base dimension of the breadboards of 1 m x 1 m. It was set based on the practical size limit is of what could be machined in a single piece in our workshop. The used CNC mill is a *Deckel FP-50-CC*, it provides a programmability of 1 µm, the precision of the translation stages and wear of the drills leads to a measurable precision of the machine of around 10 µm [57]. Repositioning of the parts on the mill during the manufacturing process was performed, when necessary, by selecting reference edges and relative placement of the tool head with dial gauges. Following these base dimensions, the central aperture and central axis of the breadboards

were set. However, the vacuum chamber must enter from the side, which creates additional constraints. We are using a 2D-MOT setup, which radially extends out from the vacuum chamber (see Section 4.2); therefore, the 2D-MOT optics must not collide with the FOR when the vacuum chamber is inserted. This limited the size of the FOR in the direction towards port 0. Furthermore, the neck of the glass cell has only a limited length, yet the chamber has to extend to the center axis of the framework. This gave rise to the small rectangular cutout visible in Figure 3.6 on port 0. Enabled by this cutout, the mounting of the vacuum chamber and the vacuum chamber itself can reach far enough into the FOR to position the glass cell on the central axis, above the high-NA objective.

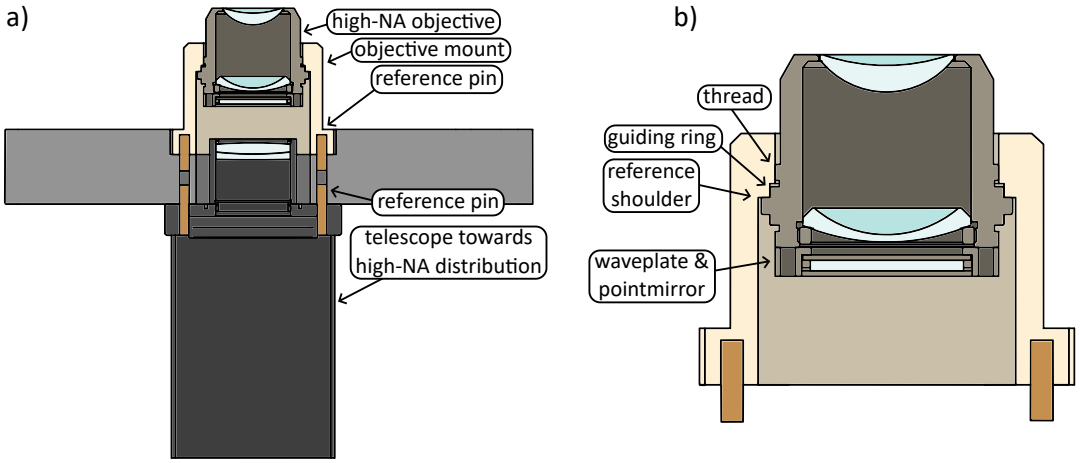

Figure 3.7: Annotated sketches of the mechanical mounting of the high-NA objective of HQA-ONE. The mounting concept, however, is also adaptable to other objectives than the one used here. **a)** presents the mounting mechanics of the objective holder and connected optics in the FOR, **b)** focuses on the mounting of the objective inside the custom-made objective holder.

The mounting of the objective and the following optics is sketched in Figure 3.7. The high-NA objective itself is mounted in a holder machined from which sits in a pocket of the FOR. The housing of the objective itself is machined from ULTEM. Using these non-magnetic and non-conductive Materials makes them suitable to be placed near the center point of the FOR in close proximity to the magnetic field coils. As depicted in Figure 3.7 a), both the objective mount and the optical components directly behind the objective's rear aperture are positioned with respect to the FOR using around 4 mm wide brass pins. Two pins in each mount position the optomechanical parts in the same locating holes without any degrees of freedom before they are secured with screws. To find the tightest possible fit for these brass pins, we machined several with varying diameter tolerances and selected the best-fitting ones. As neither the objective mount nor the telescope towards the high-NA distribution path are assemblies and therefore not intended to be regularly exchanged, these fits can be on the micrometer level. Unlike the pins for the PoCs that we will introduce in Section 3.6, the brass pins do not need to be in the sweetspot between precision and usability; they can be solely tailored to achieving the highest possible precision. This procedure aligns the respective mechanical central axes of the components with the central axis of the FOR. However, it has to be mentioned that the optical axis of the components might not perfectly overlap with the mechanical axis. This tolerance and its implications

will be discussed in Section 3.7.

The objective itself is mounted in the PEEK holder via a M40x0.75 thread and a reference shoulder as depicted in Figure 3.7 b). The objective is screwed into the holder from below, guided onto the central axis by a ring structure on the objective until the reference shoulder touches the dedicated stop in the mount. This effectively locks the objective via the thread and the guiding ring onto the central axis of the mount and via the reference shoulder onto the intended height, so that the focus of the objective is located on the center axis of the FOR and in the right height to sit as close as possible to the mechanical centerpoint of the FOR.

Besides the central aperture and mounting points for the objective, other notable features of the FOR breadboards, depicted in Figure 3.6, include on the one hand a 1 mm wide gap from port 0 all the way to the central aperture of the breadboards. This slit, in the sketch also referred to as *eddy current breaker*, breaks the continuous symmetry around the central axis and helps to suppress eddy currents, induced by magnetic field switching, from flowing in a complete loop around the central axis of the system and inducing magnetic stray fields at the center point. It is positioned near port 0, as this provides the shortest possible cut through the structure that breaks the rotational symmetry. On the other hand, a 18 mm wide and 17 mm wide trench on the top side of level 1 and the bottom side of level 2 allow to lead the wires of the magnetic field coils out of the FOR within the breadboard and therefore without blocking any of the ports on level 1.

3.3.2 Structural stability

With the general design of the FOR now being set, a very fundamental question, however, remains to be discussed: What material should be used to manufacture the structure, and what performance can be estimated? As we want to utilize the precision of modern CNC machines, that boils the selection of possible materials down to those that are millable on a CNC machine. That leaves the option of most metals and engineering plastics like PEEK or ULTEM. While the latter have the advantage of being non-conductive and are therefore immune to eddy currents, they are less durable, especially the threads that are cut into them, compared to their mechanical counterparts. For the metal options, one has to take care that they are not magnetic, in order not to distort the magnetic fields from the coils. With this in mind, the most common materials used are non-magnetic stainless steel (e.g., SST 316L or SST 316LN) and Aluminum (e.g., EN-AW 5083), with an anodizing layer to enhance the durability and scratch resistance of the Aluminum. In order to gauge their suitability for the FOR, we performed finite element analysis (FEA) simulations with Autodesk Inventor and its integrated FEA tools of the FOR made from either material and compared the results. These simulations, however, take simplifications into account to be computable with the mentioned solver.

First, the contacts to the optical table, the surface between the feet on level 0 and optical table, are set as fixed boundary conditions and are therefore not allowed to move in the simulation.

Second, the contacts between the different parts of the assembled FOR, e.g., between the breadboards and the feet, are approximated as perfect contacts. This means they are treated as if these parts are glued together or machined from a solid piece of material. The effects of the bolts holding together the feet and breadboards are not included in the

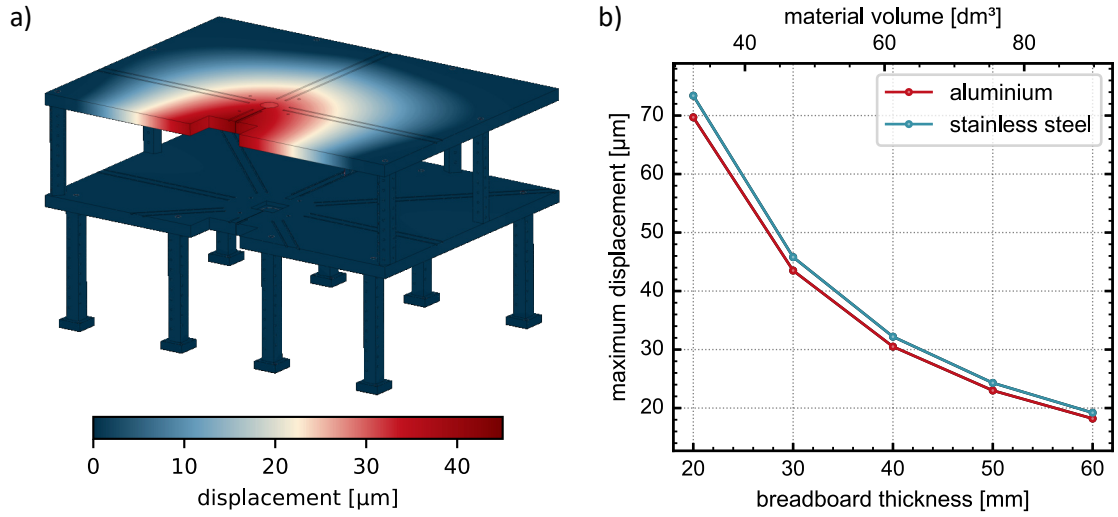

Figure 3.8: Finite-element simulation of the static deformation of the FOR due to its weight. **a)** presents the bending of the structure for 30 mm thick breadboards and the entire structure made from an Aluminum alloy with anodized hardened coating layer. The absolute value of the deviation from the initial position without the gravitational load is color-coded to visualize the distribution of the deformations. **b)** shows the maximum displacement in these simulations for various thicknesses of the breadboards for stainless steel and an aluminum alloy with an anodization layer as the material of the FOR. The change in mass is displayed via a second abscissa indicating the change in material volume. To obtain the mass for the given materials, this number has to be multiplied by their respective density. These are $2.7\,\frac{\mathrm{kg}}{\mathrm{dm}^3}$ for the Aluminum alloy and $8.0\,\frac{\mathrm{kg}}{\mathrm{dm}^3}$ for stainless steel.

simulations.

Third, the FOR design is simplified by removing the M6 hole pattern from the breadboards. This simplifies the net of the structure and, therefore, the number of triangles to be computed in the simulation drastically. The M6 holes are evenly distributed over the breadboards with their 25 mm x 25 mm grid, given their 5 mm tap drill diameter, this reduces the average density of the breadboards by around $\frac{\pi(2.5\,\mathrm{mm})^2}{(25\,\mathrm{mm})^2} \approx 3.1\,\%$. As the holes are distributed evenly and the material reduction is low, their influence is neglected in these simulations. Other critical features of the breadboards, which were already explained before, like the central aperture, the eddy current breaker, or the trench to guide the wires out of the FOR, are taken into account.

Figure 3.8 shows the FEA results of the bending of the entire FOR structure under its own weight. Figure 3.8 a) shows examplary the bending of the structure for 30 mm thick breadboards made from an Aluminum alloy with anodized hardened coating layer (EN AW 6061 AHC) where the absolute value of the deviation from the initial position is color-coded to see where the structure bends the most. One can see that the biggest displacement occurs on level 2 of the structure between the central aperture and the entry direction of the vacuum chamber. As the feet between level 1 and level 2 are radially symmetrically placed around the central aperture, but with no support between port 0 and port 1, as well as port 7 and port 0, due to size constraints, this part of the level 2

breadboard has the largest distance to the nearest mechanical support. The eddy current breaker at that position further weakens the structural integrity. Compared to the bending of level 2, level 1, where the support feet are evenly distributed, deforms at least a factor of 3 or 4 times less.

Figure 3.8 b) depicts how the maximum displacement of the FOR changes with the thickness of the two breadboards for the entire structure being made either from stainless steel or the above-mentioned Aluminum alloy with an anodizing layer. The second abscissa shows the corresponding change of the total material volume of the FOR structure when increasing the breadboard thicknesses. To obtain the weight of the entire structure, this value has to be multiplied by the density of the respective material. These are $8.0\,\frac{\mathrm{kg}}{\mathrm{dm}^3}$ for stainless steel and $2.7\,\frac{\mathrm{kg}}{\mathrm{dm}^3}$ for the Aluminum alloy [67].

The trend in Figure 3.8 b) can be understood by comparing it to the bending of a cantilever, a beam which is suspended only on one side and under the load of its own weight. The maximum displacement s_{max} of such a beam under uniform load is described by [68]

$$s_{max} = \frac{\omega_g L^4}{8EI} \tag{3.1}$$

where ω_g is the uniform load per unit length, L is the length of the cantilever, E is the Young's Modulus of the material, and I is the area moment of Inertia. In the discussed case of the bending due to the cantilever's weight, the load per unit length can be described by $\omega_g = \rho \cdot b \cdot d \cdot g$ [68]. ρ is the density of the material, b and d are the width and thickness of the rectangular cantilever, hence $b \cdot d$ is the cross-section area, and g is the gravitational acceleration. The moment of Inertia for a rectangular beam is given by $I = \frac{1}{12} b d^3$ [69]. Inserted into Equation 3.1, one finds a scaling of

$$s_{max} \propto \frac{\rho}{E} \cdot \frac{L^4}{d^2} \tag{3.2}$$

where the first term is material dependent while the second term is solely dependent on the geometry.

The maximum displacement in Figure 3.8 b) depending on the thickness d of the breadboards heuristically agrees with a scaling between $\frac{1}{d}$ and $\frac{1}{d^2}$. This indicates that the geometry-dependent scaling is similar, yet not fully comparable to the model of a cantilever. The presence of multiple mounting points on the breadboards and features on the surface makes the geometry of the FOR more complex, leading to a slight deviation in the scaling compared to the simplified model.

The material-depended term of the cantilever model, however, accurately describes the influence of the material in the FEA simulation. Equation 3.2 states that for bending due to the cantilever's weight, the figure of merit of the material is the ratio between its density and its Young's modulus. For stainless steel with a density of $\rho_{sst} = 8.0\,\frac{\mathrm{kg}}{\mathrm{dm}^3}$ and a Young's modulus of $E_{sst} = 193\,\mathrm{GPa}$ this give a similar, yet slightly worse ratio, than the Aluminum alloy with $\rho_{Al} = 2.7\,\frac{\mathrm{kg}}{\mathrm{dm}^3}$ and $E_{Al} = 69\,\mathrm{GPa}$ [67]. The increase in mechanical strength of the stainless steel cannot fully compensate for its higher density, resulting in an increased load under its weight. This agrees with the results of the FEA simulation, which makes the Aluminum alloy an preferable choice, even comparable to more exotic, yet more expensive and harder to machine metal choices like grade 5 Titanium (Ti6Al4V) with $\rho_{Ti5} = 4.4\,\frac{\mathrm{kg}}{\mathrm{dm}^3}$ and $E_{Ti5} = 114\,\mathrm{GPa}$ [70]. The situation changes once the structure's weight is no longer

the predominant load on the structure. If additional external forces contribute, the role of Young's modulus becomes more important and predominantly defines the deformation of the part [68]. For the FOR, it is not expected that this regime will be entered, as the modules that will be added to the structure are light compared to the overall FOR. Additionally, the thickness of the PoCs will be added to the structure's thickness once bolted to it. The effects of adding and removing PoCs from the FOR will be discussed in Section 3.6.

Another aspect to be looked at in these simulations, besides the static deformations due to gravity, is the dynamic response of the structure to perturbations. While the exact response function to external perturbations is dependent on both the frequency and the amplitude of the external drive and therefore hard to simulate for the general case, one can look at another important figure to gauge the dynamic behavior of the structure, the frequencies of its Eigenmodes, the so-called natural frequencies.

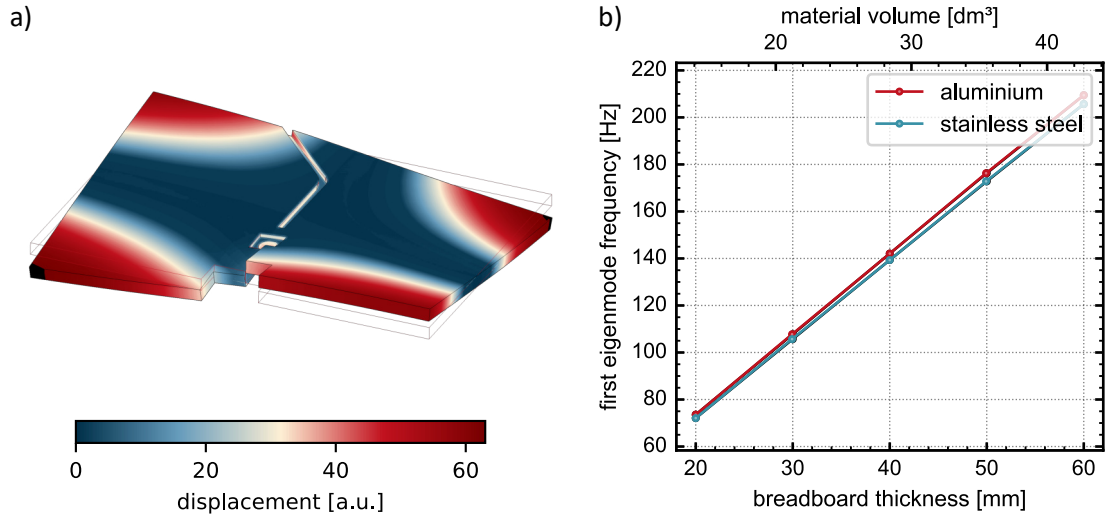

Figure 3.9: Finite-element simulation of the first eigenmode of the level 1 breadboard of the FOR. **a)** depicts how this mode looks on the breadboard, taken from the simulation for a 30 mm thick board made from the Aluminum alloy. The absolute value of the deviation from the initial position without motion is color-coded to visualize the distribution of the deformations. The solid lines indicate the undeformed shape of the board. **b)** shows the scaling of the frequency of the first eigenmode with the thickness of the breadboard for the discussed materials. The change in mass is displayed via a second abscissa indicating the change in material volume.

Figure 3.9 shows the first eigenmode for the unsuspended breadboards. The first mode is located along the diagonals of the breadboard, giving the longest possible wavelength of the excitation. The snapshot of the simulation in Figure Figure 3.9 a) shows the corners along the diagonals of the breadboard oscillating out of phase with respect to each other in the first eigenmode, leading to the visible deformations compared to the nominal layout of the part depicted by the solid lines. An effect of the Eddy current breaker is visible. Figure 3.9 b) presents how the frequency of the first eigenmode, so the first potential resonance frequency, changes with the thickness and material of the board. Heuristically, a linear scaling can be observed with only marginal differences between the two materials.

The behavior can be compared to scaling in the natural frequencies of a free monolithic plate with no additional features cut into it [71]. For those, the frequency of the m,n-th eigenmode $\omega_{FOR,mn}$ is generally described by

$$\omega_{FOR,mn} = \sqrt{\frac{D}{m_A}\frac{u_{m,n}}{(\frac{L}{2})^2(\frac{b}{2})^2}} \tag{3.3}$$

where L and b are the length and width of the plate, m_A is the mass per unit area, $u_{m,n}$ describes the strain due to the mode shape and D the flexural rigidity of the material. The latter can also be written expressed by $D = \frac{Ed^3}{12(1-\nu^2)}$ with E Youngs modulus, ν poissons ratio, and d the thickness of the plate. The mass per unit area is directly proportional to the density of the material. The frequency of the first eigenmode scales

$$\omega_{FOR,mn} \propto \sqrt{\frac{E}{\rho(1-\nu^2)}} \cdot \sqrt{\frac{d^3}{\rho(L^2B^2)}} \tag{3.4}$$

where the first term is material-dependent and the second term geometry-dependent. This scaling with the thickness of the breadboard roughly agrees with the scaling observed in Figure 3.9 b), which has been heuristically described as linear. It also shows that the marginal difference between Aluminum and stainless steel can be expected. As already discussed above, the ratio of Young's modulus and the density is very similar for both materials. The last contributing material property is the Poisson's ratio ν, which describes the relative transverse deformation of a material under load. For the Aluminum alloy we discuss here, it is 0.33 and for stainless steel 0.30 [67], hence no significant material difference is to be expected.

It can be concluded that it is not possible to shift the excitation frequency of the first resonance of the FOR breadboards very far by changing the material or the thickness of the plate within reasonable bounds. This means that it will not be possible to shift the first resonance so far up that the frequencies of all potential sources of vibration are far below the first resonance frequency of the FOR. In the case of HQA-ONE, the most significant source for potential vibrations is the turbulent cooling water flux through the magnetic field coils. In principle, this can lead to excitation frequencies of up to 2 kHz (see Section 4.4), far above a possible shift of the first breadboard resonance frequency.

All in all, the results of these simulations led to the decision to select the Aluminum alloy as the material of choice for the FOR. It provides similar or even slightly better performance than stainless steel, is cheaper, and simpler to machine and handle. We opted for a breadboard thickness of 30 mm to achieve reasonable performance while limiting the weight per breadboard of the FOR to around 60 kg to simplify the construction of the structure on the optical table by enabling assembly without needing special equipment like portable floor cranes.

3.3.3 Performance of the FOR design

With the whole design of the mechanical reference system now being set, we can conclude the FOR design by simulating the mechanical performance for the full system. The simulations generally include the same simplifications as those before. In addition to the general FOR design, these simulations now also include the four M8 threaded rods made from

Titanium near the central axis of the structure that will be used in Section 3.4 to mount the magnetic field coils. Although this makes the simulations slightly more specific to the use of that coil mounting, it is expected that these rods will have a significant influence on the static bending of the structure, as they are mounted in proximity to the section that bent the most in the other simulations. The simulation of the chosen FOR design without the Titanium rods has been presented Figure 3.8 a).

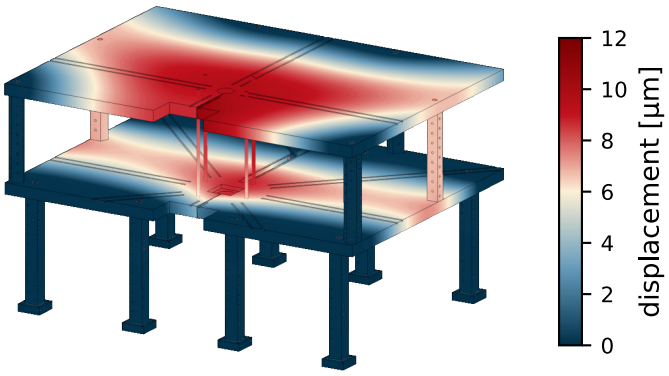

Figure 3.10: Finite-element simulation of the static deformation of the FOR due to its weight with the chosen breadboard thickness of 30 mm and the Aluminum alloy as the material. Additionally, the influence of the Titanium rods around the central axis that are used in the mounting of the magnetic field coils is included. The absolute value of the deviation from the initial position without gravity is color-coded on the structure.

Figure 3.10 now shows static deformation of the structure with the rods. The Titanium rods act as struts near the central axis and provide additional support to the center of the breadboard of level 2, which was identified as a weak spot in the simulations above. When comparing the two simulations, one observes that the titanium rods reduce the maximum static deformation roughly by a factor of four and limit the bending to around 10 µm, with the deformations of level 1 and level 2 being on a similar scale. Therefore, when adapting HQA for other atomic species where other coil geometries and mountings are needed, it is advisable to include support structures like these rods near the central axis to reduce deformations of the mechanical frame of reference.

Looking into the dynamical properties of the full FOR, the first six eigenmodes and respective frequencies are simulated and presented in Figure 3.11. One observes that the first five modes are set by the feet of the FOR. The first two modes are in phase oscillations of the two breadboards in the two principal directions structure, along the axis of port 0 and port 4 (mode 1) as well as along the axis of port 2 and port 6 (mode 2). The third mode is a rotational mode around the center axis of the rectangular breadboard, which, however, does not coincide with the designed central axis of the FOR. Modes 4 and 5 are out-of-phase oscillations of the two breadboards, and mode 6 appears to be the first excitation mode of the breadboards themselves. This means that there are modes present, due to the feet, which can be excited even below the first breadboard mode. However, these modes have different effects on the modularity aspect of the design. The first five modes provide translational oscillations of the breadboards, but barely deform them. That means that these modes disturb the alignment of the mechanical central axis with

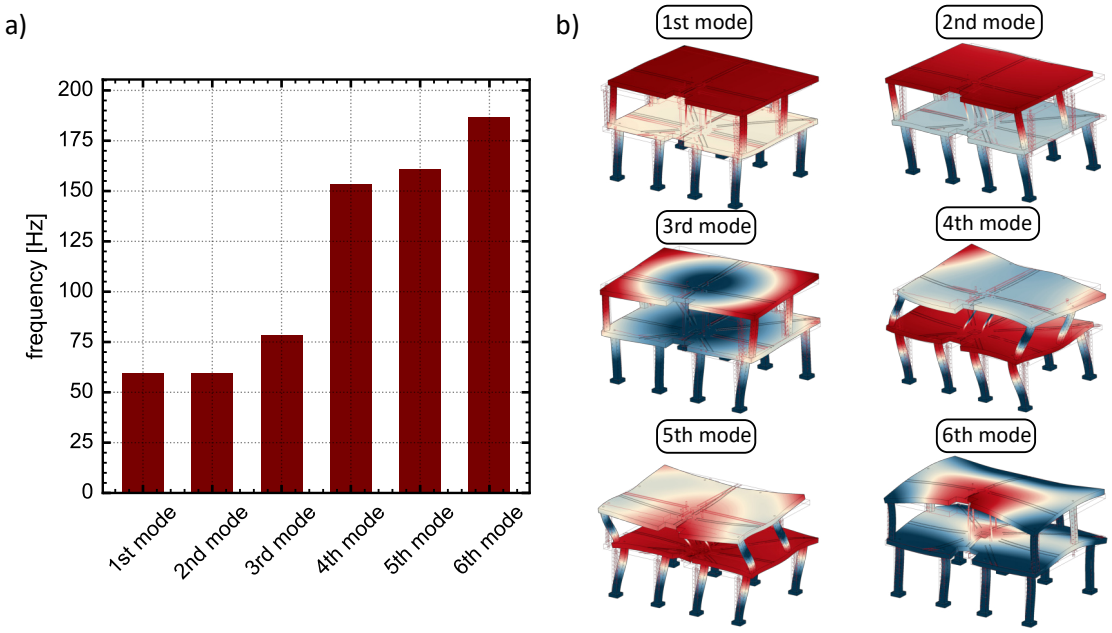

Figure 3.11: Finite-element simulation of the first six eigenmodes of the FOR for the setup according to Figure 3.10. a) depicts the natural frequency of the first six eigenmodes, b) depicts these modes in analogy to Figure 3.9 a) with the absolute value of the deformations in motion accordingly color-coded. The unperturbed, stationary position in indicated by the solid lines. Modes 1 and 2 are in phase swinging modes in the two principal directions of the structure. Modes 4 and 5 are opposing phase swinging modes in the two principal directions. Mode 3 is a torsion mode around the symmetry axis boards which is not the designed central axis of the FOR. Mode 6 is the first breadboard mode of the FOR, so the first one which is associated to the thickness of the FOR boards and not the feet.

respect to levels 0,1, and 2. However, the modules on these levels themselves will locally remain referenced to each other, just commonly shifted. Mode 6 is the first mode to introduce disturbances on the level itself. Mode 3 might also introduce some disturbances to the individual level, as the rotation axis does not overlap with the designed central axis. Therefore, this mode might introduce both intra-level and inter-level shifts in the structure.

While adding modules and optics to the FOR will undoubtedly alter the exact number for the static deformations (see Section 3.6) and the resonance frequencies, it can be helpful to understand the frameworks structural integrity and modal structure to estimate what kind of an effect future modifications to the FOR have on the system without performing extensive FEA simulations. However, a key takeaway should be that the magnetic field mounting can significantly improve the stability of the structure. The mounting for our Lithium realization of HQA, HQA-ONE, will be presented in the next section.

3.4 Magnetic Field assembly

With the layout of the FOR now being set, we can move on to the features of HQA that are crucial to define the functionalities of the experiment later. These features, depicted

in Figure 3.1 as the puzzle pieces on the right, include the capabilities for magnetic field addressing and modular optical access. This section is dedicated to the semi-permanent magnetic field assemblies. The magnetic field addressing requirements, however, can significantly differ depending on what atomic species the specific experiment was built for. Therefore, it is not very practical to develop a one-size-fits-all solution for the magnetic field coils in the scope of HQA, but to individually develop these assemblies for the used species. Applying the concepts of HQA to different elements or isotopes will therefore require potential adaptations to the coil geometry.

Nevertheless, as discussed in Section 3.3, the mounting of the magnetic field assembly can help improve the stability of the FOR and be utilized for the placement of diagnostic tools (see Section 3.5). In order to comply with the presentation of general and broadly applicable concepts of HQA in this chapter, this section will only present the mounting we use for the magnetic field assembly at HQA-ONE. These are designed for the coil geometries required for working with ^{6}Li but are in principle also adaptable to other coil geometries. Details about the coils themselves, their control, and the magnetic field addressing are waived and will be discussed in Section 4.3 along with other specifics of HQA-ONE.

3.4.1 DC magnetic fields

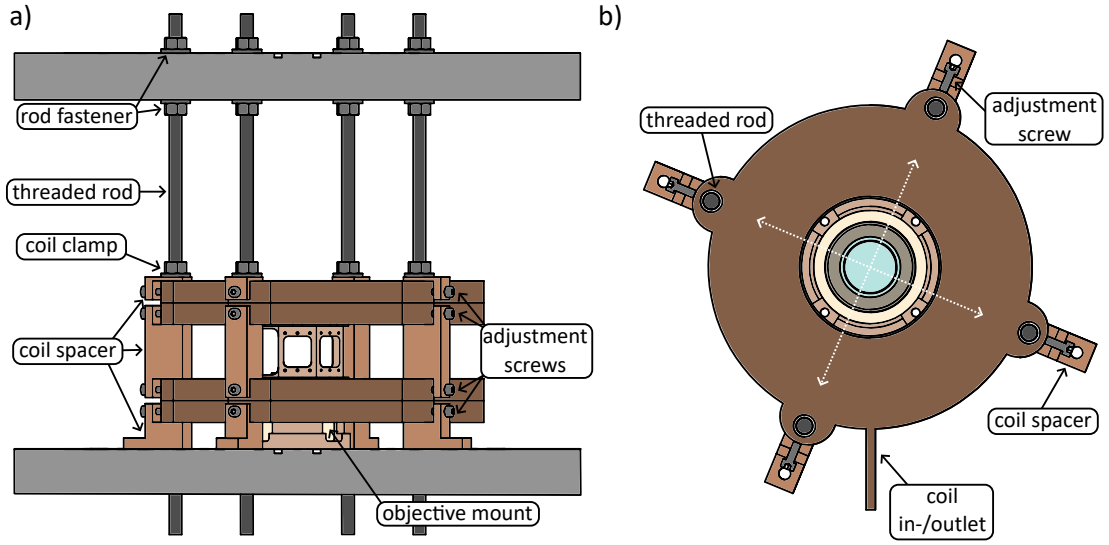

Figure 3.12: Annotated sketch of the magnetic field assembly of HQA-ONE optimized for ^{6}Li experiments within the concept of HQA. **a)** depict how the magnetic field coils are mounted in the FOR. **b)** illustrates the mechanism with which the magnetic field coils can be positioned to overlap their symmetry axes.

The mounting of HQA-ONE's DC magnetic field coils in the FOR is depicted in Figure 3.12. These coils can provide the magnetic quadrupole field required for a MOT as well as large offset fields up to 2000 G required for interaction control in experiments with ^{6}Li. To achieve this, the assembly consists of four differentially controllable coils, each separately encapsuled in a high-temperature-rated epoxy resin[9] designed for high thermal

[9] Araldite and Aradur 229

endurance and thermal conductivity compared to other resins. Each epoxy mold with a coil inside is 14 mm thick, has a inner diameter of 70 mm and an outer diameter of 160 mm.

Two coils are placed above the designated center point of the FOR, two of them below. The upper and lower stacks of coils are placed such that their respective center are in a Helmholtz configuration. That means that driving all coils equally will result in a homogeneous offset field. Balancing the current in both stacks relative to the inner and outer coils also allows control over the magnetic field curvature at the designated center point of the FOR. For example, driving the outer coils with more current than the inner coils leads to the stacks no longer being in a quasi-Helmholtz configuration and will introduce a curvature at the center.

To position the coils accordingly, we use threaded rods and spacers. The general mounting of the assembly is shown in Figure 3.12 a). There are four M8 threaded rods made from Titanium around the center axis of the FOR. Each with a 90° angle to each other and a 22.5° angle relative to the axes of the respective level 1 ports on the FOR to avoid blocking optical access. These rods are screwed into corresponding threads in the level 1 breadboard and pass through the level 2 breadboard via through holes. Nuts above and below the upper bread clamp the rod tightly into the FOR structure and additionally provide support for the level 2 breadboard with the rods serving as struts (see Section 3.3). On each rod are spacers made from PEEK to position the coils accordingly for a center point of the FOR 62.7 mm above the level 1 breadboard. This height is chosen to match 12.7 mm thick modules in that plane with 50 mm beam height. More on that in Section 3.6. The PEEK spacer has a through hole to be attached to the rods and an M4 screws for each coil pointing radially towards the center axis. The angle of the lowest spacer is set on the FOR with a through hole for an M6 screw to fasten the spacer in the position which does not obstruct level 1 access.

The epoxy body of the coils has four 11 mm wide through holes for titanium rods. With this, all coils can be coarsely placed around the central axis of the FOR. However, the 11 mm hole provides around ±0.75 mm clearance for the M8 rod. As depicted in Figure 3.12 b), this clearance can be used to position the coils parallel to the breadboard plane via the M4 adjustment screws provided by the PEEK spacer. Loosening the adjustment screw on one side while tightening the opposing screw moves the respective coil in that axis as indicated by the white arrows in Figure 3.12 b). This degree of freedom (DoF) is needed because the position of the coil inside the epoxy body is not specified with sufficient precision for a purely passive approach. Once positioned, additional M8 nuts and washers on the threaded rods (coil clamps) are tightened to clamp down and lock the coil assembly in its desired position.

To summarize, the coils can provide a magnetic quadrupole field in an anti-Helmholtz configuration, as required, for example, for the MOT. The zero of the quadrupole field affects the MOT and especially the compressed magneto-otical trap (cMOT) position. It can be shifted parallel to the level 1 breadboard by mechanically adjusting the coils with the adjustment screws, and vertically by tuning the common offset current between the two coils that provide the quadrupole field. Therefore, it is possible to overlap the position of the cMOT with the designated centerpoint of the FOR. The coils can also provide an offset field when operated in Helmholtz configuration.

Additionally, the magnetic field curvature can be tuned by differential control of the coils in each stack. However, the resulting saddle in the middle of each coil can differ from the geometric center axis, for example due to the influence of the lead wires and

broken radial symmetry at the in-/outlets. In the future, when precise control of the magnetic field saddle becomes important, one can use ferromagnetic pieces of steel and place them around the coils such that they deform the magnetic field lines and therefore shift the saddle. This is a well-established technique in our group and has proven to allow positional accuracies on the order of a few tens of micrometers [72]. In this assembly, with the tuneable curvature, this has to be performed for either one set of curvatures, while keeping the other aligned positions in place, or for many sets iteratively, depending on the experimental requirements. At the time this thesis is being written, the magnetic field saddle control is not yet implemented.

3.4.2 Addressing cage

Mounted in the center of the large DC magnetic field coils, around the objective mount, is a second layer for the magnetic field interface in the assembly. A structure, CNC-machined from PEEK, the so-called *addressing cage*. It is shown in detail in Figure 3.13 and visible in relation to the large magnetic field coils in Figure 3.12 a). The addressing cage is an adaptation of a similar system developed by Naman Jain in the group of Dr. Philipp Preiss at the Max Planck Institute of Quantum Optics in Garching. The general geometry of the cage follows their design and was, with prior agreement, adapted to be used as a part of HQA-ONE. The specific features that were adapted from their design will be pointed out in the description of the addressing cage.

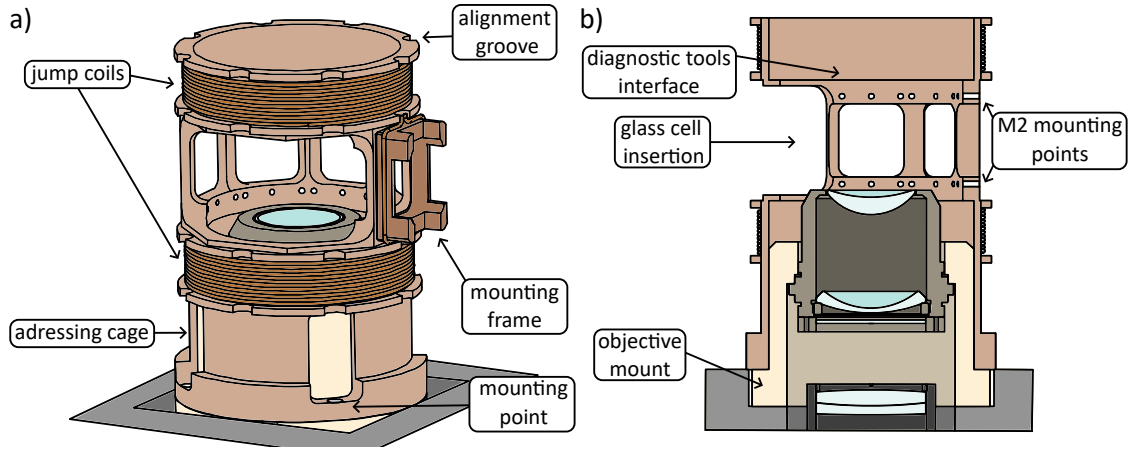

Figure 3.13: Annotated sketch of the addressing cage around the experiment's objective mount. **a)** presents an overview over the of the addressing cage, its design, and its functions. **b)** shows a cross-sectional view of the addressing cage and how it is mounted on the objective mount.

Just like the objective mount, the tower-like structure has an outer diameter such that it fits through the center clearance of the DC magnetic field coils. Both can be taken out of the setup without disassembling the coils. The maximum outer diameter of the cage is 68 mm, the inner diameter of the coil body is 70 mm. So, even after relative displacement of the DC field coils with their respective adjustment screws, both the cage and the objective mount can still be taken out with the coils in place.

As shown in Figure 3.13, the cage is placed on top of the objective mount and machined such that it just fits around the outer diameter of the objective mount in order to passively

overlap their respective center axes and therefore to indirectly place the addressing cage on the central axis of the FOR. The objective mount has four through holes for M4 screws to secure the mount on the FOR. Two of these are used to secure the objective mount and are therefore mounted slightly recessed below the addressing cage. The other two screws pass through the respective mounting holes of both the cage and the objective mount. A narrow clearance of the M4 screw in the through hole of the cage defines its angle around the central axis. This screw placement allows the removal of the addressing cage from the FOR without necessarily taking out the objective as well, despite being mounted together. The alignment grooves in Figure 3.13 are sized such that it is possible to reach the screws on the mounting points with a long hex key when installed in the platform inside the DC magnetic field coils.

Beyond the dimension and mounting, the addressing cage mainly serves three different functionalities.

First, it provides five mounting points for small mounting frames (see Figure 3.13) which can be attached to the cage via plastic M2 screws. The frames can be used, for example, to position coils and antennas for RF or MW addressing in close proximity to the latter atom position without any metal parts shielding them. Having these mounted on the frames allows for easy placement on the platform or for exchanging them. This allows for modularization of these components. The mounting points are provided on all ports between port 2 and port 6 (compare Figure 3.6), each with one opening in the cage with six mounting points per port. The other three ports must remain unobstructed to allow the glass cell to be slid into position for the FOR center point, around which the addressing cage is located. The cage is dimensioned such that it allows the glass cell to fit inside, without limiting the NA on the side windows. This geometry was copied with consent from the design of Naman Jain at the Max Planck Institute of Quantum Optics in Garching.

Second, the cage provides the mounting point for an additional set of DC magnetic field coils, the so-called *jump coils*. These are much smaller than the large outer set of coils, which in principle allows them to be switched much faster, as with the smaller volume, also the total amount of energy stored in the magnetic field, which has to be dissipated, is much smaller. These coils are not intended to provide high magnetic fields, but to work in tandem with the large DC field coils and allow faster magnetic field jumps for interaction quenches [13]. At the time this thesis is being written, these coils are not manufactured nor integrated at HQA-ONE. They remain an optional upgrade for the future.

Third, it provides an interface for in situ diagnostic tools. A fundamental goal of HQA is to allow the deployment of diagnostic tools in the setup, both for pre-characterization of the modules as well as in-situ diagnosis (see Figure 3.1). When the glass cell is retracted from the platform, the addressing cage provides an ideal platform to place sensors, for example, cameras, at the center position of the platform with the modules still installed. For this, the addressing cage provides a well-defined cylindrical step on the inside on which sensor mounts can be placed. Grooves on the directions towards all eight ports break the continuous rotational symmetry of the internal step and allow the design of diagnostic tools that are passively oriented to the ports. This topic will be further discussed in Section 3.5.

3.4.3 AC magnetic fields

As presented in the previous paragraphs, the addressing cage provides a versatile platform for coils and antennas for RF or MW to address the atoms in the center of the FOR.

It allows to easy placement and replacement of the coils and antennas on the mounting frames. A second layer of modularity is added at HQA-ONE for the matching electronics of the coils on the frames. To achieve this, we decouple the impedance matching of the coil from the mounting frame. The coil is placed on the mounting frame and equipped with an SMA connector. A printed circuit board (PCB) is connected via an SMA cable and equipped with two capacities, one in series and one in parallel with the coil, to match the impedance of the coil to the incoming signal at the desired frequency. As these PCBs are only connected via cables, exchanging them and operating the same coil matched to a different frequency becomes possible and provides an alternative to having multiple coils matched for different frequencies attached to the addressing cage. In experiments with ^{6}Li this is important, as, due to the Zemann shift in the wide range of magnetic offset fields, RF transition frequencies can drastically vary. It is not possible to frequency match a RF-coil over the full range of magnetic fields up to 2000 G for high Q-factors. The described decoupling of the coil and matching circuit is only applicable for the RF transitions in ^{6}Li, MW frequencies do not allow additional lead lines, as these would be long compared to their wavelength, leading to radiation losses [18].

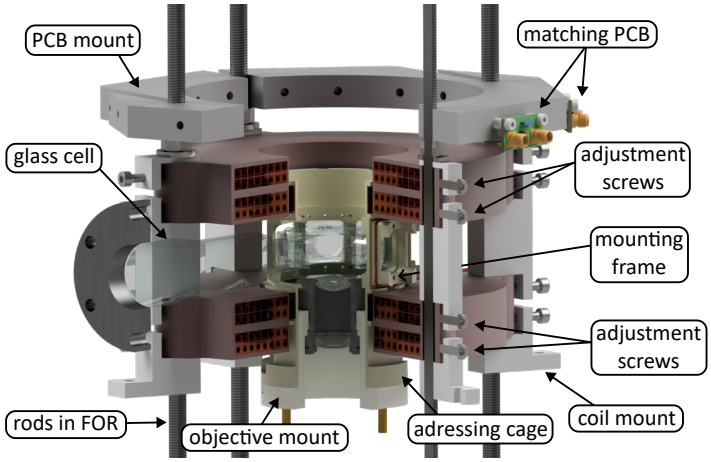

Figure 3.14: Rendering in a 3/4-cross-sectional view of the entire magnetic field assembly of HQA-ONE with the glass cell inserted.

Figure 3.14 shows an annotated rendering of the entire magnetic field assembly with the glass cell inserted and all previously discussed components visible. Additionally, a PCB mount is depicted above the upper coil stack. This 3D printed structure is inserted around the four Titanium rods via three slits and resting on the four nuts that clamp down the large DC field coils. The PCB mount provides two threads per port to mount the PCBs for RF matching. Its position is not critical, and due to its mounting with three slits, it can be removed from the assembly without affecting any other component.

3.5 Diagnostic tools

The next puzzle piece of Figure 3.1 to be discussed is how to utilize diagnostic tools within HQA. For this, we differentiate between the external characterization tools for the PoC (Section 3.6) and mPoC (Section 3.7) modules and the in-situ diagnostic tools to verify the field distributions at the center point of the FOR. As the former are not physically

attached to the FOR structure, they will be discussed in the respective sections of the modules; options for the latter will be discussed in this section.

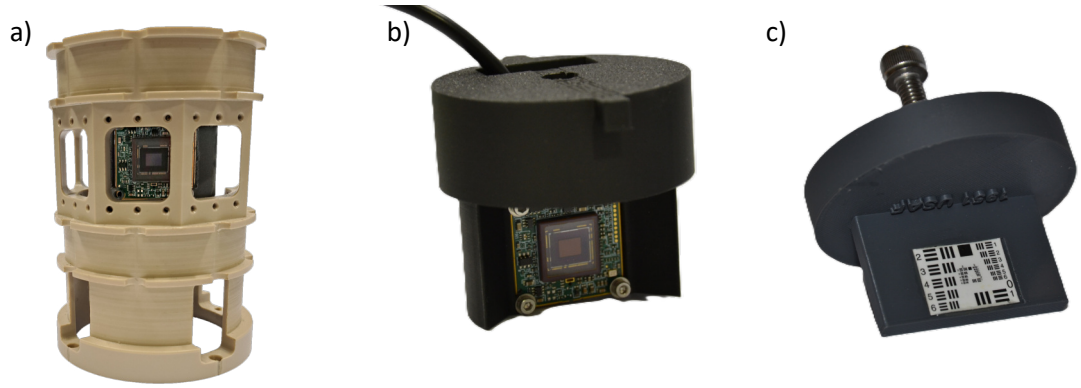

Figure 3.15: Selection of diagnostic tools that can be inserted into the addressing cage. **a)** shows a sideward-facing camera chip as part of a diagnostic tool in a mockup of the RF-cage. **b)** shows a side-ward facing camera chip in a 3D printed mount with alignment hooks for use in the addressing case. **c)** shows a 1951 USAF resolution test target on a 3D printed mount for magnification and imaging calibration.

Section 3.4 showed that the addressing cage as part of the magnetic field assembly can provide a well-suited interface for in-situ diagnostic tools. This mounting point will be the first one we look into. Accordingly, Figure 3.15 presents a selection of corresponding tools that can be inserted into the addressing cage to probe the center point of the FOR. At the time this thesis is being written, we mainly use 3D printed sensor mounts[10] for the diagnostic tools, as this provides quick iteration times and flexibility. Manufacturing these mounts from other materials, like Aluminum, is also possible.

The general design of these tool mounts contains a cylindrical base that can be inserted into the addressing cage from the top and rests on the cylindrical step (see Figure 3.13 b)). Combined with being sized such that it just fits inside the inner diameter of the cage, it provides a well-defined position inside the cage and indirectly in the FOR. With this positioning mechanism, the mounting structure for arbitrary tools can be rapidly added, aligning the sensor position with the center point of the FOR on the base of the part in the design and manufacturing the mount for the diagnostic tool, for example, by 3D printing.

Figure 3.15 a) shows a mock-up of the addressing cage with a side-ward facing camera diagnosis tool inserted to demonstrate how these can be positioned. The camera chip on the PCB of a regular machine vision camera[11] is mounted in a 3D printed holder such that it is placed at the center point of the FOR. Such camera tools can be used for final alignment and in situ overlapping of lightfields provided by different modules.

Figure 3.15 b) is a photograph of another side-ward diagnosis tool design for lightfield verification and alignment, Figure 3.15 c) depicts a 1951 USAF resolution test target for in-situ calibration of magnification and performance of imaging systems on the PoC modules. Both mounts feature a top thread for inserting a screw, which serves as a handle to simplify tool insertion and removal in the experiment's limited space, thanks to the magnetic field assembly and FOR around. A difference between them, however, is that the USAF target

[10] We use a BambuLab X1C as our primary 3D printer
[11] FLIR FFY-U3-16S2M-C

mount has a continuous rotational symmetry and can therefore be inserted at arbitrary angles. The camera mount has two visible hooks on the cylindrical structure. These fit into the alignment grooves of the addressing cage (see Figure 3.13 a)) and break the continuous symmetry into a discrete one to ensure the camera chip is, by design, always oriented perpendicular to the respective port on the FOR.

Other notable tools we developed include cameras facing toward the high-NA for verification and alignment of the mPoC modules, as well as light sources that provide a guide beam for optics addressing the FOR's center point. One can imagine a wide range of other diagnostic tools, for example also magnetic field probes; the only constraint is that the sensor has to physically fit into the addressing cages internal volume.

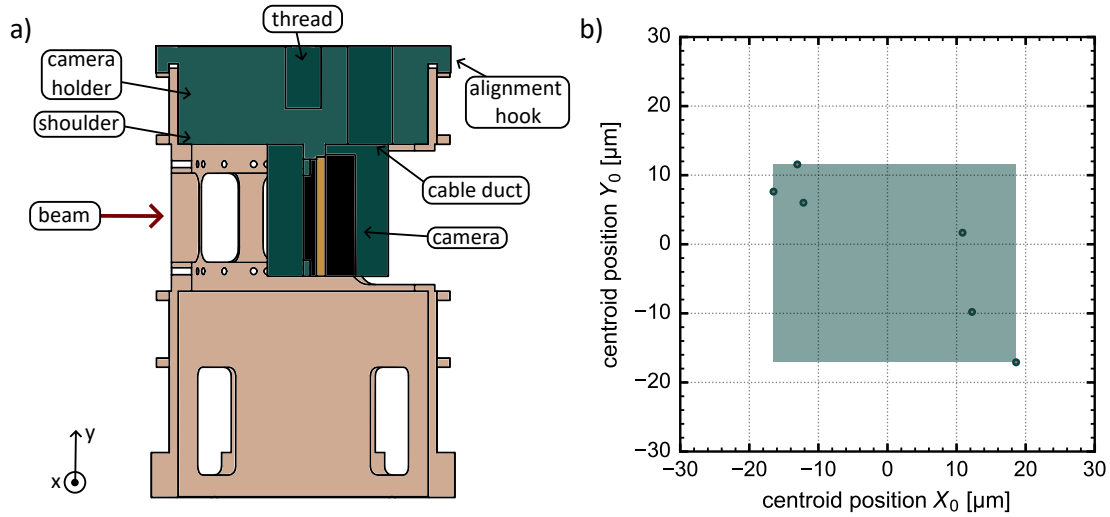

Figure 3.16: a) Annotated cross-sectional sketch of a sideward-facing camera tool in the addressing cage. The tool depicted is the 3D printed one in Figure 3.15 b). b) Positioning repeatability (precision) of the camera tool in the RF-cage when placing it multiple times in the addressing cage and measuring the position of a fixed beam on the camera chip. Zero point is set to the average position of the six repetitions. The box indicates the maximum deviations in both axes during the testing. It has a width of ±17.5 µm and a height of ±13.3 µm.

In order to test the precision of the diagnosis tool placement with the 3D printed mounts, we placed the side-ward facing camera tool depicted in Figure 3.15 b) in the addressing cage, irradiated the camera chip with a static, collimated laser beam, and repeatably removed and re-inserted the diagnosis tool. In each iteration, we took a picture with the camera and extracted the centroid position of the beam on the camera chip via a 2D Gaussian fitting function. A cross-sectional sketch of the setup is shown in Figure 3.16 a). The resulting centroid locations for six iterations relative to the mean position of the centroids are plotted in Figure 3.16 b). The box in the background quantifies the maximum deviation between the datapoints in both axes.

On the x-axis, locked in position by the two alignment hooks in the respective grooves, one finds a maximum deviation of ±17.5 µm. Notably, the data points cluster near the two extremes of the spread. This can be explained as the points where the hooks touch the edges of the grooves. When re-inserting the camera mount into the cage, it easily happens

that it is placed with one side touching the edge of the groove. The spread of $\pm 17.5\,\mu m$ can therefore be attributed to the clearance of the alignment hooks in the respective grooves.

On the y-axis, locked in position by the cylindrical base of the mount resting on a step in the cage, one measures a maximum deviation of $\pm 13.3\,\mu m$. Also, here, the data seems to cluster, leading to clusters in two corners of the box. This can be explained by either imperfections in the interface between mount and cage, meaning that they are not perfectly parallel, or by a slight tilt in the camera mounting in the 3D printed part, both resulting in rotation-dependent shifts of where the camera center sits vertically. Either way, the extreme positions on the x-axis can lead to corresponding shifts in the y-direction.

Beyond the described placement method for diagnostic tools, it is also possible to place them on the PoC modules and have an arm-like structure with a sensor that reaches into FOR's center point. As presented in Figure 3.6 c), port 0 provides a PoC interface just for the reason of using it for sensors. However, other ports can be used as well, but might already be occupied with other modules. Port 0 always remains accessible with the glass cell retracted. Mounting the diagnostic tools on PoCs is especially viable for large tools with translation stages or large attachments to the actual sensor, which cannot be placed in the addressing cage. Of course, the foundation of this is to provide a design and to understand the capabilities of the PoCs and their mounting. A topic we will look into in the next section.

One final remark on the diagnostic tools, however, is that Figure 3.16 b) shows that while the tools can provide optimal relative measurements, for example in overlapping two beams on the same camera chip, and medium precision for placing the tools in the cage with variations on the scale of a few ten micrometers, the offset from the center point of the FOR is hard to determine. This means that the mechanical realization of the diagnosis tools provides a precise, yet not necessarily accurate, toolbox. This differentiation between precision and accuracy is also something that needs to be discussed for the development of the modules and their mechanisms.

3.6 Optical modules - pieces of cake

This section deals with the first of two types of optical modules in HQA, the so-called Piece of Cake (PoC) modules for optical access to the center point of the FOR perpendicular to the central axis. As modules in the sense of Figure 3.1, they are intended to allow regular exchange. Therefore, the mounting mechanism must balance sufficient precision for passive alignment of the PoC with ease of use to allow regular and user-friendly exchange.

As a first step, we will therefore look into the positioning requirements to achieve passive alignment in the sense of HQA with the modules.

3.6.1 Operative regions

An essential concept for modularization and passive alignment in the context of HQA is the operative region (OR). The essence of each optical module is to provide a light field distribution at the center position of the FOR where it intersects with the light fields from all other modules and where, in the end, the atomic clouds will be located. Each light field has to fulfill predefined requirements for nominal operation. Depending on the function of the light field, these requirements can include, for example, shape, trap frequency, or

contrast. We refer to the region in space in which the module and its optics can generate a light field that complies with these requirements as operative region (OR). Within this region, the light field can be shifted around while still fulfilling its performance criteria. In the simplest case of a ODT generated from a focused beam, this corresponds to the three-dimensional region in which the focus can be moved around by fine adjustment of the optics while maintaining its critical design parameters, for example, the beam waist. The precise shape of the operative region (OR) for each module depends on various factors like the desired light field functionality and its implementation on the module. Limits can arise, for example, due to the DoF and their tunability on the optical setup, clipping due to the size of the used optics, or their FOV potentially underperforming compared to the requirements for large displacements. Dimensions of the OR can range in principle from a few micrometers to several millimeters. The challenge for the modules and their mounting in the context of modularization is to passively place them such that even when exchanging, there is still sufficient overlap between the ORs of all modules such that all modules can work as required at the same time. [57]

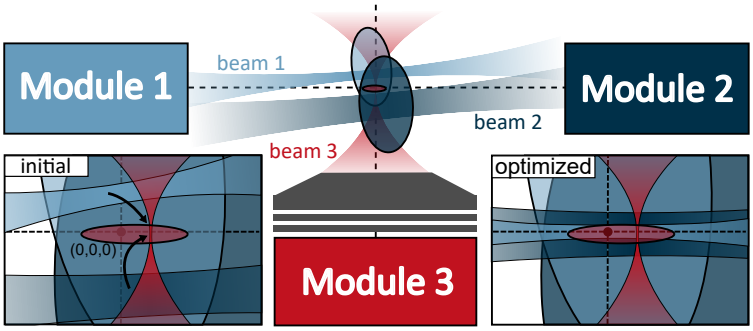

Figure 3.17: Sketch of the passive interfacing concept of three different light fields generated by three different optical modules. Each module has an operative region (OR), here shown as ellipses, within which the generated light field can fulfill the desired requirements. In order to get all modules running at the same time, these operative regions have to overlap. The light field from each module can be fine adjusted within its respective operative region, which remains static. This optimization step is depicted in the inset. The fundamental idea behind passive alignment within HQA is to mechanically ensure that all modules are placed such that the operative regions overlap. This directly leads to position requirements for the mounting mechanisms of the modules. Figure and caption adapted from [57].

Figure 3.17 presents this concept in a sketch. The picture shows the intersection of 3 different light fields generated from three different modules with their ORs drawn as ellipses. One can think here, for example, of the overlap of three different ODTs. In the sketch, two PoC modules (blue) are supposed to be overlapped with a mPoC module (red), which provides a light field with high-NA access via the objective. All modules are to be placed on the FOR with its own designated center point indicated by the dashed grey lines. All modules are pre-aligned on a separate testbench such that they should in principle be aligned to the center point of the CNC machined FOR. However, due to the tolerances and potential offsets when transferring the modules to the FOR they will not be perfectly positioned. This would require a zero-tolerance mechanism which is not feasible.

But, if the tolerance is smaller than the second smallest OR, a passive overlap of the ORs can be achieved. That means all modules can be operated according to their requirements simultaneously. We call this scenario passive alignment of the modules. They are passively placed such that they allow common operation. In the sketch, this is displayed in the inset in the 'initial' depiction.

With all modules set, one now has to optimize the overlap of the light fields of the modules within their ORs. To do this, it can be helpful to keep one beam as a reference constant. As depicted in Figure 3.7, the high-NA objective of our setup is mounted directly to the FOR without any degree of freedom. A diffraction-limited optical tweezer generated with this objective will have a small OR due to the high-NA and diffraction-limited performance. It will be located in close proximity to the mechanical center point of the FOR with a slight offset of less than a few tens of micrometers due to imperfect mounting and manufacturing tolerances (more on that in Section 3.7). Therefore, as the modules are pre-aligned to the mechanical center point, a narrow tolerance mounting for the PoC modules will ensure that their ORs also passively overlap with the OR of the optical tweezer.

The final alignment step with the modules integrated into the FOR is to move their light field with the DoF of the optics to the optical tweezer position. Depending on the size and function of the light field (for example an ODT) optimization will already with an initial signal that can be optimized (in the example loading atoms between trap and the tweezer) or for features smaller than the tolerances by finding the initial overlap with the in-situ diagnostic tools which provide very precise relative measurements (for example by imaging the light fields on the same camera chip). The final situation post fine alignment is sketched in the inset labeled 'optimized'.

3.6.2 PoC design

The Piece of Cake (PoC) modules, intended for modular optical access through the side windows of the glass cell, are supposed to be mounted on level 1 of the FOR (see Figure 3.6). We designed them as smaller breadboards on which standard optical and optomechanical components could be mounted, just like one would build them on any other breadboard. The only difference would be that for the PoC breadboard, there would be a mechanism in place to know precisely where it is placed on the CNC machined FOR while still resting directly on top of each other and their surfaces sliding on each other during insertion and removal of the module. Anodizing both the FOR and the PoC breadboards is supposed to provide a hardened, scratch-resistant surface.

Just like the port symmetry on level 1 of the FOR due to the glass cell, the shape of the glass cell, the PoCs have to fit the octagonal symmetry, leading to a triangular base shape of the module breadboards. It is this shape that led to naming them Piece of Cake (PoC)[12]. Figure 3.18 shows the general shape and placement mechanism of the PoC breadboards. Their size and shape in Figure 3.18 c) started from the mentioned triangular base shape, limited by the size of the FOR. The top part of the triangle is cut off as the center part of the FOR houses the coil assembly (see Section 3.4). The smaller cutouts left and right of the top are a result of the space taken by the PEEK mounts of the DC magnetic

[12] Additionally, their usability is supposed to make adding and changing optical setups on quantum gas apparatuses a piece of cake. Coincidentally, PoC also commonly stands for proof of concept, which is exactly what we are doing for HQA in building HQA-ONE. Hats off to Tobias Hammel for this creativity!

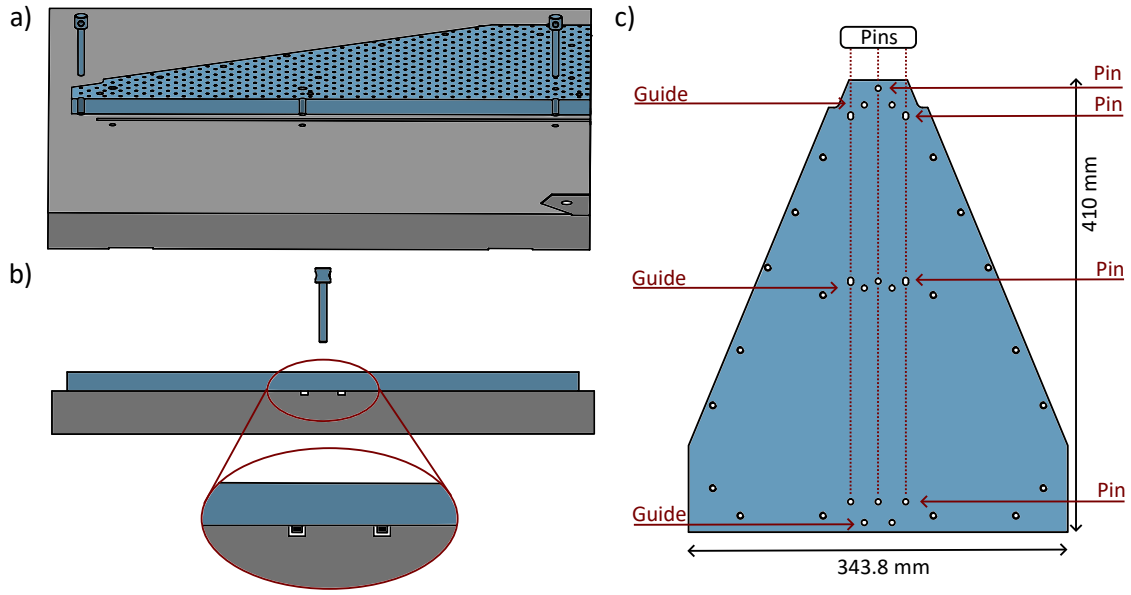

Figure 3.18: Sketch of the mounting mechanism and layout of the PoC modules for modular optical access on level 1 of the FOR. **a)** A single PoC on the simplified FOR without any holes in it. The two pins required for the placement of the module are shown above the respective insertion position. The PoC is shown in a cross-sectional view for easier identification of the holes for the pins. **b)** detail of the guiding pins of the PoC which slide in grooves of the FOR and provide coarse alignment during insertion of the module. **c)** General size of the standard PoCs with indication of the positioning pin placement options, the guiding pin positions, and the mounting threads for securing the PoC on the FOR. The matching hole pattern can be found on every port of level 1 of the FOR.

field coils in the magnetic field assembly. Moving down the sketch, the triangular base shape is visible. However, the outer edge of the legs of the triangle is narrowed in parallel by 2.5 mm per side compared to the full usable width. The resulting 5 mm gap between neighboring modules simplifies inserting and removing them without risking hitting and misaligning the module next to it accidentally. The larger cutouts towards the base of the triangle allow the placement of the feet between the level 1 and level 2 breadboard of the FOR.

The placement of the PoC modules on the FOR is done with stainless steel reference pins. Such Pins are standard precision components in mechanical engineering and are commercially available in various sizes and lengths with narrow width tolerances. We use pins with a diameter of 4.98 mm and place them in 5.00 mm precision drilled holes. This yields a tolerance of the pins in the drilled holes of around $\pm 10\,\mu$m minus the thickness of the anodization layer of the Aluminum which effectively shrinks the hole by a few micrometer. During the initial prototyping phase, we also experimented with pin combinations with a tighter tolerance. However, we found that these regularly did not fit into the holes or got stuck in them. A possible reason for this is that the central axis of the hole for different parts is not necessarily perfectly parallel, as these pieces cannot be drilled together on top of each other. The chosen diameter subjectively appeared to be the sweet spot between

narrow tolerance and usability.

Figure 3.18 a) shows a PoC breadboard in a cross-sectional view on a simplified depiction of the level 1 breadboard of the FOR. Two pins are depicted hovering above their intended position. An Aluminum head with a hole in it, mounted to the pin, provides a stop and prevents the pin from falling through the boards. Additionally, the hole serves as a gripping point to pull the pin out if it ever gets stuck. When placing the first pin through the PoC breadboard in the FOR, one effectively defines a rotation axis (within the tolerance of the pin and the hole) for relative movement between the two parts. The insertion of the second pin consequently only has to constrain the angular movement around the rotation axis. For that reason, it is generally helpful to place the two pins as far away from each other as possible. The larger baseline will not increase the precision of the rotation axis but lock the angular constraints tighter.

Despite only needing two pins at a time for fully constraining the part, the FOR and the PoC breadboards provide a total of nine positions in which the pins can be inserted, three towards the front of the module, three roughly in the middle and three towards the back of the module (see Figure 3.18 c)). This was done to ensure redundancy in case one hole might be damaged or blocked. The left and right pin positions on the front and the middle of the module are provided by elongated holes[13]. Following the described mechanism, these holes can provide the necessary angular locking, but they cannot adequately define the rotation axis. When picking two pin positions, one must therefore not pick two elongated pin holes in the PoC.

The pins are chosen in length such that they can be used from the top as depicted in Figure 3.18 a) but also from below to account for situations in which the pin position is blocked by optomechanics built on the breadboard. Without any guidance, however, it can be challenging to find the overlap of the precision holes in the PoC and the FOR with their narrow tolerances by eye. To simplify the insertion of a PoC, we therefore added guiding rails, which help find the correct position for the pins. This detail is enlarged in the sketch in Figure 3.18 b). We cut two 5 mm wide grooves parallel to the insertion direction of the PoC in each port of the FOR. A total of six small 5 mm wide stainless steel pins, three per groove, are placed in the PoC. The lower part of these, sticking into grooves, is milled down to a diameter of 4.6 mm. These guiding pins can slide inside the grooves during module insertion, providing coarse positioning that simplifies finding the correct pin position and minimizes the risk of hitting a neighboring module.

Figure 3.18 c) shows the general size of a PoC module and the relative placement of the different types of pins. Additionally, one sees several M6 threads around the outside of the PoC module and two in the center. These are intended for securing the module on the FOR after which the pins can be removed again. In general, not all M6 mounting points are required for the PoC; we typically use four screws, but it provides different options for placing the mounting screws. The decision to insert the mounting screws from below through the FOR board into threads in the PoC and not vice versa was driven by three factors.

First and foremost, there is more room to access the mounting points from below. As shown in Figure 3.6, the available space below the level 1 breadboard is 30 cm, between level 1 and level 2, even without including the thickness of the PoC breadboard, only 22.5 cm.

[13] This was done to compensate for the four respective precision holes in the FOR being misplaced by 20 µm along the insertion axis of the PoC.

With optical components mounted on a functional PoC, accessibility of the mounting points from the top would be even worse.

Additionally, having an M6 thread inside the PoC breadboard saves space on the module for placing optomechanical components. When choosing a proper length of the mounting screw which does not extend beyond the upper surface of the PoC, one can still place components on that part of the module without blocking that mounting point. Inserting the screws from the top would require these places to be saved for potentially placing screws.

Lastly, one can argue that placing the screws from below could lower the local stress in the material near the components mounted on top of the module. When looking at the stress distribution threads and screw contacts [73–75], one observes that most stress in the material is applied below the head of the screw which is pressed against the metal plate it is holding and the first few revolutions of the thread. The stress in the thread quickly drops off along the insertion direction. This means, that if one screws down the PoC from on top, the local stress applied by the screw head might affect the components on the module, whilst if screwed down from below, most stress is applied in the first few revolutions of the threads on the bottom of the PoC and therefore further away from the optomechanical components.

The thickness of the PoC breadboards was chosen to be 12.7 mm (0.5"). A decision made such that both PoC and mPoC modules have the same thickness, which matches with standard COTS breadboards (for example from Thorlabs), which can therefore also be used as the base for a compatible module, especially for the mPoCs. Additionally, this choice keeps the weight of the PoC relatively low (around 3 kg for an empty PoC), which makes it easier to handle it during exchange and transport between storage, test bench, and FOR.

A concern might be the stability of a breadboard of that thickness; however, one has to keep in mind that it can only (reversibly) bend during transport. In operation, it will always be placed on the much thicker breadboards of the FOR or the test bench. These will add additional support to the PoC and prevent it from bending beyond what the FOR allows (see Figure 3.10). However, in reality, neither the PoC breadboards nor the FOR breadboards will be perfectly planar. Despite careful processing, they can always have a slight bending or deformation after machining and handling. Placing them on top of each other will therefore create small gaps. These are closed when screwing the parts with the M6 bolts together, forcing the surfaces to touch. A critical question is now, which of the two structures will deform? In general, it should be better if the PoC (reversibly) deforms during mounting. Such a deformation can be included in the initial development on the test bench. After transfer and mounting on the FOR, this deformation is repeated as long as the test bench and the FOR are similarly flat and the initial gap was mainly created by a bending of the PoC. If the FOR bends during the integration of a new module, this will not only affect the new module, but will also deform the FOR structure as a whole. As a result, other ports will also be slightly deformed, potentially creating crosstalk between the ports.

In this case, the thickness of the PoC breadboard of 12.7 mm is beneficial. As discussed in Section 3.3, a key metric for the deformation of a plate under load is its area moment of inertia I. The area moment of inertia for a plate scales with the thickness cubed [69]. For the a FOR breadboard thickness of 30 mm the ratio between the area moments of inertia is

$\frac{I_{FOR}}{I_{POC}} = \frac{(30\text{mm})^3}{(12.7\text{mm})^3} \approx 13$. Therefore, it is expected that potential bending will mainly occur in the PoC. If the thickness of the PoC breadboard is increased without increasing the FOR thickness, this means that if bending due to imperfect machining or static deformation of the FOR occurs, it is more likely to deform the FOR structure, leading to crosstalk. More on the topic of crosstalk will be discussed later in this section.

Now with the shape and mounting mechanism of the blank PoC breadboard being set, this metal plate can be equipped with any mounting hole pattern for optomechanics of your choice. It is possible to place a 25 mmx25 mm M6 grid on the modules, like one has on most optical tables, as well as any other mounting grid one desires.

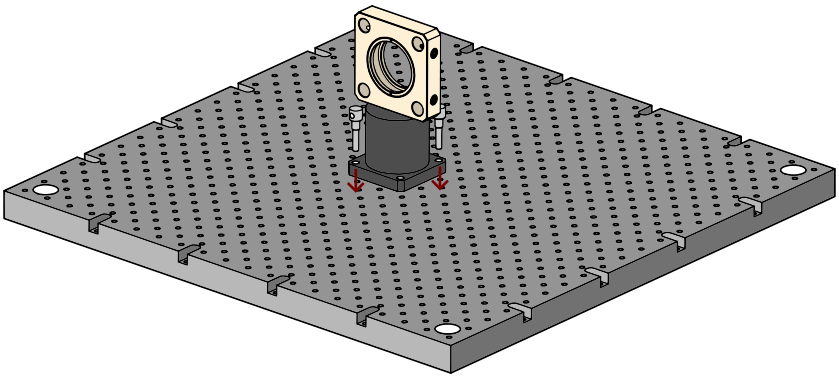

Figure 3.19: Demosketch of an O-Lego mount on the corresponding 12.5 mm double density grid of M3 threads on a demo breadboard. A post for to mount a Thorlabs 30 mm cageplate to 50 mm beam height is shown. Additional pins for passive placement of the mounts on the hole pattern are shown above their intended position, and their insertion is indicated with arrows.

At HQA-ONE, we equipped our modules with a 12.5 mmx12.5 mm double density grid of M3 threads compatible with our own optomechanical system, nicknamed *O-Lego*. As already mentioned in Section 3.1, this system is an adaptation of an original system developed in the Team of Christian Gross at the Max Planck Institute of Quantum Optics in Garching [60]. Our system is built to 50 mm beam height. Figure 3.19 shows a sketch of an exemplary mount of this system to convey the idea. In essence, this system enables breaking the rotational symmetry of typical clamping fork-based optomechanical mounts, facilitating compact optical setups and enhancing building efficiency through predefined component positioning.

Just like with regular posts, the functional components are mounted on a base, which is then attached to the breadboard. In the O-Lego system, these mounts are tailored to the part they will provide in the setup (cage plates, mirror mounts, etc.). This allows for placing stops on the mount such that the mounted component can be locked in angle and position with respect to the base. The base itself has four M3 through holes to mount the component to the board. When placing the part, we use two pins which match the through hole diameter on the top and the inner thread diameter on the bottom. This passively positions the base on the hole pattern by matching the symmetry axes of the through holes with the axes of the threads. With the base referenced to the hole pattern, the well-oriented part mounted on the base is indirectly also referenced to the pattern.

For suitably placed components on the base, one can ensure that the working axis of the functional part aligns with the holes along which optical beam propagation is commonly built. For example, one can ensure that the mirror surface of a mirror mount is placed directly above an M3 hole. After positioning with pins, the two other holes of the base are used for fastening the part. Afterwards, the pins are removed. By experience, this procedure allows positioning of the components well within 100 µm, which mainly depends on the fit of the pin in the thread which itself depends on various factors like the production method of the thread, the wear of the production tool, anodization layer thickness, and over time the wear of the thread itself.

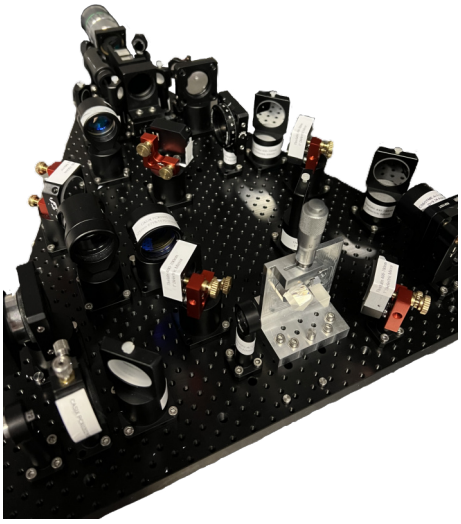

Figure 3.20: Exemplary picture of a setup built with O-Lego on a PoC. Notably, this picture was taken during construction without all components in place; the final component density on these modules can therefore be higher than shown in this picture.

The key benefits of this mounting system are, on the one hand, that it allows for quick and simple building of optical setups, where all components (lenses, mirror mounts, etc.) can be immediately placed by hand roughly in the intended position with the pins, leading to a passive coarse adjustment. Fine adjustment with the integrated DoF of the optical setup, like the tilting screws on mirror mounts, is afterwards needed, just like it is with any optomechanical mounting. On the other hand, the system omits clamping forks[14] and therefore reduces large unused spaces on the breadboard which the clamping forks would otherwise occupy. This allows for building very compact optical setups with high spatial component density. Figure 3.20 shows an exemplary PoC on which O-Lego optics have been built.

3.6.3 PoC testbench

The test bench for the development of new PoCs and the initial alignment of their optics is a simplified copy of the FOR, which provides the same mounting points but also has to

[14] The system also includes the option of small clamps which are usable on the M3 pattern, but their use is limited o few application, like placement of pickup photodiodes behind a mirror were the beam propagates off-axis without adjustment DoF.

account for the use of a broad spectrum of diagnostic tools and usability in the lab. The realization of a test bench for the PoC modules used at HQA-ONE is shown in Figure 3.21.

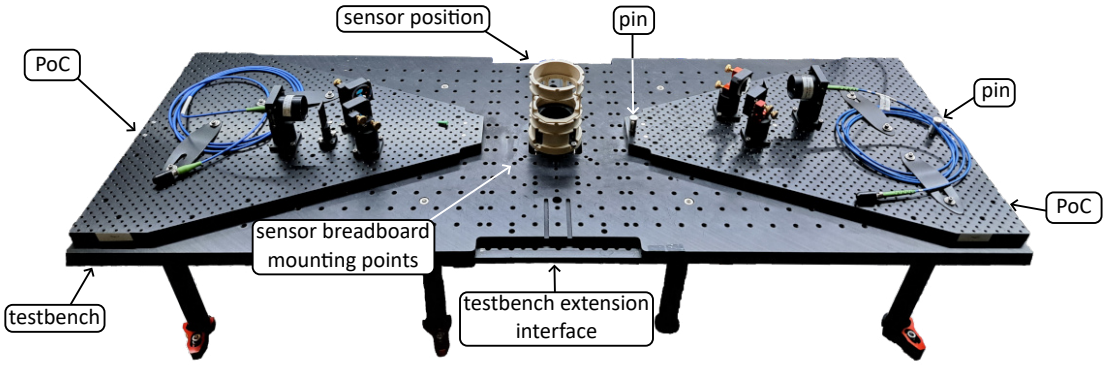

Figure 3.21: Annotated photograph of the test bench for the PoCs. This test bench can be used for external development, testing, and debugging of PoC modules. The photograph shows two opposing PoCs on the test bench. The indicated test bench extension interface allows adding the ports for the two perpendicular ports as well, if two or more PoCs have to be developed in tandem, for example, because they share a beam.

The presented test bench, CNC machined from a single plate of Aluminum, incorporates two opposing ports for PoC modules, with a removable Objective mount and addressing cage mock-up in the same relative distance as it is in the FOR. This allows the use of the in-situ diagnostic tools from the FOR described in Section 3.5 also on the test bench during development and construction of a module. To accommodate tools that are too large for the addressing cage, such as wavefront sensors or cameras with additional optics, it is possible to remove the objective mount and cage. This allows for the placement of smaller square breadboards with an O-Lego pattern in the central position of the testbench, where these tools can be mounted. These boards are dimensioned such that they can be placed even with both ports occupied by PoC modules. The placement of these auxiliary sensor breadboards is enabled by a set of pin positions, identical to those for the PoC placement, near the center point. Should even larger optical diagnosis setups become necessary for the test of a single module, one can also place the optics on the opposing PoC breadboard.

A different concern for the test bench, however, is that, unlike the FOR, we did not plan it as a permanent structure. To match the agility of development, assembly, and testing, the test bench should not be bound to one optical table where it is permanently based. This might be hindering, for example, if work in that lab, e.g., by a student working on a new module, would disturb experimental runtime of the apparatus or require the student, with the experiment running, to follow additional (laser) safety regulations that would slow down the development process. On the other hand, not all laser sources required for testing are always available in every laboratory. For that reason, one should be able to move the test bench around from time to time between different laboratories and preparation laboratories.

We incorporated this consideration by limiting the size and the mass of the test bench, such that it can be carried around and stored, e.g., in a shelf, if necessary. The main body of the test bench only hosts two opposing PoCs, the minimal number to cover the full test envelope we described earlier. In some cases, however, it might be necessary also to

include the perpendicular modules on the test bench. This could be the case, for example, when modules share beams,[15] for example, to form an optical lattice under 90° AOI. To account for this possibility, the test bench is equipped with extension interfaces left and right of the PoC ports. Extension plates to provide the full perpendicular ports can be attached via pins if necessary. The connection holes for the extension boards were drilled with both parts connected with a single drill; therefore, the precision that can be achieved when connecting these pieces is even better than for the PoC pins. Having these ports as extensions enables a large use case envelope while keeping the permanent size and mass of the test bench in its everyday use manageable.

Additional measures to reduce the mass include reducing the board thickness from 30 mm to 20 mm, which reduces the mass by 33 %. Compared with the findings from Section 3.3, this was not an option for the FOR, but should be acceptable for the test bench, which has a different support post placement, no eddy current breaker slit, and no wire trench for the coil wires. We did not observe any issues in the laboratory with the different thicknesses for the test bench and FOR, but should it ever arise as an issue, one can always build a second version of a test bench with adapted thickness.

The main body of the test bench is supported by a total of eight removable posts, four per port. These are fastened on the ground by standard clamping forks, making the test bench usable on every optical table or sufficiently large breadboard with an M6 threaded hole pattern. The extension boards for the test bench are also supported by 4 Aluminum posts per port.

3.6.4 PoC mounting performance

The last step in the development of the PoCs is now to verify their performance to gauge the suitability of the design in the pursuit of modularity according to Section 3.1.

The first test will be to verify the functionality of the positioning pins with the PoC modules by measuring the precision of the placement method. These measurements are taken on the test bench by placing a Shack-Hartmann wavefront sensor[16] on the center point of the test bench setup. The sensor is illuminated by a collimated laser beam with a diameter of 3 mm. This light, with a wavelength of 671 nm, is delivered via a polarization maintaining optical fiber to an optical setup on a PoC module, which forms the beam that is sent onto the sensor. The wavefront sensor allows subsequent measurement of the centroid position on its chip and the AOI of the wavefront. Knowledge of these characteristics can then be used to gauge the precision of the PoCs. We repeatedly remove the PoC breadboard from the test bench and reinsert it with the pins. In each iteration, the beam centroid position and AOI onto the sensor are measured. To account for noise in the measurement data from the wavefront sensor, we take 5 measurements shortly after each other and use the mean value with the standard deviation of the measurements as an error bar. We replicate the measurements afterwards with a second PoC module on the same port with the same pins to test not only the precision of a single module but also to test for performance consistency across other modules. This is done to rule out performance fluctuations between batches of independently manufactured PoC breadboards.

[15] Sharing beam between modules opposes to some extent the disentanglement of optical setups that we try to pursue with HQA (see Section 3.1). However, it is possible and might be worth doing in selected applications.

[16] Thorlabs WFS31-5C/M

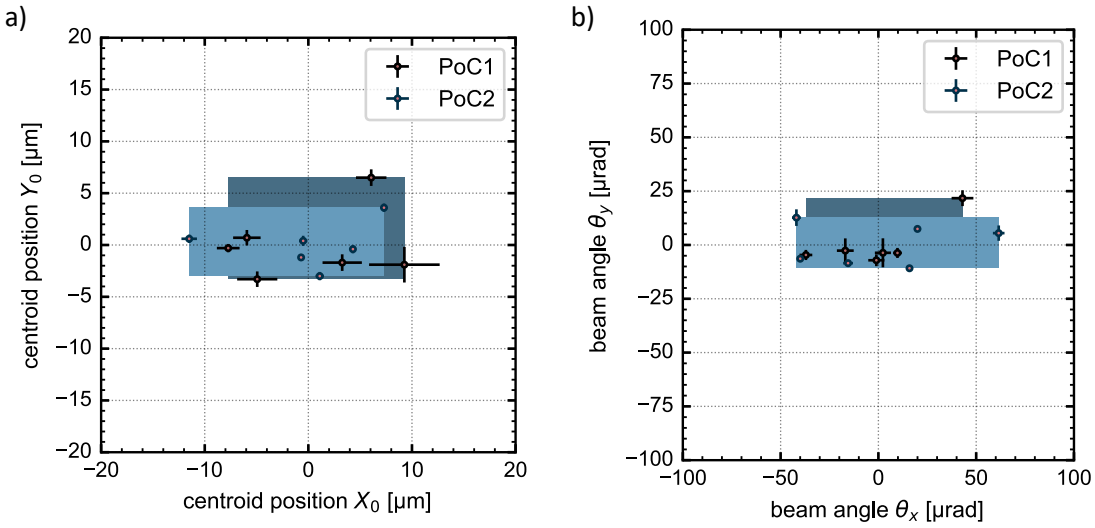

Figure 3.22: Precision of the mechanical placement of the PoCs with two positioning pins on the test bench, taken by sending a laser beam from the PoC onto a Shack-Hartmann-Sensor at the center position of the test bench and therefore the simulated FOR. The PoC was taken off the test bench and re-positioned with the pins. For each iteration, the centroid position and beam angle were measured. These measurements were repeated with a second PoC with the same pins to factor in machining variations. **a)** shows the varying centroid position of the beam on the Shack-Hartman Sensor relative to its average centroid position of the six iterations per PoC. **b)** shows the varying incident angle of the beam on the Sensor relative to its average per PoC. In both plots, each data point displays the mean of five wavefront measurements, and the error bars correspond to the standard deviation. The box indicates the maximum deviations in both axes during the testing. The dark blue box corresponds to PoC1, the light blue one to PoC2. One observes variations of the centroid position of less than ±10 µm in the horizontal x-axis and below ±5 µm in the vertical y-axis. Angle fluctuations are below ±60 µrad parallel to the plane of the testbench breadboard and below ±15 µrad perpendicular to that plane. Plots are adapted from [57].

The results of these measurements are shown in Figure 3.22. Shown are the beam positions and angles for six iterations of the PoC placement with the pins centered around the common mean value. Additionally, boxes are drawn for each of the two tested modules, which capture the largest observed fluctuations around the common mean position and angle. These boxes serve as a guide to the eye.

In the plane of the testbench surface and the PoC breadboard (x-direction), the precision is set by the pins; one observes maximum variations in line with what one would expect from the specified dimension of the pins and the clearances in the holes of around ±10 µm. The centroid position variations are within these expected bounds. However, not only does the common displacement of the PoC around the pins contribute to the positional shift of the beam, but also an angular shift and the subsequent propagation over the distance to the sensor can account for shifts. The pins in the test are placed in the two pin positions of the pattern that are furthest away from each other, as this provides the best possible

angular precision. Their baseline distance is 375 mm combined with ±10 µm clearance of each pin in its hole, one expects an angular precision of better than ±60 µrad. The measurements in Figure 3.22 b) agree with these expectations. If the last optical element is placed on the tip of the PoC breadboard, the largest possible shift due to this angle variation is 19 µm. Notably, if the PoC is positioned in this extreme position with both pins on the edge of the pins, no further common displacement of the PoC and therefore the centroid is possible. This means that these ±19 µm are the theoretical lower size limit for the in-plane OR on the PoCs.

In the perpendicular plane, vertical on the PoC breadboards (y-axis), the precision is determined by the interface between the two anodized Aluminum breadboards, the surface on which the PoC and test bench slide on top of each other. This means that the precision in the y-axis is set by the combined flatness of the two Aluminum plates (EN-AW5083) after anodization. There is no viable estimate of how precise one would expect the common flatness to be after machining and anodizing. In Figure 3.22, however, one observes that the variations for position and angle are consistently smaller in the y-direction compared to the x-direction. One can therefore consider the plates flat and the resulting deviations small compared to the pin positioning mechanism [57].

Along the direction in which the PoC is inserted, hence the beam propagation direction in this case, no data was taken. However, the placement in this direction is defined by the pins with symmetrical tolerances as in the x-direction, therefore, one can assume similar behavior as for the common displacement in the x-axis. In general, all variations and therefore the minimal size requirements of the OR are small compared to OR one would expect for optics with < 0.3 NA, the limit of what can be sent through the side windows of the glass cell and therefore reasonably placed on the PoCs.

In the next step, when working with the PoC, it is to secure them on the FOR with M6 screws after placing them with the pins. This is again tested on the test bench with a PoC that generates a collimated beam with a diameter of 1 mm. The beam is imaged with an in-situ camera in the mockup of the addressing cage and therefore in the center position of the test bench. The camera image is fitted with a 2D rotated Gaussian fitting function to extract the centroid position of the beam. Four M6 screws are used to bolt down the PoC breadboard on the test bench and tightened with a torque wrench. Fastening the bolts is always performed in a star pattern and in the same order to achieve consistency between iterations. We gradually increase the torque of the mounting screws, but always undo them before increasing the torque further to check for inelastic deformations. The centroid position during each iteration is monitored via the camera.

Figure 3.23 shows the resulting drift of the centroid relative to the initial position, which was set by the pins only. Figure 3.23 a) shows the drift in the vertical plane, perpendicular to the breadboard, and Figure 3.23 b) the drift in the horizontal plane, parallel to the breadboard. Arrows in a) indicate the steps of the testing procedure.

In Figure 3.23 a), in the direction defined by the two breadboards lying on top of each other, one observes two different regimes. For low torque, one can observe an elastic deformation of the beam position. The bolts force the two plates on top of each other, which closes the gaps due to imperfect flatness between them. Following the argument about the area moment of inertia, discussed earlier in the section, with a ratio of $\frac{I_{bench}}{I_{PoC}} \approx 3.9$, one can assume that the bending mostly happens in the PoC breadboard. When the bolts are released, the beam centroid jumps back to its initial position, marking these deformations

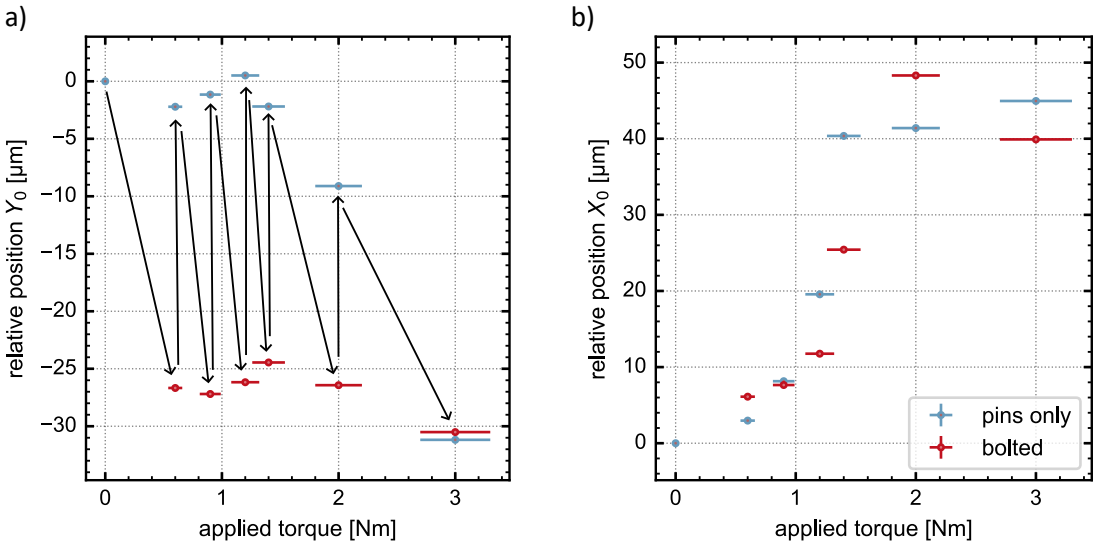

Figure 3.23: Drift of the Centroid position of a beam on a PoC during mounting on the test bench, measured with a camera in the test bench center position, and centroid extracted with a 2D Gaussian fit of the camera image. The torque on four M6 screws that secured the PoC on the test bench was iteratively tightened with a torque wrench, loosened again, and tightened further. The resulting drift of the centroid position relative to the initial position set with the pins without any screws is plotted. **a)** shows the relative drift perpendicular to the breadboard plane, **b)** the drift parallel to the breadboard plane. Arrows in a) indicate the sequence of the measurement. Figure and caption adapted from [57].

as elastic. Above a threshold of around 2 N m, however, it enters the second regime where the beam position with the tightened screws remains constant, but upon releasing the bolts, it no longer jumps back. This behavior indicates a regime of inelastic deformations and a resulting permanent displacement of the beam pointing of the optics placed on the PoC. It seems advisable to stay within the inelastic regime when working with the PoC modules.

In Figure 3.23 b), in the direction defined by the pins, one would, in principle, expect no drift at all if the screws were only applying force in the vertical direction. However, one observes a more continuous drift along the x-direction with increasing torque, which remains even after loosening the screws. This indicated that fastening the bolts also introduces shear forces that lead to the drift in this direction. If that leads to a deformation of the pins which hold the PoC in place, this would explain why the deformation does not jump back when the screws are loosened. For torque values that correspond to the elastic regime in Figure 3.23 a), these deformations are, however, still on a similar scale as the clearance of the pins in their holes. This observation again hints that it is advisable to stay within the inelastic regime.

When discussing the fastening of the PoCs on the test bench and the FOR, another question that naturally arises is how mounting the PoCs affects not only itself but also the other ports. We want to understand what kind of crosstalk one would expect. In order

to gauge this quantitatively, we can use the FEA models used in Section 3.3. However, these simulations will include the same simplifications discussed in the respective section. Especially relevant in the case of placing PoC breadboards on the FOR, the simulations will assume contact of perfectly flat plates (no machining defects or bending taken into account) and perfect, quasi-monolithic contact with an ideally constrained interface (effects of screw placement not taken into account).

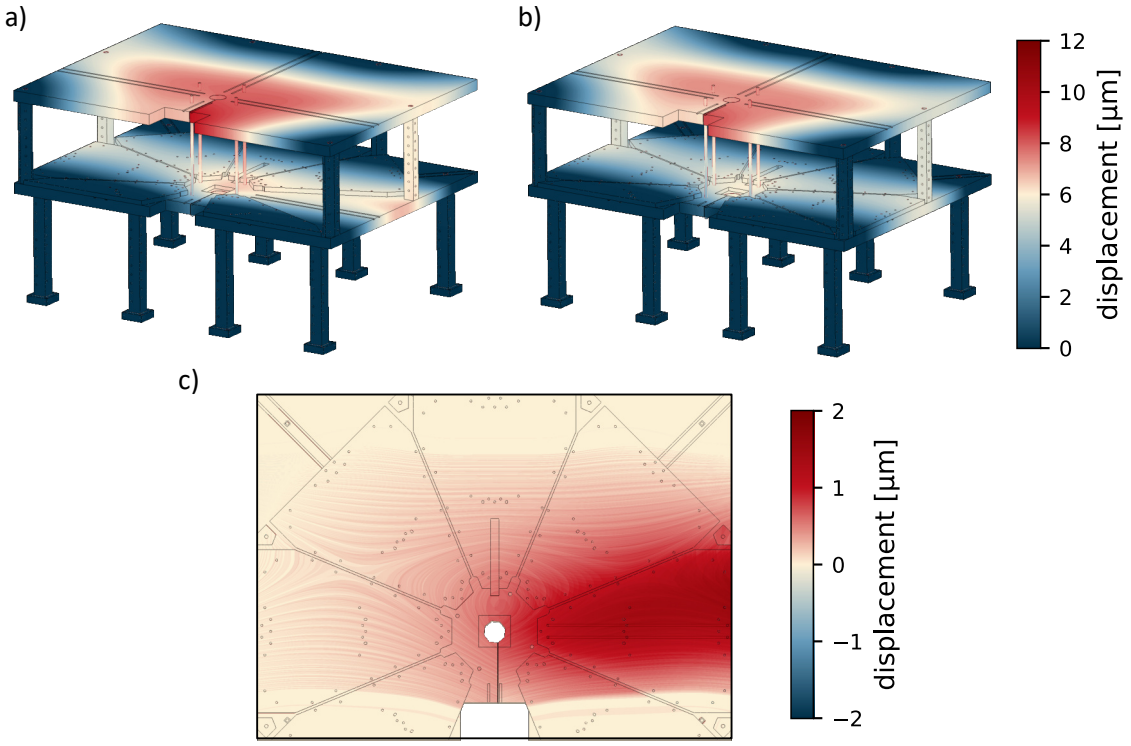

Figure 3.24: FEA simulation of the crosstalk that can be expected between the PoCs. a) shows a simulation of the absolute value of the gravitational deformation of the FOR with all PoCs except the one on port 2 inserted. b) shows an equivalent simulation with all PoCs in place on the same colorscale. c) shows the difference between both simulations on level 1 of the FOR to gauge the crosstalk effect of an individual PoC on the other ports. One observes a change in the gravitational displacement of the other ports below 1 µm between the module being placed and removed from the FOR.

Figure 3.24 shows such a simulation of the crosstalk effect by showing the difference between the FOR under its weight with all ports occupied and the constellation with one port empty. The empty port was chosen to be port 2, as Figure 3.10 showed that it is the port where the most significant deformations are expected when all ports are left empty. Therefore, one can assume that it will also be the port that has the most considerable crosstalk effect on the other ports and serve as an upper limit for the expected crosstalk in the simulations.

Figure 3.24 a) shows the color-coded gravitational displacement from the load-free FOR structure with all ports, except port 2, occupied by PoCs. Figure b) shows the corresponding simulation with all ports occupied on the same colorscale. One observes slightly less deformations with all ports occupied, as the inserted breadboard effectively thickens the

FOR board and provides additional support, which stiffens up the structure as a whole. Again, this is simulated for perfect contact between PoC and FOR, but Figure 3.23 a) showed that the PoC bends to the same position, more or less independent from the applied torque, indicating plane contact between the plates when the screws are fastened. Therefore, ideal contact in the sense of additional support to the FOR can be assumed as a valid approximation. However, Figure 3.23 a) also shows that in reality, the interface is not perfectly flat. Tightening the screws causes bending. But given the large ratio between the area moments of inertia $\frac{I_{FOR}}{I_{PoC}} \approx 13$, most of the bending happens in the PoC, the common FOR is expected only to experience slight bending, which makes the simulations plane contact simplification a valid approximation.

Figure c) shows the difference between Figure a) and Figure b) in a top view of level 1 of the FOR. It is evident that most of the displacement difference occurs on port 2 itself, with minimal crosstalk effects, measured on a micrometer scale. Effects on port 2 are below 2 µm. For most applications, except extremely sensitive modules like optical lattices or super lattices with alignment criteria on the order of the wavelength, the crosstalk between modules is therefore expected to be negligible.

This has been experimentally verified at HQA-ONE, by placing an ODT module on port 3 and monitoring its position with an in-situ camera (see Figure 3.15), while placing and removing a PoC on port 2. We observed shifts of the ODT center on the camera of less than one pixel (3.45 µm), which agrees with the scale found in the simulations.

Eventually, we now want to test the full procedure of using the PoC. We want to test what precision can be expected when building a module, positioned and fastened on the test bench, and then transferring it to the FOR, to position and fasten it there. We call this precision the *transferability*, a quantity that defines how repeatable the suggested workflow for the PoCs is. In essence, it depends on all previously discussed steps and manufacturing differences between the test bench and the FOR.

Measurement of this quantity was performed using two separate in-situ cameras, one on the center point of the test bench and one in the respective position of the FOR. For both sensors, we do not know how well they are positioned in the respective addressing cage, but as long as they are not moved, the position of the respective camera chip stays constant, which yields excellent relative position measurements. We equip a PoC with optics generating a collimated beam with a diameter of 1 mm and place it on the test bench with the pins. The PoC is secured by four M6 bolts, placed in the same positions as in the torque test, which are fastened with 1.4 N m. The centroid position of the beam on the camera chip is measured and extracted via a rotated 2D Gaussian fit of the camera image. Afterwards, the PoC is taken off the test bench, brought to the FOR, and mounted following the same procedure and on the same mounting positions. The beam position on the in-situ camera in the FOR is measured accordingly. The figure of merit in this test is now the difference in position on the two cameras, which allows to cross-out contributions of the imperfect absolute position of the cameras with respect to the center points of test bench and FOR. This is measured for several iterations of the described test protocol.

Plotted in Figure 3.25 is this difference, the transferability of the PoC centered around their mean value. One observes variations on the vertical y-axis of below ±10 µm and below ±30 µm in the x-axis, which agrees with expectations from adding up the contributions from the individual steps of the procedure that have been discussed before. This size determines the minimal size of the OR for each PoC module for overlap in the plane

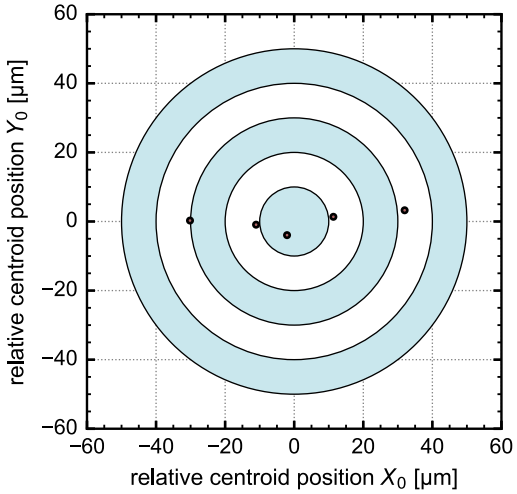

Figure 3.25: Transferability between the PoC development and testing on the testbench and the integration into the experiment. The data is taken by placing diagnosis tool cameras in the addressing cage of both the FOR and the test bench and transferring a PoC between them. As long as both cameras are not moved, they can have an individual offset from the center position due to their mounts, but they provide very repeatable data, as the camera chip is not moved. The PoC is bolted down with a torque of 1.4 N m on 4 M6 screws on the same points on both the test bench as well as the FOR for the measurements. Measurement of the relative distance between the centroid position on the test bench camera and the FOR camera for each iteration allows for the determination of the offset between the camera position on the FOR and the test bench. As both cameras remain stationary between iterations, the fluctuation in the measured distance provides a measure of merit for the combined effect of bolting a PoC and transferring it between the construction on the test bench and its use in the experiment. These distances for multiple iterations relative to the average distance are plotted. The x-axis is parallel to the FOR breadboard, the y-axis perpendicular. The rings serve as a guide to the eye. Figure and caption are adapted from [57].

of level 1 of the FOR. It is smaller than the typical diffraction-limited FOV of high-NA objectives defining the OR of the mPoCs, at HQA-ONE around 100 µm, hence passive overlap of the ORs and therefore passive alignment is feasible. The implementation of these modules for high-NA optical addressing, the mPoCs, will be discussed in the next section.

3.7 Microscopy modules - microscopy pieces of cake

The last general puzzle piece in the system design, according to Figure 3.1, is the second type of modules for optically addressing the center point of the platform. Unlike their counterpart, the PoCs, which address that position directly from the side, these modules are designed to allow high-NA access to the center position via the microscope objective of the platform, hence the name Microscopy Piece of Cake (mPoC).

3.7.1 Modularity of the high-NA path

The high-NA objective used at HQA-ONE is custom made by *Special Optics*[17] and designed for apochromatic performance with light of wavelengths of 532 nm and 1064 nm, for general ODT applications, as well as 671 nm, the resonance of the D_2 line in ^{6}Li. The objective is matched to compensate for the effects of the glass cell window thickness and provides a numerical aperture of ≈ 0.66 with a rear aperture diameter of 24.8 mm. The diffraction-limited FOV in the atom plane is specified to be larger than $\pm 100\,\mu$m. A transverse displacement of a point source to the edge of the FOV (shift of 100 µm in the focal plane) corresponds to an exit angle of the collimated beam on the rear aperture of around 5 mrad.

An additional feature of the objective is that it was designed such that the back focal plane, near the rear aperture, sits 1.9 mm outside of the objective housing and is therefore accessible. We use this feature to retro-reflect collimated beams that enter the objective from the direction of the atoms. For that, we use a dual-wavelength waveplate with a diameter of 30 mm onto which we sputtered a central point mirror with a diameter of 1 mm. The waveplate is mounted with a holder made from PEEK on the rear aperture of the objective such that collimated which enter the objective, leave the rear aperture, pass through the waveplate, are focused and retro-reflected on the point mirror, pass through the waveplate and the objective a second time and leave the objective collimated again (see Figure 3.7). The waveplate is designed as a $\lambda/4$ waveplate for 671 nm light, leading to a total phase delay of $\lambda/2$ in dual passage required for the in MOT operation. Additionally, it is designed as a $\lambda/2$ waveplate for 1064 nm light, leading to a phase delay of λ in dual passage, which can be used to generate infrared standing wave lattices. As the point mirror is small compared to the rear aperture and placed in the Fourier plane of the atom position, it has negligible influence on the generation of individual point-like traps, like optical tweezers, and imaging of point-sources, like trapped fluorescent atoms, in the atom plane.

An overview of the characteristics of the objective that is used at HQA-ONE is given in Table 3.1. A detailed characterization and discussion of its specified and actual performance can be found in [17].

The passive mounting of the objective, without any degree of freedom, was already presented in Section 3.3 and depicted in Figure 3.7. This was done to place the objective in a fixed position relative to the CNC machined interface of the FOR. It is mounted along the designated center axis of the FOR and its height placed such that is focal plane is parallel and 62.7 mm above level 1 of the FOR. This will be the designated center point where we expect the atoms to be roughly placed in later experiments. That specific height was chosen to account for the 12.7 mm thick PoC breadboards and 50 mm beam height for the optical components placed on the module.

As discussed in Section 3.2, the exact position of the atoms in the glass cell does not change the optical performance of the objective. However, it is necessary to fulfill a certain level of parallelism between the objective and the window of the glass cell. A thick, tilted glass plate in the strongly converging beam of the objective would introduce aberrations in the form of astigmatism and lower the optical performance as well as shrink the usable diffraction-limited FOV. Simulations showed that for the objective at HQA-ONE, one must provide parallelism to within 1 mrad to obtain the specified performance [17, 57]. The alignment of the glass cell with respect to the optical table, and therefore indirectly

[17] www.navitar.com

Table 3.1: Overview over the properties of the custom high-NA objective of HQA-ONE. Table adapted from [57]

Parameter	Value
Numerical aperture (NA)	0.655
Working distance (total)	13.7 mm
in air	1.0 mm
in fused silica	6.35 mm
in vacuum	6.35 mm
Apochromatic design wavelength	532 nm
	671 nm
	1064 nm
Focal length	18.8 mm
Rear aperture diameter	24.8 mm
Housing diameter	45 mm
Physical length	40 mm
Back focal distance	1.9 mm
Diffraction limited field of view (FOV)	
@ 532 nm (simulated)	±110 µm
@ 671 nm (measured)	±104 µm
@ 1064 nm (simulated)	±130 µm
Relative angle between optical and mechanical axis	2.2 mrad ± 1.6 mrad

the mechanical mounting of the objective, is done by tilting the vacuum chamber with the feedback of a tilt-sensor as discussed in Section 3.2. However, these measurements indirectly link the parallelism of the top window of the glass to the mechanical axis of the objective of the glass cell, which optically enters through the bottom window of the glass cell. Deviations in the parallelism of the two glass cell windows with respect to each other therefore lead to a mismatch of the mechanical objective axis. Additionally, as found in [17], the mechanical axis of the objective, which sets the mounting position, might deviate from its optical axis by more than 1 mrad. Therefore, the best way for final precision alignment of the lower glass cell window to the passively mounted objective is to prepare an optical tweezer, load atoms into it, and to iteratively maximize the trap frequency of the optical tweezer by tilting the vacuum chamber with the mechanism described in Section 3.2. This procedure was performed at HQA-ONE for optimal tweezer preparation; the results will be described in Chapter 5.

With the objective passively mounted in the FOR, the central idea to achieve modularity on this interface is to send all beams from modules for potential high-NA access through the same objective and a common distribution path. This path provides a common transfer function for all ports. Placing the interfaces for the modules appropriately with respect to the optics of the distribution path allows manageable mechanical requirements even for modules intended for high-NA access to the platform.

Figure 3.26 shows a sketch of the underlying idea behind the modularity of the platform in the high-NA path and mPoCs. In this example, assume point sources in different

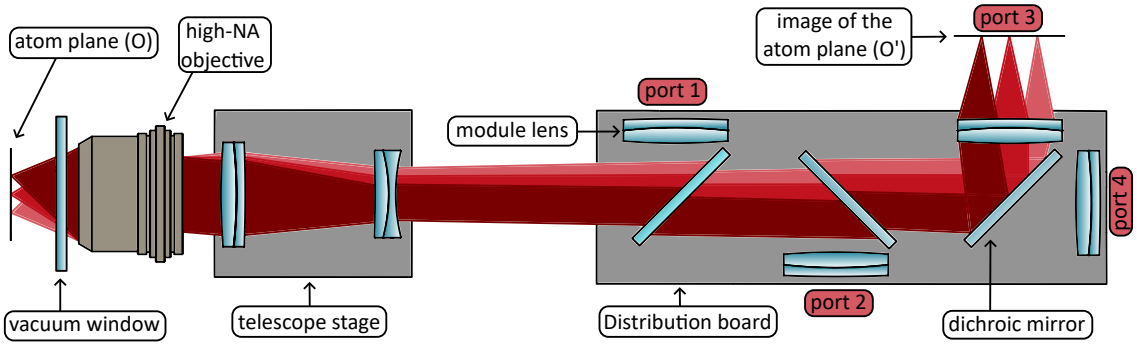

Figure 3.26: Sketch of the principal idea of the distribution concept for the mPoC ports. The core idea is to provide a common image path that relays an image of the atom plane on the different ports of the distribution to which the modules will be attached. Placing the magnified image at the connection point between the common distribution path and the module provides a robust interface for the modular optics, as imperfections in the module placement are demagnified according to the optical setup on the distribution path. Unlike the PoC interface, these ports do not separate depending on the direction of optical access, but by wavelength of the used light and reach the center point and the atom position via a common path through the high-NA objective. The sketch shows the distribution principle exemplary for a total of four ports, but it can be adapted to a different number of ports depending on the choice of the dichroic mirrors. Figure adapted from [57].

transversal positions of the diffraction-limited FOV in the focal plane of the objective. These are indicated by different shades of red in the sketch. Their light emission is captured according to the solid angle covered by the NA of the objective, leading to collimated beams leaving the rear aperture of the objective. The transversal shift in the FOV translates to different outgoing angles of the collimated beams with respect to the optical axis. Next, the collimated beams pass through a telescope stage that demagnifies the diameter of the individual beams. However, this demagnification necessarily leads to a magnification of the angles of the beams originating from different points in the FOV to the optical axis. After this passage, the common path of the collimated beams is split by a set of dichroic mirrors, reflecting light of a specific wavelength band to different parts of the distribution board. Each of these ports is equipped with a module lens mounted on the distribution board that focuses the light of that band to form an image O' of the original atom plane O. By changing the focal length of the module lens in the distribution path, one can set the magnification of the image O' of the atom plane. As the image is formed outside of the distribution path, the tolerance of mechanically attaching another breadboard to the distribution path, a mPoC module, is in reference to the image size of O'. The mechanical tolerance and their misplacement of the module with respect to the atom plane O is therefore demagnified according to the optical path. This path can be followed from the atom plane O to the image plane O', e.g., for collecting fluorescence of a point source like atoms in an optical tweezer, or vice versa, from a light field in O' demagnified to the atom plane O, e.g., for trapping light forming an optical tweezer potential.

In theory, this idea does not require the telescope stage behind the objective. However, the technical realization of the setup without a telescope stage leads to additional challenges

and costs.

The rear aperture of the objective has a diameter $d_{obj,rear}$ of 24.8 mm and point sources on the edge of the diffraction limited FOV, shifted by ±100 µm, leave the objective under an angle $\alpha_{obj,FOV}$ of around ±5 mrad. This means, without any optics behind the objective, according to geometrical optics, the lightfield diameter $d_{field,coll}$ after a propagation distance s_{prop} is

$$d_{field,coll} = d_{obj,rear} + 2s_{prop}\, tan(\alpha_{obj,FOV}) \approx d_{obj,rear} + 2s_{prop}\, \alpha_{obj,FOV}. \tag{3.5}$$

For typical propagation distances in an experimental platform of up to 1 m, this leads to light field sizes of up to 34.8 mm that have to be processed with the dichroic mirrors and the module lenses.

For the mirrors, which are placed with an angle of 45°, this means that they have to be at least a factor of $\sqrt{2}$ larger to capture the light field, leading to mirror sizes of more than 49.2 mm just to be able to address the specified diffraction limited FOV without clipping the beam. If one wants to be able to address a FOV slightly larger than the specified diffraction-limited one, the size requirements increase further. Dichroic mirrors of this size are expensive and cannot be as thin as their smaller COTS counterparts, which are typically only a few millimeters thick. For a large diameter dichroic mirror, such a thin substrate could lead to bending during mounting and therefore introduce axis-dependent wavefront curvatures on the reflected port, effectively leading to astigmatism. Custom thick substrate dichroic mirrors are commercially available, but require sufficient collimation on the incoming light to avoid astigmatism on the transmitted port. Slight vergence has negligible effects on a single dichroic mirror, but with multiple ones behind each other, as shown in Figure 3.26, their contributions can add up.

For the module lenses, focusing light fields of that size becomes challenging, as the focal plane has to be constant across a large fraction of the lens. Aberrations like spherical aberration have to be minimal. This is challenging for most lenses[18] and restricts the minimal usable focal length, with large curvatures of the lens. As a consequence, this also sets a lower limit for the magnification of the transfer between the atom plane O and the image plane O'.

Using a telescope allows for the reduction of the collimated beam diameter of the propagating individual beams $d'_{obj,rear}$. However, it increases the original propagation angle $\alpha_{obj,FOV}$ according to its magnification. Looking at Equation 3.5, this means that the first term shrinks while the second term grows with the magnification. A benefit of the telescope, however, is that the propagation according to this enlarged angle only starts after the second lens of the telescope. This means that the telescope stage provides the benefit of bridging a gap in the beam propagation path of its length, therefore reducing the propagation distance s_{prop} by several tens of centimeters. For a Kepler telescope, the beams even cross after the second lens, due to image inversion, which further increases the bridged gap.

In order to allow the use of smaller, less demanding optics in the high-NA path, we therefore opted to use a telescope stage in the setup.

[18] We discuss single lenses as a module lens. Multi-lens setups can address this issue.

3.7.2 Telescope stage

The first step in developing this telescope for the HQA-ONE and as a basis for adaptation in general for HQA is to understand which demagnification of the telescope would be favored. For this, a size estimation of the light field according to geometric optics, depending on the chosen telescope magnification, will be performed.

The first quantity to look at when selecting the telescope lenses with focal lengths f_1 and f_2 is the resulting diameter of a collimated beam $d'_{obj,rear}$ after the telescope stage in Figure 3.26. This size is described by

$$d'_{obj,rear} = d_{obj,rear}\,\frac{f_2}{f_1} = 24.8\,\text{mm}\,\frac{f_2}{f_1} \tag{3.6}$$

where $\frac{f_2}{f_1} = \frac{1}{M_{tel}}$ is the telescope de-magnification of the beam. Vice versa M_{tel} is the magnification of the telescope.

The next quantity is the magnified size of the diffraction-limited FOV in the atom plane O transferred to the image plane O'. This size FOV_{mag} depends additionally on the focal length of the objective f_{obj} and the focal length of the module lens f_{mod}. For a diffraction-limited FOV specified with a radius $FOV_{r,spec}$ of above 100 µm, the light field diameter $2\,FOV_{mag}$ in the focal plane of the module lens can be calculated as

$$\begin{aligned} 2\,FOV_{mag} &= 2\,FOV_{r,spec}\,\frac{f_1}{f_{obj}}\,\frac{f_{mod}}{f_2} \\ &= 2\cdot(100\mu\text{m})\,\frac{f_1}{18.8\text{mm}}\,\frac{f_{mod}}{f_2} \end{aligned} \tag{3.7}$$

given the objective's focal length of 18.8 mm.

The third and last quantity to be calculated in this estimation is the size of the light field diameter on the module lens $d'_{field,mod}$. For this outgoing angle, after the telescope α'_{tel} matters. This angle is given by $\alpha'_{tel} = M\,\alpha_{obj}$ [76]. For a beam entering the telescope originating from the edge of the specified diffraction-limited FOV, the incoming angle is around 5 mrad. This means, depending on the free propagation distance and in analogy to Equation 3.5, the light field diameter on the module lens for the specified FOV is described by

$$\begin{aligned} d'_{field,mod} &= d'_{obj,rear} + 2s_{prop}\,tan(\alpha'_{tel}) \\ &= \frac{d_{obj,rear}}{M_{tel}} + 2s_{prop}\,tan(M_{tel}\,\alpha_{obj}) \\ &= \frac{24.8\text{mm}}{M_{tel}} + 2s_{prop}\,tan(M_{tel}\,5\text{mrad}). \end{aligned} \tag{3.8}$$

The resulting scaling of these quantities depending on the magnification of the telescope is depicted in Figure 3.27.

Figure a) shows the light field diameter in the focal behind the module lens as described by Equation 3.7 for a FOV in the atom plane of ±100 µm and different focal lengths of the module lens depending on the selected telescope magnification M_{tel} in blue, according to Equation 3.7. The size of the collimated beam diameter behind the objective $d'_{obj,rear}$ for the corresponding magnification, according to Equation 3.6, is plotted in red. Additionally, the smallest length of standard camera chip formats is shown as dashed lines as a reference to the image size.

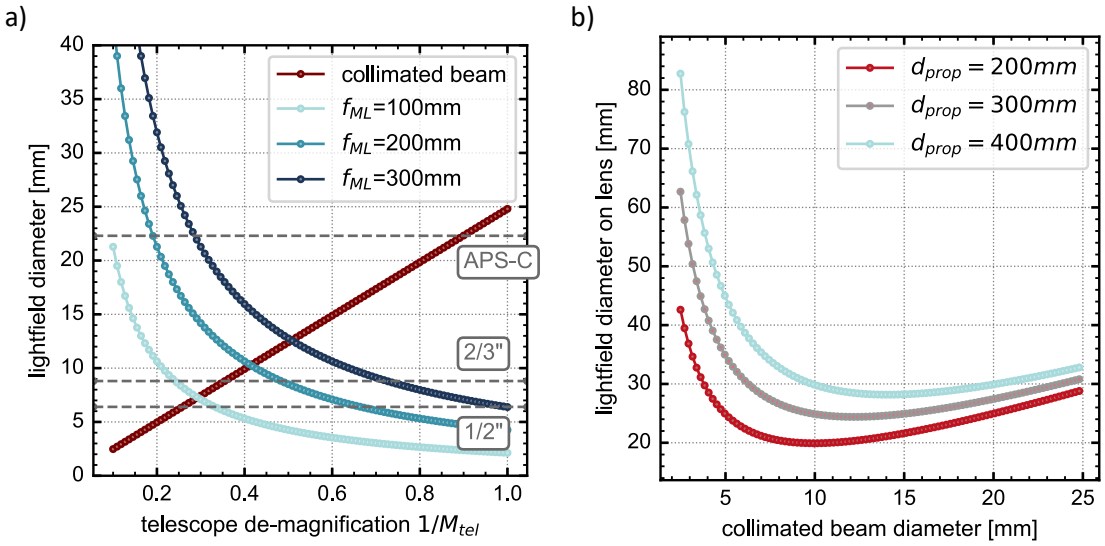

Figure 3.27: Plots of the effect of the magnification of the intermediate telescope in the common distribution path of the mPoCs on the light field size on different positions in the platform according to geometrical optics. **a)** Light field diameter of the image of the atom plane O' for a FOV of $\pm 100\,\mu m$ for several module lens focal lengths f_{ML}. This is put into perspective by the size of the small axis on typical camera sensor formats indicated by the labeled dashed lines. Additionally, the expected size of the collimated beam from the objective after the telescope and before the module lens is shown. **b)** Size of the light field on the module lens depending on the chosen collimated beam diameter produced by the telescope for an FOV in the atom plane of around $\pm 200\,\mu m$ and multiple propagation distances between the intermediate telescope and the module lens.

Figure b) presents a plot of the light field diameter on the module lens $d'_{field,mod}$ for different propagation distances between the last lens of the telescope and the module lens s_{prop} following Equation 3.8 depending on the collimated beam diameter after the telescope $d'_{obj,rear}$ which can also be mapped on the magnification of the telescope via Equation 3.6.

Figure 3.27 b) indicates that for expected propagation distances between the last lens of the telescope stage and the different ports in Figure 3.26 of a few hundert millimeter a minimal light diameter on the module lenses, depending on the propagation distance of the port allowing use of 1 or 1.5 inch optics, can be achieved for beams de-magnified to a diameter $d'_{obj,rear}$ roughly between 8 mm and 13 mm. These correspond to a magnification of the telescope stage of between 0.32 and 0.52.

Provided with this range, Figure 3.27 a) shows that for magnifications between 0.32 and 0.52, typically available lenses with focal lengths of a few hundred millimeters provide image sizes in the millimeter range, which are on relevant scales for typical cameras or can be further processed with additional optics on the modules. We find that commercial off the shelf available lenses with sizes between 1 and 1.5 inch and a large catalogue of standard focal lengths of few hundert millimeter can be used to select the magnification of the distribution path between the atom plane O and the image plane O', when using a magnification of the telescope stage between 0.32 and 0.52.

The next consideration that has to be taken into account for the telescope stage design is that we prefer to build this simple two-lens telescope from COTS available lenses ourselves instead of using a custom-designed and expensive complete system. Nevertheless, we still want the telescope to perturb the wavefront as little as possible. For example, for optical tweezers sent from the image plane O' to the atom plane O, that have to be focused as tightly as possible, any added wavefront error in the telescope stage before entering the objective will cause a loss in performance and effectively deform or broaden the tweezers in the atom plane.

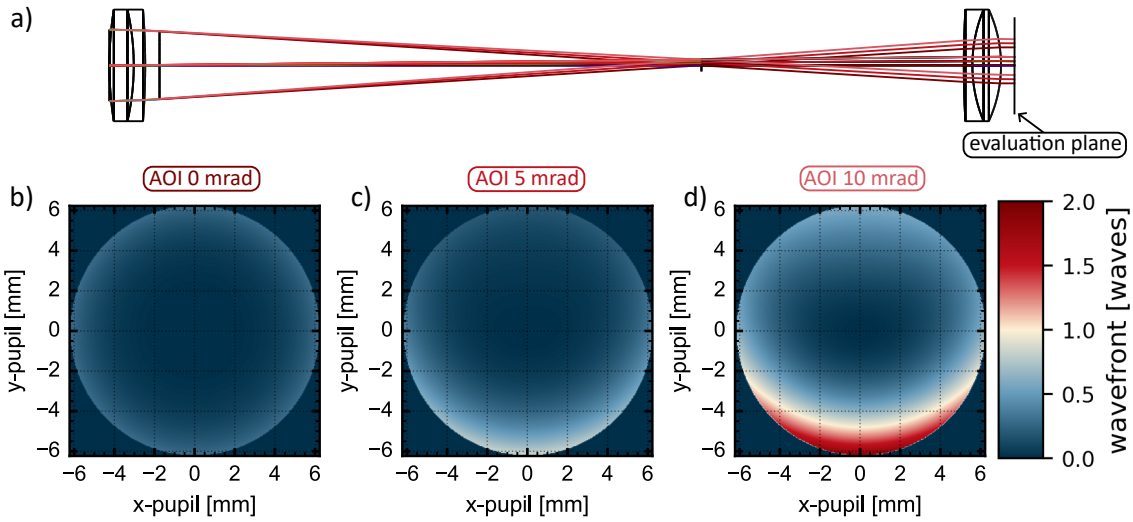

Figure 3.28: Ansys Zemax OpticStudio simulation of the performance of a telescope demagnifying a collimated beam with a diameter of 25 mm. The telescope consists of COTS achromatic lenses, in this case an Edmund Optics 49383 with a focal length of 200 mm and an Edmund Optics 63725 with a focal length of 100 mm. **a)** depicts a sketch of the simulated setup with three different AOI and an evaluation plane a few millimeters behind the second lens. **b)** shows plots of the wavefront error in the evaluation plane for the three different AOI. For the objective of HQA-ONE, these angles correspond to a radial shift in the focal plane of the objective of approximately 0 µm, ±100 µm, and ±200 µm respectively.

The tool of choice to test various commercially available standard lenses was Ansys Zemax OpticStudio. Figure 3.28 shows an exemplary picture of conducted simulations. Figure a) depicts the simulated setup of a Kepler telescope composed of two exemplary lenses. The setup is illuminated with a collimated 25 mm diameter beam with a wavelength of 671 nm from the left with either 0, 5 or 10 mrad AOI. These settings correspond roughly to the size of the objectives rear aperture and the exit angles for shifts in the atom plane of 0 µm, 100 µm (edge of the specified diffraction limited FOV), and 200 µm (edge of the potentially usable, yet not diffraction limited FOV according to [17]). The lens separation is optimized for minimal beam vergence after the second lens for the 0 mrad beam. The metric that is used to quantify the performance of the lens pair forming the telescope is the wavefront error in an evaluation plane 5 mm behind the second lens. Figure b) shows the resulting wavefront error map for different AOI of the telescope in a).

When used within HQA and more specifically in HQA-ONE, light of additional wave-

lengths will propagate through the distribution path and therefore through the telescope stage. This means that light for which the lens separation was not optimized must also be transmitted without imprinting wavefront error. To test this, wavefront errors for the same beams, yet with a wavelength of 532 nm and 1064 nm, are simulated. Together with the results of the 671 nm simulation, this provides data for all three apochromatic design wavelengths of the objective and samples across the entire relevant spectral range of light. An overview of the results of these simulations for a variety of different lens pairs is given in Table 3.2.

It provides a total of twenty different lens pair combinations, all standard COTS available lenses with various focal lengths, diameters, and resulting magnifications of the telescope. The lens spacing in all setups was optimized for 671 nm light. With this setting, the RMS wavefront error in the evaluation plane was simulated for all apochromatic design wavelengths of the objective. Shown in the table are the results for each wavelength for an AOI of 0 mrad (top value) and 10 mrad (bottom), which indicate the on-axis performance and the performance on the edge of the in principle usable FOV.

Looking at the simulation results in Table 3.2, especially lens combinations 16, 17, 18, and 20 seem like reasonable choices, as they introduce comparably little wavefront errors across all simulated scenarios. However, out of these four candidates, options 16 and 17 provide magnifications outside of the desired range according to the beam size estimations in Figure 3.27. Therefore, these lens combinations are deemed unfavorable, narrowing the choice of lens pairs down to options 18 and 20.

Judging by the simulated performances, option 18 was to be favored; however, lens *EO 62494* was not available with an anti-reflection coating that covers the entire optical spectrum between 532 nm and 1064 nm. Consultation with Edmund Optics showed that it was also not possible to purchase small batches of these lenses coated with their standard *VIS-NIR coating* that covers the relevant spectral range. Therefore, this lens is also deemed unfavorable.

This leaves option 20 as the lens pair of choice[19] for the telescope stage. Off the shelf, the AR coating of the second lens *TL ACN254-100-B* also does not cover the full relevant optical spectrum. However, we were able to buy a custom-coated version of the lens, with the same optical properties of this lens but coated with Thorlabs' broadband *-AB* anti-reflection coating to allow use in HQA-ONE. For this reason, the optical performance of the lens is described by the part with the number *TL ACN254-100-B*, yet the official name of the lens is *TL ACN254-100-AB*, which is not officially listed in the Thorlabs catalog.

As a final remark on the selected lenses in the simulations, an additional aspect one has to keep in mind is that the telescope stage is also restricted in length as it has to be adequately mounted. The telescope stage is a critical optical path in the high-NA distribution of the platform, where additional wavefront disturbances have to be avoided as much as possible. This includes that both lenses have to be centered on the same mechanical axis to avoid loss in performance due to misalignment. It can be achieved passively by mounting both lenses in a single structure, for example, connected lens tubes. However, this means that the entire telescope stage including its mounting has to fit vertically between level 1 and level 0 of the FOR (see Figure 3.6) to be placed in a single structure close to the objectives rear aperture without requiring a complex CNC machined, monolithic, L-shaped mounting. The distance between level 1 and level 0 in the FOR is 300 mm, of

[19] which is in essence option 18 with the second lens replaced by a corresponding lens from the Thorlabs catalog.

Table 3.2: Results of Zemax simulations of various COTS telescope lens combinations in analogy to Figure 3.28 (No.2). Shown are key characteristics like focal lengths f_L for the demangification, lens diameter D_L, and the respective part numbers (EO = Edmund Optics, TL = Thorlabs). Results are the root mean square (RMS) wavefront errors for 0 mrad (upper) and 10 mrad (lower) AOI. Missing values indicate clipping. All telescopes were collimated for 671 nm light.

No.	f_L [mm]	D_L [mm]	lenses	rms wavefront error [waves]		
				671 nm	532 nm	1064 nm
1	200:100	40:25	EO 49383	0.05	0.35	0.90
			EO 49360	0.15	0.45	0.85
2	200:100	40:40	EO 49383	0.08	0.39	0.91
			EO 63725	0.38	0.49	0.86
3	200:100	30:25	EO 49377	0.06	0.39	0.91
			EO 49360	0.16	0.49	0.86
4	300:75	30:12.5	EO 49378	0.01	0.18	0.51
			EO 49330	-	-	-
5	300:50	30:25	EO 49378	0.01	0.38	0.58
			EO 17329	0.23	0.63	0.46
6	300:100	30:25	EO 49378	0.01	0.63	0.75
			EO 17333	0.13	0.77	0.69
7	250:125	40:18	EO 49384	0.02	0.23	0.73
			EO 49347	-	-	-
8	300:50	40:25	EO 49378	0.01	0.14	0.47
			EO 67422	0.07	0.21	0.43
9	50:50	25:25	EO 67422	8.75	10.03	1.85
			EO 67422	8.27	9.54	1.79
10	300:100	30:12.5	EO 49378	0.01	0.18	0.55
			EO 49333	-	-	-
11	300:50	30:12.5	EO 49378	0.05	0.21	0.45
			EO 49328	0.32	0.51	0.37
12	200:40	30:25	EO 49377	0.07	0.28	0.65
			TL TRH254-040-A	0.18	0.38	0.60
13	300:75	30:15	EO 49378	0.01	0.17	0.51
			EO 49338	0.18	0.36	0.42
14	150:50	30:15	EO 49376	0.10	0.42	1.02
			EO 49337	0.39	0.72	0.90
15	150:60	30:18	EO 49376	0.12	0.52	1.03
			EO 49344	0.29	0.68	0.95
16	300:-75	30:25	EO 49378	0.00	0.06	0.29
			EO 62493	0.05	0.03	0.33
17	250:-50	40:12.5	EO 49384	0.00	0.10	0.38
			EO 62488	0.08	0.05	0.43
18	300:-100	30:25	EO 49378	0.00	0.05	0.28
			EO 62494	0.03	0.02	0.30
19	150:50	30:18	EO 49376	0.10	0.47	0.98
			EO 49343	0.25	0.67	0.85
20	300:-100	30:25	EO 49378	0.00	0.30	0.38
			TL ACN254-100-B	0.10	0.23	0.43

which some space has to be reserved for a mirror redirecting the beam path to level 1. This consideration provides a limit for the selection of suitable focal lengths[20]. In general, due to their smaller lens spacing, Galilean telescopes allow the use of longer focal lengths while still allowing the discussed placement compared to Kepler telescopes.

With option 20 from Table 3.2 selected as the optics for the telescope stage in the setup, one can now simulate the optical performance of the combination of the telescope stage with the high-NA objective and compare it to the performance of the objective without the telescope. These simulations were again performed using Ansys Zemax OpticStudio. In the simulation, we illuminate the rear aperture of the objective[21] with a collimated beam and test for wavefront error across the FOV in the focal plane. For simulations that include the telescope, we place it in front of the rear aperture of the objective, illuminate it with a smaller, collimated beam, which is magnified by the telescope and illuminates the full rear aperture of the objective. Also, with this model, we test for wavefront errors across the FOV.

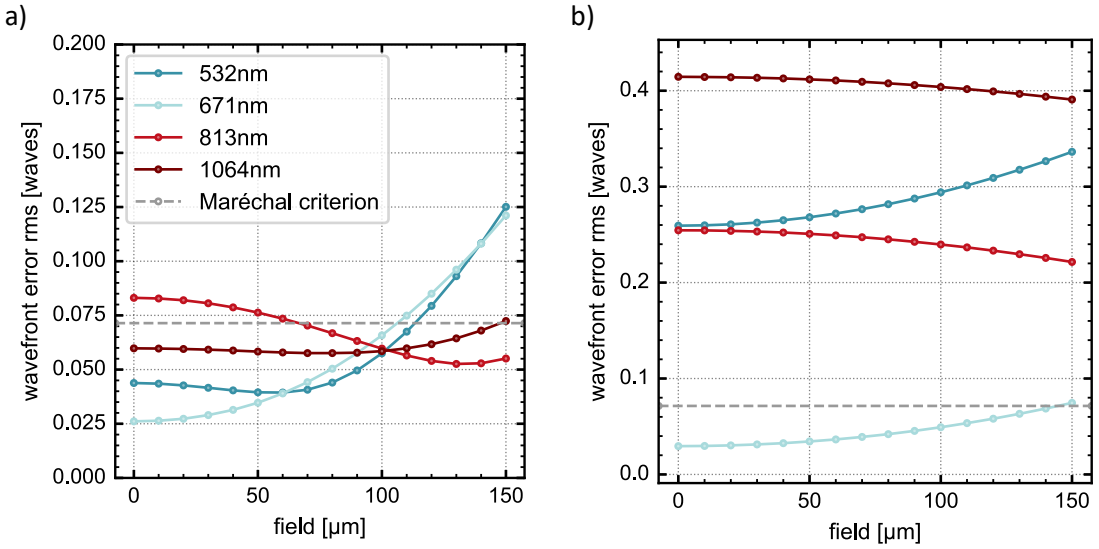

Figure 3.29: Ansys Zemax simulation of the RMS wavefront error in the focal plane of the high-NA objective across its FOV for different wavelengths. For reference, the Maréchal criterion for diffraction-limited performance is plotted as a dashed line. a) shows the performance of the objective alone, while b) depicts the performance of the combination of the intermediate telescope (No.20) and the objective.

Figure 3.29 shows the results of these simulations for the objective in figure a) and the telescope objective combination in figure b). The abscissa shows the radial displacement across the FOV in the atom plane, the ordinate presents the corresponding RMS wavefront error. Another wavelength of light, besides the apochromatic design wavelengths at 813 nm, is added in the simulation. This light will be of interest for later applications of HQA-ONE (see Chapter 6). The Maréchal criterion, a standard indicator for diffraction-limited

[20] Not all combinations in the table fulfill these spatial requirements, but were added to see the scaling of the performance with the focal length of the lenses.
[21] We have a blackbox model of our custom high-NA objective at hand for such simulations.

performance, which states that a wavefront can be considered diffraction-limited if its RMS error $W_{err,rms}$ is below a fourteenth of the light wavelength λ [17]. Therefore, the regions in the figure that satisfy

$$W_{err,rms} < \frac{\lambda}{14} \tag{3.9}$$

can be considered to provide diffraction-limited focal points. Looking at figure a), this criterion is valid for all three design wavelengths of the objective within a certain radius around the optical axis, which matches the specification for the diffraction-limited FOV to be larger than ±100 µm. The RMS wavefront error from the objective for 813 nm light violates this criterion slightly for parts of the FOV.

Figure b) shows that the combination of objective and telescope violates the criterion for diffraction-limited performance for all wavelengths, except 671 nm, the wavelength for which the lens separation of the telescope was aligned. This indicates that the misalignment of the telescope stage for the other wavelengths leads to a residual wavefront curvature of the light that enters the rear aperture of the objective which causes the wavefront error in the focal plane. To verify this hypothesis, one can look for the different contributions to the wavefront error in the atom plane according to the Zernike standard modes.

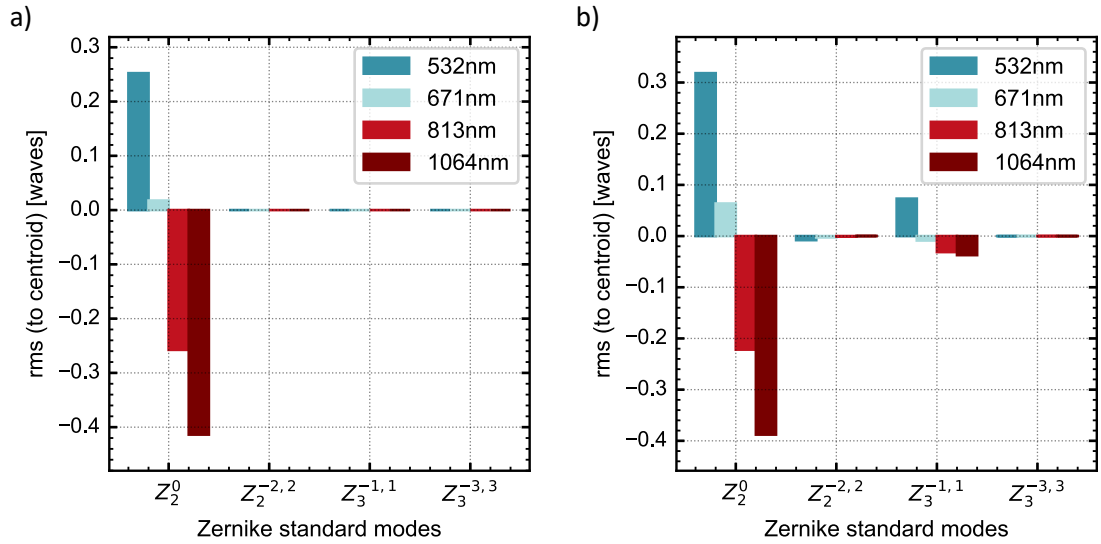

Figure 3.30: Zernike polynomial resolved RMS wavefront error contributions with respect to the centroid for Figure 3.29 b). **a)** presents the the beam in the center of the FOV, **b)** a beam shifted by 150 µm off-axis. The plotted Zernike polynomials are attributed to defocus (Z_2^0), astigmatism ($Z_2^{-2,2}$), coma ($Z_3^{-1,1}$) and trefoil ($Z_3^{-3,3}$) respectively in the two principal directions [77]. For aberrations that have two terms corresponding to the two principal directions, the bar indicates the sum of their absolute values.

Figure 3.30 shows the contributions of selected Zernike standard modes to the wavefront error. Figure a) depicts the on-axis position with 0 µm transversal shift in the atom plane, figure b) depicts the contributions for 150 µm transversal shift, the data points on the very right in Figure 3.29. The data is about the centroid of the beam, contributions of piston (Z_0^0) and tilt in the two principal directions ($Z_1^{-1,1}$) which do not change the shape

of the wavefront are removed and therefore not plotted [77]. The plotted contributions are following low-order terms in the Zernike polynmials which correspond to defocus (Z_2^0), astigmatism ($Z_2^{-2,2}$), coma ($Z_3^{-1,1}$), and trefoil ($Z_3^{-3,3}$) [77]. Terms with two exponents summarize the contributions of effects that can have two principal directions. In the plot, the absolute values of their respective contributions were added up to provide the total contribution to the wavefront error.

One observes that the most relevant contribution to the wavefront error is given by the defocus, which matches the hypothesis that the telescope introduces a residual curvature of the wavefront before it enters the high-NA objective. Only for substantial shifts within the FOV, as depicted in Figure 3.30 b), other contributions to the wavefront error, especially aberrations from coma, arise. Depending on the wavelength, these contributions alone reach values around the Maréchal criterion, yet they are small compared to the defocus contributions. Aberrations from coma and the other bi-directional terms are difficult to compensate; however, the defocus can be corrected with an additional lens that introduces a second defocus, compensating for the original defocus during propagation through the lens system. In the proposed setup in Figure 3.26, this can be achieved by the module lenses. There is a module lens for each wavelength port; therefore, the defocus for each wavelength can be compensated individually.

This can be verified in the simulations by adding a module lens as depicted in Figure 3.31 a). In this exemplary setup, without dichroic mirrors, a point in the image plane O' is imaged via the module lens, the telescope, and the objective onto the atom plane O. In this example, the module lens is identical to the convex lens in the telescope stage, a standard achromatic lens from *Edmund Optics* (EO 49378) with a focal length of 300 mm.

To introduce a defocus of the beam that enters the telescope stage, the distance between the imaged plane O' and the module lens is varied. For each wavelength, it is optimized to achieve the tightest possible focus (radial size) in the center of the atom plane O. The resulting wavefront error in the atom plane for the different wavelengths with individually optimized distances between O' and the module lens is plotted in Figure 3.31 b). One observes, compared to Figure 3.29, that it is indeed possible to compensate for the defocus, which is introduced by the telescope, and to achieve optical performance of the full stack comparable to the limitations of the objective alone.

The wavefront error of the 813 nm light fulfills the Maréchal criterion near the center of the FOV. It gradually increases towards the edges, matching the behavior of the other beam in the atom plane. However, this represents a change in behavior compared to Figure 3.29. This could be explained by the field curvature across the FOV of the image in the atom plane. The objective design was not optimized for use with 813 nm light, it is not a design wavelength, and it is not apochromatic there. This means that, due to chromatic aberration, the focal plane for a collimated beam of that wavelength entering the objective in Figure 3.29 will lead to a shifted focal plane with the minimal spot radius along the propagation axis of the beam. Observed in the fixed plane O, the performance will therefore be worse. Towards the edges of the plane, where field curvature of the focal plane happens, this leads to shifts towards O in propagation direction of the light, improving the optical performance. This could be the reason, the performance increases towards the edge of the FOV in Figure 3.29. The distance between O' in Figure 3.31 a) was optimized at the center point in O, which means the defocus of the module lens additionally shifts the focal plane for that wavelength to O, leading back to the expected behavior.

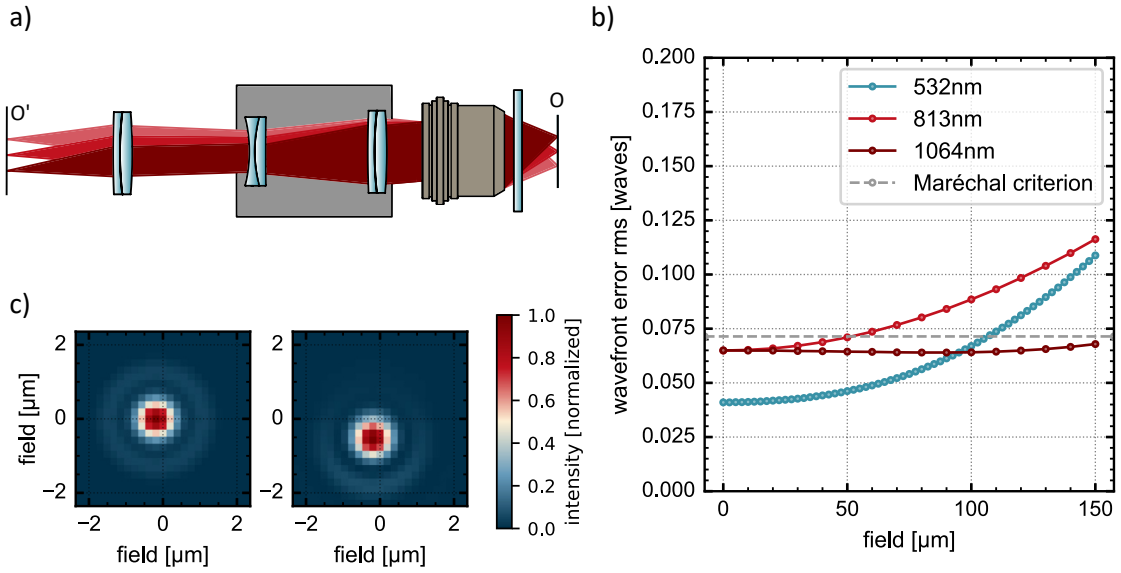

Figure 3.31: Demonstration of the defocus correction with the module lens for wavelengths for which the telescope stage was not aligned. a) shows the setup of the Ansys Zemax OpticStudio simulation, neglecting any (dichroic) mirrors for simplicity. A point in the image plane O' is transferred to the atom plane O. The distance between O' and the module lens can be varied to introduce a suitable defocus. The module lens used exemplarily in this simulation is identical to the convex lens in the telescope stage (EO 49378). b) Resulting RMS wavefront error for the wavelengths the telescope was not optimized for across the FOV. The distance between O' and the module lens was optimized for each wavelength in order to minimize the on-axis spot size, resulting in the presented wavefront errors. c) Simulation of the spot in the atom plane for 1064 nm in the optimized configuration. Left: Spot on axis, in the center of the FOV, Right: Spot shifted by 150 µm across the FOV in the atom plane.

Arguably, the most important wavelength for diffraction-limited use is 1064 nm. This wavelength is commonly used to form the potentials of diffraction-limited optical tweezers. Figure 3.31 b) shows that the wavefront error in the optimized scenario for this wavelength is below the Maréchal criterion across a wide range of the FOV. This means that the optical setup in principle allows the placement of diffraction-limited optical tweezers across a wide range of the atom plane, leading to a large OR for the use of diffraction-limited tweezers. The corresponding spot size and shape for such optical tweezer beams in the atom plane, normalized to the maximum, is shown in Figure 3.31 c). The left plot corresponds to the center position and the right plot to a shift of 150 µm in the FOV. In the simulations, the shift is performed along the vertical direction in the image of the spots, leading to a slight, yet visible deformation of the symmetry of the first side maximum of the airy disc. The central region, defining the trapping potential of the optical tweezer, however, approximately keeps its shape.

The last step of the telescope stage design is to develop the mechanical mounting with which the chosen lens system can be attached to the FOR. As already mentioned, the ideal position for the telescope is vertically between level 1 and level 0 of the FOR. This

position, offering only 300 mm space the between the lower side of the level 1 breadboard and optical table forming level 0 (see Figure 3.6), is possible with the chosen telescope optics requiring a lens separation of around 200 mm.

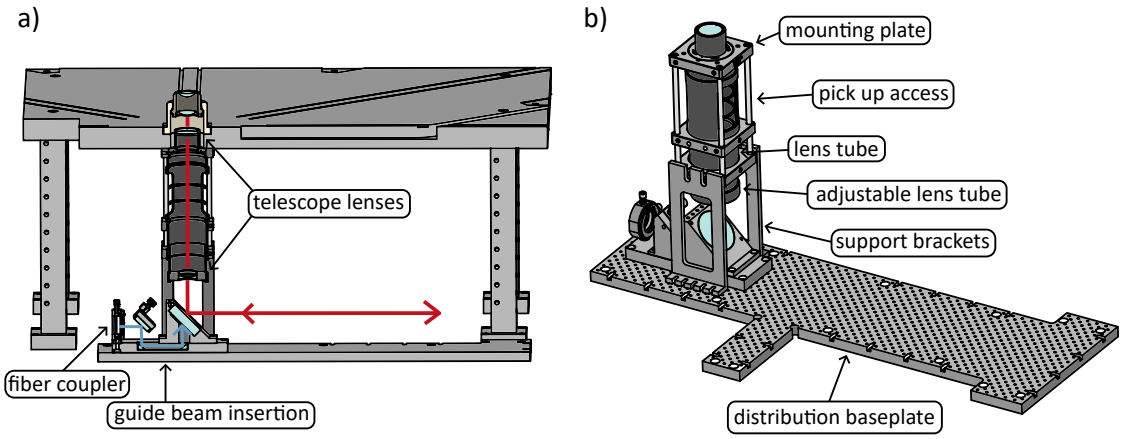

Figure 3.32: Annotated sketch of the mechanical mounting of the telescope stage and the attached breadboard of the high-NA distribution path. a) shows a cross-sectional view of the FOR with the telescope and breadboard for the optics of the distribution path. Indicated in red is the objective path used for the high-NA modules, blue indicates the insertion path for a possible guide beam that can be reflected off the point mirror. This path is not used at HQA-ONE at the moment. b) shows a detailed sketch of the full structure without the FOR.

Figure 3.32 shows an annotated sketch of the mounting of the telescope stage and the attached optical breadboard for the high-NA distribution path connecting the objective with the individual ports in the sense of Figure 3.26. The central part of the mechanical telescope stage structure is the mounting plate, visible in Figure 3.32 b). This is a standard 60 mm cage plate from Thorlabs[22] into which we drilled positioning holes for 4 mm brass pins. These pins correspond to and are placed in the same positioning holes as the objective mount pins (see Figure 3.7) and ensure sufficient overlap of the central axis of the mounting plate used for the telescope with the central axis of the objective. The mounting plate is fastened via four M6 screws, for which we drilled through holes into the mounting plate. An adapter[23] allows the plate to provide a thread for 30 mm lens tubes towards the objective and 2" lens tubes facing away from the objective.

The 30 mm lens tube, which houses the first lens of the telescope stage, reaches into the FOR breadboard right below the objective to minimize the distance to the rear aperture of the objective. However, this also places the lens tube close to the lower stack of coils. To avoid magnetic stray fields from induced Eddy currents in the lens tube, this part was custom-made from plastic in our workshop[24]. The 2" lens tubes facing away from the objective are also screwed into the threads of the mounting plate. The intermediate

[22] LCP34/M
[23] SM2A11
[24] The mounting plate has no Eddy current breaker slit; should one observe in the future issues arising from this, one can still add the cut later. By experience, the telescope assembly can be taken out of the apparatus and reinstalled with experimental down times of less than half a day, due to the positioning with the brass pins

segment of multiple stacked lens tubes consists of a slotted lens tube[25] that can be opened up to allow optical access for beam pick-ups. Inserted into the last part of the 2" lens tube stack is an adjustable lens tube[26] which holds the second lens of the telescope and can be translated up and down the lens tube direction by changing the insertion depth of that adjustable lens tube. This allows alignment of the lens separation when constructing the telescope stage before integration into the platform. A locking ring secures the adjustable lens tube once it is positioned. All lens tubes are screwed directly into the mounting plate; therefore, external forces that could bend the lens tube stack are omitted, making the central axes of the parts overlap according to the tolerances of their threads and their intrinsic bending.

In order to protect the lens stack from external forces and to provide additional mounting points for the pick-up access, cage rods and two cage plates with through holes for the 2" lens tube[27] are attached to the mounting plate. This external support structure does not touch the lens tube stack and therefore does not introduce stress, potentially leading to deformation. It is positioned by the cage rods and supported by two L-shaped support brackets, which are clamped on the distribution baseplate of the high-NA path and via M6 screws to the lower cage plate. The treads for these were added in-house to the components purchased from Thorlabs.

Placed between these clamps, see Figure 3.32 b), is a custom mount for a 2" silver mirror that reflects the beam horizontally onto a distribution baseplate on which further optics for the high-NA distribution path can be placed. For this, the 12.7 mm baseplate breadboard is equipped with the O-Lego pattern and the mirror placed such that it leads to a beam height of 50 mm, allowing the use of the same O-Lego optomechanical mounts as on the PoCs. The custom, CNC machined board is mounted with M6 screws directly on the optical table and referenced to the hole pattern on it with the same placement pins used to reference the FOR to the hole pattern on the optical table (see Section 3.3). The thickness of the distribution baseplate was chosen as 12.7 mm to allow later use of custom-made breadboards for the mPoCs as well as COTS breadboards with minor adaptations. Details about the mechanical interfacing of these will be discussed later in this section.

An additional feature of the 2" mirror mount is that it is equipped with the possibility to provide a guide beam for the high-NA path. As visible in Figure 3.32 a), a fiber coupler mounted in a 2D-translation stage can provide a beam which is reflected off an adjustable mirror mount and two right-angle prisms, which are glued into the mount, onto the backside of the mirror. Light leaking through is sent towards the objective. Via the DoF of the 2D stage and the first mirror mount, it can be aligned to be reflected off the point mirror and back on the 2" mirror to provide a guide beam in the plane of the high-NA distribution. However, this requires the use of a backside polished mirror with a dielectric coating, which allows some light transmission at the wavelength used for the guide beam. At HQA-ONE we installed a regular 2" silver mirror, for availability reasons; therefore, the guide beam option is not used at that specific apparatus.

[25] SM2L30C
[26] SM2V15
[27] LCP36

3.7.3 Dichroic mirror mounting

Following Figure 3.26, one now has to place the dichroic mirrors and lenses on the distribution baseplate. Especially the dichroic mirror mounting is not a trivial task, as these are typically only a few millimeters thick and therefore easily bend when mounted. This causes problems, especially in the light field reflected off the dichroic mirror. Bending of the mirror surface introduces an equivalent radius of curvature (RoC) of the wavefront. In the case of symmetrical bending causing defocus, which could in principle be compensated, in the more probable case of unsymmetrical bending, this will lead to other aberrations like astigmatism, which is much harder to compensate.

At HQA-ONE, we equipped the high-NA distribution path with five ports for mPoCs, providing spectral ports for light with wavelengths of 532 nm, 638 nm, and 1064 nm to form trapping potentials, as well as 671 nm and 813 nm to address and image internal transitions of the used ^{6}Li. We decided to use COTS available dichroic mirrors form *Semrock*[28] in their standard rectangular size of 25.2 mm x 35.6 mm with a thickness of 3 mm, the recommended option for dichroic mirrors in imaging paths due to the improved resilience to bending compared to the 1 mm thick option. In terms of mounting them, we decided after consultation with the German retailer for Semrock products, to glue the mirror into their mounts instead of clamping them. Mechanically clamping these thin glass plates always results in local stress leading to deformation, which impacts the mirror's performance.

Glues which are commonly used for mounting optical components are ultraviolett (UV) curing glues. These adhesives are available for a wide variety of specifications, e.g., which types of materials are to be glued together or whether mechanical strength or strain-reduction is to be preferred, and offer user-friendly alignment times as they only start to bond when exposed to UV light. The intensity of the UV light can be used to set the speed at which the glue hardens; however, parts that are not exposed to the UV light, e.g., in corners of mounts, will not cure. Additionally, we were advised that silicone glue can also be used effectively to mount these mirrors. The silicone glue cures slowly, over several days, and due to its elastic properties, it reduces strain and therefore deformation of the mounted glass plates.

In order to test the mounting options for the dichroic mirrors and to understand what performances one would expect, we built a test stand, following the approach presented in [78]. We use mock-up silver mirrors with identical dimensions as the dichroics (Edmund Optics 43-875) and measure the change in their flatness after gluing them into their mounts with different adhesives.

Figure 3.33 shows an annotated sketch of the setup and visualizes the measurement principle. Light from an optical fiber with a wavelength of 671 nm is collimated with an aspheric lens[29] with a focal length of 18.4 mm and magnified with a Galilean telescope[30] to provide a collimated beam with a diameter of around 7 mm given the mode field diameter of the fiber with 4.5 µm. This beam passes through a polarizing beam splitter (PBS) cube with a $\lambda/2$ waveplate in front to regulate the transmission of the light, which illuminates a test surface. In this case, the mirror surface of which we want to measure the bending. A $\lambda/4$ waveplate ensures that the reflection of the mirror surface gets reflected on the PBS cube

[28] www.idex-hs.com/semrock
[29] Thorlabs C280TMD
[30] f=-125mm lens and f=250mm lens, both from FOCtek (www.foctek.net)

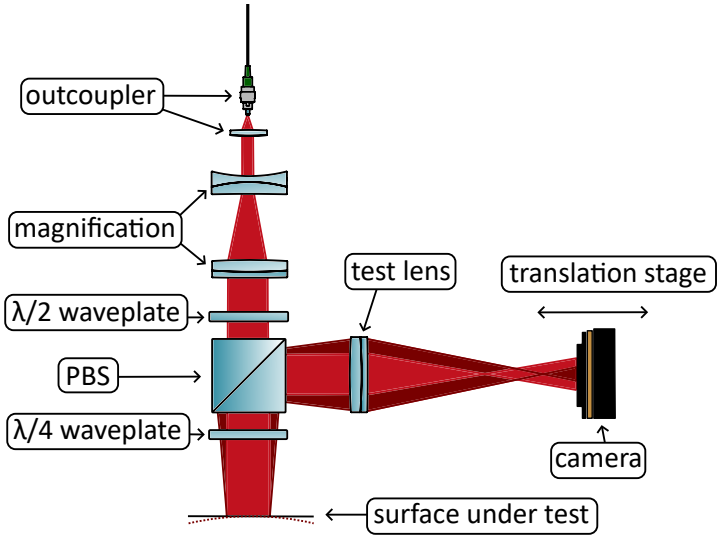

Figure 3.33: Annotated sketch of the test stand used to measure the change in bending of a glass substrate due to mounting by mapping the bending of the part to a focus shift of a beam, which can be resolved with a camera on a translation stage. Measurement concept and setup based on [78].

in back propagation. This beam is reflected onto a lens, specifically an achromatic lens[31] with a focal length of 400 mm, and then focused. The relative position of the focus can be probed by measuring the beam width along its propagation direction with a camera[32] on a linear translation stage[33]. The entire optical setup is mounted vertically, allowing the surface under test to lie flat on its back and be tested without any mounting stress. Stops are mounted that allow the mirror and its mount to be repeatably placed, probing the same location on the mirror before and after applying the glue. The fundamental idea of the measurement is now that bending of the surface under test will result in a changed curvature of the wavefront which is sent onto the test lens. This leads to a shift in focus, which can be measured with the camera. Therefore, even with mock-up mirrors, with a flatness specification much below the dichroic mirrors, a relative change of the curvature due to the bending can be measured.

Figure 3.34 a) shows a photograph of the test mount in which the mock-up mirrors are glued[34]. The mount is inspired by [79] and provides a flat plane on which the outer part of the back of the mirror rests and a 2 mm wide gap surrounding the mirror's outer edge. The glue is placed as four drops, two per side of the long axis of the rectangular mirror, approximately splitting the side in three equal parts. Glue is placed such that it only touches the outer edge of the mirror and the Aluminum mount, creating a chamfer-like drop shape. No glue is placed between the mirror and the mount. This allows for the volumetric shrinkage of the glue to happen upon curing without exerting stress perpendicular to the

[31] Thorlabs AC254-400-B
[32] FLIR CM3-U3-13Y3M-CS
[33] Thorlabs PT1/M
[34] The final mount of the dichroic mirror on the high-NA distribution looks identical expect that it is CNC machined as a single piece with a post to fit on the O-Lego system and anodized the reduce reflections and ghosting in the optical path.

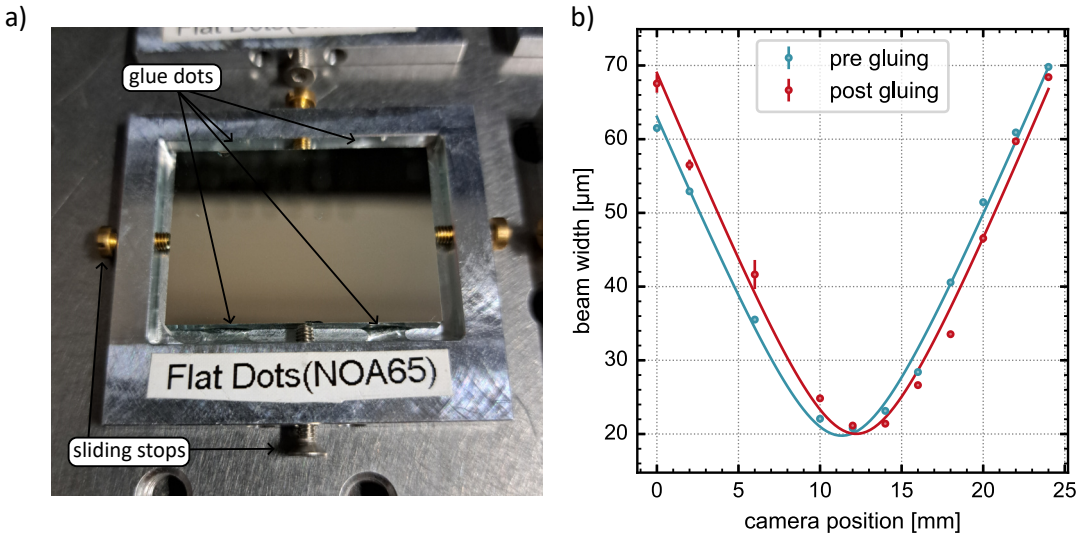

Figure 3.34: **a)** Picture of the mount into which the mock-up mirror and later the dichroic mirror are glued. It provides a flat surface on which the backside of the mirror rests and a gap on the sides to place a total of four glue drops. These only touch the outside of the mirror and the Aluminum frame it is glued to, i.e., there is no glue between the backside of the mirror and the metal piece. This allows for volumetric shrinkage of the glue, which does not result in stress perpendicular to the reflecting surface, the direction along which the mirror tends to bend. Four screws are placed as sliding stops. They do not touch the mirror, but provide stops to avoid larger accidental movement of the mirror when placing the glue, which could lead to glue getting between the mirror and the mount. **b)** Exemplary measurement of the focal position for the horizontal axis of the camera chip before and after gluing. The data points are retrieved from a 2D Gaussian fit of the camera image. The solid lines represent the fitting function of the evolving beam width of a Gaussian beam.

mirror surface along which bending is prone to occur [79]. To allow placing the glue in the gap with a syringe, without accidentally sliding the mirror around, which could lead to glue getting between the mirror and the mount, four screws, one per side, can be inserted to serve as stops. These screws do not touch the mirror; they only serve as stops to prevent the mirror from sliding around when applying the glue. In principle, they can be removed after curing. We tested in our setup a total of three different glues. The standard UV curing glue in our laboratory *NOA61*, a UV curing glue optimized to reduce strain in the glue materials *NOA65*, both manufactured by *Norland Products*[35], and a silicone glue[36] as suggested by the Semrock retailer.

With these mock-ups, we can now measure the focal of the beam and retrieve the relative position before and after gluing. Figure 3.34 b) shows exemplary the resulting measurements for one axis of the mirror glued with the silicone glue. A camera image of the light field distribution at a position around the focus is taken as a first step. The beam width at that position ($1/e^2$ radius) along the vertical axis of the camera chip (y-

[35] www.norlandproducts.com
[36] Momentive TSE399C

axis) and horizontal axis (x-axis) is retrieved via a 2D Gaussian fit of the image. Notably, these directions do not coincide with the axes of the rectangular mirror; they are rotated compared to these. Comparing the shift due to gluing between these two arbitrary axes still allows insight into the induced astigmatism of the mirror, which will most likely not deform equally along both axes. This measurement of the beam width is repeated for a total of 24 mm along the propagation axis of the beam. The translation stage provides relative positional placement. The resulting evolving beam width can be fitted with a function describing the expected evolution for a Gaussian beam [76]. The width w along the propagation direction is given z by

$$w(z) = w_0\sqrt{(1 + \frac{z - z_0}{z_R})} \tag{3.10}$$

where w_0 is the waist of the Gaussian beam, z_R its Rayleigh length, and z_0 the position of the waist relative to the linear translation stage indicator. The measurement shown in Figure 3.34 b) corresponds to the beam width evolution of the beam width along the x-axis of the camera chip for testing the Silicone glue. The fits of the evolution are shown as solid lines and provide the position of the waist. The difference of this position due to gluing the parts $\Delta z_0 = z_{0,post} - z_{0,pre}$ to reconstruct the induced bending.

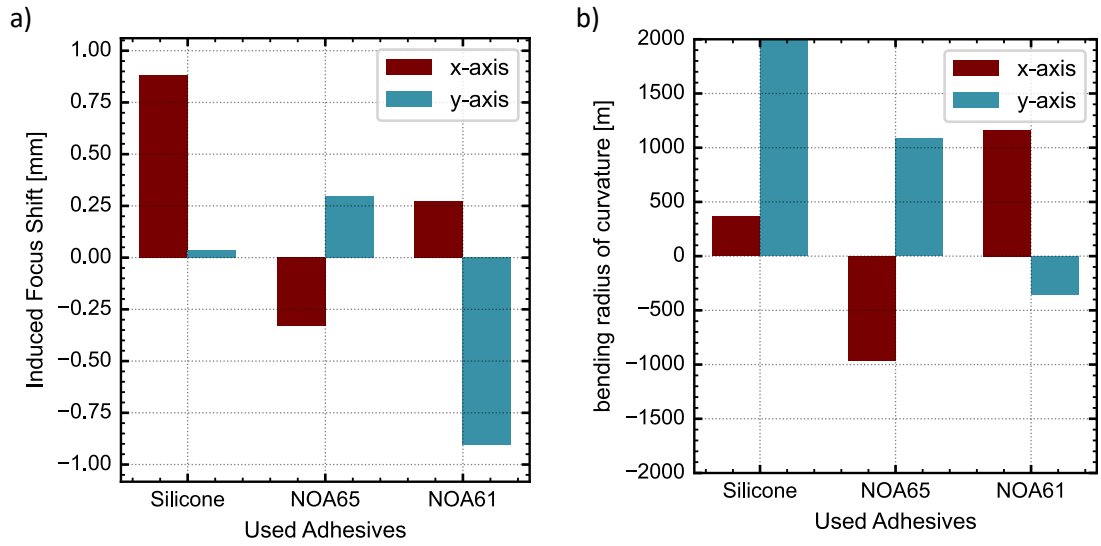

Figure 3.35: Results of the glue testing with the mock-up mirrors, depending on the type of glue used. **a)** presents the observed focal shift due to the gluing in the two principal axes of the camera chip, **b)** presents the corresponding change in the radius of curvature for the focal shifts shown in a). The value for the y-axis for silicone is clipped for better visibility; it is around 9000 m.

Figure 3.35 a) shows the measured induced focal shifts due to gluing the mirrors with different glues along the two principal axes of the camera. As discussed earlier, the critical metric is the difference in behavior for the two axes causing Astigmatism, which cannot be easily compensated. One observes that the glue NOA61, the UV curing glue which was not optimized for strain release, yields the most significant difference in bending for the two axes, indicating the worst performance out of these three. The UV curing glue NOA65,

optimized for strain relief, and the Silicone glue yield similar values for the difference along the two axes. Arguably, NOA65 slightly outperforms the Silicone glue as both axes experience a shift, yet the respective absolute values of the shifts are smaller than for the silicone-glued mirror.

The measured focal shift can be calculated back to a change in the respective RoC of the mirror in the respective axis. The shift of the focal point corresponds to a change of the RoC of the wavefront after the test lens between the two iterations. Therefore, one can write

$$\Delta z_0 = RoC - RoC'. \tag{3.11}$$

The resulting focal length of a mirror bend with radius R is given by $f_{mirror} = R/2$ [76]. Assuming that the focal length of the mirror is very long compared to the distance between the mirror and the test lens, the radius of curvature of the wavefront going into the test lens RoC_{in} is given by $RoC_{in} = R/2$. With a small bending of the mirror under test corresponding to focal lengths of several hundred meters and a distance between the mirror under test and the test lens of a few tens of centimeters, this approximation can be considered valid. The RoC of the wavefront leaving the test lens for an incoming wavefront RoC_{in}, can be calculated with the lens equation [76] as

$$\frac{1}{RoC} = \frac{1}{f_{test}} - \frac{1}{RoC_{in}} \tag{3.12}$$

where f_{test} is the focal length of the test lens. Inserting Equation 3.12 into Equation 3.11 yields

$$\begin{aligned} \Delta z_0 &= RoC - RoC' \\ &= \left(\frac{1}{1/f_{test} - 1/RoC_{in}}\right) - \left(\frac{1}{1/f_{test} - 1/RoC'_{in}}\right) \\ &= f_{test}\left(\frac{1}{1 - f_{test}/RoC_{in}} - \frac{1}{1 - f_{test}/RoC'_{in}}\right) \end{aligned} \tag{3.13}$$

Approximating the of the incoming wavefront as planar, $RoC'_{in} \approx \inf$, setting this situation as a perfectly planar mirror for reference, Equation 3.13 simplifies to

$$\Delta z_0 = f_{test}\left(\frac{1}{1 - f_{test}/RoC_{in}} - 1\right). \tag{3.14}$$

Given that $RoC_{in} = R/2$, Equation 3.14 can therefore be written as

$$R = \frac{2f_{test}}{1 - \left(\frac{1}{(\Delta z_0/f)+1}\right)} \tag{3.15}$$

connecting the measured focal shift due to the glue to the change in the bending radius of the mirror under test. The resulting changes in curvature R according to Equation 3.15 for the focal shifts in Figure 3.35 a) are shown in Figure 3.35 b).

These curvatures have been measured over a 7 mm sampling diameter of the mirror, which was illuminated by the collimated light beam in the test stand. Given this light field size on the mirror, the change in peak-to-valley-flatness for a radius of 400 m is around

31 nm corresponding to around $\lambda/20$ for the 671 nm light. Which is locally less than the specifications for typical optical mirrors.

In the end, we decided to use the Silicone glue to mount the dichroic mirrors in mounts similar to the presented test mount, except being anodized and machined with a post to fit on the O-Lego grid of the high-NA distribution base plate. Choosing NOA65 would have also been a valid option, but given their similar performance, we decided to go with the glue recommended by the retailer.

3.7.4 mPoC interface

The placement of the lenses in the optical path of the high-NA distribution to follow Figure 3.26 is much less critical in placement and mounting than the dichroic mirror, mounting with lens tubes in O-Lego mounts with their respective placement is sufficient. This leaves the interface between the high-NA distribution and the mPoC modules as the last building block to be discussed.

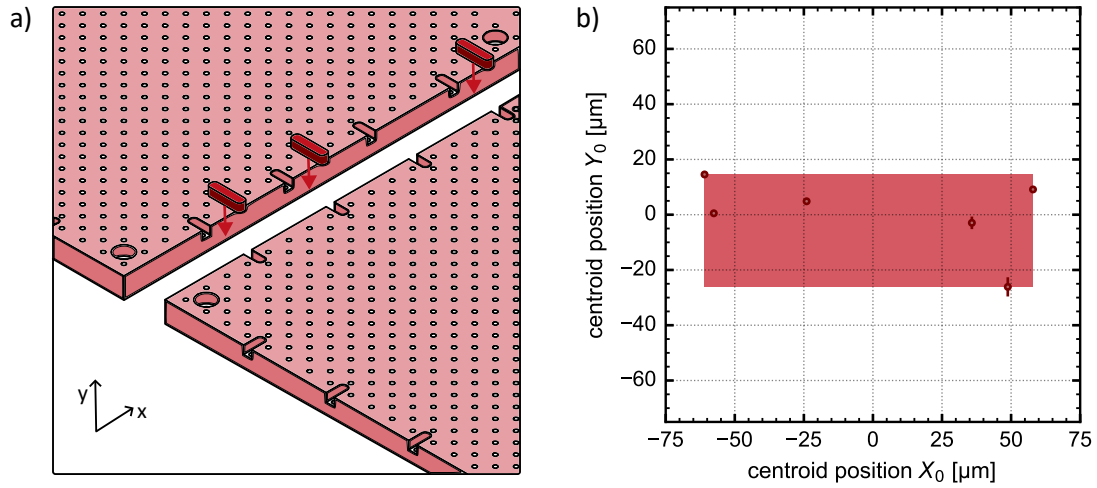

Figure 3.36: Mounting mechanism of the mPoC interface. a) depicts a sketch of two breadboards which can be attached via notches and parallel keys, the mechanism used to attach the mPoCs to the high-NA distribution base plate. The edges of the breadboards are positioned, the parallel keys used for locking, are COTS available standard parts in mechanical engineering. b) depicts a measurement of the precision of attaching two breadboards accordingly. Measurements were taken with a camera on one breadboard and a 3 mm diameter beam outcoupled on the other breadboard. These optics were spaced around 160 mm apart from each other during the test. The maximum variation, depicted by the box as a guide to the eye, is ±59 µm parallel to the plane of the breadboards and ±20 µm orthogonal to them.

Just like the PoCs, the mPoCs are essentially breadboards that can be attached as modules to the main structure. The optical paths are built with respective components, e.g., O-Lego mounts, on the hole pattern of the breadboards. Unlike the PoCs, these modules do not have to follow a special symmetry; therefore, we use a rectangular base shape for these modules. We chose a thickness of 12.7 mm such that one can either use a custom-made breadboard like we do at HQA-ONE or adapt COTS available breadboards

to work as mPoC modules.

Figure 3.36 a) shows the general mounting mechanism used to connect the mPoCs to the high-NA distribution baseplate. CNC machined notches in these breadboards are used to position them relative to each other with parallel keys, a standard COTS available part in mechanical engineering. Used in this design are keys with a width and height of 5 mm and a length of 20 mm. The notches in the breadboards are sized accordingly. When connecting two breadboards, a single or multiple parallel keys are placed in one of the notches, and the other board is slid into place accordingly until their edges touch. Effectively, this constrains the breadboard angle via their edges; the keys lock their relative parallel position. This means that in principle, one key is sufficient to place the boards relative to each other; in practice, usually two keys are used. After placing the mPoC breadboard relative to the distribution baseplate, it is fastened via M6 screws directly in the optical table, forming level 0 of the FOR. The lack of a custom-machined structure below these modules necessitated a different placement approach compared to the pins of the PoCs. The parallel key mechanism works in principle on every optical table. Adding the required notches for the parallel keys to COTS purchased boards with a CNC mill to use them as modules with this mechanism is easily possible.

Figure 3.36 b) shows a test of the precision of this mechanism, in analogy to the testing of the PoCs in Section 3.6. A camera[37] is placed on one breadboard equipped with the mechanism, a fiber outcoupler generating a Gaussian beam with a diameter of 3 mm on the other one. The relative position of the centroid of the beam on the camera is retrieved via a 2D Gaussian fit. The breadboards are repeatably removed and re-positioned with the keys leading to the presented data. For the optics which are separated by around 160 mm one finds a repeatability of $\pm 59\,\mu$m in the plane of the breadboards and $\pm 20\,\mu$m orthogonal to it. If these were purely angular, this would correspond to a precision of ± 0.3 mrad and ± 0.1 mrad, respectively. This is significantly larger than precision provided by the pins and PoCs, yet due to the design of the high-NA distribution path where the image on the module O' is demagnified to the atom plane O, these variations in the placement of the module plane, effectively also get demagnified with respect to the center of the FOR. Therefore, the precision of this mechanism is compatible with PoC positioning precision and sufficient for use.

3.7.5 high-NA distribution path and mPoC interface at HQA-ONE

All these parts combined yield the mechanical realization of the mPoC concept of HQA according to Figure 3.26 within HQA-ONE. This is sketched out in Figure 3.37.

The telescope stage, together with the 45° mirror, forms the telescope assembly, connecting the optical path of the objective to the baseplate of the high-NA distribution, where subsequent optical components are placed. HQA-ONE is designed to provide a total of five spectral ports for the mPoC modules. Given the available selection of COTS dichroic mirrors from Semrock, leads to a T-shaped arrangement of these mirrors. The first mirror[38] on the breadboard is a longpass filter that reflects 532 nm to its respective port. It can be used for blue detuned ODT potentials. The next mirror[39] reflects light with wavelengths $\lesssim 698$ nm, which is subsequently split by the third mirror into light of 638 nm and

[37] FLIR CM3-U3-13Y3M-CS
[38] Di03-R561-t3
[39] Di03-R685-t3

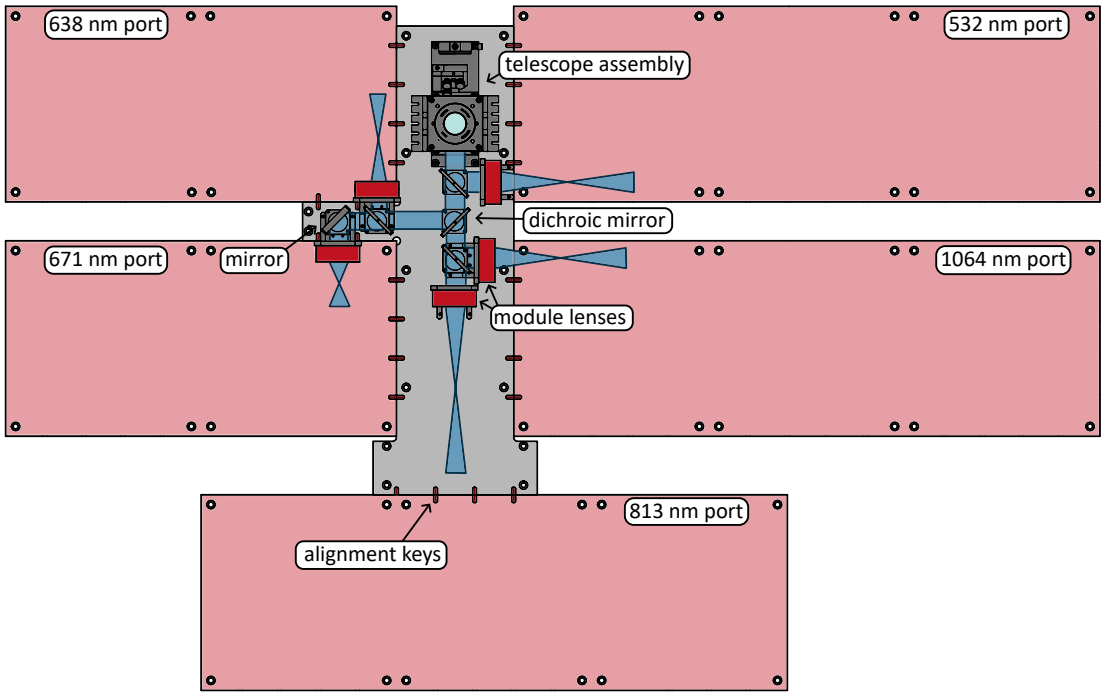

Figure 3.37: Annotated sketch of the mechanical realization of the high-NA distribution and mounting of the mPoCs within HQA, the ports and dichroic mirror selection represents those used at HQA-ONE.

671 nm port. The initial split-out is necessary, as there was no dichroic mirror available that separates these wavelengths while fulfilling the spectral transmission requirements of the subsequent ports. The 638 nm port is intended for the generation of blue detuned ODT potentials from spatially incoherent light [80]. 671 nm light is resonant with the ^{6}Li D_2 Line is and is primarily intended for imaging. On the distribution baseplate light with wavelengths $\gtrapprox 698$ nm is separated by a shortpass dichroic mirror[40] splitting guiding it to a port for 1064 nm light, dedicated to red detuned ODT applications, and a port for light between ≈805 nm and ≈820 nm, corresponding to trapping and manipulation utilizing the $|2p\rangle \rightarrow |3s\rangle$ transition of ^{6}Li at around 813 nm [81].

The light irradiating the dichroic mirror stack covers an AOI of 45°±1.83° to enter the telescope stage such that it allows transversal shifts in the atom plane of up to ±200 µm. Variations in the AOI in dichroic mirrors can lead to spectral shifts of the reflection/transmission edge of the component. Simulations with Semrocks *MyLight Tool*[41] show that the stack of selected dichroic mirrors, not including other optics in the high-NA path, provides the transmission of the respective ports for an AOI of 45°±2° as shown in Table 3.3.

The mounts are individually placed such that beams are illuminated centrally, the respective beam displacement of 0.9 mm in the plane of the breadboard when transmitted by the 3 mm thick mirrors under 45° AOI is compensated with shifted mounting holes on the mirror mounts. Nevertheless, the addressable FOV in the atom plane is limited by

[40] FF880-SDi01-t3
[41] www.idex-hs.com/store/product-detail/di03_r561_t3_25x36/

the size of the dichroic mirrors. The FOV shown in Table 3.3 has been calculated using the specified usable aperture of the shortest axis of the rectangular mirrors for an AOI of 45° following Equation 3.8. Physically larger versions of the same dichroic mirrors are, in principle, available upon request, yet mounting larger glass plates with the same thickness will increase the difficulty of mounting them while limiting induced bending. Therefore, one has to consider this trade-off when magnifying the addressable FOV.

Table 3.3: Expected Transmissions of the dichroic mirror stack in HQA-ONE for an AOI of 45°±2°, not including the objective or telescope stage. The stated FOV corresponds to the minimal dichroic mirror size limited axis in the atom plane following the specified clear aperture of the rectangular mirrors and Equation 3.8.

Port	Transmission T_{s-pol} [%]	Transmission T_{p-pol} [%]	$\mathrm{FOV}_{\mathrm{port}}$ [µm]
532 nm	99.1	97.2	±240 µm
638 nm	92.3	88.2	±150 µm
671 nm	88.8	96.6	±150 µm
813 nm	81.8	98.5	±175 µm
1064 nm	87.1	89.4	±175 µm

Mounted directly behind the dichroic mirror are L-shaped lens mounts placed on the O-Lego pattern. These provide an SM2 thread to which lens tubes with respective module lenses can be mounted. These are shown in dark red in Figure 3.37. The combination of a fixed mount and the lens tube ensures that the module lens can be easily exchanged without significant displacement compared to the 8.3 mm diameter beam it focuses. Placement of the dichroic mirror mounts, which compensate for the beam displacement due to the transmission of the glass plates, allows all module lenses to be centered on the O-Lego hole pattern. Only the 813 nm port does not allow this propagation, as it is composed of an odd number of glass plates in a straight line. Therefore, the module lens mount is also shifted to allow central illumination of the lens; however, the beam propagation is parallel shifted to the hole pattern by 0.9 mm.

The best position of the focus can be found via a Zemax OpticStudio Simulation, which includes the distances of all optical elements in the beam path, standardized for every port. A module lens intended for use can be inserted, and the distance to the focus optimized for best optical performance, yielding the image plane of the atom plane on the mPoC. Knowledge of this plane, allows development and construction of the module that generates its magnified, designated light field in this image plane which is subsequently transferred to the the atom plane[42]. The magnification of the image plane, leading to light field sizes of typically several millimeters, omits the need for a testbench for the mPoC modules, sensors like cameras can be placed directly in this image plane. Using a beam-splitter cube on the module between its last lens and image plane even allows for permanently placing a camera which monitors the produced light field.

[42] In general, we found that it is good practice to mount the last lens of the mPoC which forms the image on a linear translation stage to allow optimization by hand to compensate imperfections.

3.8 Adapting HQA

HQA has been designed as a modular platform architecture that allows adaptation by other ultracold gases researcher teams, largely independent of the atomic species they plan to use. We are happy to share all design files of the platform described in this thesis upon request. At the time this thesis is being written, were in the process of setting up a repository to simplify the file sharing.

Adaptation of the apparatus for use with Lithium is straightforward and can follow the design files directly. Further adaptable specifics of HQA-ONE, a ^{6}Li realization of HQA, beyond the general aspects, are described in the next chapter. Adaptations for other atomic species, for example, leading to different properties of the high-NA objective, require re-assessment of the assemblies like the telescope- or the magnetic field assembly, the design choices of which were influenced by the intended use of ^{6}Li. Similarly, specific requirements like decoupling of the magnetic field assembly from the FOR or adding a second high-NA objective[43] can alter the details of the precise technical realization of the platform, yet, the general concept of HQA, its modularization, and large parts of its technical realizations remain applicable.

[43] for this, one would keep one of the objectives passively mounted and place the other objective on an adjustable stage to overlap the ORs of the objectives which can be as small as few micrometer along the focus of the beam.

4 Specifics of HQA-One

This chapter is dedicated to the specifics of HQA-ONE beyond the realization of HQA in a representative apparatus. The chapter covers the functionality and technical implementation of additional systems necessary for laboratory operation of HQA-ONE as a quantum simulator platform based on fermionic ^{6}Li. Most of these systems are described in detail in respective Bachelor's or Master's theses within the scope of which these systems were built. This chapter provides a synopsis of these; details are deferred to further reading in the respective thesis as cited in the sections or listed in Table 1.1.

Section 4.1 presents the laser systems of HQA-ONE which power the apparatus, by providing the trapping, cooling, and imaging light for the optical modules and in the end effectively the used ^{6}Li atoms. Section 4.2 details the compact vacuum chamber and integrated atom source for the experiments. Section 4.3 provides insight into the used magnetic field assembly at HQA-ONE, its operation, stabilization, and use for interaction- and internal state control. Section 4.4 deals predominantly with the resulting Joule heating of the magnetic field assembly and how this is taken care of. Eventually, Section 4.5 provides an overview of the automation of HQA-ONE, including systems for experiment control, status monitoring, and interlocking.

4.1 Lasersystems

This section will detail the laser systems that have been set up to address the ^{6}Li atoms in HQA-ONE for resonant and off-resonant atom-light interaction. In the modular approach of HQA, all modules are fed their light via optical fibers, as placing a large, heavy laser head[1] on the module is possible, but for obvious reasons impractical. Therefore, the optical setups of laser systems presented here can be seen as distribution hubs of the laser light for modules in the apparatus. These can be easily reconfigured and expanded to provide the light, within their total power budget, for other modules and their applications when reconfiguring HQA-ONE.

4.1.1 internal structure of ^{6}Li

The relevant wavelengths for use in a ^{6}Li quantum gas apparatus can be extracted by examining the atoms' internal structure and energy level scheme, a rudimentary overview of the relevant structure for the laser systems, and this thesis, is shown in Figure 4.1. This overview is based on the in-depth description of the properties of ^{6}Li, recommended for further reading, in [82].

Lithium, as an alkaline element, has a single valence electron leading to a hydrogen-like shell structure with the $|2^2s_{1/2}\rangle$ state as its electronic ground state. The first excited

[1] In some cases, the laser heads are even permanently attached to their controller, hindering relocation of the module.

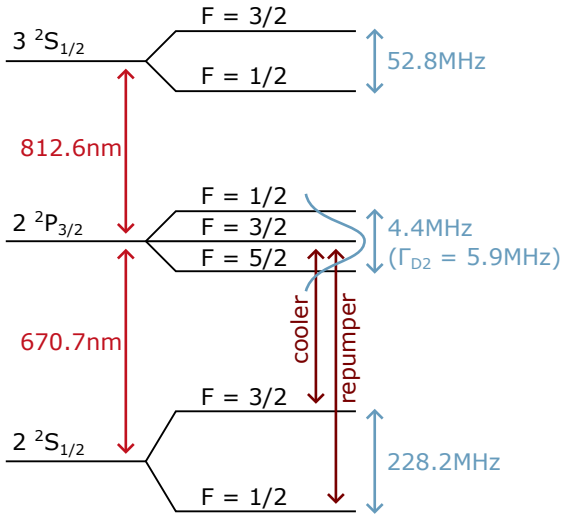

Figure 4.1: Level scheme of the electronic structure of the ^{6}Li atom in fine structure and hyperfine structure for the electronic ground state $|2^2s_{1/2}\rangle$ and the first two excited states $|2^2p_{3/2}\rangle$ and $|3^2s_{1/2}\rangle$. The unused state $|2^2p_{1/2}\rangle$ corresponding to the D_1 line is not shown for better visibility. The two frequencies for a closed MOT transition are shown in the hyperfine structure. Sketch based upon [82, 83].

state splits in the fine structure to $|2^2p_{1/2}\rangle$ and $|2^2p_{3/2}\rangle$, separated by around 10 GHz, due to spin-orbit-coupling. The transitions between the ground state and the respective first excited states are named D_1 ($|2^2s_{1/2}\rangle \rightarrow |2^2p_{1/2}\rangle$) and D_2 ($|2^2s_{1/2}\rangle \rightarrow |2^2p_{3/2}\rangle$), of which only the D_2 transition will be used in the scope of this thesis. The D_1 line, which is far detuned compared to the natural transition linewidth of the D_2 line of $\Gamma_{D2}/2\pi$ =5.9 MHz, will therefore be neglected.

^{6}Li, the fermionic species out of the two stable Lithium isotopes ^{6}Li and ^{7}Li, has a nuclear spin of $I_{6Li} = 1$ leading to hyperfine splitting of the electronic ground state into an $F = 1/2$ and an $F = 3/2$ manifold, separated by 228.2 MHz. The hyperfine splitting of the first excited state, 4.4 MHz, is less than the natural line width of the D_2 transition; these levels are therefore spectrally not resolved. The D_2 is used as the MOT transition in ^{6}Li experiments; however, it is not a closed transition on the hyperfine level. Therefore, two beams are required to close the transition for MOT operation, these are called *cooler* and *repumper*. The respective transition is shown in the level scheme in Figure 4.1.

Additionally, the second excited state, $|3^2s_{1/2}\rangle$, relevent for concepts in Subsection 6.2.1 is shown. Just like the $|2^2s_{1/2}\rangle$ state, it splits in the hyperfine regime again into an $F = 1/2$ and an $F = 3/2$ manifold, separated by 52.8 MHz [83].

The special characteristic of ^{6}Li is that it provides well-controllable s-wave collisional interactions between the hyperfine states, tunable via a broad Feshbach resonance, more on that in Section 4.3. To utilize these, experiments with ^{6}Li with tuned interaction have to be performed at magnetic offset fields of several hundred Gauss. The optically addressed energy levels of the ^{6}Li atoms will shift accordingly. Figure 4.2 a) shows the resulting shift in a magnetic offset field for the two manifolds of the $|2^2s_{1/2}\rangle$ ground state

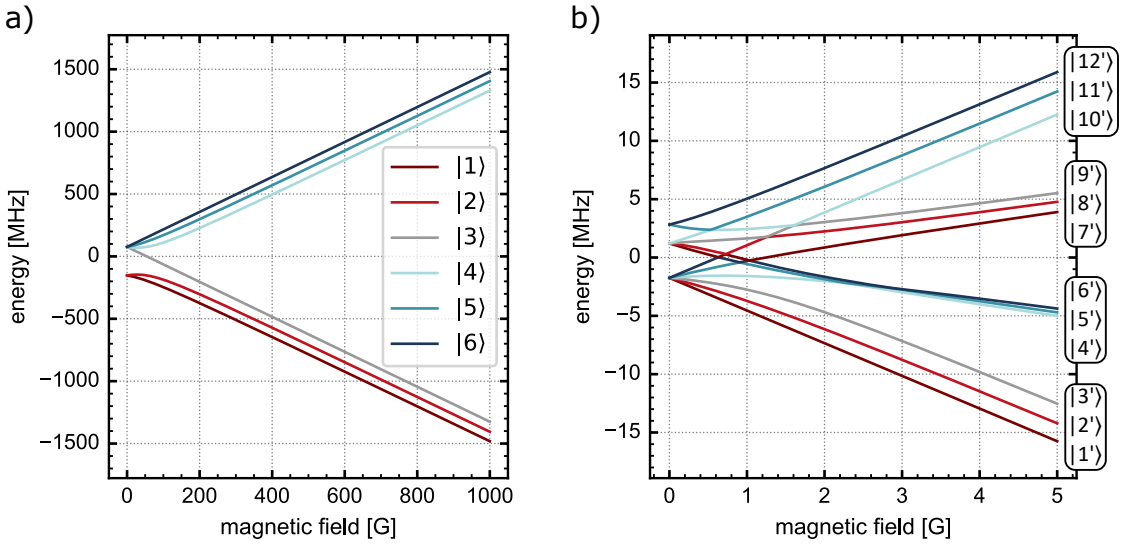

Figure 4.2: Splitting and shift of the hyperfine structure of the ^{6}Li atom in a magnetic offset field for **a)** the ground state $|2^2s_{1/2}\rangle$ and **b)** the first excited state $|2^2p_{3/2}\rangle$ from Figure 4.1. The zero of the vertical scale of the plots is set to the fine structure energy of the state. Data calculated with the Alkaline Rydberg Calculator package in Python [84].

calculated according to the Breit-Rabi formula. Calculations were performed with the Alkaline Rydberg Calculator package in Python [84]. One observes in the Paschen-Back regime above around 100 G, a splitting in a high-field seeker and a low-field seeker manifold, each composed of three states, typically labeled $|1\rangle - |6\rangle$. The energy shifts of the ground state for relevant magnetic offset fields of several hundred Gauss are on the scale of around 1 GHz. Therefore transitions between the branches are in MW-regime, transitions within the high-field seeker branch ($|1\rangle, |2\rangle, |3\rangle$) at around 80 MHz are RF-addressable.

Optically addressing the atoms for imaging using the D_2 line has to account for the frequency shift at these offset fields for the ground state Figure 4.2 a) and the excited state Figure 4.2 b) with shifts in the Gigahertz regime, therefore experimentally requiring offset locking to the zero field transition.

4.1.2 laser systems for resonant interaction

First, the optical setups for resonant interaction with the D_2 line for ^{6}Li will be discussed. These laser systems and their distribution feed the modules and assemblies dedicated to MOT operation and imaging.

MOT distribution

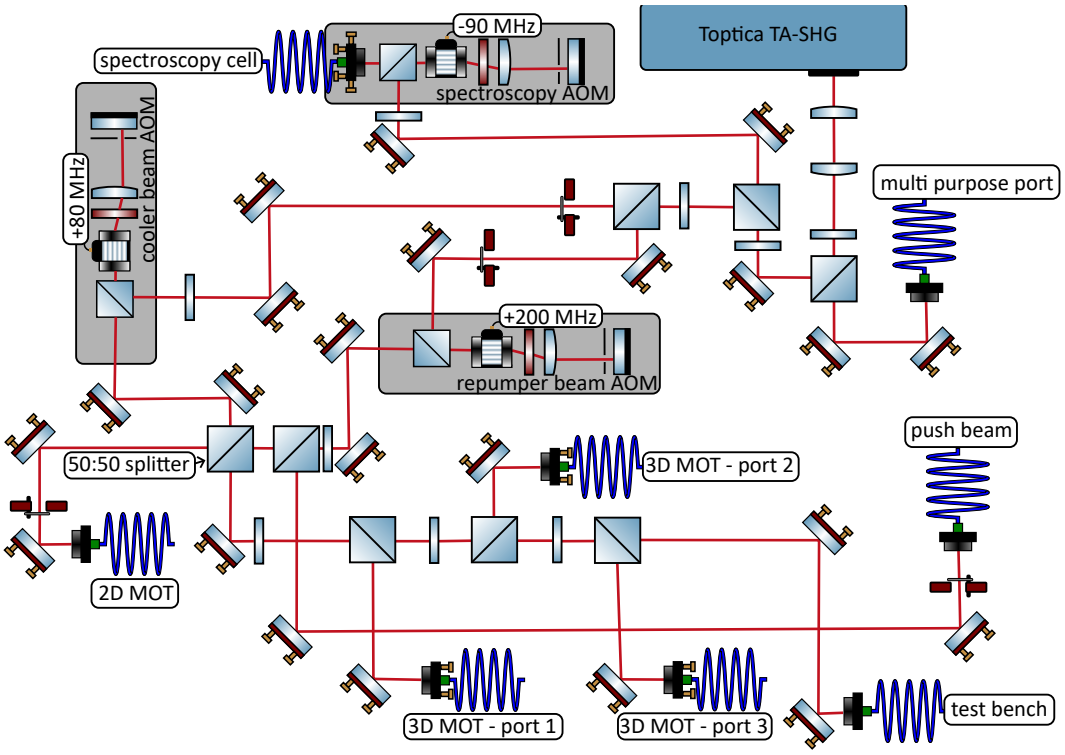

Figure 4.3: Annotated sketch of the optical distribution setup that provides light resonant to the D_2 line for 2D- and 3D-MOT operation as well as the push beam for improved transfer between 2D- and 3D-MOT. The symbols used in this sketch are explained in Appendix A.

The light source for the light resonant to the D_2 line for MOT operation is a *Toptica* laser system[2] providing a nominal output of 1 W of 671 nm light. A detailed description of the laser's working principle and the initial setup of the distribution path and the laser locking is given in [19].

A fundamental decision made when planning and constructing the light distribution for this laser system, as shown in Figure 4.3, was that we wanted to keep the laser frequency static. Omitting frequency modulation of the laser itself allows sharing of the excess laser power with the other two experiments in the group. During the time of this thesis, this has been primarily used to temporarily provide spectroscopy light, which can be used for laser locking of their laser systems. Nevertheless, in principle larger quantities of the light can be shared via the multi-purpose port[3] in Figure 4.3.

[2] TA-SHG pro system

[3] At the time this thesis is being written, all available power of the TA-SHG system is used at HQA-ONE.

The fraction of the light that is not sent to the multi-purpose port is split into a primary path for use in the MOT beams and a path for locking the laser. The light in the latter is frequency shifted in an AOM double pass by $-180\,\mathrm{MHz}$ and send via an optical fiber to a locking setup with a ^{6}Li vapor cell, described in detail in [14]. The setup uses modulation transfer spectroscopy, a Doppler-free spectroscopy approach, to generate an error signal for locking the laser to the $F = 3/2$ (cooler) transition of the D_2 line. The laser, locked with the integrated locking module of the laser controller[4] [19], is therefore frequency shifted to the transition by the AOM double pass shift.

Light in the main path is subsequently split into a cooler and a repumper path, which generate the light resonant to the respective transitions (see Figure 4.1) by controlling intensity and shifting frequency with individual AOM double passes. These allow for individual shift and control of the frequency and intensity of the cooler and repumper light before they are recombined. With the chosen AOM double pass frequencies, we can shift the detuning of the cooler from $10\Gamma_{D2}$ to resonance and for the repumper from $5\Gamma_{D2}$ to resonance, both on the red detuned side of the transition [19, 57]. One drawback is that the control over intensity and detuning is coupled for 2D- and 3D-MOT with this setup, to maximize the available power.

The cooler and repumper paths are recombined on a 50:50 non-polarizing beam splitter (NPBS) and split into the 2D-MOT fiber port and three ports for the individual arms of the 3D-MOT as well as an auxiliary port providing light to the module test bench. Ratios of the splitting into these separate paths can be adjusted with waveplates and PBS cubes. Light for the push beam is split out from the repumper path only. This limits the number of recoils of the atoms from the push beam interaction as the transition is not cycled, such that the push beam can be used to (re-)direct the trajectory of the atoms when loading from the 2D-MOT into the 3D-MOT without introducing significant heating, accelerating the atoms above the capture velocity of the 3D-MOT.

All AOM doubles passes in this setup are built as monolithic modules for improved stability. Details about their design and development can be found in [16].

[4] Toptica DLC pro

high-field imaging light

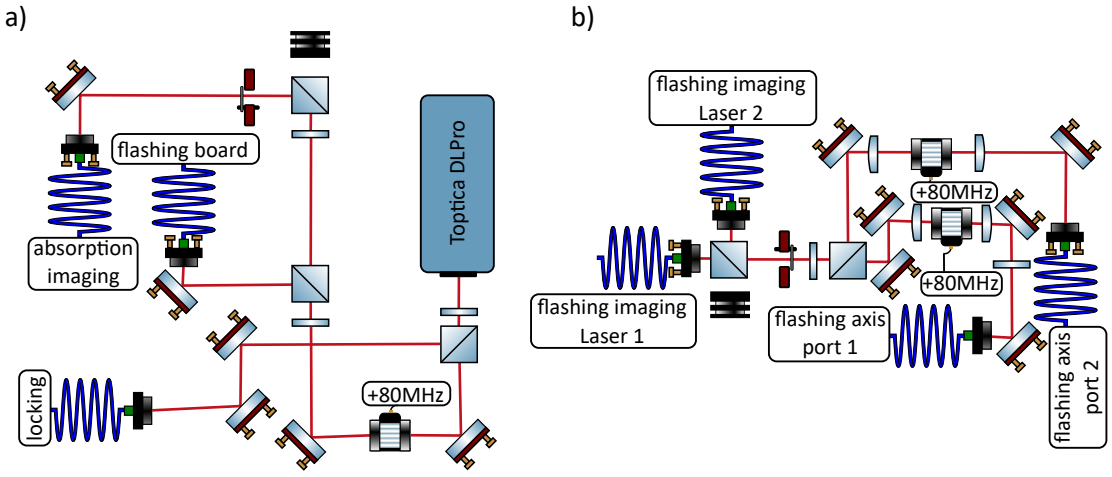

Figure 4.4: Annotated sketch of the optical distribution setup that provides light with tunable frequency resonant to the D_2 line at large magnetic offset fields required for absorption and fluorescence imaging. a) shows one of the two identical light source setups, b) shows the flashing setup required to generate pulses of resonant light for the single-atom fluorescence imaging technique [85]. The symbols used in this sketch are explained in Appendix A.

Imaging light for resonant interaction at large magnetic offset fields, which shift the D_2 line on the Gigahertz scale (see Figure 4.2), is provided by two identical, tunable *Toptica* laser systems[5] providing a nominal output of 25 mW each. Two laser systems are required to image mixtures of two hyperfine states at large offset fields simultaneously, one per imaging transition, each frequency shifted for resonance of the given hyperfine transitions.

The distribution of the two identical laser systems is shown in Figure 4.4 a). A fraction of the laser light is split out of the beam path with a waveplate and a PBS directly behind the laser head and coupled into an optical fiber port. This light is used for locking the laser frequency. However, it needs to be shifted compared to the MOT distribution, which is locked on a spectroscopy cell. To achieve this, a beat of the locked spectroscopy light and the imaging light is generated, and an optical phase-locked loop (OPLL) is used to stabilize the laser. The direct locking process of the laser is performed respectively with a Red Pitaya acquisition and processing board[6]. Frequency offset shifts of the imaging laser relative to the locked spectroscopy light up to several Gigahertz[7] can be achieved and digitally tuned. The OPLL laser locking at HQA-ONE and its initial testing is described in detail in [23].

The remainder of the imaging light in the setup is sent through an AOM in a single pass setup with a fixed RF frequency. The RF power is used to modulate the imaging light intensity further down the beam path. The subsequent beam path is split into two ports: one directly sends the resonant light to the modules, such as for absorption imaging, while

[5] DLpro system
[6] Red Pitaya STEMlab 125-14
[7] Tests in [23] and used detunings in the daily lab work are below 2 GHz, however in principle lock offsets of above 6 GHz are feasible with the setup.

the other sends light to an optical setup dedicated to generating resonant light pulses for fluorescence imaging.

The optical setup for generating these flashing pulses is shown in Figure 4.4 b). Light from the respective ports of the two lasers, each set up for one transition frequency of a hyperfine mixture of two states, is overlapped with an 50:50 NPBS. Subsequently, the light is split into two equal paths, each containing both frequency components, using a waveplate and a PBS. Each path contains an AOM single-pass into which the beam is focused, recollimated, and subsequently coupled into a polarization-maintaining optical fiber for guiding light to the modules. Focusing the light into AOMs allows rapid modulation of the light field, a necessity for deploying the single-atom free space imaging techniques [59, 85]. The required generation of counterpropagating square pulses of light with periods around 2 MHz can be provided via these two ports for both frequencies simultaneously.

At the time this thesis is being written, this flashing technique is already in use at HQA-ONE for fluorescence imaging; however, for now without spatial single-atom resolution. Direct high-field imaging and therefore this setup is not a necessary tool for the essential aspects and experimental demonstrations covered in the main body of this thesis. However, it is an important tool for future experiments at HQA-ONE, partially covered in Chapter 6.

4.1.3 laser systems for optical trapping

Next, the optical setups for off-resonant interaction with the ^{6}Li atoms will be presented. These setups can be used to power optical dipole trap (ODT) applications ranging from diffraction-limited optical tweezers to large box potentials.

red detuned optical dipole traps

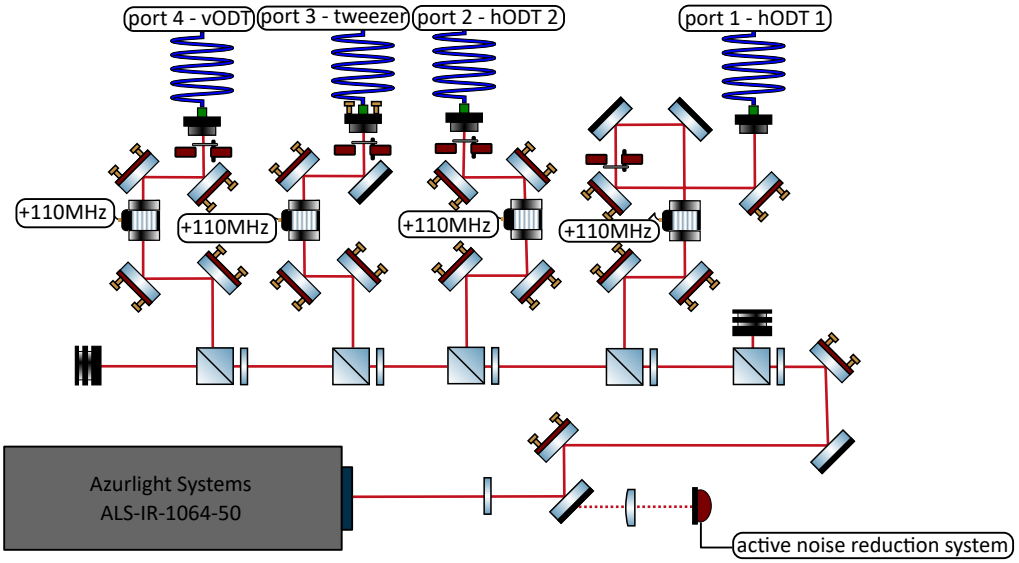

Figure 4.5: Annotated sketch of the optical distribution setup that provides off-resonant light for the generation of red detuned optical dipole trap potentials. Assignment of the ports, i.e., optical tweezer and other ODT names, corresponds to the assignment at the time this thesis is being written, yet the ports can be used for arbitrary ODT applications when redistributing the power budget of the laser between the ports. The symbols used in this sketch are explained in Appendix A.

The first optical setup for providing ODT light in this context, utilizes a laser system from *Azurlight Systems*[8] amplifying a seed from a *Coherent*[9] laser and providing an optical output power budget of 45 W at a wavelength of 1064 nm. This light, red detuned to the ^{6}Li D_2-line, can be used for attractive optical dipole trapping in intensity maxima, for example, generating optical tweezer potentials [56].

ODT laser systems do not need to be frequency locked, as frequency drifts of free-running lasers are small compared to the detuning from the D_2-line and therefore have a negligible effect on the resulting trapping potential. However, intensity fluctuations of the beam directly lead to direct proportional fluctuations of the formed trap potential, resulting in a need for low-intensity noise light sources. This laser system and its distribution, shown in Figure 4.5, tackle this problem with the amplifier's active noise reduction system, essentially placing a sensitive, fast photodiode in the beam path and feeding back the signal to the controller, stabilizing the optical output power of the laser amplifier. This results in relative intensity noise specifications of the light source of below 0.008 % of the RMS

[8] ALS-IR-1064-50, the company Azurlight Systems is nowadays part of Toptica Group.
[9] Coherent Mephisto

average power in the frequency band between 1 kHz and 10 MHz, which is the range of the trap frequencies in typical ODT applications, at which the trapped atoms are prone to heating. The pick-up power for the photodiode is tunable with the adjustment of a waveplate, which regulates the transmission through the mirror, to allow operation of the photodiode in the optimal regime even when changing the power output of the laser head[10].

The optical setup of the main path of the light source, distributing the light to different fiber ports to send the light to the respective modules, consists of a stack of PBS cubes with $\lambda/2$-waveplates to adjust the outcoupling from the main path to the respective port. These ports are equipped with AOMs in a single-pass setup to control and stabilize the power sent via the optical fiber to the module. This setup with the stacked PBS cubes allows easy expansion of the setup with more cubes to provide additional ports in the future if necessary.

[10] Experience with other 1064 nm laser has shown that, when applicable, it can be beneficial to operate high power laser in general at the power which is actually needed instead of the maximum specified output power to prolong the lasers lifetime.

blue detuned optical dipole traps

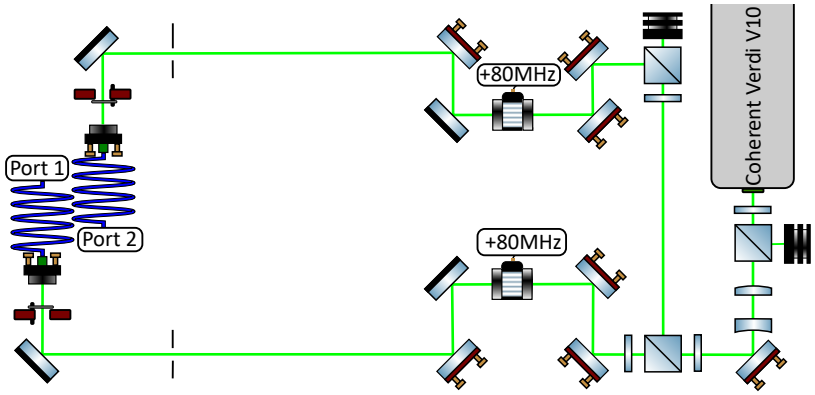

Figure 4.6: Annotated sketch of the optical distribution setup that provides off-resonant light for the generation of blue detuned optical dipole trap potentials. The symbols used in this sketch are explained in Appendix A.

Blue detuned ODT light is provided by another *Coherent*[11] laser system with an optical output power budget of 10 W at a wavelength of 532 nm. This light can be used for repulsive optical dipole potentials, for example, in forming box potentials.

The distribution setup, shown in Figure 4.6, using PBS cubes with $\lambda/2$-waveplates, follows the same design as the red detuned optical dipole trap distribution shown in Figure 4.5. For this laser source, however, the distribution features only two ports at the time this thesis is being written, which is based on the lower power budget of 10 W and fewer applications for this light. At the moment, the light source and subsequent distribution is operational at HQA-ONE, however, it is not used on modules required for the essential aspects and experimental demonstrations covered in the main body of this thesis. Nevertheless, modules utilizing this light source like a DMD module and an optical accordion module are developed, constructed and ready for use in the platform. These modules are covered in Section 6.2.

[11] Coherent Verdi V10

shielding optical dipole traps

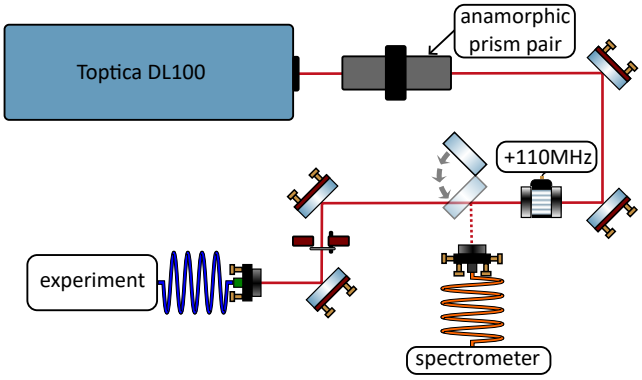

Figure 4.7: Annotated sketch of the optical distribution setup that provides off-resonant light for the generating of red detuned optical dipole trap potentials, yet close to the $|2^2p_{3/2}\rangle \rightarrow |3^2s_{1/2}\rangle$ transition to generate AC-Stark shifts of the $|2^2p_{3/2}\rangle$ state while trapping. The symbols used in this sketch are explained in Appendix A.

The last laser light source and distribution discussed in this section is arguably used in a both resonant and off-resonant application. The light is provided by a *Toptica* laser[12] yielding an optical output power of 25 mW at a wavelength around 813 nm, tunable by several nanometers. This light is off-resonant to the ^{6}Li D_2-line and can therefore lead to attractive optical trapping of the ground state, however, it is close to the $|2^2p_{3/2}\rangle \rightarrow |3^2s_{1/2}\rangle$ transition (see Figure 4.1) and can therefore lead to large AC-Stark shifts of the first excited state $|2^2p_{3/2}\rangle$ whilst providing a trapping potential for the ground state. This idea will be further discussed in Chapter 6.

The laser radiation from the light source is guided through an anamorphic prism pair[13] for beam shaping to enhance the fiber coupling efficiency of the low-power light source and a AOM single-pass for power regulation and stabilization. A flip mirror allows the beam to be guided either to a spectrometer[14] for laser wavelength tuning or to the fiber port, from which it can be directed to the module for experimental use. This power budget of the setup sketched in Figure 4.7 is sufficient for generating an optical tweezer, yet too small for other applications. For that reason, at the time this thesis is being written, a fiber seeded tapered amplifier (TA) from *Toptica Eagleyard*[15] is about to be integrated into the setup. The fiber-coupled seed of the TA will be provided and tuned by the sketched laser system, increasing the available power budget of the setup to 2 W.

[12] Toptica DL100
[13] Thorlabs PS875-B
[14] Thorlabs CCS175/M
[15] Toptica Eagleyard EYP-TPA-0810

4.2 A compact vacuum chamber for ^{6}Li

The compact vacuum chamber of HQA-ONE and its high-flux atom source have been developed as part of the Master's thesis of Tobias Hammel [13]. Initial testing of the 2D MOT optics, attached to the vacuum chamber, has been covered in [15].

4.2.1 vacuum chamber layout

The vacuum chamber plays a central role in all quantum gas experiments, providing the atom source for the iterative preparation of experimental samples for many years of operation time, protecting these dilute, ultracold samples from the high energetic background atoms as well as possible, and in non-modular experiments, providing the experimental center piece to which surrounding mechanical structures and optics are tailored[16].

These aspects had to be taken into account when designing the layout of the vacuum chamber for HQA-ONE, the result is sketched in Figure 4.8. The desired use of a glass cell within HQA, as discussed in Section 3.2, requires no direct line of sight between the oven section and the glass cell to avoid coating the glass cell's internal window surfaces with the untrapped fraction of the ^{6}Li originating from the effusive oven[17]. This can be circumvented by using a dual chamber approach, preparing a 3D MOT and subsequent cold gas sample in one section of the vacuum chamber and transporting it into the glass cell [62, 63]. However, using a Zeeman slower with mechanical shutters and a transport system increases the cycle time of the experiment significantly. HQA-ONE was intended and designed to achieve rapid, multi-Hertz cycle rates; therefore, these approaches were deemed unfavorable, and a 2D-MOT approach for the atom source was pursued, enabling the use of a glass cell without requiring mechanical shutters in the path of the atoms [13].

The compact vacuum chamber consists of two distinct sections, the higher pressure high vacuum (HV) section with the atom source and the lower pressure ultra-high vacuum (UHV) section with the glass cell where the experiments will be performed. In the molecular flow regime[18] , these sections are decoupled by a differential pumping stage (DPS), a 44.5 mm long, 2 mm diameter conical tube with an opening angle of 10 mrad towards the UHV-side with the glass cell to account for residual divergence of the propagating atom beam. Within the molecular flow regime, a background gas conductance of the differential pumping stage (DPS) of 0.15 $\frac{\mathrm{L}}{\mathrm{s}}$ is expected [57].

Each side of the differential pumping stage, atom source section, and glass cell section is equipped with a vacuum pump from *SAES Getters*[19]. Both pumps in the high vacuum (HV)-section[20] and the UHV-section[21] are devices combining a sputter ion pump with a non-evaporable getter pump for operation down to the UHV regime. A vacuum gauge

[16] This is what makes the vacuum system in operating experiments arguably the most important asset. Leakage of the vacuum almost necessarily leads to major reconstruction of the surrounding optomechanics for re-baking the vacuum chamber. As a former supervisor once put it: *There is one hard and fast rule in the world of quantum gas experiments - never break the vacuum.*

[17] A direct line of sight would only be possible when constantly heating the glass chamber windows to thermally prevent the accumulation of atoms, yet heating the glass cell, close to sensitive surrounding optics does not seem like a good approach.

[18] mean free path of the background gas much longer than the chamber dimensions

[19] www.saesgetters.com

[20] NEXTorr Z100

[21] NEXTorr Z200

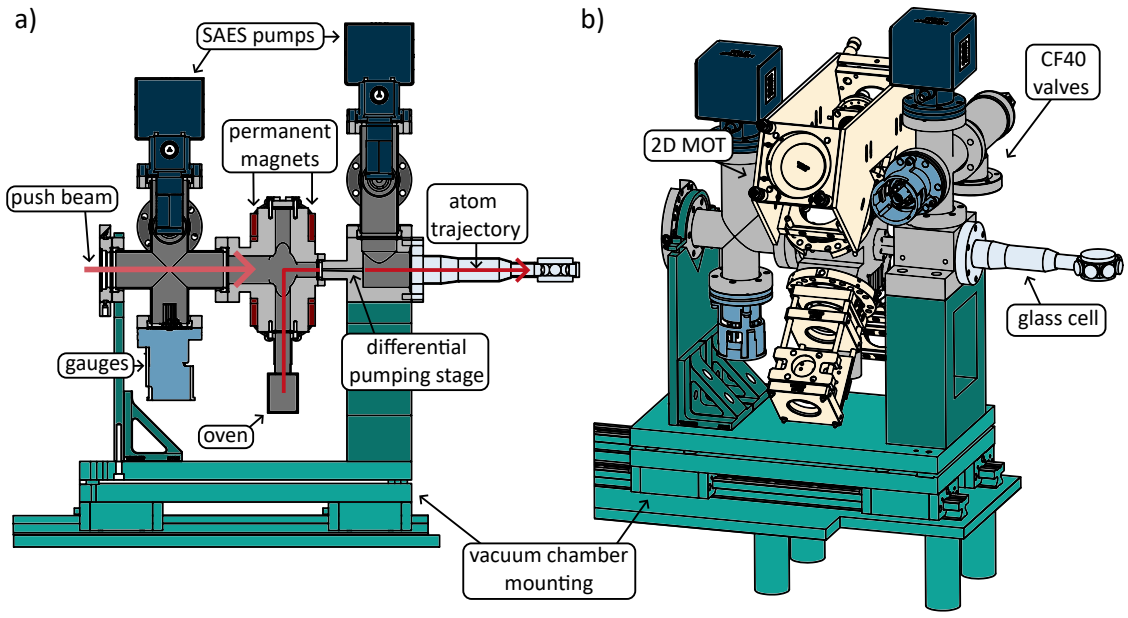

Figure 4.8: Annotated and colored sketch of HQA-ONE's compact vacuum chamber mounted on the translation stage mounting as introduced in Figure 3.5. Different functional sections are color-coded as a guide to the eye. Turquoise represents the mounting structure (with different shades for the sled system and specific chamber mounting), gray denotes general vacuum chamber parts and connectors, light blue indicates pressure gauges, dark blue signifies vacuum pumps, red denotes permanent magnet mountings for the 2D MOT stage, and yellow corresponds to the 2D MOT optics. **a)** presents a cross-sectional view of the chamber in the plane of the center axes of the oven and the glass cell. The trajectory of the atoms that end up in the 3D MOT is sketched in red, and the insertion direction of the push beam is displayed in a lighter shade of red. **b)** Full sketch of the vacuum chamber with 2D MOT optics attached.

from *Leybold*[22] on both sides of the DPS[23] allows for monitoring respective pressures when necessary. When the oven is turned off, these typically read pressures of below 10^{-10} mbar in the HV-section and around 1×10^{-11} mbar in the UHV-section. During regular up-time of the apparatus, however, we usually keep the gauges turned off to minimize disturbance of the experiment operation, especially prolonging the vacuum lifetimes and protecting the imaging from the gauge's black body glow. Additionally, each side of the DPS is equipped with a (closed) right-angle valve [13] to which further pumps, e.g., turbomolecular pumps, and additional equipment for initial pump-down and bake-out can be attached.

The mounting of the chamber on the linear translation stage carriage is performed with four M6 screws and through holes in the connector which houses the DPS. These screws are milled down in diameter to allow for transverse adjustment of the vacuum chamber position on the carriage and the mounts. The HV side of the chamber is not screwed down, as this would lead to stress perpendicular to the central axis of the chamber. Instead, the left part of the chamber in Figure 4.8 rests on polytetrafluoroethylene (PTFE) wedges, positioned

[22] www.leybold.com
[23] IONIVAC IE414 in the HV-section and IONIVAC IE514 in the UHV-section

with a mechanical dial gauge such that the chamber does not experience additional bending forces. Such forces could cause a leakage on the CF16 connector between the 2D-MOT section and the DPS.

This vacuum chamber design provides all three previously mentioned core functionalities of the vacuum system. The respective performance of these functionalities is characterized in the corresponding subsections.

4.2.2 atom source

The atom source in the vacuum chamber is a custom-machined large-aperture effusive oven. This oven, made from non-magnetic stainless steel, is kept at 350 °C with a cold lead heating wire wrapped around the outside of the cylindrical reservoir and controlled with a PID-controller[24] with feedback from a thermocouple fastened onto the outside bottom of the reservoir. We filled the reservoir of the oven in a home-built glovebox holding a protective Argon gas environment with 9.0 g of enriched ^{6}Li and 0.1 g of Lithium in natural abundance, which predominantly consists of the bosonic ^{7}Li-isotope[25].

The oven is attached via a CF16 flange to the 2D-MOT chamber. The geometry of the oven, especially the neck between the reservoir and the chamber, was carefully designed in [13] such that heat transfer from the oven into the 2D-MOT chamber is suppressed and that the emission solid angle of the oven does not allow coating the windows of the 2D-MOT chamber with the emitted Lithium atoms. The atom source setup and Lithium emission cone design are depicted in Figure 4.9.

Figure 4.9 a) shows the general setup of the atom source with oven and 2D-MOT in a cross-sectional view of the vacuum chamber. The Lithium emission cone is indicated by dashed lines. As seen in the photo of Figure b), taken through one of the windows near the oven in the 2D-MOT chamber, this designed solid angle is valid. One observes a sharp line between the sections of the vacuum chamber that have been coated with Lithium from the oven, and the polished, uncoated sections of the vacuum chamber. A sketch of the emission cone was added as a guide to the eye. Under operation, at 350 °C oven temperature, we expect a flux of around 1×10^{16} atoms/s from the oven into the 2D-MOT chamber, with enough Lithium present for around a decade of operation time before requiring an oven exchange [13].

While the oven performs as expected, one other experiment that adapted the oven design reported clogging of the neck. As this issue was only encountered by one realization of the oven, one possible explanation is that this oven was potentially overfilled, beyond its reservoir. The neck design of the oven reduces heat flow towards the 2D-MOT chamber; potentially, some lithium did not properly melt in the neck, leading to the reported clogging. Therefore, it seems important to avoid overfilling the oven beyond its intended capacity.

For the design of the 2D-MOT, we follow the scaling presented in [86, 87], indicating that

[24] Red Lion PXU40020 regulating the output of a Voltcraft PPS-11360 power supply

[25] For all Lithium labs replicating this design: We learned the hard way, that one really needs an Argon environment to process the Lithium and fill the oven. Easier-to-use and professional Nitrogen gloveboxes may work for small amounts of Lithium, but for larger amounts, one will encounter the problem of Lithium reacting with the Nitrogen to form lithium nitride. This exothermal reaction $6\mathrm{Li} + \mathrm{N_2} \rightarrow 2\mathrm{Li_3N}$ is slow at room temperature, but once started in multiple Lithium chunks in the oven, the excess heat accumulating in the reservoir accelerates the reaction, causing a runaway process.

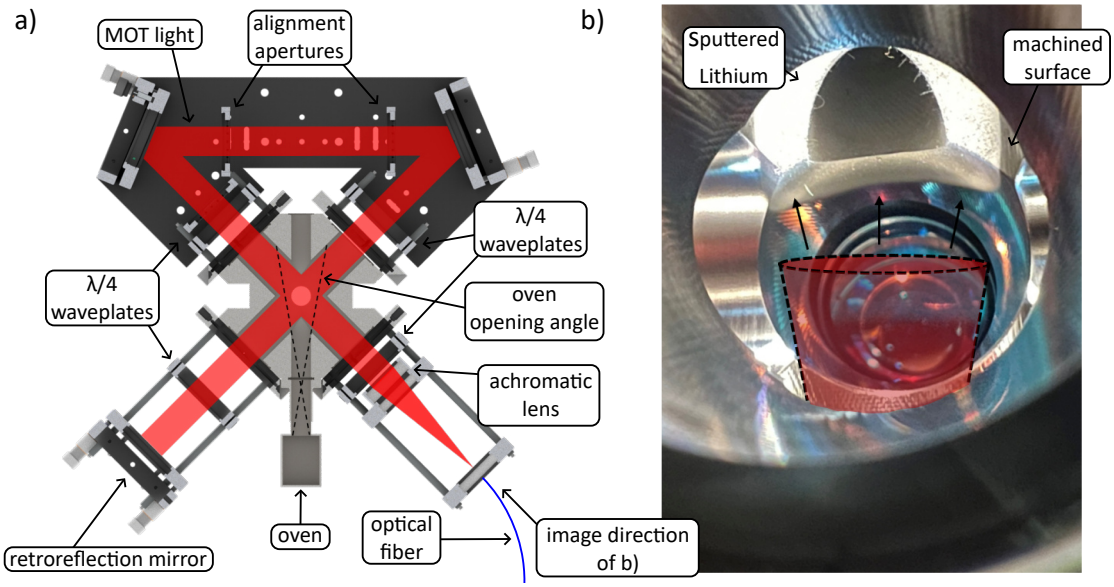

Figure 4.9: **a)** Annotated rendering of the atom source of HQA-ONE consisting of a large aperture effusive oven and a 2D-MOT chamber with attached optics. **b)** Annotated image of the interior of the vacuum chamber through one of the viewports after operation of the oven with smooth machined walls and regions covered in the deposited Lithium visible. Figure adapted from [57].

large 2D-MOT beams with increased detuning from the resonance and increased power, lead to higher 2D-MOT loading rates [57].

Therefore, we use 30 mm diameter 2D-MOT beams in a retroreflected bowtie configuration[26] to maximize the usuable power. The optics are attached to the windows of the 2D-MOT chamber with adapters[27]. Cooler and repumper MOT light are provided via the same polarization maintaining single mode fiber[28] and the collimated beam shaped by a single achromatic lens[29] with a focal length of 150 mm. This provides a beam diameter slightly larger than the desired 30 mm, yet, smaller beams proved the 2D-MOT to be less stable and more sensitive to alignment. We attribute this to the fact that for the smaller beams, larger fractions of the weaker edges of the Gaussian envelope are probed by the atoms, effectively bending the 2D-MOT and leading to an observable 'banana'-shape. Atoms from this deformed 2D-MOT are more challenging to guide through the DPS, lowering the effective 3D-MOT loading rate in the glass cell.

Permanent magnets provide the magnetic field in adjustable mounts in the positions shown in Figure 4.8 a). To reduce the distortion of the magnetic field lines, the 2D MOT chamber is CNC machined from Titanium instead of stainless steel.

[26] A nice trick for the alignment of the retroreflection is to continuously sweep the laser frequency around the resonance while overlapping the beams. As the hot atoms enter the beams from one side of the cross, their Doppler shifts allow us to distinguish two different segments of the beam passages. In the frequency scan, these flash alternatingly and their distance can be minimized and the overlap positioned in line of sight with the DPS.
[27] Thorlabs VFA275/M
[28] Thorlabs P3-630-PM-FC-10
[29] Thorlabs AC508-150-A-ML

Transfer from the 2D-MOT into the glass cell, and therefore the 3D-MOT, is supported by a push beam visible in Figure 4.8 a). We found empirically that the alignment of the push beam, along with its properties such as power and detuning, plays a pivotal role for the achieved loading rates.

Table 4.1: Overview of the MOT parameters at HQA-ONE. Detunings and saturation intensity given for the Lithium D_2 Line used for the MOT transition with saturation intensity I_{sat} =2.54 $\frac{\text{mW}}{\text{cm}^2}$ and linewidth Γ =5.9 MHz. Table adapted from [57]

Parameter	Value
2D-MOT	
beam waist	15.6 mm
power (cooler)	120 mW
	6.2 I_{sat}
detuning (cooler)	8 Γ
power (repumper)	80 mW
	4.1 I_{sat}
detuning (repumper)	3 Γ
Push beam	
beam waist	1.0 mm
power	340 µW
detuning	3 Γ
3D-MOT	
beam waist	5.0 mm
power (cooler)	40 mW
	20 I_{sat}
detuning (cooler)	8 Γ
power (repumper)	20 mW
	10 I_{sat}
detuning (repumper)	3 Γ

To test the 2D-MOT performance, which lacks diagnosis tools[30] such as a 2D-MOT imaging system, we probe the loading rate into the 3D-MOT after alignment of the 2D-MOT. The atoms are guided through the DPS with the push beam and loaded into a 3D-MOT in the glass cell. The parameters of the tested 2D-MOT and 3D-MOT are listed in Table 4.1, and the loading performance is plotted in Figure 4.10. The push beam contains only repumper light, which limits the transition cycles and therefore the collisions with the atoms, in order to redirect them, yet not to accelerate them above the capture velocity of the 3D-MOT.

The time-dependent loading of the 3D-MOT for the fully aligned 2D-MOT is shown in Figure 4.10 a) with the parameters of the 2D- and 3D-MOT according to the list in Table 4.1. These parameters correspond to the maximum available power for the MOT. As

[30] The 2D-MOT chamber does not provide a viewport for imaging of the 2D-MOT from the side. In future realizations of this chamber, we recommend incorporating this feature.

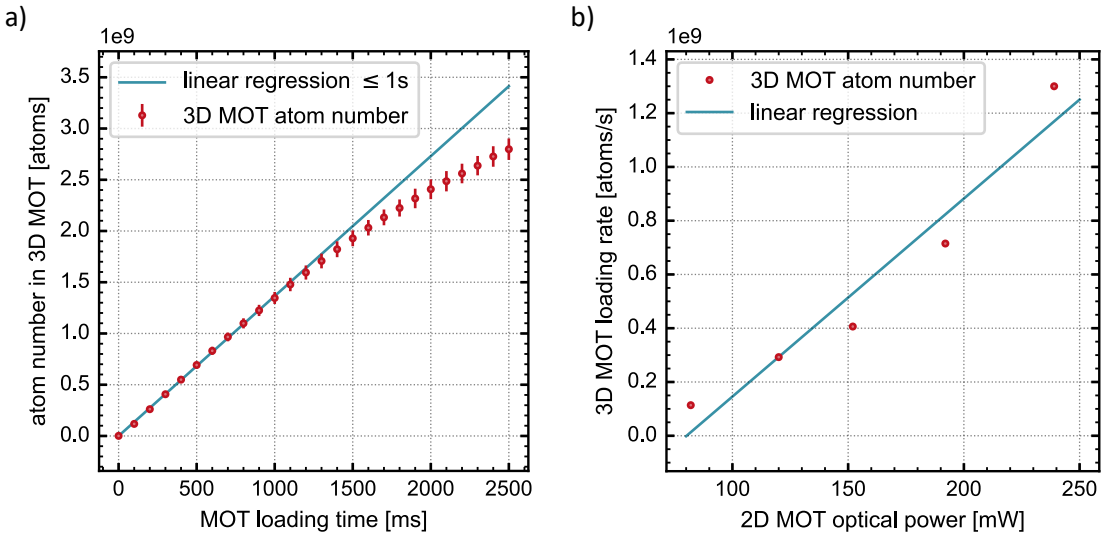

Figure 4.10: 2D-MOT performance indirectly characterized via the 3D-MOT loading rates with the parameters listed in Table 4.1. **a)** shows the time-resolved loading of the 3D-MOT for different loading times with a linear regression fit for all data points within the first second of loading to obtain the initial loading rate of the 3D-MOT. The regression in this plot yields a loading rate of 1.3×10^9 atoms/s. **b)** shows the 3D-MOT loading rate dependent on the total optical power in the 2D-MOT with constant 3D-MOT parameter. A linear regression is displayed as a trend line. Measurements in a) correspond to the maximum available power in b). Figure adapted from [57].

presented in Section 4.1, the laser distribution system for the MOT light requires coupling of the detuning of 2D- and 3D-MOT, to increase the available power, yet independent tuning of the parameter would most likely lead to different detunings for 2D- and 3D-MOT, as they address different velocity classes upon loading.

The atom number for different loading times is retrieved via fluorescence imaging of the MOT. This imaging system provides single-atom counting resolution (more on this system in Chapter 5). We divide the obtained signal from the MOT by the signal of a single atom in the MOT to retrieve the atom number. Notably, the optimized MOT parameters for single atom counting deviate from the MOT parameters for large clouds shown in Table 4.1, leading to around 30 % less signal per atom compared to the MOT for counting. This means that the atom number measurements presented here are a lower bound; the actual atom number could be around 30 % higher.

The loading rate is retrieved from Figure 4.10 a) via a linear regression of all data points up to 1 s MOT loading time, before the atom number starts to saturate. With the maximum available 2D-MOT power, as depicted in Figure a), one finds a loading rate of 1.3×10^9 atoms/s.

When lowering the optical power of the 2D-MOT compared to figure a), one observes an approximately linear reduction of the loading rate of the 3D-MOT. This scaling, including a linear regression, is plotted in Figure 4.10 b). It still agrees with the scaling observed in [87] for the higher 2D-MOT powers used at HQA-ONE. It can be concluded that even at these 2D-MOT laser powers, more optical power results in higher loading rates. Therefore,

if one attaches a more powerful light source to the 2D-MOT of HQA-ONE, the loading rates would increase accordingly.

The power ratio between cooler and repumper follows [87]. The optimal detuning, however, is found by scanning the respective detunings of cooler and repumper and measuring the resulting 3D-MOT loading rates. The result is plotted in Figure 4.11 a). One observes a double peak structure consistent with observations in previous Lithium 2D-MOT setups [87]. In the measurements presented here, these two maxima yield comparable loading rates relative to each other.

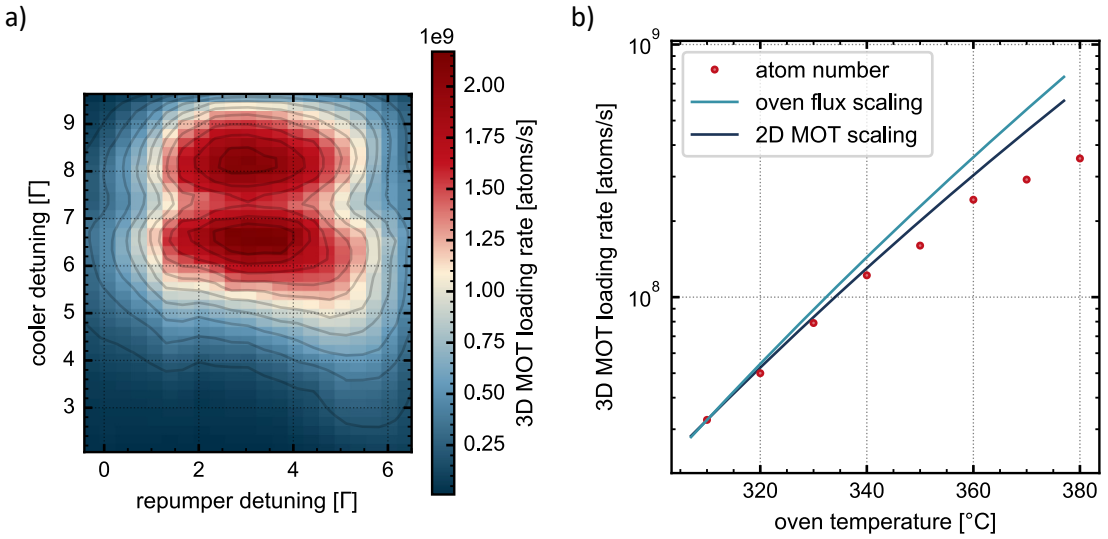

Figure 4.11: Scalings of the 2D-MOT performance with different parameters. **a)** shows a scan over various cooler and repumper detunings for the powers shown in Table 4.1. The heatmap plot has been enhanced with contour lines to guide the eye, making the double peak structure in the scan more visible. **b)** shows the influence of the oven temperature on the 3D-MOT loading rate. The scaling of the solid lines is applied to the lowest temperature data point. It follows the increase of the flux from the oven and the expected scaling of the 2D-MOT performance, respectively. Notably, these measurements were not performed with an optimal 2D MOT alignment, hence the deviation of the absolute numbers from a). Figure adapted from [57].

While more laser power can increase the loading rates according to Figure 4.10 b), it is usually not available on a short timescale. Therefore, another parameter has to be used to increase the MOT loading rate temporarily. A parameter suitable for this is the oven temperature. An increase in the oven temperature increases the flux out of the oven by around one order of magnitude per 50 °C temperature increase [13]. However, this shortens the lifetime of the oven before it has to be replaced accordingly. Figure 4.11 b) shows corresponding measurements for different oven temperatures around its designed operation point of 350 °C.

The 2D-MOT loading rate R_{2D} can be understood as proportional to the atom flux Φ_{oven} out of the effusive oven and the capturable fraction of the Boltzmann distribution F_{cap} as

$$R_{2D}(T) \propto \Phi_{oven}(T) \cdot F_{cap}(T) \tag{4.1}$$

with both contributions oven temperature T dependent. The flux term $\Phi_{oven}(T)$ is again proportional to the atom number density n_{oven} and the average velocity $\bar{v}_{oven}$. Therefore, the first temperature-dependent factor can be written as

$$\Phi_{oven}(T) \propto n_{oven}(T) \cdot \bar{v}_{oven}. \tag{4.2}$$

The thermal velocity $\bar{v}_{oven}$ is described by $\bar{v}_{oven} = \sqrt{\frac{8k_BT}{\pi m_{Li}}}$ [88] with k_B the Boltzmann constant and m_{Li} the mass of the Lithium atoms. The scaling of the atom number density with temperature can be described according to the ideal gas equation by

$$n_{oven}(T) \propto \frac{P_{sat}(T)}{k_BT} \tag{4.3}$$

where $P_{sat}(T)$ is the saturation vapour pressure of Lithium at that temperature. This can be described by the Antoine equation [89] following

$$log_{10}P_{sat}(T) = A - \frac{B}{T+C} \tag{4.4}$$

with $A = 4.98831$bar, $B = 7918.984$bar/K, and $C = -9.52$K for ^{6}Li [89, 90]. Therefore, the flux out of the oven scales according to

$$\begin{aligned} \Phi_{oven}(T) &\propto \frac{P_{sat}(T)}{T} \cdot \sqrt{T} \\ &= \frac{P_{sat}(T)}{\sqrt{T}} \end{aligned} \tag{4.5}$$

The captured fraction of the oven emission can be calculated with the integral of the Maxwell-Boltzmann velocity distribution up to a set capture velocity. In the limit of a small capture velocity compared to the average velocity of the atoms, the scaling of the captured fraction follows $F_{cap}(T) \propto T^{-3/2}$ [87]. This means the scaling of the 2D-MOT loading rate in Equation 4.2 with the oven temperature follows

$$R_{2D}(T) \propto \frac{P_{sat}(T)}{T^2}. \tag{4.6}$$

The respective scaling of the oven flux and the expected scaling of the 2D-MOT loading rate is applied to the lowest temperature data point in Figure 4.11 b) and displayed as a solid line. One observes the expected scaling for small temperature changes in agreement with the 2D-MOT loading rate scaling. For larger temperature changes, where the data points start to deviate, other effects, such as changes in the captured fraction in the 3D MOT, start to contribute. Nevertheless, scaling the loading rate up with the oven temperature is possible.

4.2.3 vacuum lifetimes

The second central function of the vacuum chamber is to provide protection of the ultracold gas samples from the highly energetic background gas atoms at room temperature. Collision of the cold atoms in the trap with these background gas atoms removes the atom from the trapping potential, in the case of few particle physics, rendering the sample useless.

A key metric to describe the rate at which samples in the vacuum chamber collide with background gas atoms is the vacuum-limited lifetime of a dilute MOT. It can also be seen as a benchmark number for the preparation fidelity in few-atom systems, where background gas collisions destroy the sample, even if only one atom is removed from the trap.

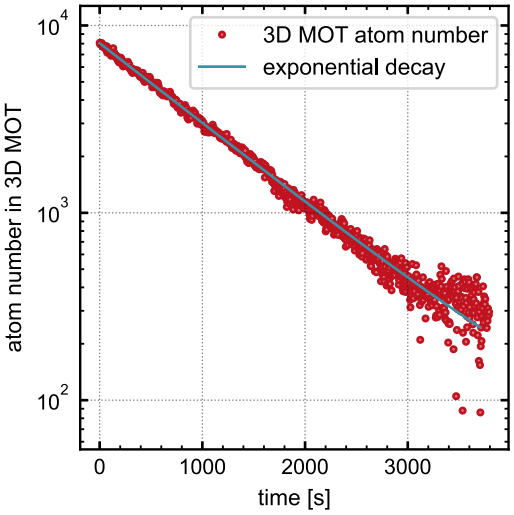

Figure 4.12: Plot of the time-resolved decay of a dilute 3D-MOT of a few thousand atoms in the regime where the dominant loss channels are collisions with background gas atoms. An exponential decay fit of the data with a lifetime of 1013 s is additionally shown. Figure adapted from [57].

The vacuum-limited lifetime of a 3D-MOT is tested at HQA-ONE by preparing a dilute 3D-MOT of a few thousand atoms, where the predominant loss channel is attributed to background gas collisions. After loading, the 2D-MOT is turned off, and therefore, the atom flux to the 3D MOT is turned off. The 3D-MOT remains on, and the atom number is continuously measured via the calibrated fluorescence imaging. The corresponding decay of the signal and therefore the atom number over time is plotted in Figure 4.12.

The vacuum-limited lifetime of the atoms in the 3D-MOT is retrieved with an exponential decay fit of the data, yielding a lifetime of 1013 s. This lifetime of more than 15 min slightly surpasses the lifetimes observed in the other experiments in our research group. We attribute this to the smaller volume of the chamber and simplified layout, leading to higher effective pumping efficiencies.

Additionally, we observed an increase in the vacuum-limited lifetime over the operation time of the apparatus. In March 2023 we observed lifetimes of around 500 s, in May 2024 970 s, and the measurement shown in Figure 4.12 yielding 1013 s was taken in December 2024. This could be understood from a combination of a reduction in slow outgassing of vacuum chamber components over time and Lithium deposited on the vacuum chamber walls (see Figure 4.9 b)), acting as an additional getter surface, both lowering the background pressure and therefore increasing the vacuum limited lifetime.

4.2.4 mechanical centerpiece

Lastly, the vacuum chamber serves as the mechanical centerpiece in most non-modular quantum gas experiments. Due to the modular nature of HQA with its FOR as the center piece, this does not apply to HQA-ONE. The vacuum chamber on its translation system is just a building block of the experimental apparatus, not the centerpiece.

However, treating the mounting carriage with a vacuum chamber as an individual building block also requires that the vacuum system and its attached 2D-MOT are independent from the rest of the experiment. This is achieved by mounting the 2D-MOT and the push beam setup directly on the windows of the vacuum chamber and providing light always via polarization-maintaining single-mode fibers. This setup allows moving the entire atom source, which shoots the atom beam into the center of the glass cell, together with the vacuum chamber and the mounting carriage. The 3D-MOT optics and magnetic field coils remain on the FOR. Notably, we do not observe changes in the 3D-MOT loading rate after moving the vacuum chamber with its atom source out of the FOR and reinserting it. This highlights the stability and robustness of the modular approach for the vacuum chamber.

An additional benefit of being able to move the vacuum chamber out of the surrounding mechanical structure and optics is that we did not need to place a valve between the two sections of the vacuum chamber. One would typically do that to allow exchanging the oven in the future without breaking the vacuum in the glass cell section. Preserving the vacuum in the glass cell omits the need for tedious re-baking of the vacuum chamber to get back to the low UHV-regime. The downside of this valve, however, is that it increases the total length and volume of the chamber between the source and the glass cell, increasing pumped volume while decreasing the transfer between 2D-MOT and 3D-MOT due to the longer distance. The vacuum chamber of HQA-ONE can be moved out of the surrounding mechanical structure with a mounting carriage on the 1.2 m long rail system on its pedestal. This simplifies performing work on the vacuum chamber, such as once a decade[31] exchanging the oven[32] and re-baking the chamber.

4.3 Magnetic fields for interaction- and internal state control

As already mentioned in Section 4.1, a special characteristic of ^{6}Li is its broad magnetic Feshbach resonance between dual-state mixtures of the states $|1\rangle, |2\rangle, |3\rangle$ in the high-field seeking manifold of the hyperfine ground state (see Figure 4.1 and Figure 4.2). This resonance allows for precisely setting and continuously tuning the scattering properties and, therefore, interactions between these state mixtures, an essential tool for quantum simulations. In essence, the resonance arises from the virtual coupling of the two colliding atoms to a bound state, leading to a scattering phase shift. If the state of the scattered atoms exhibits a different magnetic moment from the bound state, their relative energy and therefore the coupling can be magnetically tuned. This process leads to magnetically tunable interactions in these state mixtures [91, 92]. The resulting change of the s-wave scattering length a_{3D} in three-dimensional (3D) systems of these dual-state mixtures depending on the offset magnetic field B is described by [92]

[31] according to the designed oven lifetime

[32] It might be necessary to exchange the 2D-MOT chamber together with the oven, because of the sputtered Lithium on the walls. If the oven is empty, a significant fraction of the 9 g of Lithium will be deposited on the 2D-MOT chamber wall, heating the chamber to around 200 °C during baking will cause the Lithium to liquefy which could cause problems for the viewports and the gaskets.

$$a_{3D}(B) = a_{bg}\left(1 - \frac{\Delta_{res}}{B - B_0}\right) \tag{4.7}$$

where a_{bg} is the background scattering length, B_0 is the magnetic position of the resonance, and Δ_{res} its width.

As we aim to leverage this interaction tunability for quantum simulations at HQA-ONE, the position and width of this resonance determine the offset fields that HQA-ONE's magnetic field coils must provide. The Feshbach resonance of all three state combinations has been precisely mapped in [93]; the corresponding data and values of the parameters in Equation 4.7 have been plotted in Figure 4.13.

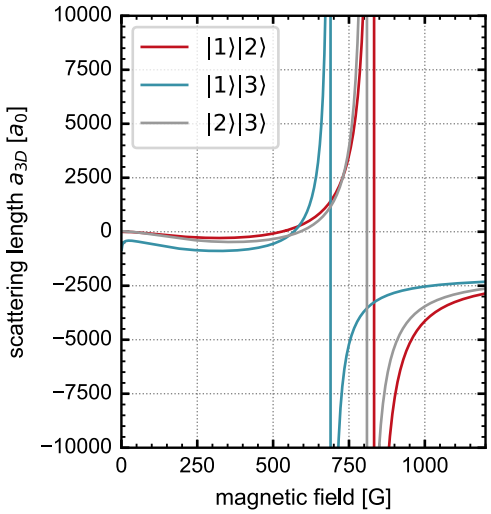

Mixture	Pole B_0	Width Δres	Background a_{bg}
|1⟩|2⟩	832.2 G	-262.3 G	-1582 a_0
|1⟩|3⟩	689.7 G	-166.6 G	-1770 a_0
|2⟩|3⟩	809.8 G	-200.2 G	-1642 a_0

Figure 4.13: Plot of the s-wave scattering length depending on the applied offset magnetic field due to the Feshbach resonance for all state combinations in the high-field seeking manifold of the ground state. Plotted data taken from [93]. The table displays the corresponding parameters of the resonance for Equation 4.7.

Following the resonance position and their shape in Figure 4.13, the coil assembly of HQA-ONE should provide offset magnetic fields up to at least around 1250 G to allow utilizing the full Feshbach resonance for all state combinations.

Additionally, AC magnetic fields are required to drive the magnetic dipole transitions between the different states $|1\rangle, ..., |6\rangle$. As discussed in Section 4.1, transition frequencies within the high-field seeker manifold between neighboring states are typically around 80 MHz and around 2 GHz between the high- and low-field seeker manifolds around the Feshbach resonance. These transitions, therefore, have to be addressed with magnetic fields oscillating at these respective RF and MW frequencies.

4.3.1 DC magnetic fields

The offset and gradient magnetic fields at HQA-ONE are generated with one large set of four magnetic field coils. These coils were designed and simulated as part of [13] and

commercially manufactured by *Krämer Energietechnik*[33]. Their setup is sketched in Figure 4.14 a), their mounting mechanism is detailed in Section 3.4.

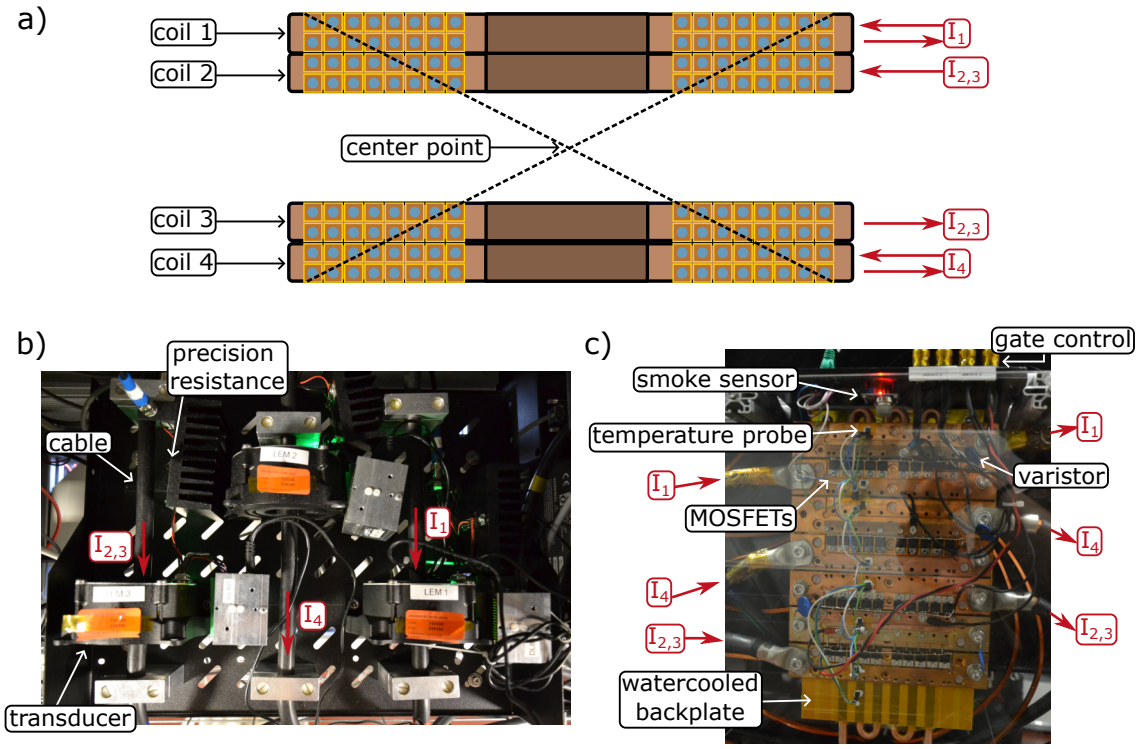

Figure 4.14: **a)** Cross-sectional view of the HQA-ONE's magnetic field coils. The four individual coils and their electric wiring are shown (red). Each coil consists of a 2x8 winding of a rectangular hollow core wire, insulated on the outside (yellow) and water-cooled on the inside (blue). Each coil is encapsulated in a high-temperature epoxy resin(brown) for improved stability and mounting. The black dashed lines schematically indicate the Helmholtz configuration. **b)** Annotated photo of the current stabilization for the coils via a transducer feedback. Cables carrying the coil currents are marked. **c)** Annotated photo of the MOSFET switching setup for the coil currents.

The coil assembly consists of two coil stacks, one above and one below the center point of the apparatus, in a Helmholtz configuration. Each stack is composed of two coils wound in a 2x8 configuration from an insulated, square-shaped, hollow core copper wire with an outer diameter of 5 mm x 5 mm and an inner hole diameter of 3 mm. The hollow core wire allows coolant flow through the interior of the magnetic field coils, a topic that will be discussed in detail in Section 4.4. The helicity of the coil winding, left-handed or right-handed winding, alternates between the coils to minimize disturbances arising from the step when changing layers in the winding in the separate stacks, yet providing equal handedness between the two stacks [94]. Each coil is encapsulated in a high-temperature and thermal-load-suitable epoxy resin described in Section 3.4.

Current for the coils is provided by power supplies[34] from *Delta Elektronika*[35] with their

[33] www.kraemer-energietechnik.com
[34] SM 15-400-P069-P154-P166
[35] www.delta-elektronika.nl

fast programming option delivering a maximum voltage of 15 V and a maximum current of 440 A. Given the coil resistances in the milliohm range, the full current range of 440 A is usable for the coils.

The outermost coils, coil 1 and coil 4, are driven individually by separate power supplies; the inner coil pair is connected in series and driven with a third power supply. This individual control of the coils allows detailed tuning of the magnetic field geometry at the center point. According to the simulations in [13], if all coils are driven with equal current, they provide in their Helmholtz configuration a homogeneous offset field at the center point of up to 2000 G. Differential driving of the inner and outer coil in each stack allows the generation of quadrupole fields as required, for example, for the MOT, as well as control over the magnetic field gradient and curvature at the center point to shape magnetic traps usable, for example, for matterwave magnification protocols in the future [95, 96].

These capabilities require flipping the polarity of the inner pair of coils with an H-Bridge setup. Such a system has been developed and constructed in [25], but at the time this thesis is being written, integration into HQA-ONE is still pending, providing an off-the-shelf near-future upgrade of the magnetic field assembly. As of now, the coil polarity has been wired such that the outer pair (coil 1 and coil 4) is always used for generating the quadrupole field, and the inner coil pair (coil 2 and coil 3) provides the offset field. This temporary configuration we measured offset fields[36] at the center point of 2.78 $\frac{\mathrm{G}}{\mathrm{A}}$ and gradients[37] of 0.5 $\frac{\mathrm{G}}{\mathrm{cm\,A}}$.

Stabilization of the currents fed into the coils is performed using high precision direct current current transducer[38] from *LEM International*[39] capable of measuring nominal currents up to 500 A with a relative noise of 1.5×10^{-6} [25]. The measurement current from the transducers is sent through precision resistors to convert the current signal into a voltage signal by measuring the voltage drop over the resistor. The obtained voltage signal is fed into the experiment control (see Section 4.5), providing a digital proportional-integral-derivative (PID) controlled feedback loop for the power supplies. This stabilization mechanism is provided for all three power supplies individually. Figure 4.14 b) shows an annotated sketch of the current stabilization setup with the lead wires of each power supply, the current transducers, and the precision resistors visible. Beyond this brief description given here, further reading about the system and its testing can be found in [25].

Rapid switching of the coil currents, to quench the magnetic field, utilizes for each power supply a stack of ten high-power MOSFETs[40] connected in parallel as a switch for shutting down the currents of the respective coil. The MOSFETs are protected from high voltage induction spikes during switching by a varistor[41] connected in parallel, limiting the maximum induced voltage to around 43 V [25]. The system with the implementations for each power supply is shown in an annotated photo in Figure 4.14 c) with the copper blocks housing the MOSFETs mounted on an electrically insulated, water-cooled backplate acting as a heat sink for the MOSFETS. With this setup, we achieve magnetic field ramp rates of around 2000 $\frac{\mathrm{G}}{\mathrm{ms}}$ [57]. More information about the MOSFET switches can also be

[36] Measured via the magnetic field dependence of the $|1\rangle \rightarrow |2\rangle$ RF transition in Figure 4.2
[37] Measured with a magnetic field probe [25]
[38] LEM IN500-S
[39] www.lem.com
[40] IRFB3077PbF
[41] S20K11

found in [25].

4.3.2 AC magnetic fields

As mentioned above, AC magnetic fields are used to drive the RF and MW transitions between the states in Figure 4.2 a). The modular mounting structure for these coils and their electronics is discussed in Section 3.4. Details about RF coil development can be found in [18] and [24].

At the time this thesis is being written, there is one operational RF coil installed at HQA-ONE. This rectangular-shaped coil, placed on one of the mounting frames, has a dimension of 30 mm x 22 mm and is placed 36 mm away from the central position of the FOR. It is connected to the matching electronics with a short SMA cable. The matching electronics are designed to support tuning of the RF frequencies, enabling the addressing of atoms in different states and at varying magnetic fields, albeit at the cost of reduced coupling strength due to the limited Q-factor. Future implementations, using the modular coils mounting mechanism, can be optimized for higher coupling, sacrificing operational frequency bandwidth. The RF signal is provided by a homebuilt direct digital synthesis (DDS) board amplified with a 100 W amplifier[42] from Minicircuits[43].

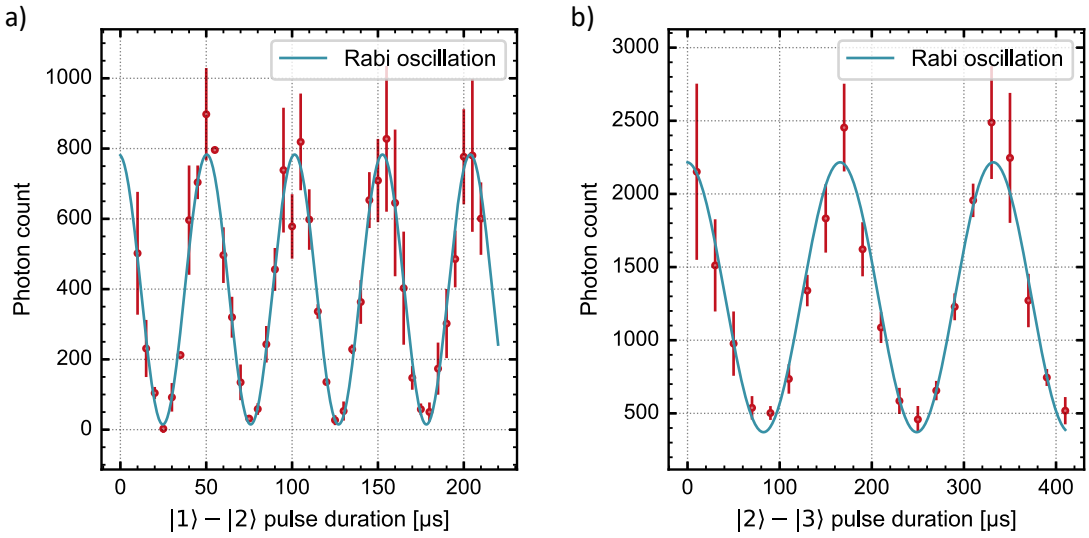

Figure 4.15: Representative data for Rabi oscillations for varying RF pulse durations between **a)** state $|1\rangle$ and state $|2\rangle$ and **b)** state $|2\rangle$ and state $|3\rangle$. Shown via the photon count in fluorescence imaging is the population of one of the states, in this case $|2\rangle$. The blue line shows a sinusodial fit of the data yielding Rabi rates of around $2\pi\times20$ kHz for the $|1\rangle \rightarrow |2\rangle$ transition and around $2\pi\times6$ kHz for the $|2\rangle \rightarrow |3\rangle$ transition.

The operationality of the implemented RF coil is tested by driving Rabi oscillation in the high-field seeking manifold of the ground state with it. An optical tweezer is prepared, filled with around 500 atoms in state $|2\rangle$ at an offset field of 527 G, the zero crossing of the Feshbach resonance for the interaction between $|1\rangle$ and $|2\rangle$ (see Figure 4.13). The

[42] Mini-Circuits ZHL-100W-52-S+
[43] www.minicircuits.com

corresponding RF signal for the $|1\rangle \rightarrow |2\rangle$ transition is applied, and the population in $|2\rangle$ is measured by fluorescence imaging. The obtained signal on the camera for varying RF pulse durations is plotted in Figure 4.15 a). A sinusoidal fit yields a Rabi oscillation frequency of $2\pi\times19.6\,\mathrm{kHz}$ for the transition, which is high compared to the typical Rabi oscillation frequencies in the other experiments of the group around $2\pi\times6.2\,\mathrm{kHz}$. However, other groups have demonstrated that these can still be improved [97].

The $|2\rangle \rightarrow |3\rangle$ transition is probed analogously with the fluorescence signal for the state $|2\rangle$ for varying pulse length plotted in Figure 4.15 b). The sinusoidal fit yields a Rabi oscillation frequency of $2\pi\times6.0\,\mathrm{kHz}$ for the coupling to the transition.

At the time this thesis is being written, MW coil development is still underway; initial signals have, however, been obtained with the first prototypes. A concept pursued in this direction is to make the coil as PCB that can be mounted directly to the addressing cage. However, development on this is still ongoing.

4.4 Thermal management

A critical topic for the high-field DC coils, operating at currents up to 440 A, is thermal management. Joule heating of the copper wire at these currents leads to significant thermal loads on the coils, leading, if not correctly taken care of, in the best case to a heat source in the FOR disturbing the measurements of the apparatus, and in the worst to destruction of the coil assembly.

4.4.1 water cooling the DC magnetic field coils

The initial step to handle this is to wind the coils from hollow core copper wire through which cooling water can be fed. This 5 mmx5 mm rectangular wire has a circular internal hole with a diameter of 3 mm for the coolant. Each coil is wound from 5.5 m of this wire with an additional 2 m lead length, resulting in a total wire length of 9.5 m. With this information, the pressure-dependent volumetric flow rate of the coolant through the wire can, in principle, be calculated.

However, it is first important to understand the scaling and which simplifications can be made for the problem, especially for adaptations of these calculations for other experiments. When being taught the basics of electricity and electric currents in middle school, teachers often draw comparisons between the scaling and behavior of water flux to connect electric currents to an existing empirical understanding of an analogous system. Over time, as it becomes more natural to work with electric systems, this analogy becomes less present[44] in the everyday lab work. However, when faced with the less common situation of developing these water cooling systems, one can use the inverse approach and connect the problem to electrical systems, which are much more commonly encountered for experimental physicists, providing a base intuition.

Ohm's law, which connects a potential difference U with a resulting current I through a connection with a given proportionality constant, the ohmic resistance R_{el}, can be expressed as $U = R_{el}I$. The equivalent for laminar water flow is the Hagen-Poiseuille law, which connects in essence the potential difference pressure p_{hyd} to a resulting volumetric water current Q_{hyd} via a resistance R_{hyd} to $p_{hyd} = R_{hyd}Q_{hyd}$. In the tur-

[44] at least it did for me

bulent flow regime, in which water cooling systems typically operate, this changes to $p_{hyd,turb} = R_{hyd}(Q_{hyd})Q_{hyd}^2$ according to the Darcy-Weissbach equation, where R_{hyd} depends on the volumetric flow via the Reynolds number, however, it can be considered constant in turbulent flow with large Reynolds numbers, as the scaling contributes mainly in the laminar and transitional regime [98].

For the four coils that need to be cooled, connecting them in parallel ensures that all coils receive equal water temperature. As they are identical, consequently, the resistance $R_{hyd,coil}$ is equal for all coils. This means, as the applied pressure is equal for all coils, the water current in each coil $Q_{hyd,i}$ will be identical and the total current through all coils $Q_{hyd,all} = 4Q_{hyd,i}$, allowing the problem to be simplified to a single water cooled coil [98].

To calculate this pressure-dependent current, one can use the complete Darcy-Weisbach equation for a cylindrical pipe to determine the volumetric flow-dependent friction-based pressure loss Δp in the pipe, analogous to the voltage drop across electrical resistances. It can be written as [98, 99]

$$\Delta p = \lambda_{hyd} \frac{8\rho_{water} L}{\pi^2 d_{in}^5} \cdot Q_{hyd,i}^2 \tag{4.8}$$

where the first term represents the resistance. ρ_{water} is the density of the cooling water, L the length of the pipe and d_{in} the internal pipe diameter. λ_{hyd} is the Darcy friction factor [100], which scales the resistance depending on the Reynolds number and hence the flow regime leading to the previously described scaling. The precise value of this factor can be complicated to determine; it is empirical, such that there are multiple models and standardized numerical tables that apply depending on the exact system.

However, the tubes in our geometry are not straight pipes, as assumed by Equation 4.8, but wound to form the coil. Bending the tube in such a shape induces additional vortices in the coolant flow, leading to an increase in the flow resistance [101]. As a simplified model to gauge the contribution of this effect, one can calculate the added resistance term for helical tube coils with a constant bending diameter. Following [101] for the internal coil diameter of the coils of 3 mm and a assumed bending diameter[45] of 120 mm, one finds[46] an increase of the flow resistance of the helical tube coil compared to the straight pipe of around 5 %. Hence, the expected small contribution of the coil winding is deemed negligible and will not be taken into account in further calculations to keep the model simple.

In addition to coil tubes, connected in parallel, routing the cooling water system requires lead tubes between the chiller and the coils, leading to additional individual pressure drops according to Equation 4.8 or added resistances for the full circuit. However, as the lead tubes of HQA-ONE provide an inner diameter of 19 mm and scaling of Equation 4.8 with $\propto 1/d_{in}^5$, the contribution of the lead tubes of a few meter length will be around 10^4 times smaller than the coils. For that reason, lead tubing is negligible.

Following the discussion above, the water cooling of the coils can be effectively modeled with a single, straight segment of the hollow core wire, leading to insight into the performance of the thermal management of the entire coil system. In order to omit the use of the somewhat complicated Darcy friction factor for now, we will follow [102] and use the Hazen-William equation, an empirical explicit approximation of the Darcy-Weisbach equation, for the calculation. It can be expressed in SI units as [103]

[45] This number represents approximately the average bending diameter of the coils, as bending diameter while winding increases for the outer wires and decreases for the inner wires

[46] Assuming approximate volumetric flows of 2.8 L/min and a wire length of 6.1 m

$$\Delta p = \frac{10.67 \rho_{water} g L}{C_{cu}^{1.852} d_{in}^{4.8704}} \cdot Q_{hyd,i}^{1.852} \tag{4.9}$$

with g the gravitational acceleration and C_{cu} the wall smoothness of the copper tube, which can be approximated as $C_{cu} \approx 130$ [104].

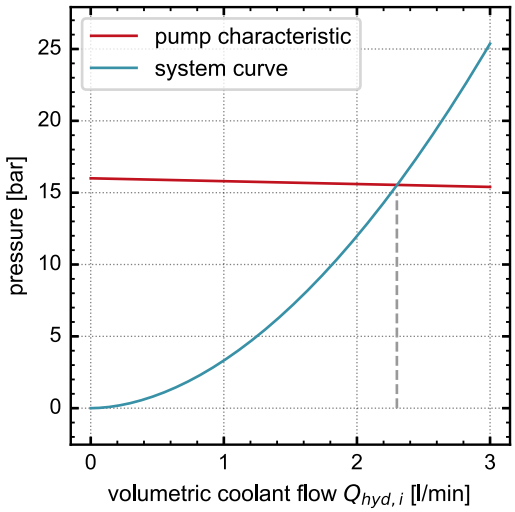

Figure 4.16: Plot of the system curve for one of the magnetic field coils at HQA-ONE according to the Hazen-Williams equation in blue, providing the required pressure to achieve a given volumetric flux through the system. Shown in red is a linear regression of the known pump parameters of the cooling system in order to estimate the pump characteristic curve, which states how much pressure the pump can provide while delivering a given volumetric coolant flux. The intersection point between both, at a volumetric flux of 2.30 L/min is marked with the grey dashed line.

The resulting scaling of the volumetric water flow per coil with the applied pressure is plotted in Figure 4.16. This curve is commonly referred to as the system curve. The operation point of how much volumetric flow will actually occur, depends on the pump characteristic curve of the coolant feed water pump[47]. In Figure 4.16 this is approximated by linear regression between the specified pump performance points of 16 bar at zero flow and 13 bar at a total volumetric flow of 15 L/min, corresponding to 3.75 L/min per coil in the parallel connection, plotted in Figure 4.16. The determined operation point and volumetric coolant flow for the coils in HQA-ONE is 2.30 L/min per coil.

Knowledge of the water flow through the coils allows calculation of the expected heating during operation. The thermal power $P_{thermal}$ due to Joule heating of the coils is described by [102]

$$P_{thermal} = \frac{\rho_{el,cu} L}{A_{wire}} I^2 \tag{4.10}$$

[47] This can be understood comparably to the voltage and available current characteristic of electronic power supplies.

where $\rho_{el,cu} \approx 1.65 \times 10^{-8}\,\Omega\,\mathrm{m}$ [102] is the electrical resistivity of the copper wire, A_{wire} its cross-section area and I the applied current.

Upon a single pass of the coils, if this power is fully dissipated into the cooling water, it leads to an temperature increase ΔT of the cooling at the exit of the coils compared to the entry of [102]

$$\Delta T = \frac{P_{thermal}}{\rho_{water} c_{v,water} Q_{hyd,i}} \tag{4.11}$$

with $c_{v,water}$=4.18 $\frac{\mathrm{kJ}}{\mathrm{kg\,K}}$ the specific heat capacity of the cooling water. The expected heating of cooling water in single passage according to Equation 4.10 and Equation 4.11 is plotted in Figure 4.17.

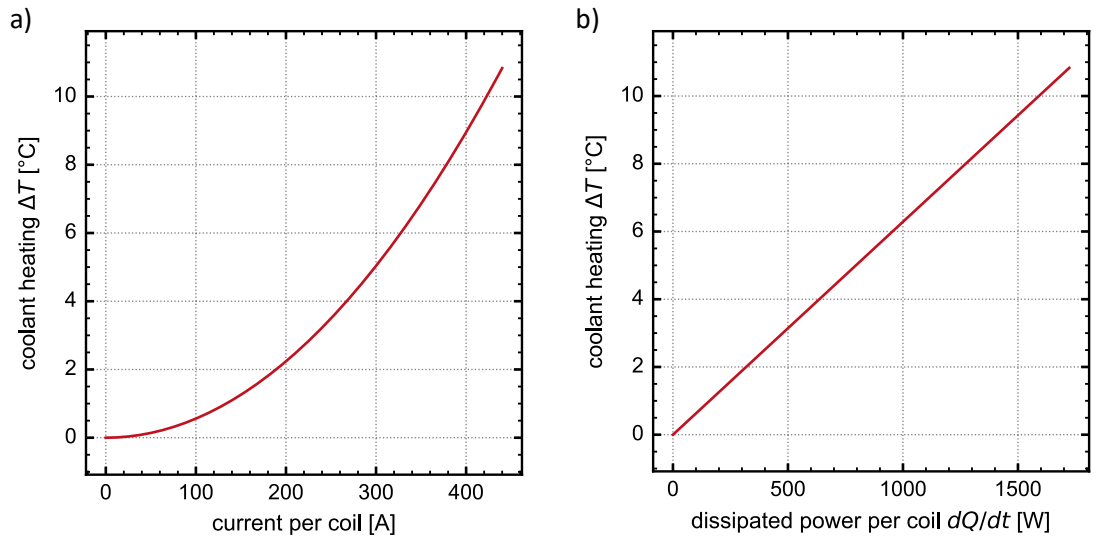

Figure 4.17: Expected heating of the water coolant when passing through the coils. In the equilibrium case, this temperature corresponds as well to the overall heating of the coil itself. **a)** Depict the coolant heating while passing the hollow core wire, depending on the applied coil current, assuming perfect thermal contact. **b)** Plots the same quantity dependent on the dissipated thermal power of the coil into the cooling water. For perfect thermal contact between coils and coolant, where the entirety of the Joule heating is transferred into the coolant, these curves are equivalent.

Figure 4.17 a) shows the heating of the water coolant upon coil passage depending on the applied coil current, Figure 4.17 b) dependent on the power dissipated by the coil into the coolant. In essence, these plots directly correspond to each other, except that the presentation in Figure 4.17 a) assumes perfect thermal contact, where the entire produced Joule heating is transferred into the cooling water. In this case, in thermal equilibrium, with constant water temperature at the coil inlet, this temperature increase equals the heating of the coil itself. For high-pressure fed internally cooled coils, ideal thermal contact, and therefore Figure 4.17 a), can be understood as a valid approximation[48].

[48] It breaks down, for example, when using a heat pad interface limiting the thermal conductance [105].

High pressure in the narrow coil wire leads to turbulent flow[49] which is desirable in cooling applications as it mixes the cooling water during passage and heating in the coil, preventing the formation of boundary layers in the water lowering the cooling performance. However, turbulent flow produces vortices in the flux, leading to small vibrations of the cooling water and indirectly of the coils. While precise calculations can be complicated [106], a ballpark figure for the relevant vibration frequency range of the coolant can be estimated with the flow velocity $v_{flow} = Q_{hyd,i}/A_{core} = Q_{hyd,i}/\pi(\frac{d_{in}}{2})^2$ and the internal diameter of the pipe. Given the operation point of 2.30 L/min, this corresponds to a flow velocity of 5.4 $\frac{\mathrm{m}}{\mathrm{s}}$. A vibration frequency range estimate is given by the largest possible transversal oscillations in the pipe, corresponding to the full internal diameter, which can occur at most with the fluid's propagation velocity, leading to buffeting of the pipe. The range of the water vibrations can be coarsely estimated by $f_{max} = v_{flow}/d_{in}$, leading for the presented specifications to 1.8 kHz. As the coils are rigidly connected to the FOR at HQA-ONE, this means that these vibrations can, in principle, lead to vibrations of the FOR; however, they have to couple to the excitation spectrum of the coil bodies and subsequently to the excitation spectrum of the FOR. Up until the time this thesis is being written, there were no flutter or other issues observed at HQA-ONE due to mechanical vibrations. If they are observed and relevant for the operation of the apparatus, one possibility for control is partially closing the valves in the coil lead lines, increasing the resistance and lowering the volumetric flow rate, which changes the flow turbulence slightly, potentially just enough to avoid resonances; however, it increases the expected heating of the coils.

Other implementations of HQA, like the experiment by Dr. Philipp Preiss at the Max Planck Institute of Quantum Optics in Garching, mounted the coils separately from the FOR, trading full decoupling for a more complex, less space-efficient, mechanical structure.

4.4.2 general water cooling system

The realization of the full thermal management system of HQA-ONE in the sense of a closed dual-secondary-circuit water cooling system is sketched in Figure 4.18, a legend for the used connection and device symbols can be found in Appendix A.

The water cooling system consists of an open primary circuit and two closed secondary circuits for cooling applications in the lab, connected by a system separator[50] from *Van der Heijden Laboratory Technology*[51]. This device uses a heat exchanger to stabilize the temperature of a reservoir tank with a primary circuit, leading to a fully decoupled water reservoir from which the secondary circuits can be fed.

The institute's cooling water supply provides the primary circuit of the system with a temperature of typically 16 °C and an available pressure fluctuating around 4 bar, leading to a water flow in the primary circuit of typically 32 L/min. This cooling water flow is used to cool and stabilize[52] the water temperature in the 50 L reservoir tank to a setpoint of 21 °C. The specified cooling power[53] for the reservoir in the steady state is 7 kW, enough to cool the coils even under constant maximum current operation with headroom for additional cooling applications.

[49] A flow rate of 2.3 L/min in a tube with 3 mm corresponds to a Reynolds number of around 16000, well above the turbulence threshold around 2300.
[50] Van der Heijden Kuehlmobil 423-WW-B400
[51] www.vdh-online.com
[52] The system can only cool the reservoir water; there is no tank heater installed.
[53] for a 20 °C tank setpoint and 1650 $\frac{\mathrm{L}}{\mathrm{h}}$ primary circuit flow at 17 °C

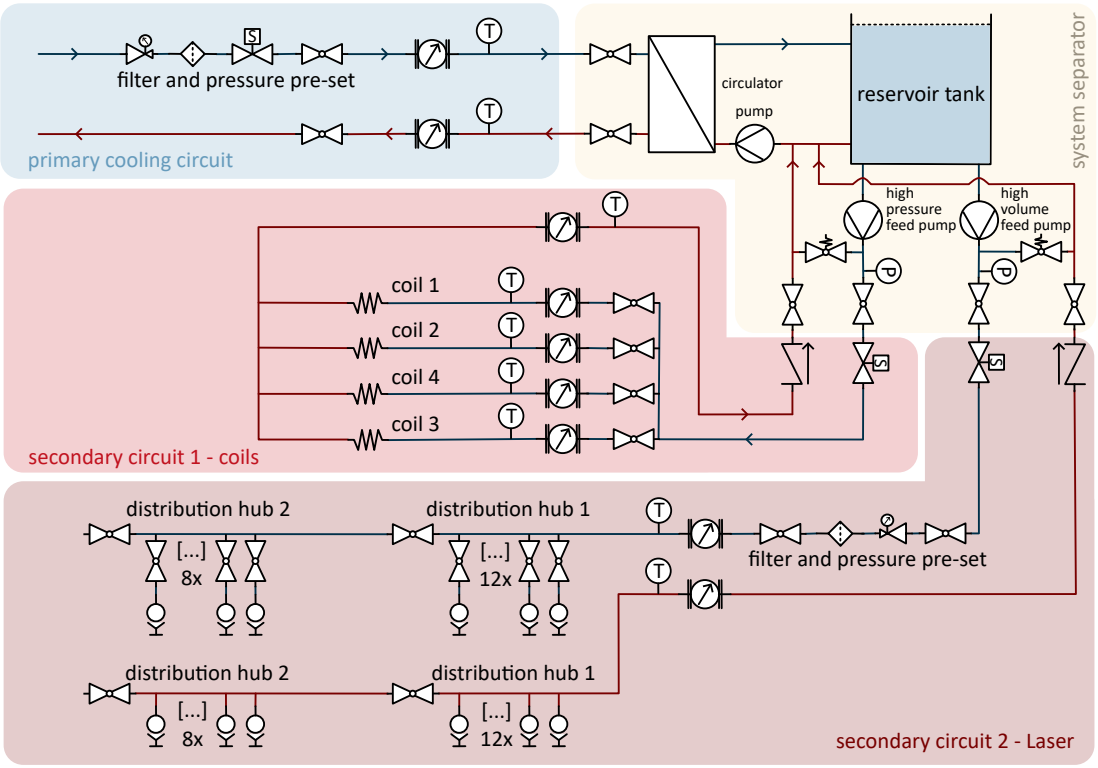

Figure 4.18: Sketch of the water cooling system constructed at HQA-ONE. As a guide to the eye, different functional groups of the system are highlighted in different colors. In essence, a COTS available system separator (yellow) is used to stabilize the temperature of a reservoir tank in a closed secondary system via a primary cooling circuit provided by the institute's water cooling supply (blue). Details of the stabilization system and piping of the commercial system separator are not shown. This tank feeds two secondary cooling circuits (red), each with its own individual feed pump. One circuit houses a pump for high pressure with a low flux for cooling the coils, the other circuit provides lower pressure, yet high flux capabilities for other water cooling applications in the laboratory, e.g., a laser. This system is equipped with a modular, spill-free quick connector hub system for easy and rapid installation of new water-cooled devices. Symbols shown in the figure are explained in Appendix A.

The reservoir tank is filled with demineralized water as a coolant medium with a corrosion inhibitor[54] as an additive. It feeds two separate secondary cooling circuits, the permanent coil circuit and a multi-purpose circuit, for example, for a water-cooled laser. The latter has the requirement of simplifying water cooling installation for new devices. In a single circuit, adding new tubes and devices changes the total resistivity of the circuit and therefore also the coolant's flow behavior. The dual circuit approach in our system allows us to avoid affecting the coil cooling when adding or removing new devices in the multi-purpose circuit.

Secondary circuit 1, the coil circuit, is fed with a high-pressure, low-volumetric-flow feed pump delivering a pressure of up to 16 bar. This provides a convenient pressure limitation

[54] Bioanalytic ThermoClean CPX

for the water circuit installation, as most brass fittings and standard components are rated for permanent operational pressures up to 16 bar. As shown in Figure 4.16, the expected volumetric coolant flow per coil is 2.30 L/min, the measured flow with the flowmeter in the circuit is around 2.2 L/min. The relative deviation of a few percent fits the regime expected for the contribution of the neglected winding of the coil wire in the model. The flowmeters[55] do not contain moving parts; they measure the flow rate by measuring the time transit difference for upstream and downstream propagating ultrasonic wave pulses. Therefore, they are not expected to contribute significant pressure losses.

Secondary circuit 2, the multi-purpose or laser circuit, is fed with a low-pressure, high-volumetric-flow feed pump delivering a pressure of up to 5.4 bar. It includes a water filter[56] with an integrated pressure reducer to keep the reservoir tank clean and to lower the applied pressure for devices in the circuit if necessary. The circuit is equipped with two distribution hubs, one for each optical table, with the possibility of expanding the system to add more hubs if necessary, and if sustainable by the pump and the cooling power of the system separator. These two hubs provide a total of 20 ports, equipped with valves and spill-free quick connectors[57] from *Colder Products*[58] for rapid and convenient installation of new water-cooled devices and flow control in the channel. The total volumetric flow in the circuit depends on the number of devices attached to the hubs and the pressure reducer setting. At the time this thesis is being written, it is typically around 25 L/min.

4.4.3 testing of the DC coil's thermal management

As a last step, the performance of the thermal management system for the coils is to be tested. For this, the current on all four coils is set to 300 A, leading to a joule heating of around 800 W per coil according to Equation 4.10. The temporal response of the coolant temperature and the coil bodies is measured with the sensors shown in Figure 4.18 and PT100 temperature sensors glued to the copper wire of the coils. The corresponding data, relative to the temperatures with the coils off, is plotted in Figure 4.19.

Figure 4.19 a) depicts the temperature change of the copper coil wire and the coolant in the common backflow after passing the coils before being recooled in the heat exchanger and pumped back into the reservoir tank. The 300 A current in the coils is turned on at time $t = 0$, leading to a steep temperature increase on all measurement positions. After around 2 min, the temperature readings start to saturate, reaching a constant equilibrium temperature after around 5 min. The initial overshoot of the steady state temperature is attributed to the control electronics of the system separator regulating the reservoir tank temperature.

The water backflow temperature increases by approximately 5.5 °C. Expected for a current of 300 A, according to the model in Figure 4.17, is around 5 °C, which agrees with the expected value given the slightly reduced flow compared to the model and the inaccuracies of the temperature sensor. In the steady state, peak-to-peak temperature fluctuations are below 0.2 °C; however, it is not clear to what extent these include sensor noise, yet providing an upper limit of the temperature fluctuations.

The coil wire temperature follows the water backflow behavior, with an offset to both the water temperature and the temperatures of the other coils. While the flow rate in

[55] Audiowell FS0001 and FS0002
[56] Honeywell Primus Plus FKN 74 CS-3/4A
[57] PLC-Series
[58] www.cpcworldwide.com

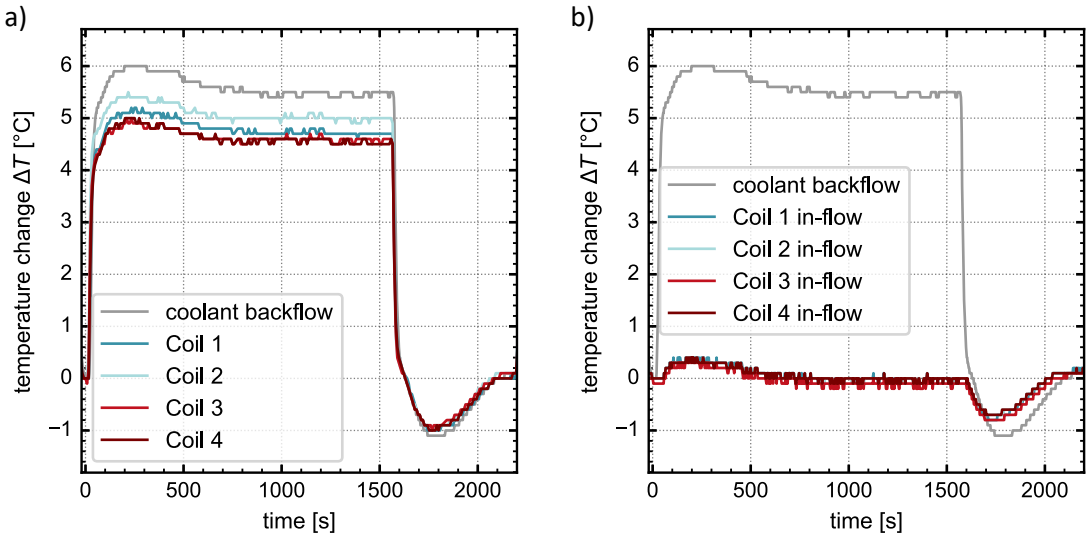

Figure 4.19: Thermal testing data of the temperature response over time of the coils and the cooling water when driving all four coils with a current of 300 A each. Turning on and off the current is visible by the sharp edges in the temperature logging. a) plots the temperature change of the outside of the coil's hollow core copper wire for each of the coils, together with the temperature change of the cooling water backflow after passing the coils. b) Shows with the same scaling again the cooling water backflow temperature, along with the in-flow water temperature before passing the coils for each individual coil.

the separate coils is marginally different, it is more likely that the measurement offsets originate predominantly from the sensors and their placement. The difference in water temperature measurement can be attributed to the PT100 sensors being mounted on the lead wire section of the backflow of the coil wires, outside the FOR. For a single wire far outside the coil body, convection could lead to an additional cooling channel, lowering the sensor reading. Additionally, the sensors are glued with thermoconductive glue onto the Kaptop-insulated copper wires. Variations in the thermal contact for the different sensors could also lead to offsets in the water temperature and the sensor readings between them.

At around t =1600 s, the coil power supplies are turned off, leading to a sudden decrease of all temperature measurements and an overshoot of the steady state temperature, again, most likely due to the internal PID controller of the system separator. This assumption is backed in Figure 4.19 b) by analyzing the inflow water temperatures for each coil. One observes that the overshoot for switching the coils on and off is also visible in the inflow water temperatures. Additionally, one observes that the overshoot amplitude is larger when switching off the coils. This behavior can be attributed to the system separator's ability to control cooling through the heat exchanger. However, its lack of an internal heater limits control authority over increasing the water temperature, particularly with minimal external heat from the secondary circuits.

In the everyday operation of the cooling system, one essentially always works in a steady state with the running experiment. Sequences iterate on a time scale of one or two seconds with even faster changes of the applied currents, much faster than thermal responses, leading to an effective thermal load lower than the values in this test. The effective thermal

load depends highly on the experimental sequence. However, as ballpark numbers, we typically observe a heating of the coils of about 2 °C with peak-to-peak fluctuations after initial thermalization of about 0.1 °C, consistent with the measurements in Figure 4.19.

4.5 Automation and Labcontrol

The sensors in the thermal management system are part of the automation of HQA-ONE responsible for running sequences on the apparatus by controlling, for example, the different laser sources and the light on their ports as well as the magnetic fields. Additionally, the automation system needs to monitor the experiment and environmental status to provide an automated emergency shutoff, a so-called interlock, for unsupervised operation of the apparatus, for example, during night runtime.

4.5.1 experiment control

When discussing the laboratory automation in general, the most fundamental system is experimental control system. It defines the run sequence, controls the lab devices during the sequence's time steps, and repeats the sequence iteratively for sufficient statistics, is an exact replication of the system already in use in our group, controlling the other quantum gas experiments in our labs. The system is also described in [51].

The hardware is based on a real-time processor[59] from *Jaeger Messtechnik*[60]. The modular rack structure of the device can be equipped with different, synchronized insets depending on the setting it is used in. At HQA-ONE, we use it with two analog-to-digital converter (ADC) insets, two digital-to-analog converter (DAC) insets, and two digital-IO insets. This provides a total of 16 analog input and 16 analog output channels with a 16-bit resolution, as well as 64 digital-IO channels, which can be individually configured both as inputs and outputs. The time steps of the processor are 2 µs for the analog channels and 0.5 µs for the digital channels, allowing to run PID feedback loops, for example, to stabilize laser power or the coil current, digitally on the experiment control.

While the fundamental control of the ADwin system is programmed in a software specific to the device, called ADBasic, it is controlled by the lab user with a top-level interface provided by LabVIEW on a desktop computer. The essential core of this LabVIEW interface to control the ADwin as well as other lab devices, at the time this thesis is being written, has been developed as part of [107].

However, many extensions of the LabVIEW control have been developed by multiple PhD students of the group. A special extension of HQA-ONE's LabVIEW control, to be mentioned here, was the integration of M-LOOP implemented by Daniel Dux. It is an open-source Python package[61], called machine-learning online optimization package (M-LOOP), which can be used for machine-learning-based multi-dimensional parameter optimization of the experimental sequence. It has been successfully used in other experiments across the quantum gases community [108] and also provided us with a helpful tool for optimizing the experiment's performance for various cost functions.

In the future, with added possibilities for mechanical control of the beam pointing of the modules by the control software, for which the Bachelor thesis of Jonathan Weiß (see

[59] ADwin-Pro II
[60] www.adwin.de
[61] https://m-loop.readthedocs.io

Table 1.1) lays the ground work at the time this thesis is being written, such optimization algorithms might not only optimize the sequence but also the overlap of the modules light fields in their in respective OR (see Section 3.6). This would transfer the modular structure of HQA from a purely optical and mechanical realization also into the software systems of the experiment control.

4.5.2 experiment status monitoring

Optimizer runs of the experiment can take a few hours, making it favorable to run these overnight. However, the unsupervised runtime of the apparatus, both during the night and day, requires monitoring of the experiment status, environmental parameters, and, if necessary, automated emergency shut-offs. The monitoring side of this system has been nicknamed internally *SmartLab*, and the automated emergency shut-off side is commonly referred to as interlock.

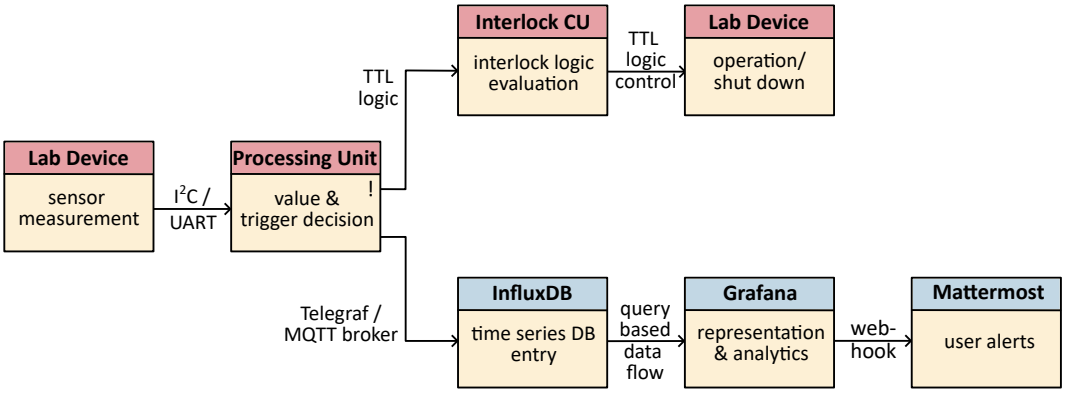

Figure 4.20: Schematic sketch of the setup and data transfer of the environmental data and operational metrics of the apparatus within SmartLab, starting from the sensor and ending back on lab devices for interlock operations or in analytical representations for performance monitoring and user alerts for a-nominal parameter. Boxes with red headers represent hardware, boxes with blue headers correspond to software.

The essential task of reading out and connecting multiple sensors, processing their data, and providing action based on the operational metrics is a common problem from large-scale industrial automation to smart home systems in private. If the internet partly provides the connection, the fundamental concept is commonly referred to as internet-of-things (IoT). This broad spread of equivalent tasks led to the development of many high-level open-source software solutions for these problems, which can be utilized for SmartLab. The general concept of SmartLab is sketched out in Figure 4.20.

Measurements from a sensor, such as a temperature reading, are initially converted by electronic readout and then transferred to a processing unit via digital communication, making the system more robust against added noise during data transfer. For most devices at HQA-ONE, this either follows the I^2C communication protocol or specific UART serial communication protocols required by the sensor.

Once received by the processing unit, this device has two functions. The priority function is the upper branch in Figure 4.20, providing a status report to the interlock control unit if the value is nominal, no value has been received, or equivalently if the value is out

of predefined bounds in the processing unit. To increase the robustness of the system, this report is given as an IO error flag with TTL logic levels. The interlock control unit evaluates the status of the different systems according to its interlock logic and shuts down lab devices via IO commands, if necessary. This will be detailed in the next subsection. However, it should be noted that not all metrics collected by SmartLab are fed to the interlock system. Parameters, such as the laboratory's climate data, are only processed in the lower branch.

The lower branch in Figure 4.20, the software branch of SmartLab, is optional in the processing units code execution. This means that, if execution of this branch fails, for example, due to network connection problems, the upper branch ensuring emergency shut-off is still operational. Measurement values are sent via data collection agents like Telegraf or an MQTT broker to a time-series database, hosted on our servers, forming a time-series database entry. The database is based on the open-source software InfluxDB[62]. The time-stamped data is queried by a locally hosted, open-source representation and analytics software called Grafana[63]. This software provides the user multiple customizable dashboards to monitor the operational status of the apparatus, track and correlate time traces, and an archive for the measured sensor data. An exemplary snippet of one of HQA-ONE's dashboards in SmartLab is shown in Figure 4.21.

Figure 4.21: Example snippet of HQA-ONE's Grafana homescreen for operations status and metric monitoring. Visible in this snippet are performance representations of the water cooling system, alert status, and environmental data of the laboratory from the different air conditioning units and individual custom sensors. The tabs of the sketched window illustrate different functionalities covered by SmartLab as well, including time traces for all measured metrics and a long-term data archive for these readings.

The tracked parameters include, among others, laboratory environmental data (like temperature, humidity, and dust concentration), statuses of different lab devices (like flow rates and temperatures in the thermal control system or beam position and laser lock

[62] www.influxdata.com
[63] www.grafana.com

indicators for the laser), and parameters directly of the institutes infrastructure systems (like the house cooling water or the air conditioning unit).

If one or multiple operational metrics are out of pre-defined bounds in Grafana, it sends an alert to the lab users via webhook to our locally hosted, open-source messaging platform Mattermost[64], informing them about required actions.

4.5.3 interlock

The upper branch of Figure 4.20, ensuring the interlock processes, is detailed in Figure 4.22, highlighting its connection to the central devices for a-nominal shut-down, the coils, and the thermal management system. However, the microprocessor-based interlock control unit is equipped with additional ports for expansion to other devices, such as a laser or a laser shutter.

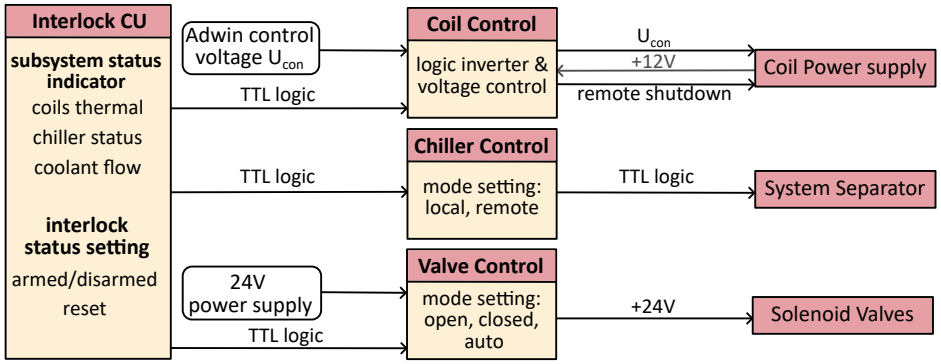

Figure 4.22: Schematic sketch of the central interlock system operation, detailing the upper branch in Figure 4.20. The central interlock, while expandable to other systems, is primarily used at the time of this thesis for interlocking the water and coil systems, which are most relevant for interlocking.

The interlock control unit uses its error flag input in different categories to identify the necessary interlock action. The coil thermal status, which includes the error flags for over-temperature of the coil wires and the MOSFET switch. The second category is the chiller or system separator status, which states whether its pumps are operating. Lastly, the coolant flow, monitoring nominal inflow rates for all coils as well as the difference between inflow and outflow for all three circuits to detect leaks in the system.

Each signal on the input and output side follows the TTL-compatible IO logic levels of an Arduino micro, where high voltage equals nominal operation and low voltage equals the error flag for a-nominal operation. This encoding covers failure and power outage of the processing units reporting the status to the interlock control unit. Additional pull-down resistors on the inputs cover cases of breaking or removing cable connections.

The output side of the interlock controller unit controls three different types of devices: All power supplies of the magnetic field coils, the pumps of the system separator, and the solenoid valves in the thermal management system (see Figure 4.18). Control of the power supplies is provided by shorting the remote shutdown pin of the power supply with a 12 V auxiliary output pin of the power supply. The system separator is built such that it allows

[64] www.mattermost.com

direct control via a TTL-level signal, and the valves are controlled via the solenoid power supply control electronics.

Relevant failure cases include over-temperature of the coils or the MOSFET bench which triggers shutdown of the coil power supplies; pump shutdown in the system separator[65] triggering coil power supply shutdown and complete chiller shutdown; and a water leakage or coil under-flow leading to a shutdown of coil power supplies, chiller, and closing of all solenoid valves. In each failure case, the interlock central unit starts an acoustic alarm and notifies the lab users via Mattermost about the interlock operation. Restarting the apparatus requires manual pushing of a button to reset the interlock. However, both the interlock and the subsystem controls of the chiller and valves can be manually disabled via a switch, which is necessary for the start-up and controlled shutdown procedure of the apparatus and supervised tests of the subsystems.

The air-cooled RF coil is separately interlocked, limiting the maximum pulse length of the 100 W RF signal sent to the coil. This system is replicated from identical existing systems in the other two experiments of the group. However, the interlock CU is built such that expansion is possible. It allows to integrate the RF interlock as well as future laser interlocks all into one central control.

[65] for example if the reservoir tank is filled below its threshold level

5 Configuration for deterministic preparation of few-fermion states

As a last step, it should be demonstrated that HQA can be used to construct quantum simulators. A fundamental requirement in quantum simulation is the ability to produce well-defined quantum states for initializing subsequent measurement aspects. This capability will be presented for HQA-ONE, following a, in our group, well-established few-fermion state preparation protocol to deterministically prepare atom number states in the trap ground state of an optical tweezer potential [109].

The scope of this thesis was mainly focused on the development of HQA and its technical realization in an exemplary ^{6}Li quantum gas experiment, HQA-ONE. Therefore, within this chapter, the demonstration of the few-fermion state preparation capabilities will be provided; however, details about the optimization and detailed considerations of each step in the protocol's implementation are deferred to the dissertation of Tobias Hammel.

In this chapter, Section 5.1 will present a configuration of HQA for these preparation capabilities, Section 5.2 will detail the corresponding experimental sequence, and Section 5.3 will show the results and characteristic step-like preparation levels of the system.

5.1 Configuration of the platform

The first step in this demonstration, following the fundamental concepts of HQA as outlined in Section 3.1, is to configure the apparatus with the corresponding modules to enable the required preparation and measurement capabilities.

This platform configuration for PoCs and mPoCs is sketched in Figure 5.1. The PoCs are equipped with two retro-reflected in-plane 3D-MOT arms with a beam diameter of 10 mm. The 3D-MOT beam, perpendicular to this plane, is injected from above, sent through the objective, and retroreflected on its point-mirror in the objective's backfocal plane (see Figure 3.7). This setup corresponds to the geometry used for the 3D-MOT loading discussed in Section 4.2.

Additionally, a PoC, in this case the one on port 6, is equipped with a camera system for resolving the fluorescence signal of individual atoms in the 3D-MOT, providing the capability to count the atom number in the MOT by knowledge of the individual atom fluorescence signals. This MOT counting setup consists of a 50 mm focal length, 1" diameter, lens to capture the light from a large solid angle of the 3D-MOT fluorescence. The fluorescent MOT is subsequently imaged with a 1:1 magnification on a machine vision camera[1]. The signal is integrated in the relevant region of interest (ROI) to infer the atom number via knowledge of the scattering rates and the detection efficiency[2] of the the MOT counting setup [110]. This combined atom-number conversion can be calibrated with optimized MOT parameters (see Section 5.2) to allow for the detection of individual atom

[1] FLIR Grasshopper3 GS3-U3-23S6M-C

[2] from the MOT fluorescence up to the counts on the camera, including, e.g., covered solid angle, transmission efficiency of the optics, and camera quantum efficiency

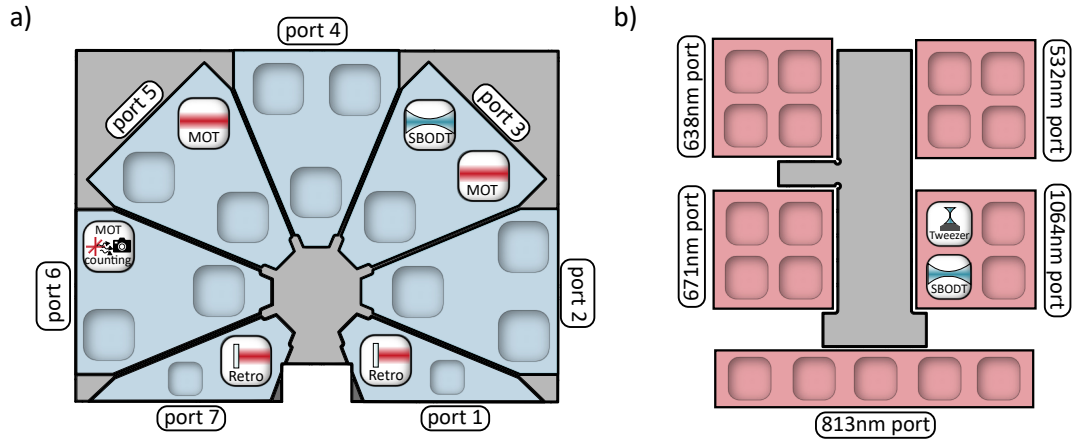

Figure 5.1: Configuration of HQA-ONE in the sense of Figure 3.3 for the deterministic preparation of few-fermion states in an optical tweezer. **a)** displays the configuration of the PoCs, consisting of modules providing the functionality for a 3D-MOT, a single beam optical dipole trap (SBODT), and a MOT counting fluorescence imaging system. **b)** shows the configuration of mPoCs, providing a SBODT and an optical tweezer on the 1064 nm port.

signals. Figure 5.2 plots an exemplary histogram for the MOT counting signal in multiple shots of the experiment in this regime of few atoms, trapped with MOT parameters like detuning and magnetic field gradient optimized for MOT counting. These MOT settings will be referred to as *counting MOT*.

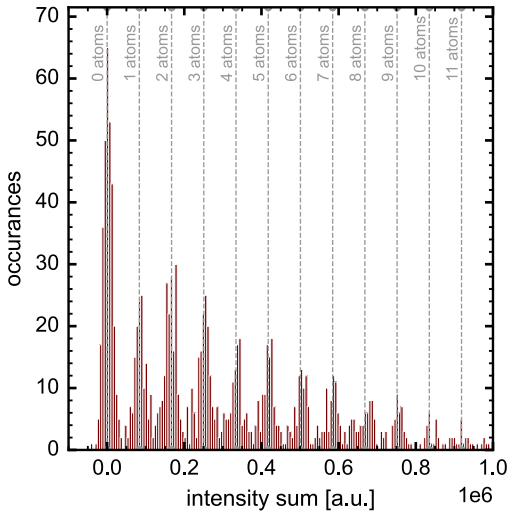

Figure 5.2: Histogram of the fluorescence signal captured by the MOT counting camera for multiple iterations of a prepared MOT with only a few atoms. The individual spikes corresponding to the atom counts in the MOT are visible. These peaks are marked and labeled in gray with their corresponding atom number. Figure adapted from [57].

The data for the histogram plotted in Figure 5.2 was measured by preparing a MOT

with the counting MOT parameter, capable of trapping up to 10^7 atoms, and performing a release-recapture of the MOT with long time-of-flights, such that only a few atoms are recaptured when turning the MOT back on. Observing the total intensity in the applied ROI, the intensity sum, in each iteration, yields in the presented histogram well-separated, regularly spaced peaks, corresponding to the captured, fluorescent atoms in the MOT. The average single-atom signal can be used as a calibration for the MOT counting system to determine the number of atoms in a MOT with an unknown particle number.

The last required functionality, provided by the PoCs, is a red-detuned single beam optical dipole trap (SBODT) with a wavelength of 1064 nm focused to a beam waist of 13.6 µm. This trap is referred to as horizontal optical dipole trap (hODT) in the following. This trap is fed on the PoC from two overlapped optical fibers to increase the available power[3] up to 10 W.

Additional optical dipole traps with a wavelength of 1064 nm are provided by the mPoCs. They provide another SBODT focused to a waist of 4.6 µm, called vertical optical dipole trap (vODT), and an optical tweezer with a waist around 1 µm defined by the NA of HQA-ONE's high-NA objective (see Section 3.7). The available power for these traps is 1 W and 30 mW respectively. The resulting trap geometry utilized in this demonstration is sketched in Figure 5.3.

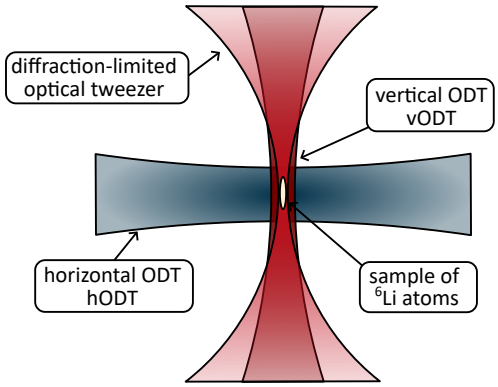

Figure 5.3: Sketch of the optical dipole trap geometry used in the configuration, presented in Figure 5.1. It consists of a horizontal horizontal optical dipole trap (hODT) and a vertical optical dipole trap (vODT) for loading and an optical tweezer in which the few fermion states are prepared.

The waist of the optical tweezer was minimized by tilting the vacuum chamber and the glass cell, with the mechanism described in Section 3.2, relative to the objective, while maximizing the measured trap frequencies in the optical tweezer as a feedback signal. Initially, the tilt of the vacuum chamber was set with the tilt sensor on the top window of the glass cell (see Section 3.2), however, as the objective uses the lower window of the cell, a slight mismatch in the parallelism between the two windows can lead to a relative tilt between the lower window and the objective introducing aberrations. After optimization, we measure radial trap frequencies of $\omega_r \approx 2\pi\times 72\,\mathrm{kHz}$ and axial trap frequencies of $\omega_z \approx$

[3] otherwise the available power would be capped by the power limitation of a single polarization maintaining single mode fiber

$2\pi\times14\,\mathrm{kHz}$ for a power of $200\,\mu\mathrm{W}$ in the optical tweezer. Therefore, the aspect ratio of the optical tweezer is $\omega_r/\omega_z \approx 5.1$.

5.2 Experimental sequence

The presented configuration of the platform describes the hardware side of the deterministic preparation of the few-fermion states in this chapter. The corresponding experimental sequence, utilizing this hardware, is qualitatively described in this section.

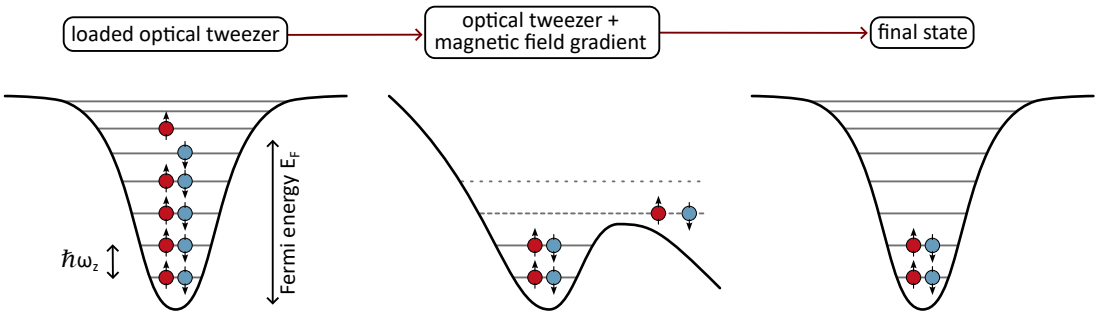

Figure 5.4: Sketch of the spilling procedure to prepare samples of deterministically set atom numbers in the ground state of a red detuned optical tweezer potential in one-dimensional (1D). First, an optical tweezer is loaded with the ultracold $^6_{\mathrm{Li}}$ atoms in two different spin states (indicated as red and blue) according to the Fermi-Dirac distribution. This results in the lowest levels of the potential being filled with near unity probability and excitations near the Fermi edge. A magnetic field gradient is applied, and the trap is lowered, resulting in higher levels becoming unbound and removed from the trap. Sufficient control over the potential allows for the spill of atoms up to a certain level, before removing the gradient potential and ramping the tweezer back, leading to a sample of well-defined atom number in the ground state of the trap. Figure adapted from [107].

At the heart of the sequence lies the spilling technique for individual level control in a 1D harmonic oscillator potential, sketched in Figure 5.4. This technique was originally developed by our group in [109] and is well-established in all experiments within the group. It is described in detail in multiple PhD theses recommended for further reading, e.g. [107, 111] including extensions of the technique to spilling in the 2D harmonic oscillator potential [96, 107].

In the 1D case, used in this demonstration, the potential is formed by the optical tweezer, providing for the lowest states in the tweezer a quasi-1D harmonic oscillator potential. This potential is filled with a mixture of ^{6}Li atoms prepared in two states of the high-field ground state hyperfine manifold (see Figure 4.2), in this case typically a $|1\rangle - |3\rangle$ mixture, to allow tunable interactions between the components.

The optical tweezer is loaded from an overlapped larger reservoir trap, which locally increases the chemical potential. The temperature of the atom cloud, however, remains unchanged [112]. As a result, the tweezer is filled with enhanced density, typically deep within the degenerate regime [107, 109]. This leads, following the Fermi-Dirac distribution, to a near-unity occupation probability of the lowest states of the tweezer potential

[109]. Thermal excitations, in the form of empty states in the state occupation, occur predominantly around the Fermi edge of the system (see Figure 5.4).

In the next step, an additional magnetic field gradient is applied, leading to a tilt of the potential for the high-field-seeking states[4] $|1\rangle$ and $|3\rangle$. Lowering the trap depth of the optical tweezer with this gradient applied allows for control over which states in the potential remain locally bound and which become unbound, leading to a loss of atoms from the tweezer potential. After the spilling of the undesired state occupations, the magnetic field gradient is removed, leading to the potential being filled with a deterministic number of atoms in the ground state of the trap.

The full sequence around this process, for the applied magnetic offset field and curvature (blue) as well as the power of the different ODTs (red), is plotted in Figure 5.5, with the different functional blocks of the sequence highlighted.

As a first step the 3D-MOT is loaded for around 600 ms with a magnetic field gradient of 74 $\frac{\mathrm{G}}{\mathrm{cm}}$ and a detuning of the MOT beams of $\Delta_{cool} \approx 6.4\Gamma_{D2}$ for the cooler and $\Delta_{rep} \approx 2.4\Gamma_{D2}$ for the repumper[5]. At this point, the MOT is loaded with around 10^8 atoms.

Subsequently, the MOT is compressed for transfer into the horizontal optical dipole trap (hODT). The magnetic field gradient is ramped to 140 $\frac{\mathrm{G}}{\mathrm{cm}}$, the MOT beams to $\Delta_{cool} \approx 1.2\Gamma_{D2}$ and $\Delta_{rep} \approx 0.3\Gamma_{D2}$, and the hODT is turned on. This spatially compresses the MOT and increases the density to load the hODT with up to 1.2×10^4 atoms.

With the atoms loaded into the hODT, the magnetic field gradient is turned off and an offset field of 770 G, close to the Feshbach resonance (see Figure 4.13), is applied, leading to strong interactions between the different spin states. An RF pulse is sent onto the atom, driving $|1\rangle - |2\rangle$ Rabi transitions which, due to the strong interactions, quickly decay into a 50:50 mixture of the two components. The offset field is ramped to 570 G, a field close to the zero crossing of the $|1\rangle - |3\rangle$ mixture where the combined scattering length for the $|1\rangle - |2\rangle$ and $|1\rangle - |3\rangle$ mixture is minimal. An RF Landau-Zener sweep around the $|2\rangle \rightarrow |3\rangle$ transition is applied, leaving the atoms at the end of the mixture preparation block in an equally balanced $|1\rangle - |3\rangle$ mixture.

In the next step, the magnetic offset field is ramped to 424 G, the atoms evaporatively cooled in the hODT and transferred to the vertical optical dipole trap (vODT), which is typically filled with between 2×10^3 and 4×10^3 atoms.

Similar to the previous step, the atoms in the vODT are again cooled by evaporative cooling and transferred into the optical tweezer. However, in this block, the evaporative cooling via the vODT power occurs entirely in the combined trap of the vODT as a reservoir and the tweezer as a dimple [113]. After transfer and evaporation, the optical tweezer is filled with around 1×10^3 atoms.

In the next step, evaporative cooling is performed in the tweezer, evaporating the gas down to the Fermi edge within a few tens of milliseconds. After evaporation, approximately 200 atoms remain in the tweezer, serving as the starting point for the actual spilling process.

The spilling starts by ramping on a magnetic field gradient of 10 $\frac{\mathrm{G}}{\mathrm{cm}}$ effectively tilting the trap potential as sketched in Figure 5.4. The optical tweezer power is ramped down with a constant ramp rate of 20 $\frac{\mu\mathrm{W}}{\mathrm{ms}}$ to the desired final depth of the tweezer. After holding this level for approximately 50 ms, the tweezer power is ramped up again, and the magnetic field gradient is ramped off. This completes the spilling procedure.

[4] The low-field seeking state experience an inverse tilt of the potential.
[5] Compared to Table 4.1 corresponding to the other peak in Figure 4.11

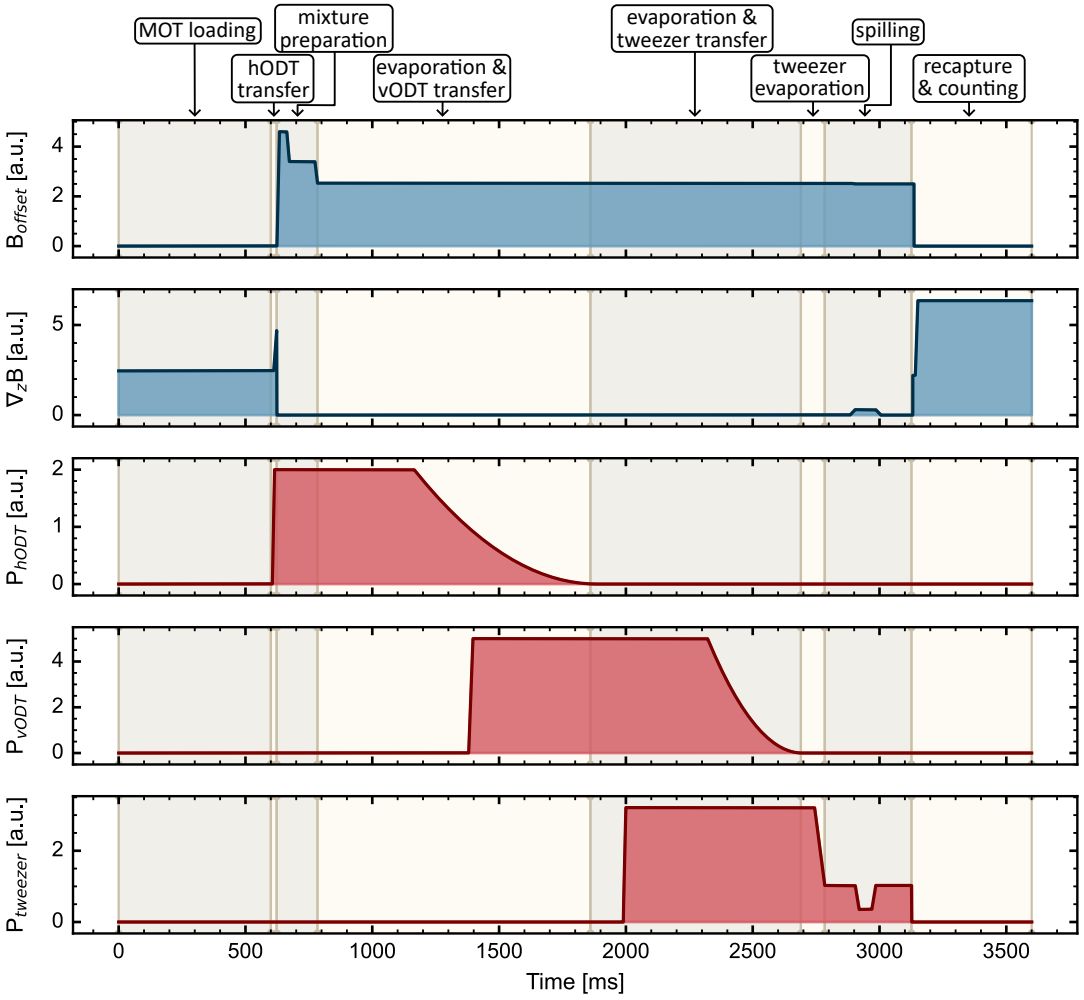

Figure 5.5: Complete experimental sequence of relevant channels for the preparation and detection of deterministic few-fermion states according to Figure 5.4. Shown in blue are the linear control signals in arbitrary units for the magnetic offset field B_{offset}, as well as the magnetic field gradient along the propagation axis of the optical dipole trap $\nabla_z B$. Shown in red is the control signal proportional to the power in all three optical dipole traps shown in Figure 5.3. The different functional blocks of the sequence are highlighted in the background for all presented channels and labeled above the plot.

As a final step, with the last block, the prepared atom number must be counted. For this, both the magnetic offset field and the optical tweezer are quenched off. The expanding atom cloud released from the tweezer is recaptured by the MOT, which is simultaneously turned on. Initially, with parameters similar to those during loading for an increased capture velocity, and subsequently ramped to the counting MOT parameter. At a magnetic field gradient of 190 $\frac{\mathrm{G}}{\mathrm{cm}}$ and detunings of $\Delta_{cool} \approx 1.0\Gamma_{D2}$ and $\Delta_{rep} \approx 0.2\Gamma_{D2}$, the MOT counting system captures the fluorescence of the MOT for 450 ms to infer the atom number in the counting MOT. Afterwards, the atoms are released and the next run of the apparatus is initialized.

5.3 Deterministic few-fermion state preparation

The resulting dependency of the captured signal from the MOT counting system on the spill depth of the tweezer, representing the capability to resolve the tweezer level structure, is plotted in Figure 5.6. The preparation fidelity for the individual levels in this measurement is provided as an inset in the figure.

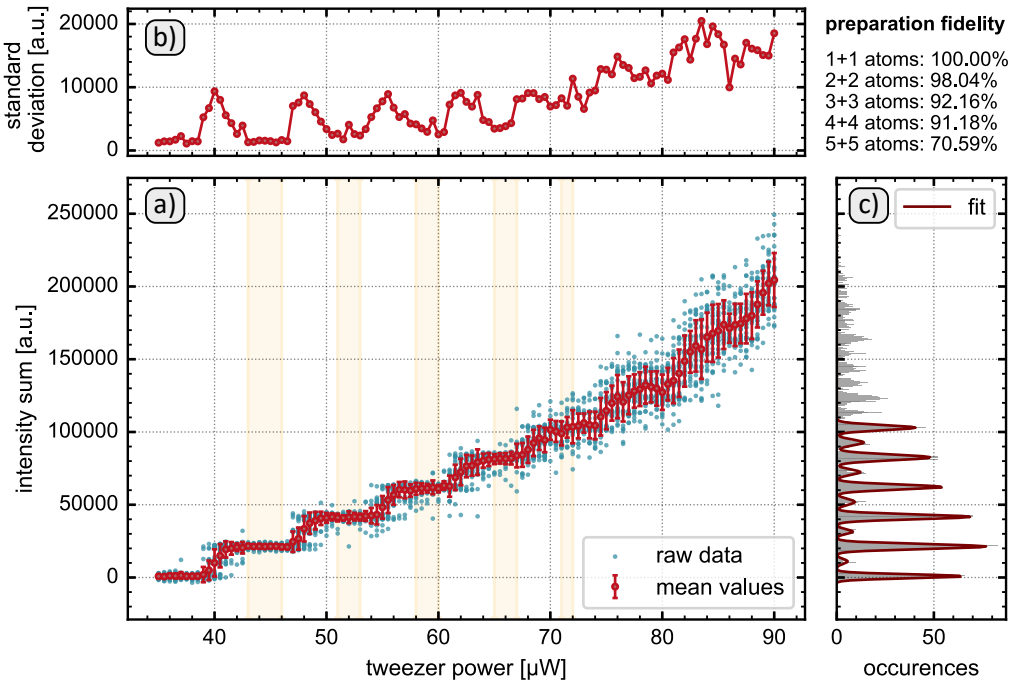

Figure 5.6: Preparation in steps of the 1D harmonic oscillator potential in the tweezer trap. a) plots the captured total fluorescence intensity in the region of interest (ROI) of the MOT counting camera for different optical tweezer spilling depths for a constant magnetic field gradient during spilling. Shown in blue are individual data points, and in red, their respective mean values with the standard deviation as error bars. Marked in yellow are the empirically set stable steps of the spilling corresponding to the spilling level between the occupied levels in the potential. b) shows the standard deviation on the data points in a), increasing each time the spill level crosses an occupied level in the potential. c) shows a histogram of the intensities in a) with individual atom levels visible. Each level is occupied by two atoms, one of each spin component. The inset shows the preparation fidelity in a) in the yellow-marked regions by determining the counts outside the corresponding atom number signal width in b).

Figure 5.6 a) depicts the total intensity in the ROI of the MOT counting camera, corresponding to the atom number in the tweezer after spilling, dependent on the tweezer spilling depth applied in Figure 5.5. Depicted are the individual points of multiple realizations in blue as well as the corresponding mean in red with the standard deviation as error bars.

One observes a step-like behavior for a total of five steps. With Figure 5.4 in mind, these plateaus correspond to the spilling depth traversing between the individual levels of the

potential, where further decreasing the spill depth does not lead to additional atom loss, as the atoms can only populate the discrete states. Once the spill depth crosses an occupied level, the atom number sharply drops, indicating loss of the two atoms, one per spin state, occupying this level, before the next plateau begins. The fact that there are five steps, or six plateaus, visible arises from the aspect ratio of the optical tweezer. As discussed in Section 5.1, the tweezers aspect ratio is $\omega_r/\omega_z \approx 5.1$. This means for the system to be quasi 1D, the lowest radial level yields five axial levels, corresponding to the steps in the plot. For higher energies, the system is no longer quasi 1D and higher radial shells are occupied. Their degeneracy leads to a breakdown of the deterministic preparation protocol.

Figure 5.6 b) depicts the standard deviation of the MOT counting signal of the individual repetitions per spill depth, effectively plotting the size of the red errorbars in a). The shell structure of the trap is again visible, leading to low fluctuations when the spill depth traverses the gaps in the shell structure and high variations close to the levels where the system's atom loss becomes sensitive to the applied spill depth relative to the energy level.

Figure 5.6 c) depicts a histogram for the detected intensity sums in the MOT counting of a). As in Figure 5.2, the peak structure, corresponding to discrete atom numbers in the counting MOT, is clearly visible. These are fitted with a function consisting of 11 Gaussian fits to retrieve the width for each plateau in a). The separation between the zero and two-atom peak, and therefore the ratio between the plateau and the step, is $6\sigma_{2atom}$ of the two-atom peak width. Additionally, one observes that the plateaus, and therefore full shells, are always double-occupied, with one atom per spin state, leading to steps of 0, 2, 4, 6, 8, and 10 atoms.

The fidelity in preparing these states deterministically is shown as an inset for the five levels. These were calculated using the yellow shaded regions in a). In these empirically set regions, the plateau is considered flat; therefore, this corresponds to a region to spill to for preparing the state corresponding to the next lower step. Within each of the marked regions, the intensity sum for each iteration is evaluated. If it deviates by more than three times the standard deviation of the corresponding peak in c), it is considered a faulty run, indicating that one or more atoms were prepared either too many or too few. Fidelity is defined by the ratio of faulty runs to total runs in the yellow-marked regions. In a), these faulty runs can be seen by the raw data points deviating from the steps. In general, very high preparation fidelities for the tweezer levels are observed. The ground state of 1+1 atoms did not result in a single faulty run out of 150 iterations, leading in principle to unity preparation fidelity. Considering the finite repetitions of 150 iterations, it is measured to be greater than 99.3 %.

This demonstrates the deterministic few-Fermion state preparation with high fidelity for HQA-ONE and, therefore, establishes the principle for other experimental platforms based on HQA. With quantum state initialization capabilities demonstrated for this exemplary technique, the architecture can be considered in principle usable for quantum simulators.

6 Summary and Outlook

6.1 Conclusion

Within the scope of this thesis, an open-source, broadly applicable modular quantum gas platform has been developed, and a first apparatus based on this system design has been constructed. The developed modular design and the apparatus have been described in detail in this thesis. The apparatus has been used to demonstrate the capabilities of the modular design and its suitability for atom-based quantum simulator applications.

Chapter 1 introduced the concept of general modular system architecture in technology based on its initial implementation in computer systems. Additionally, it provided an overview of further, more specialized literature that has been written during this project, ranging from a scientific publication [57] to multiple Bachelor's and Master's theses (see Table 1.1).

Chapter 2 puts the chances and relevance of modularity into perspective of the current pursuit of atom-based quantum computing and especially quantum simulation. It identified opportunities to make analogue quantum simulators more versatile, allow specialized and collaborative technological development, and enable reconfiguration of quantum simulators, minimizing risks in technological developments.

Chapter 3 introduced and demonstrated the modular platform architecture HQA, developed within the scope of this thesis, as a general cold atom platform, which is broadly adaptable. Modularization is achieved by decoupling the platform into subsystems which can be attached to a common mechanical centerpiece, the FOR, the relevant components of which have been machined utilizing the available precision of modern CNC machines of better than 10 µm.

These subsystems are grouped into either assemblies, which are in principle reconfigurable parts but not designed for frequent exchange (e.g., magnetic field coils), or modules, which are parts that allow regular exchange and reconfiguration of the platform. Within the rationale of HQA, the optical modules are categorized into PoCs for optical access from the side up to 0.3NA (at HQA-ONE) and mPoCs for optical access through the platform's high-NA objective yielding up to 0.66NA (at HQA-ONE). This set the architecture-based visible design rules for the modules.

Suitable interfaces and mounting mechanisms for the modules on the FOR have been identified, using positioning pins for the PoC and parallel keys for the mPoC placement. Tests of the mounting techniques yield positioning precisions of PoCs of better than ±10 µm and better than ±60 µm for the mPoCs. Including the adjustable demagnification of these deviations in the common imaging path on the mPoC interface in the FOR, operational precision with respect to the center position is expected to be similar to the PoC precision. These mechanisms set the interface-based visible design rules for the modules and the architecture.

Tools for in-situ and ex-situ performance testing and adjustment of the modules have been developed, ranging from an external testbench for the PoCs to diagnostic ports on the

FOR. A suggested workflow from external development of a module to integration in the platform has been demonstrated with passive precision from development to integration of a PoC of better than ±30 µm. The requirements along the steps of this workflow mark the standardized performance validation-based visible design rules for the modules and the architecture.

Chapter 4 introduced details of the first realization of a HQA-based quantum gas apparatus, constructed within the scope of this thesis. This apparatus is therefore referred to as HQA-ONE and provides a HQA realization for experiments with ultracold, fermionic ^{6}Li. The details covered in this chapter are beyond what is part of the general architecture of HQA and due to the chosen atomic species or the given laboratory environment. The covered topics included the constructed laser systems as light sources for the modules to address the ^{6}Li atoms, the compact vacuum chamber with its oven and 2D-MOT as an atom source, magnetic field coils for interaction- and internal state control, the respective thermal management for the laboratory and the high-current magnetic field coils, as well as automation of HQA-ONE for monitoring and experiment control.

Lastly, in order to demonstrate the suitability of HQA for use in the context of quantum simulators, in Chapter 5, HQA-ONE is configured to exemplarily demonstrate a core capability of quantum simulators, deterministic initialization of a quantum state. The apparatus is used to deterministically prepare atom number states of a $|1\rangle\,|3\rangle$ mixture of ^{6}Li atoms in the ground state of an optical tweezer potential. For states up to 8 atoms, preparation fidelities of above 90 % are measured.

The developed and presented system design now provides a tested open-source modular platform architecture for atom-based quantum simulators that can be adapted to a broad spectrum of related use cases across quantum gas experiments. It has been adapted in large parts by the group of Dr. Preiss (MPQ Garching), who, together with his team, has been a close collaborator since the beginning of the project and provided invaluable discussions and feedback for the development of the architecture. Beyond that, at the time this thesis is being written, four more experimental apparatuses are being constructed, which either have already started to implement or are considering implementing parts of HQA's modular design. In conclusion, HQA presents one possible solution[1] for large scale modularity in quantum gas platforms, which hopefully serves as a starting point for a process of developing modular technology in that field, as quantum simulators move more and more towards broader usability, that can be in the long run be as beneficial as it has been for the classical computer industry.

6.2 Outlook

Now that HQA-ONE has been constructed, its focus shifts away from demonstrating the modular system of HQA. HQA-ONE has entered its scientific operation phase, where it can be used for quantum gas experiments and quantum simulation. However, that requires a scientific toolbox; due to the architecture, this means different modules providing the experimental capabilities for the desired toolbox to conduct experiments and quantum simulations. Being independent modules, their development occurred in parallel to the

[1] However, it is at this time the only open-source, broadly applicable, tested, and complete solution for modularity in quantum gas platforms

construction of HQA-ONE, such that there is now a set of modules available to configure the apparatus. In this section, four of these will be briefly discussed, out of which the former two are implemented and under initial use at HQA-ONE, the latter two are developed, constructed, and tested, but have not yet been used as modules of the apparatus.

6.2.1 Transparency beams

The first module, utilizes light near the higher $|2^2p_{3/2}\rangle \rightarrow |3^2s_{1/2}\rangle$ transition at 812.6 nm (see Figure 4.1) to form an optical tweezer potential. Just like its analogue at 1064 nm, this is red detuned to the D_2-transition $|2^2s_{1/2}\rangle \rightarrow |2^2p_{3/2}\rangle$ at 671 nm, such that atoms in the $|2^2s_{1/2}\rangle$ ground state are trapped in the optical tweezer formed from a highly focused Gaussian beam. Just like the 1064 nm tweezer in Chapter 5, this potential can be used to deterministically prepare atom number states in the ground state of the potential.

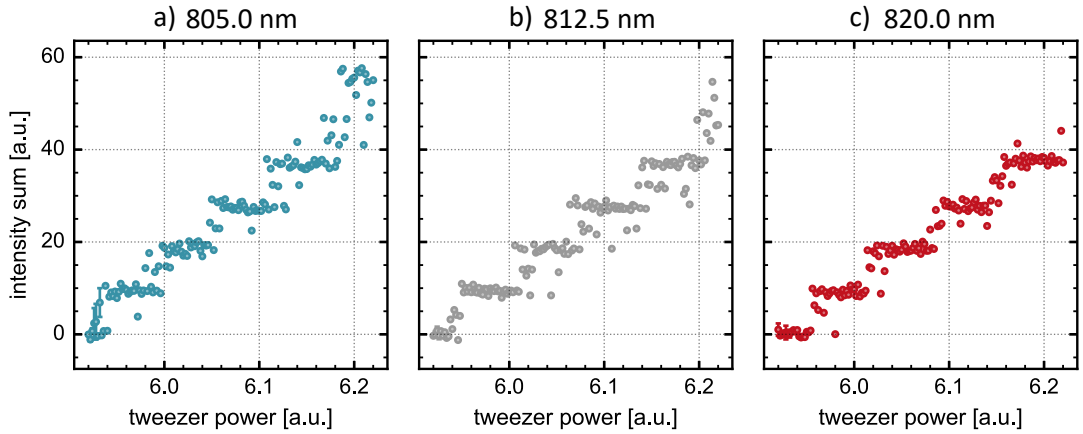

Figure 6.1: Spilling in an optical tweezer with resolved level structure of the potential, demonstrating deterministic state preparation, at different wavelengths around the $|2p\rangle \rightarrow |3s\rangle$ transition wavelength. a) is blue-detuned, b) close to, and c) red-detuned to the transition wavelength.

Figure 6.1 demonstrates the characteristic state resolution of this tweezer potential, analogous to Figure 5.6, for a tunable wavelength of the trap. However, beyond this deterministic preparation control, the close spectral proximity of the trapping light to the $|2^2p_{3/2}\rangle \rightarrow |3^2s_{1/2}\rangle$ transition allows to tune AC-Stark shifts, especially of the $|2^2p_{3/2}\rangle$ state.

This would, for example, allow for a significant shift of the D_2-imaging transition of the trapped atoms to a point where other atoms, which are not illuminated with the near resonant light, remain practically unaffected by the imaging light [114]. With this tool, one could, for example, perform local readouts in an optical tweezer array formed from 1064 nm light. A 'spotlight' beam near this 813 nm transition would illuminate one well and locally strongly shift the D_2 transition to allow global imaging of the system while only reading out one tweezer site. For ongoing dynamics between the optical tweezer sites, this corresponds to a partial measurement of the quantum system, which, if performed consecutively, can steer the quantum state. Due to the reminiscence of the protocol to the classic puzzle video game, we nicknamed this concept internally the *quantum minesweeper*.

In addition to this application, these traps and, in general, this AC Stark shift engineering could be used to provide register traps into which a system could be fully loaded to protect it from readout [46]. One possible use case would be quantum state tomography of a quantum system of atoms in an optical tweezer in a single realization instead of requiring a scan of many realizations of the system. An optical tweezer of trapping light near the $|2^2p_{3/2}\rangle \rightarrow |3^2s_{1/2}\rangle$ transition could be used to prepare the system as depicted in Figure 6.1, but spilling would be performed level-wise. The atoms that are removed from the trap are recaptured in a reservoir trap in which they are imaged. The AC Stark shift of the trapped atoms would protect them from the imaging process. In that way, the state occupation of the quantum system in the tweezer could be probed consecutively in a single realization of the system.

Beyond these ideas, it should also be possible to use this light to engineer potential landscapes which can be tuned repulsie or attractive for the $|2^2p_{3/2}\rangle$ state [115] or to experiment with enhanced dipole trap loading techniques [116].

The constructed tweezer module serves as a first starting point for these approaches, as we lack laser power for more involved systems (see Figure 4.7), however, the laser source is soon to be upgraded with a Toptica Eagleyard TA boosting the available optical power budget up to 2 W. Additionally, Finn Lubenau, a Master student at HQA-ONE (see Table 1.1), is currently developing an SLM module as an upgrade to the tweezer modules for light of this wavelength. Combined, these upgrades will pave the way towards experiments utilizing these transparency beams.

6.2.2 Fluorescence imaging

Another important scientific tool for experiments with the apparatus is to directly image the atoms via fluorescence imaging techniques as described in [85]. The laser systems for these imaging protocols are already constructed (see Figure 4.4). However, for achieving spin-resolved images of the samples, we will follow a slightly altered protocol compared to other realizations in our group [107]. While existing implementations in our group rely on imaging the two states in short succession after one another while storing the second spin component in an essentially non-interacting state, this module aims to image both spin states at the same time on different regions of the camera chip. This approach omits the reconstruction of behavior between the two images and allows camera selection from a broader catalogue of scientific cameras that are intrinsically not capable of taking several images in fast succession, as is necessary for the former approach, but allow other advantages like single photon counting.

This protocol was developed by Tobias Hammel and will be covered in detail in his dissertation and a paper, which is currently under preparation. Initial tests of the approach were conducted as part of [21].

In short, the fundamental idea of the protocol is to start with the system prepared in a $|1\rangle|3\rangle$ mixture between which the interaction is set via the Feshbach resonance. A MW transition flips $|1\rangle \rightarrow |6\rangle$, to a $|3\rangle|6\rangle$ mixture, which will be imaged via the closed $|3\rangle \rightarrow |1'\rangle$ and $|6\rangle \rightarrow |10'\rangle$ transitions, leading to fluorescence in orthogonal polarizations. This fluorescence light, respectively in the σ_+ and σ_- polarization, is captured by the high-NA objective of the apparatus. The $\lambda/4$ waveplate near the rear aperture of the objective flips circular polarized light into perpendicular linear polarized light, which can be split

with a PBS on the camera module and imaged on different parts of the chip. At the time this thesis is being written, a first demonstration of this protocol has been successfully performed. A snippet of the corresponding image can be found along with the optical setup sketch of the module in Appendix D.

6.2.3 Optical accordion

Taking this fluorescence imaging further to resolve individual atoms with the flashing technique, as in [85], requires an additional 2D-confinement to keep the atoms in the focal plane of the objective during imaging. While the other experiments in our group realize this confinement with a single layer of a standing wave ODT[2] [51], we developed an optical accordion PoC module for this purpose. The module operating with blue detuned ODT light at 532 nm is tested to allow lattice spacings tunable between 23 µm and 1.1 µm [24]. The optical accordion generation is based on beam splitting on a tilted NPBS, analogous to the approach presented in [117], generating two parallel beams which are subsequently focused with a lens, which is on this module a Mitutoyo long working distance objective[3] to allow for small large crossing angles and as a result small lattice spacings generated from small beam seperations on the rear aperture of the focusing objective.

More details about the development and realization of this module can be found in the respective theses from HQA-ONE that covered the topic. Initial testing of the accordion generation principle with an NPBS is discussed in [19], mechanical design and construction of the module is covered in [20], and final assembly and testing is described in [24].

In addition to enabling atom-resolved imaging capabilities, the optical accordion's tunable geometry and dimensionality will also allow the implementation of the spilling technique discussed in Chapter 5 in 2D [107]. The controllable geometry can thereby help to foster a deeper understanding of the mechanisms involved in the 2D spilling technique.

6.2.4 Digital micromirror device

Lastly, a DMD mPoC module, based on developments in [118] and constructed as a module in [22], will allow the implementation of a *Vialux* DMD[4] controlling blue detuned ODT light at a wavelength of 532 nm including grayscaling capabilities. This module can be used to combine optical tweezer potentials with larger, arbitrary potentials, like boxes or curvature compensation traps, further broadening the toolbox and possibilities for configurations of HQA-ONE. Further reading on the development and initial testing of the module, especially for box trap potentials of varying size, is covered by [22].

[2] Formed by two beams crossed under a shallow angle.
[3] Mitutoyo G Plan Apo 20x (t3,5)
[4] Vialux V-9501 with a DLP9500 chipset

Appendix

A Symbols in schematic sketches

This chapter provides the legend for the different schematic sketches of optical setups and cooling water circuits throughout this thesis. The symbols for the drawings of the laser setups are adapted from [119].

A.1 Optical setups

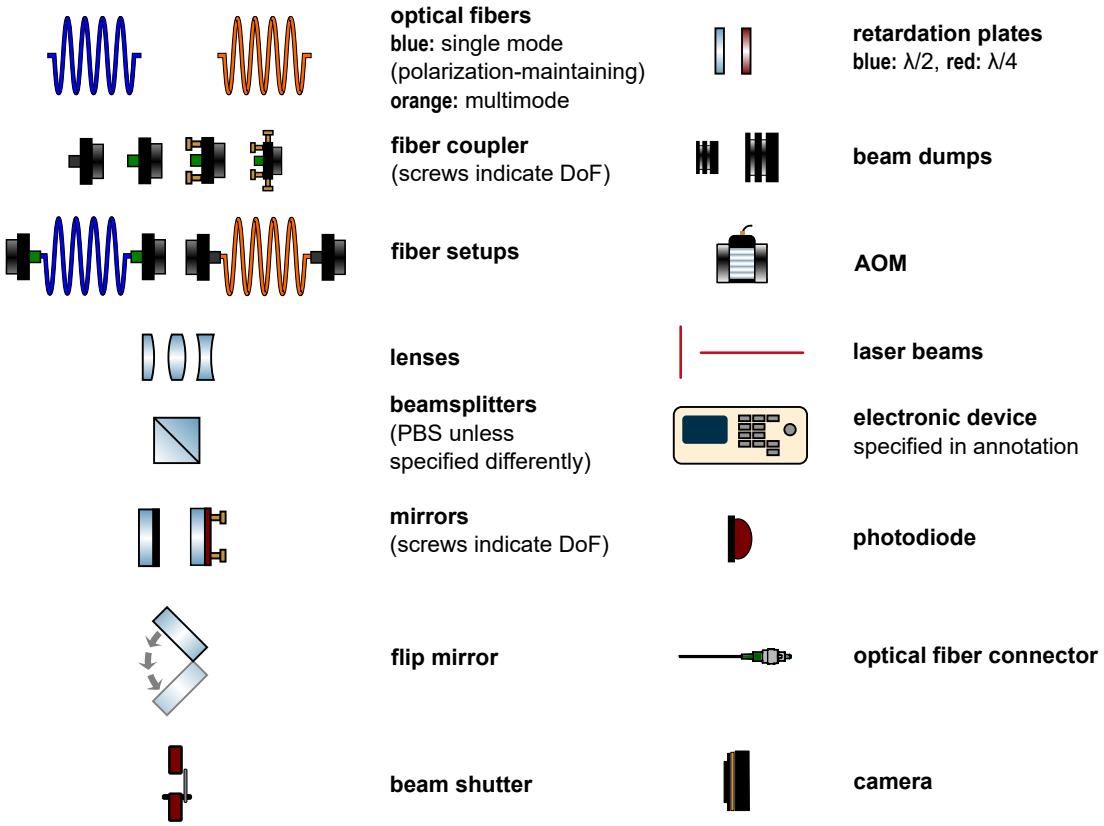

Figure A.1: Legend for the sketches of optical setups in this thesis. Symbols adapted with modifications and extension from [119].

A.2 Cooling water circuits

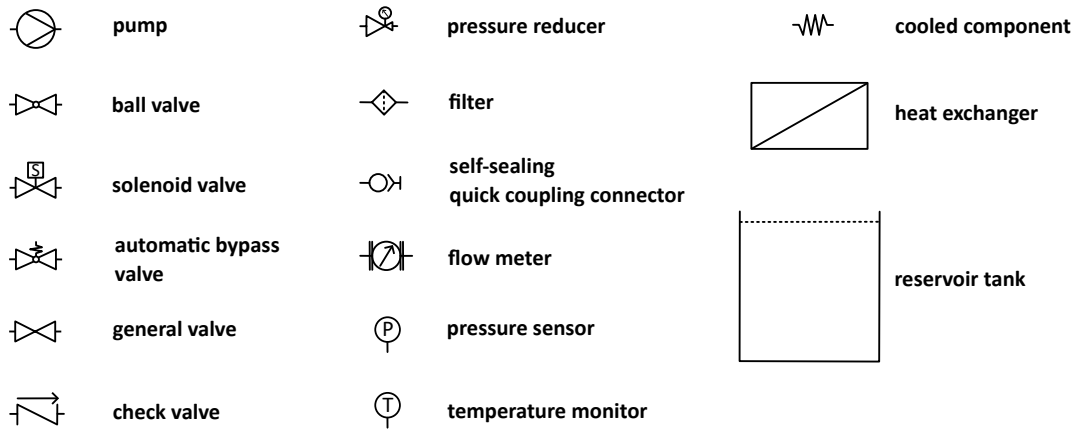

Figure A.2: Legend for the sketches of water circuits in this thesis. The symbols are based on the common standards for ISO technical drawings of piping.

B Further simulations

B.1 Dichroic mirrors in high-NA distribution

The Zemax simulations in Section 3.7 for the high-NA distribution path did not include the dichroic mirrors. However, they are place between the telescope assembly and the module lenses, where the largest wavefront errors occur (see Figure 3.29) before being corrected with module lenses (see Figure 3.31). Therefore it should be tested in a simulation if this intermediate transmission through the dichroic mirrors leads to significant abberrations on the mPoC ports.

The simulation focuses on the 1064 nm port, as it yielded the largest intermediate wavefront error in Figure 3.29 and can be considered the most sensitive port, due to it being used for optical tweezer applications. In the simulation, two 3 mm thick, perfectly flat fused silica plates were placed with a 45° angle in the beam path between module lens and telescope to mimic transmission through the dichroic mirrors (compare Figure 3.31). The wavefront error in the atom plane is simulated for the setup with and without the glass plates. The resulting field dependent wavefront error across the FOV is plotted in Figure B.1.

One observes that the effect of the glass plates is negligible in the simulated scenario.

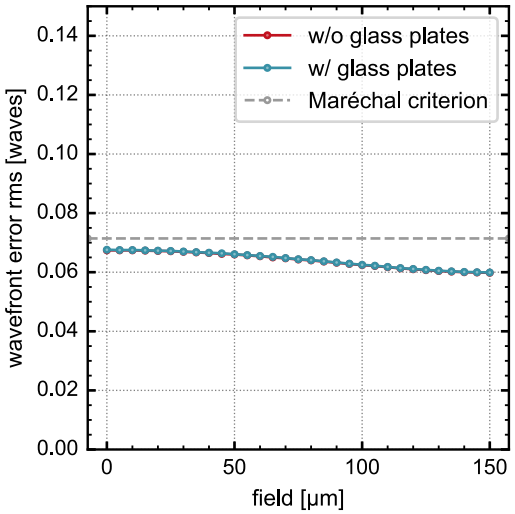

Figure B.1: Zemax simulation of the influence of placing two 3 mm thick, 45° tilted fused silica glass plates between the telescope assembly and the module lens in Figure 3.31 to simulate the influence of the transmission through the dichroic mirrors for the 1064 nm port. The setup is simulated and plotted for the scenario with and without the glass plates.

Technical realization at HQA-One

C

This chapter provides an annotated photo-based overview over the technical realizations at HQA-ONE, that have been described and presented, for visibility reasons, as schematic sketches or drawings before. In this chapter, annotated photos depict the actual physical realizations of the described concepts and selected systems. Therefore, this chapter basically provides a mini-labtour through HQA-ONE.

C.1 HQA-based realizations

The first section presents parts of HQA-ONE that are realizations of the general concept of HQA as discussed in Chapter 3.

Frame of reference (FOR)

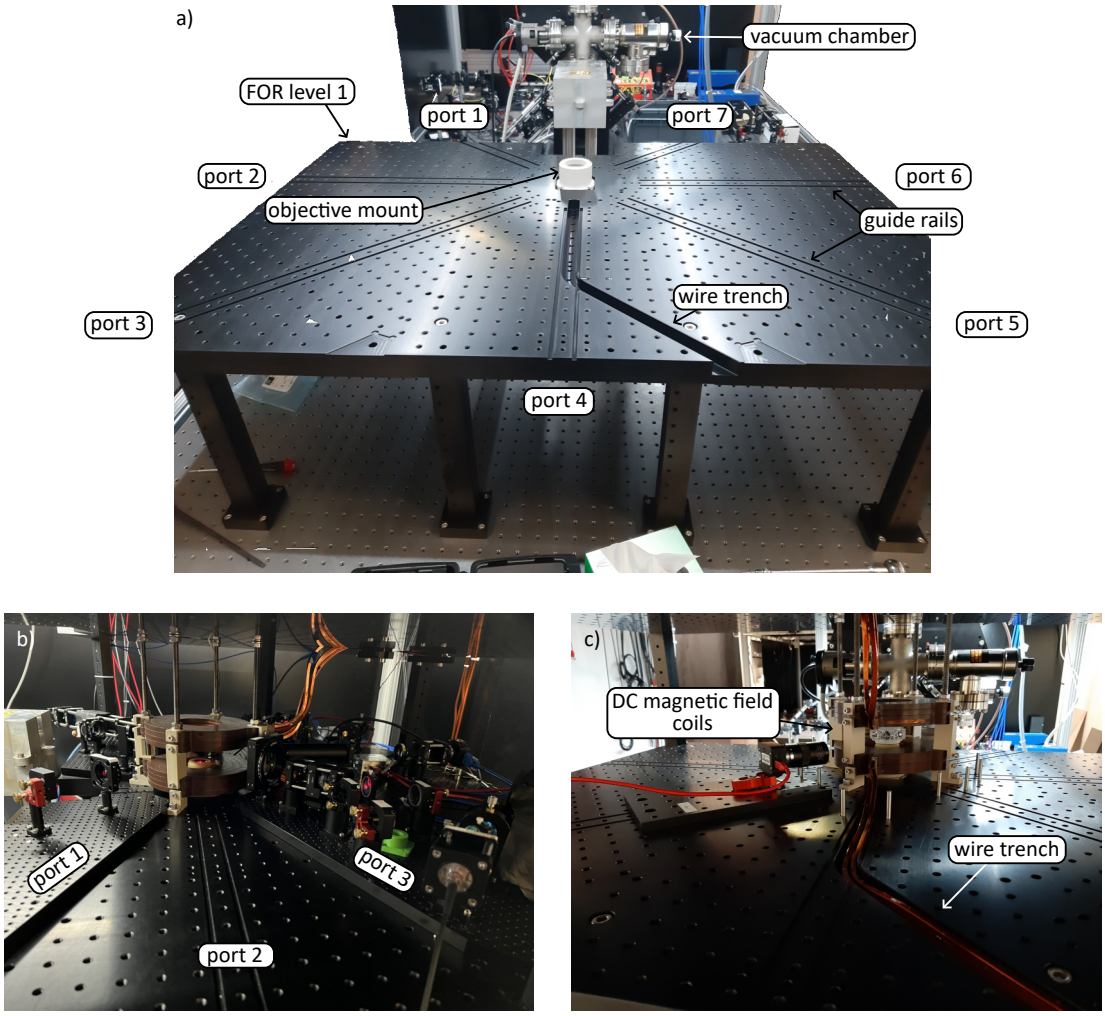

Figure C.1: Photos of the FOR realization at HQA-ONE as discussed in detail in Section 3.3. **a)** shows the FOR during assembly allowing a better view on level 1 of the structure with its core features and symmetry pattern. **b)** depicts modules placed on the FOR all ports with port 2 left empty to display the interfaces for each of the PoC modules. **c)** details the empty FOR during initial assembly and presents how the lead wire of the lower coil stack are placed in the wire trench. The wires of the upper stack are guided analogously in the upper FOR board. The shown camera module was used to triangulate and position the glass cell placement relative to the objective housing by moving the vacuum chamber within the clearance of its mounting on the translation system.

High-NA distribution path

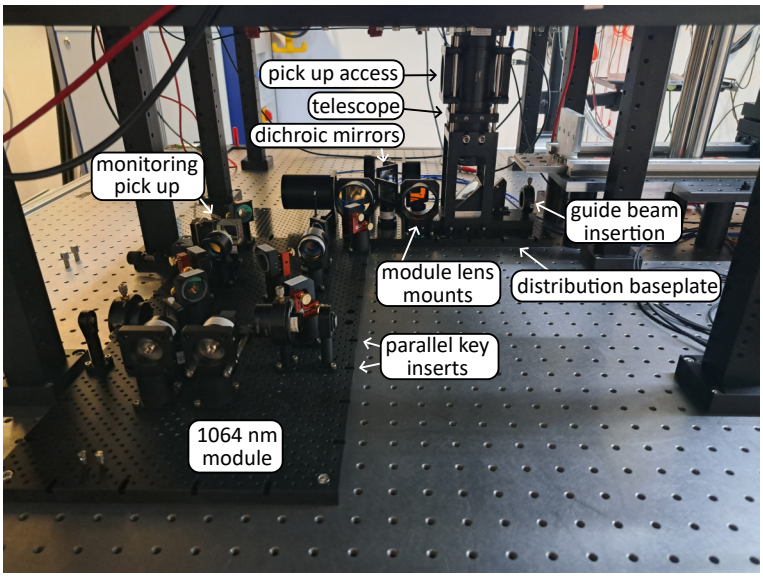

Figure C.2: Annotated photo of the FOR's high-NA distribution path at HQA-ONE as covered in Section 3.7. The installed 1064 nm mPoC module is an early version of the optical tweezer and vODT generating module described in Chapter 5 and Appendix D. Additionally visible on the pedestal of the vacuum chamber mounting is the L-shaped stop for the translation system.

Magnetic field assembly

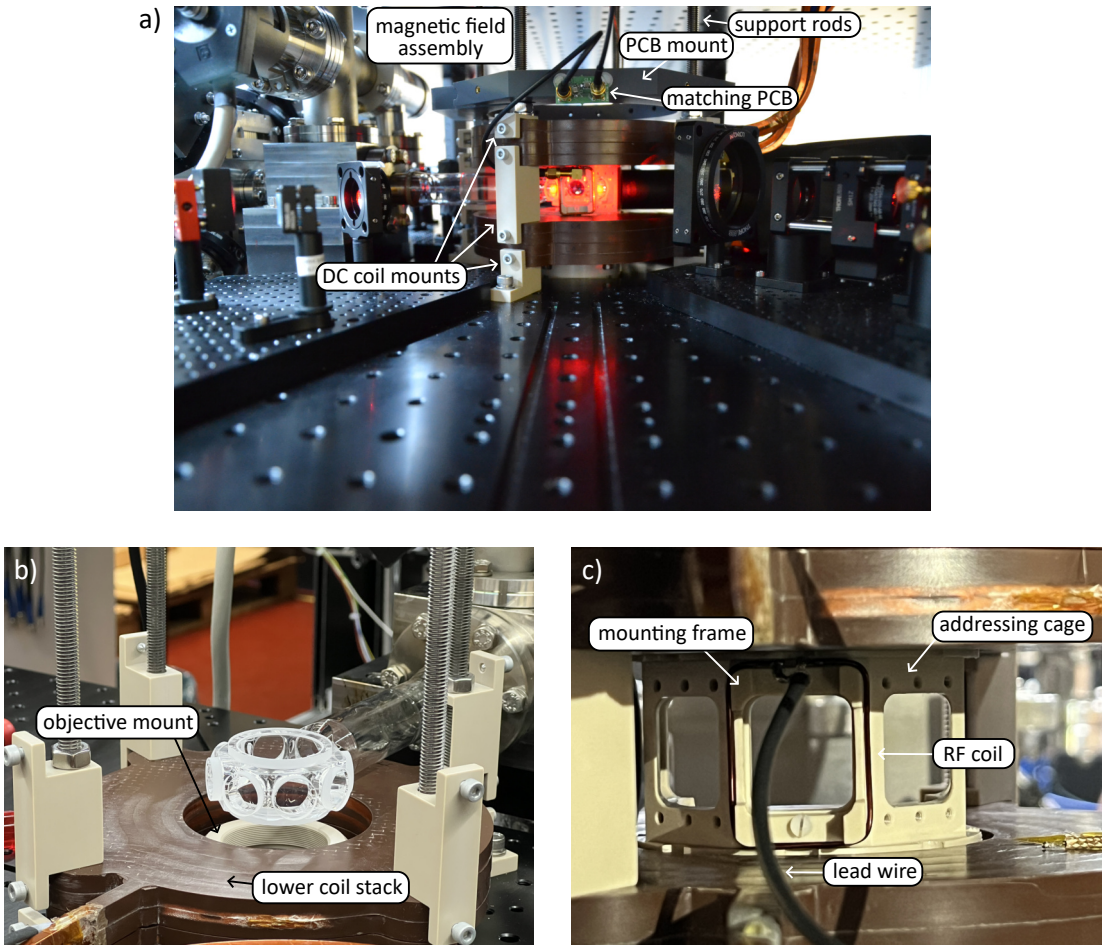

Figure C.3: Annotated photos of the magnetic field assembly used at HQA-ONE previously covered in Section 3.4 and Section 4.3. **a)** shows the full magnetic field assembly as used at HQA-ONE, similar to Figure 3.14, with the large DC magnetic field coils and a RF coil installed. **b)** details the DC coils during initial installation with only the lower stack installed. The glass cell, as well as the objective mount, are visible for reference. The support rods and the screws for translation adjustment of the coil positions are visible. **c)** details the installed addressing cage with a RF coil attached on a mounting frame.

Diagnostics

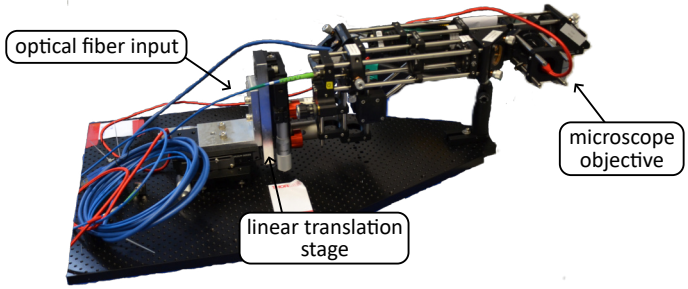

Figure C.4: Example of a diagnostic tool on a PoC module for in-situ diagnostics beyond the tools shown in Section 3.5. The depicted 'crane-like' module can be inserted on the FOR, reaching over the magnetic field assembly into the FOR's central axis to provide a high-NA point source via a microscope objective for diagnostics on the high-NA distribution path and the mPoC modules. A linear translation stage allows moving the focus around the focal plane of HQA-ONE's high-NA objective.

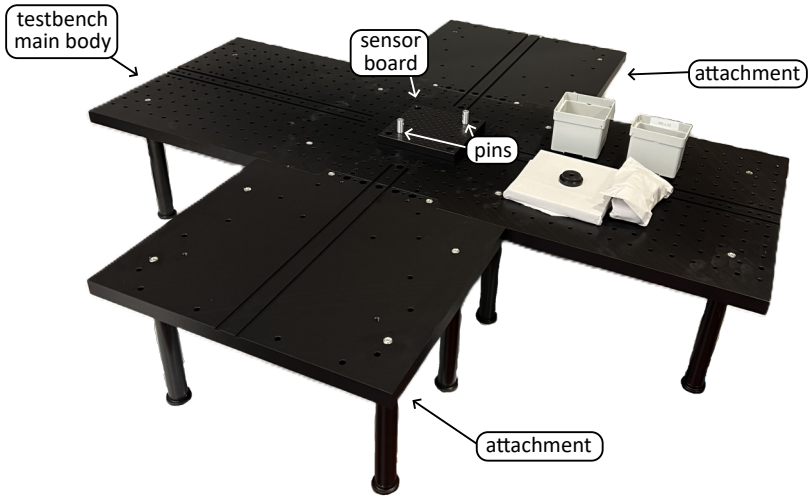

Figure C.5: Annotated photo of the PoC testbench, as shown in Figure 3.21, while being fully assembled with both side attachments to provide the maximum number of ports for simultaneous diagnostics and a blank sensor breadboard board placed with pins on the center position.

C.2 HQA-One specific realizations

The second section presents more specific parts and systems of HQA-ONE: A selection of the realizations of the systems discussed in Chapter 4.

Vacuum chamber

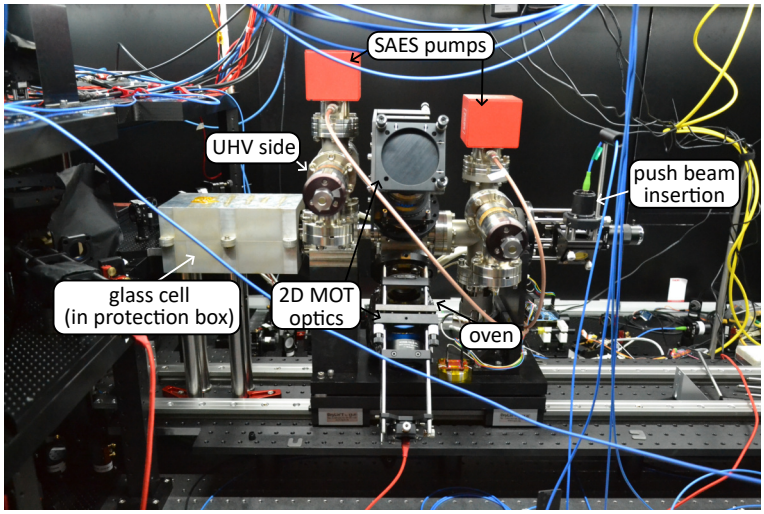

Figure C.6: Annotated photo of HQA-ONE's vacuum chamber as detailed in Section 4.2 and shown schematically in Figure 4.8. The attached glass cell, shown on a photo in Figure 3.4, is within its protection box, into which it is slid while not inserted into the FOR to protect the cell and its nano-structured surfaces from mechanical damage and dust. Notably, we moved the chamber out of the FOR and into the protection box on a daily basis for over a year, when we were not yet able to run the apparatus unsupervised over night. However, we never observed a resulting influence on the experiments performance (e.g. reduced average loading or transfer rates) after reinserting the chamber the next morning.

Thermal management

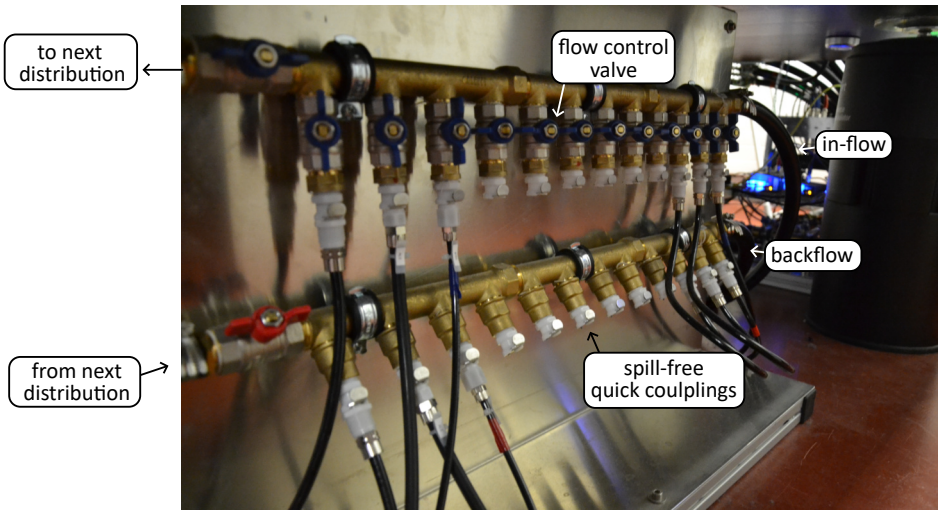

Figure C.7: Annotated photo of the distribution hubs for the cooling water in the secondary circuit 2 for multi purpose water cooling as covered in Section 4.4 and Figure 4.18. The 12 parallel channels on this hub, equipped with quick coupling, are shown on both the in-flow (blue) and the backflow (red) to the system separator.

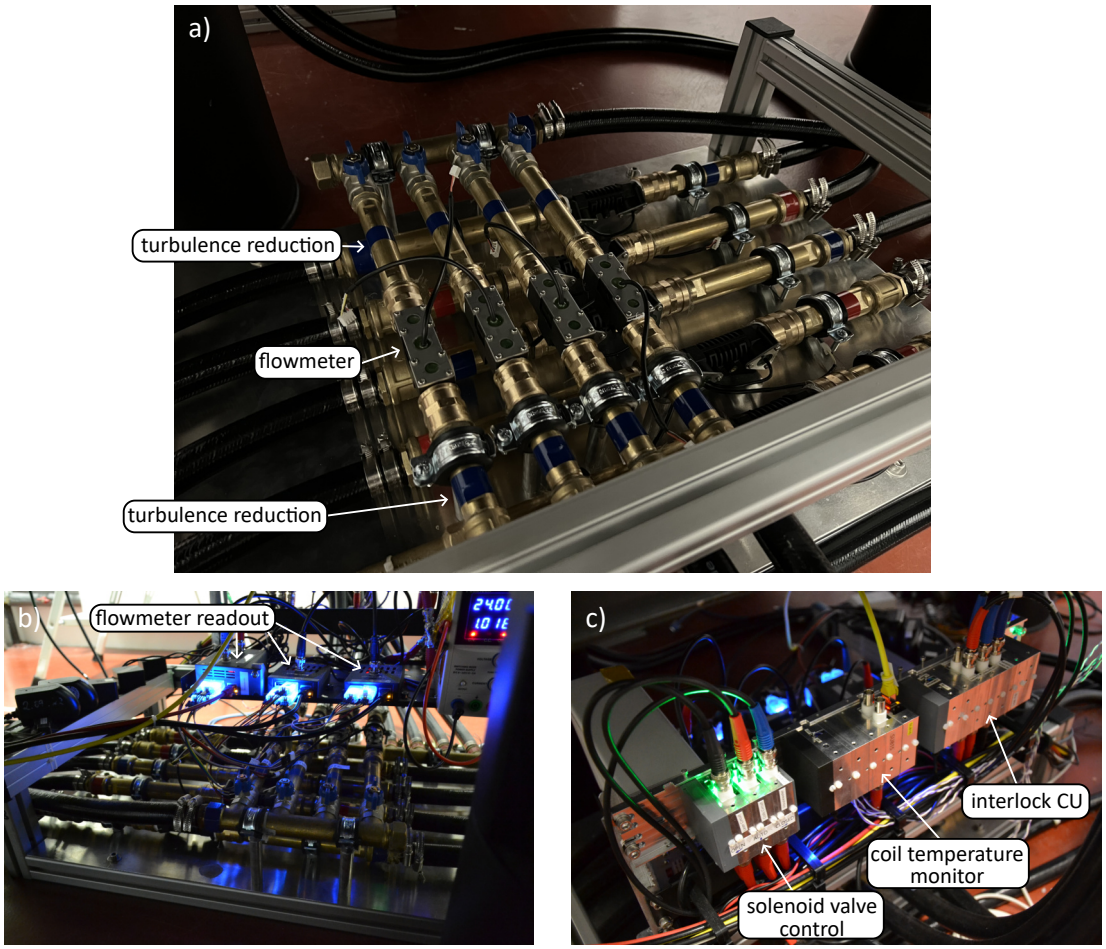

Figure C.8: Annotated photos of the water cooling control hub, which provides the flow measurements for the water circuits as shown in Figure 4.18, as well as housing for the interlock system. **a)** shows the hub during installation with the individual coil in-flow sensors on the top layer and all other flowmeters for in-flow and backflow as shown in Figure 4.18 below. These flowmeters measure the transit time difference of a forward and a backward propagating ultrasonic pulses to infer the average coolant velocity without moving parts or significant pressure drops. However, these sensors are sensitive to turbulence, leading to noise in the measurements. To reduce this noise, straight pipe segments with constant diameter, matching the sensor's inner diameter, are installed before and after the actual flowmeter. **b)** shows the same system with its electronics installed. The flowmeter read-out is performed by Raspberry Pis via UART communication. These report the flow status to the interlock CU and write the sensor readings to SmartLab. **c)** depicts the interlock electronics for the water cooling as presented in Section 4.5.

SmartLab monitoring

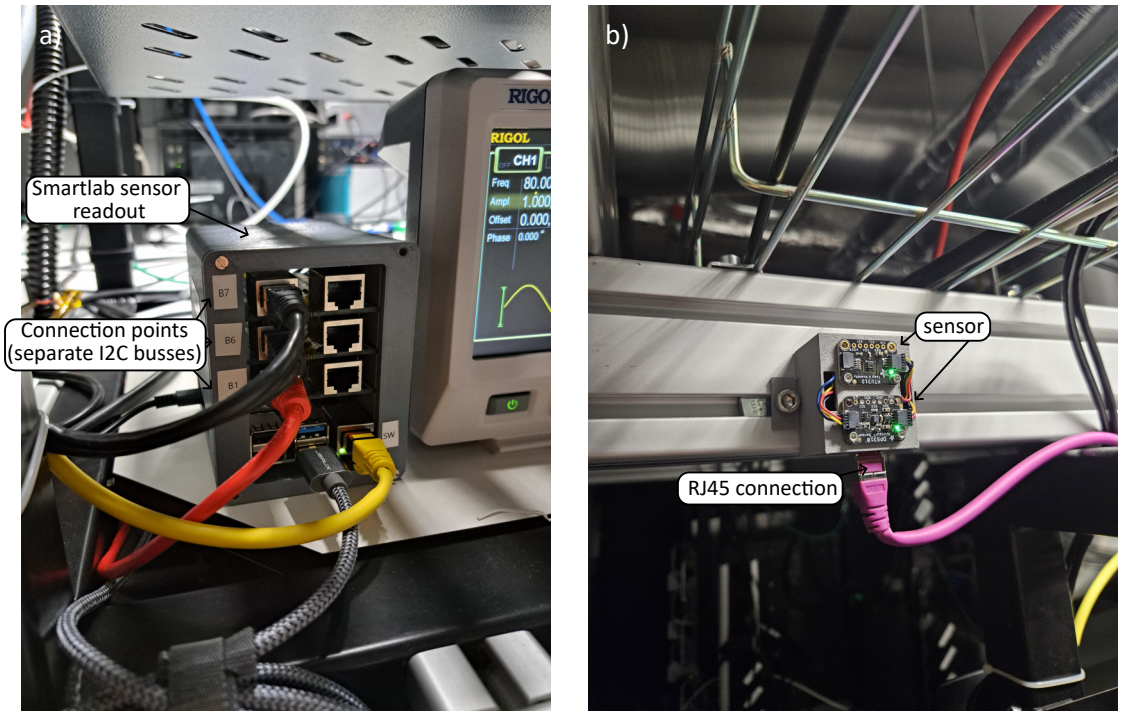

Figure C.9: Annotated photos of the custom SmartLab electronics that are used to track non-critical laboratory environmental data. **a)** shows the readout electronics, which is provided by a Raspberry Pi with attached custom PCB boards enabling a total of three I2C busses for digital communication with the sensors that can be connected in series. RJ45 connectors and Ethernet cables are used for transmission to bundle the low current power supply, ground potential, and the three I2C connections for the sensors in a single readily available cable. **b)** shows one example of a sensor box connected with the readout electronics. The depicted box provides sensors for temperature, humidity, and air pressure.

D Hidden design of the described modules

This chapter provides an overview over the technical realizations, the hidden design, of the black boxed modules used for the deterministic state preparation in Chapter 5 as presented in Figure 5.1. While the drawings of the internal setups on the modules present an overview, a detailed description of development, construction and optimization is deferred to the dissertation of Tobias Hammel.

D.1 Modules: Deterministic state preparation

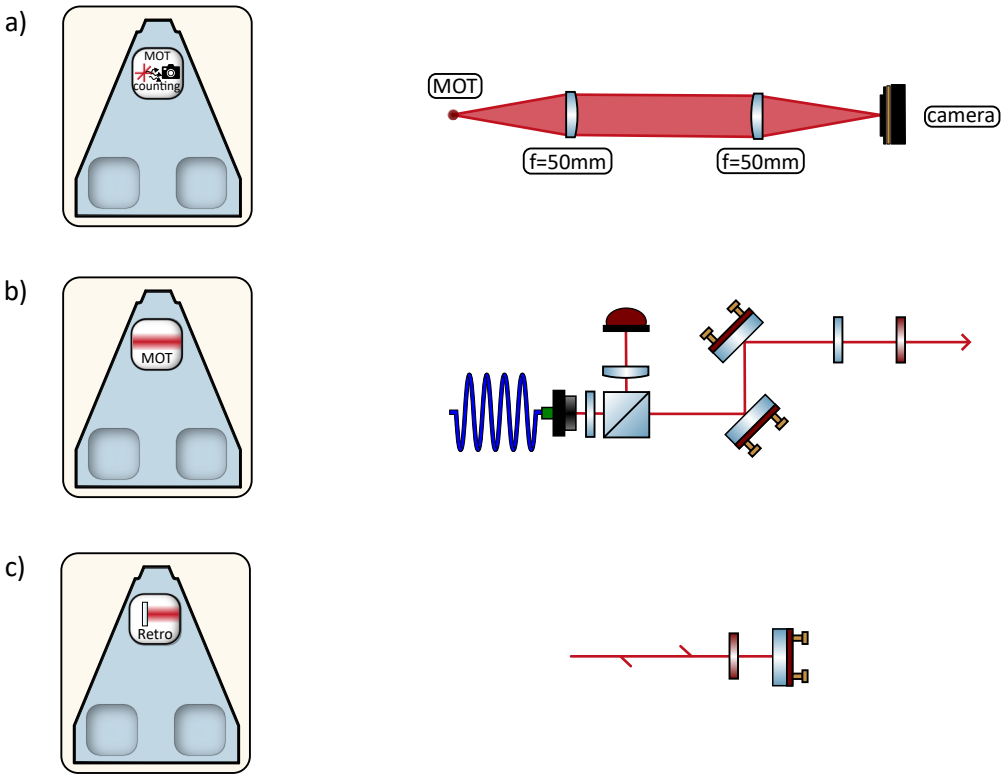

Figure D.1: Sketch of the on-module realizations of different functionalities used in Chapter 5. **a)** MOT counting module, **b)** MOT arm with power stabilization, and **c)** MOT retro-reflection.

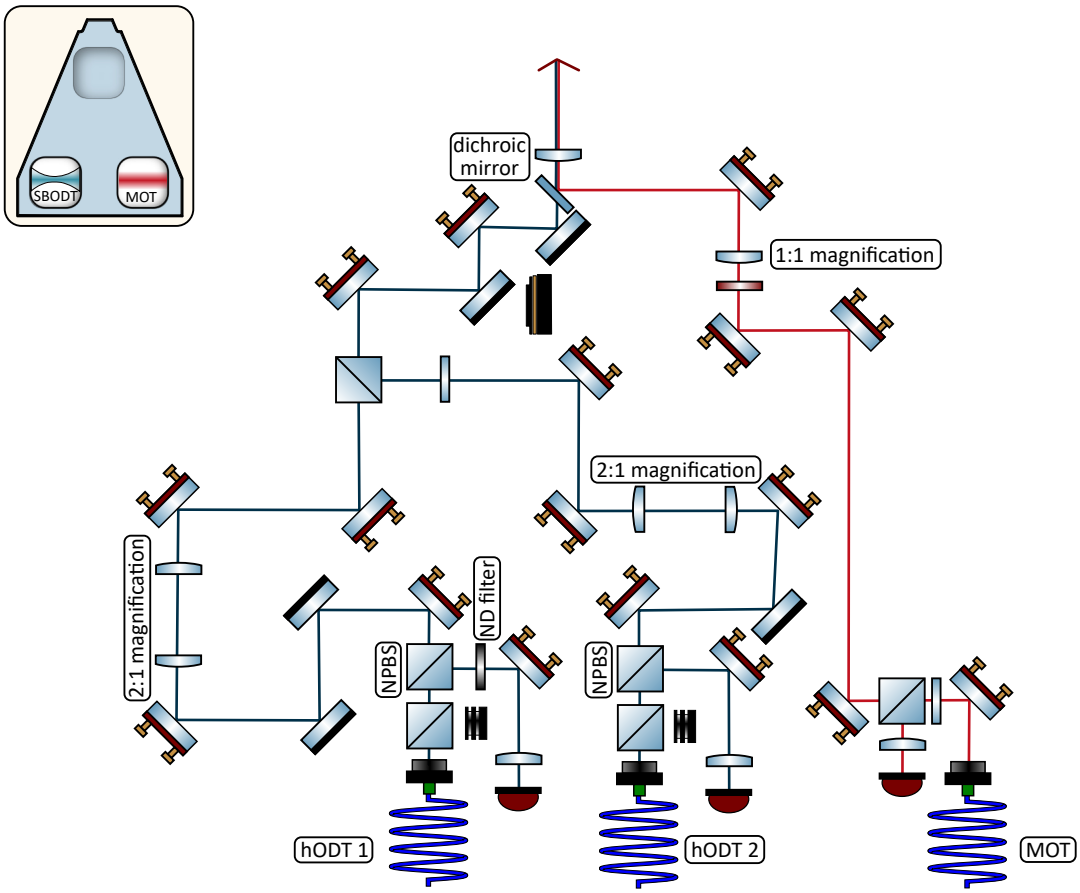

Figure D.2: Sketch of the on-module realization of the PoC providing a collimated MOT arm with stabilization photodiode, as well as the focused hODT, which is fed from two optical fibers to increase the available power.

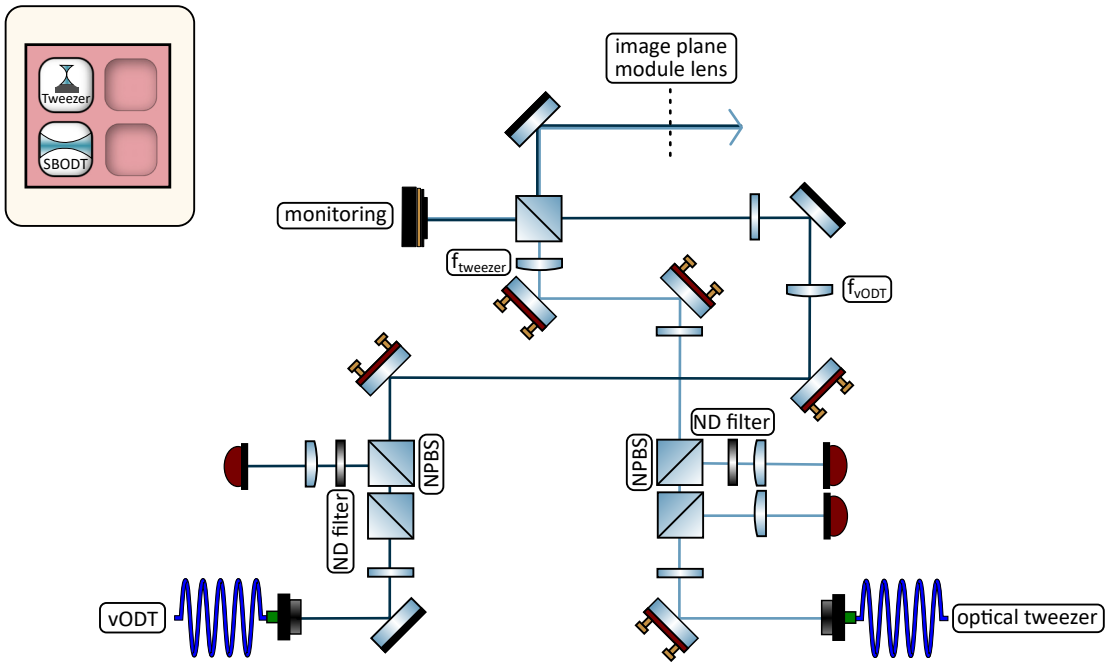

Figure D.3: Sketch of the on-module realization of the mPoC module, that provides the optical tweezer and the vODT. Both are power stabilized with a photodiode as a feedback in the pick-up sections and focused with a respective lens to the image plane of the module lens. The image in that plane, indicated in the sketch with a dashed line, is projected through the high-NA distribution path onto the atoms. A camera placed at the focus of the beams in a small split-out path is usable for monitoring and adjusting the beams relative to each other.

D.2 Modules: Outlook

While the on-module realizations for the optical accordion [24] and the DMD [22] are covered in detail in the respective theses, the single-shot state resolved fluorescence imaging has not yet been described in a thesis.

Figure D.4 a) show a schematic illustration of the imaging system on the respective module. A module lens creates an image of the atom plane on the respective module (see Section 3.7), which is imaged with a camera objective[1] onto a scientific camera[2]. In between, the path for the different polarizations, as discussed in Chapter 6, is split and recombined with a small angle relative to each other. This angle leads to a displacement of the camera chip for the two images.

Figure D.4 b) shows a first camera image resolving the two different states in a $|3\rangle\,|6\rangle$-mixture cloud in a snippet from the camera control.

More details about this imaging technique and the implementation at HQA-ONE will be covered in a publication which is currently under preparation and in the dissertation of Tobias Hammel.

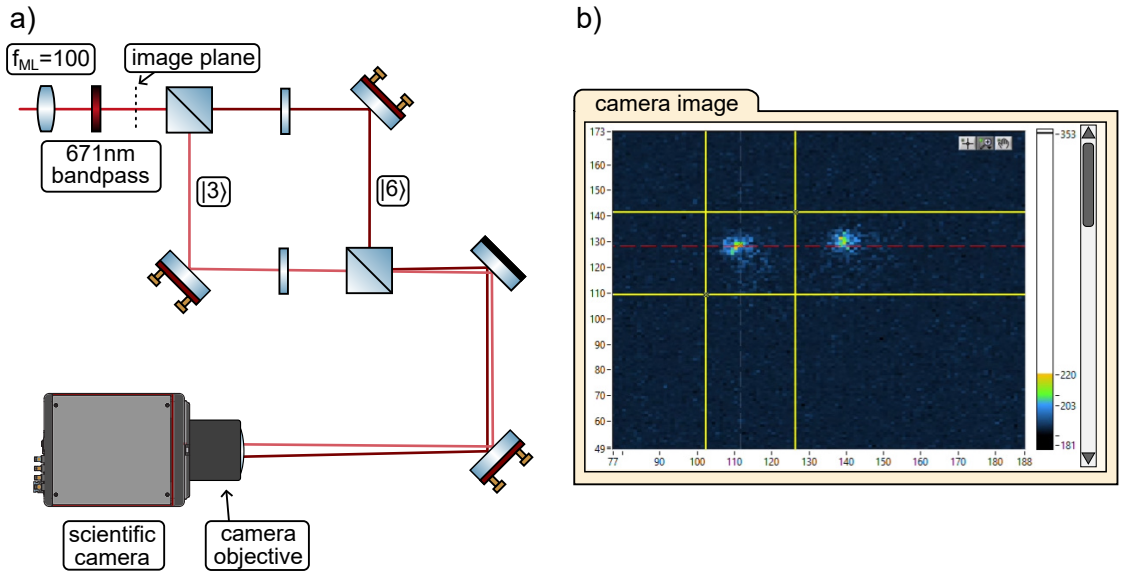

Figure D.4: **a)** schematic sketch of the setup used for state-resolved fluorescence imaging. **b)** first state-resolved image of a cloud in a $|3\rangle\,|6\rangle$-mixture with the presented setup.

[1] Canon Lens EF 50 1:1.8
[2] Hamamatsu Orca Quest II C15550-22UP

Bibliography

1. Baldwin, C. Y. & Clark, K. B. *Design Rules* (The MIT Press, 2000) (↑ 1 sq.).
2. Schilling, M. A. Toward a General Modular Systems Theory and Its Application to Interfirm Product Modularity. *The Academy of Management Review* **25,** 312 (2000) (↑ 1).
3. Baldwin, C. Y. & Clark, K. B. in *Complex Engineered Systems* (eds Braha, D., Minai, A. A. & Bar-Yam, Y.) 175–205 (Springer Berlin Heidelberg, Berlin, Heidelberg, 2006) (↑ 2).
4. Brusoni, S., Henkel, J., Jacobides, M. G., Karim, S., MacCormack, A., Puranam, P. & Schilling, M. The power of modularity today: 20 years of "Design Rules". *Industrial and Corporate Change* **32,** 1–10 (2023) (↑ 2).
5. Langlois, R. N. & Robertson, P. L. Networks and innovation in a modular system: Lessons from the microcomputer and stereo component industries. *Research Policy* **21,** 297–313 (1992) (↑ 2).
6. Baldwin, C. Y. & Clark, K. B. The Architecture of Participation: Does Code Architecture Mitigate Free Riding in the Open Source Development Model? *Management Science* **52,** 1116–1127 (2006) (↑ 2).
7. Baldwin, C., MacCormack, A. & Rusnak, J. Hidden structure: Using network methods to map system architecture. *Research Policy* **43,** 1381–1397 (2014) (↑ 2).
8. Von Hippel, E. & Finkelstein, S. N. Analysis of innovation in automated clinical chemistry analyzers. *Science and Public Policy* **6,** 24–37 (1979) (↑ 2).
9. Baldwin, C. & von Hippel, E. Modeling a Paradigm Shift: From Producer Innovation to User and Open Collaborative Innovation. *Organization Science* **22,** 1399–1417 (2011) (↑ 2).
10. Carlile, P. R. Transferring, Translating, and Transforming: An Integrative Framework for Managing Knowledge Across Boundaries. *Organization Science* **15,** 555–568 (2004) (↑ 2).
11. Fleming, L. Recombinant Uncertainty in Technological Search. *Management Science* **47,** 117–132 (2001) (↑ 2).
12. Arrieta, J. P., Fontana, R. & Brusoni, S. On the strategic use of product modularity for market entry. *Industrial and Corporate Change* **32,** 155–180 (2023) (↑ 2).
13. Tobias Hammel. *Design and Construction of a New Experiment for Programmable Quantum Simulation using Ultracold 6Li Fermions* Master Thesis (Heidelberg University, Heidelberg, 2021) (↑ 4, 17 sqq., 21, 36, 92 sqq., 98, 102, 104).
14. Leo Walz. *Modulation Transfer Spectroscopy in Atomic Lithium-6* Bachelor Thesis (Heidelberg University, Heidelberg, 2021) (↑ 4, 85).
15. Malaika Göritz. *Characterisation of a 2D-MOT for cooling 6Li* Bachelor Thesis (Heidelberg University, Heidelberg, 2022) (↑ 4, 92).
16. Marlene Matzke. *Design of a Compact Double Pass AOM Module* Bachelor Thesis (Heidelberg University, Heidelberg, 2022) (↑ 4, 85).
17. Micha Bunjes. *High-Resolution Optics for Modular Quantum Simulation* Master Thesis (Heidelberg University, Heidelberg, 2022) (↑ 4, 56 sq., 62, 66).
18. Hüseyin Yildiz. *Entwicklung von RF-Resonatoren für Spinmanipulationen in ultrakalten Quantengasen* Bachelor Thesis (Heidelberg University, Heidelberg, 2022) (↑ 4, 37, 105).
19. Vivienne Leidel. *From Cooling Atoms Towards a Two Dimensional Fermi Gas* Master Thesis (Heidelberg University, Heidelberg, 2023) (↑ 4, 84 sq., 131).
20. Jan Jonathan Ricken. *Design and Construction of a Modular Optical Accordion* Bachelor Thesis (Heidelberg University, Heidelberg, 2023) (↑ 4, 131).
21. Marta Pastori. *An optical setup for spin-sensitive imaging of ultracold atoms* Bachelor Thesis (Universita Degli Studi di Milano, Milan, 2023) (↑ 4, 130).
22. Juan Carlos Provencio Lameiras. *Design and characterization of a miniturized Digital Micromirror Device imaging setup* Bachelor Thesis (Heidelberg University, Heidelberg, 2024) (↑ 4, 131, 152).
23. Sofia Anna Regina Barth. *Realization of a Digital Laser Lock for the Imaging of Ultracold Lithium* Bachelor Thesis (Heidelberg University, Heidelberg, 2024) (↑ 4, 86).

24. Johanna Schulz. *Modular tools for deterministic preparation and manipulation of ultracold atoms in 2D* Master Thesis (Heidelberg University, Heidelberg, 2024) (↑ 4, 105, 131, 152).

25. Suraj Ramesh Iyer. *Magnetic Field Switching and Stabilization Techniques for the Heidelberg Quantum Architecture Experiment* Master Thesis (Karlsruher Institut für Technologie, Karlsruhe, 2024) (↑ 4, 104 sq.).

26. Pan, J.-W. Quantum technologies need big investments to deliver on their big promises. *Nature* **638,** 862 (2025) (↑ 7).

27. Dowling, J. P. & Milburn, G. J. *Quantum Technology: The Second Quantum Revolution* 2002. arXiv.quant-ph/0206091 (↑ 7).

28. Celi, A., Sanpera, A., Ahufinger, V. & Lewenstein, M. Quantum optics and frontiers of physics: the third quantum revolution. *Physica Scripta* **92,** 013003 (2017) (↑ 7).

29. European Quantum Industry Consortium. *QuIC Position Paper on the Quantum Europe Strategy* 2025. https://www.euroquic.org/quic-position-paper-on-the-quantum-europe-strategy/%20(13.09.2025) (↑ 7).

30. European Comission. *Quantum Europe Strategy: Quantum Europe in a Changing World: COM(2025) 363* 2025. https://qt.eu/publications (↑ 7).

31. Degen, C. L., Reinhard, F. & Cappellaro, P. Quantum sensing. *Reviews of Modern Physics* **89** (2017) (↑ 7).

32. Bongs, K., Bennett, S. & Lohmann, A. Quantum sensors will start a revolution - if we deploy them right. *Nature* **617,** 672–675 (2023) (↑ 7).

33. Bothwell, T., Kennedy, C. J., Aeppli, A., Kedar, D., Robinson, J. M., Oelker, E., Staron, A. & Ye, J. Resolving the gravitational redshift across a millimetre-scale atomic sample. *Nature* **602,** 420–424 (2022) (↑ 7).

34. Liao, S.-K., Cai, W.-Q., Liu, W.-Y., Zhang, L., Li, Y., Ren, J.-G., Yin, J., Shen, Q., Cao, Y., Li, Z.-P., Li, F.-Z., Chen, X.-W., Sun, L.-H., Jia, J.-J., Wu, J.-C., Jiang, X.-J., Wang, J.-F., Huang, Y.-M., Wang, Q., Zhou, Y.-L., Deng, L., Xi, T., Ma, L., Hu, T., Zhang, Q., Chen, Y.-A., Liu, N.-L., Wang, X.-B., Zhu, Z.-C., Lu, C.-Y., Shu, R., Peng, C.-Z., Wang, J.-Y. & Pan, J.-W. Satellite-to-ground quantum key distribution. *Nature* **549,** 43–47 (2017) (↑ 7).

35. De Forges Parny, L., Alibart, O., Debaud, J., Gressani, S., Lagarrigue, A., Martin, A., Metrat, A., Schiavon, M., Troisi, T., Diamanti, E., Gélard, P., Kerstel, E., Tanzilli, S. & van den Bossche, M. Satellite-based quantum information networks: use cases, architecture, and roadmap. *Communications Physics* **6** (2023) (↑ 7).

36. Li, Y., Cai, W.-Q., Ren, J.-G., Wang, C.-Z., Yang, M., Zhang, L., Wu, H.-Y., Chang, L., Wu, J.-C., Jin, B., Xue, H.-J., Li, X.-J., Liu, H., Yu, G.-W., Tao, X.-Y., Chen, T., Liu, C.-F., Luo, W.-B., Zhou, J., Yong, H.-L., Li, Y.-H., Li, F.-Z., Jiang, C., Chen, H.-Z., Wu, C., Tong, X.-H., Xie, S.-J., Zhou, F., Liu, W.-Y., Ismail, Y., Petruccione, F., Liu, N.-L., Li, L., Xu, F., Cao, Y., Yin, J., Shu, R., Wang, X.-B., Zhang, Q., Wang, J.-Y., Liao, S.-K., Peng, C.-Z. & Pan, J.-W. Microsatellite-based real-time quantum key distribution. *Nature* **640,** 47–54 (2025) (↑ 7).

37. Castelvecchi, D. IBM quantum computer passes calculation milestone. *Nature* **618,** 656–657 (2023) (↑ 7).

38. Brooks, M. Quantum computers: what are they good for? *Nature* **617,** S1–S3 (2023) (↑ 7).

39. Feynman, R. P. Simulating physics with computers. *International Journal of Theoretical Physics* **21,** 467–488 (1982) (↑ 8).

40. Morsch, O., Palma, G. M. & Rossini, D. *Quantum simulations of complex systems* 2025 (↑ 8).

41. Daley, A. J., Bloch, I., Kokail, C., Flannigan, S., Pearson, N., Troyer, M. & Zoller, P. Practical quantum advantage in quantum simulation. *Nature* **607,** 667–676 (2022) (↑ 8).

42. Georgescu, I. M., Ashhab, S. & Nori, F. Quantum Simulation. arXiv.1308.6253 (2013) (↑ 8).

43. Altman, E., Brown, K. R., Carleo, G., Carr, L. D., Demler, E., Chin, C., DeMarco, B., Economou, S. E., Eriksson, M. A., Fu, K.-M. C., Greiner, M., Hazzard, K. R., Hulet, R. G., Kollár, A. J., Lev, B. L., Lukin, M. D., Ma, R., Mi, X., Misra, S., Monroe, C., Murch, K., Nazario, Z., Ni, K.-K., Potter, A. C., Roushan, P., Saffman, M., Schleier-Smith, M., Siddiqi, I., Simmonds, R., Singh, M., Spielman, I. B., Temme, K., Weiss, D. S., Vučković, J., Vuletić, V., Ye, J. & Zwierlein, M. Quantum Simulators: Architectures and Opportunities. *PRX Quantum* **2** (2021) (↑ 8).

44. Fraxanet, J., Salamon, T. & Lewenstein, M. The Coming Decades of Quantum Simulation. arXiv.2204.08905 (2022) (↑ 8).

45. Castelvecchi, D. Underdog technologies gain ground in quantum-computing race. *Nature* **614,** 400–401 (2023) (↑ 8).

46. Chiu, N.-C., Trapp, E. C., Guo, J., Abobeih, M. H., Stewart, L. M., Hollerith, S., Stroganov, P., Kalinowski, M., Geim, A. A., Evered, S. J., Li, S. H., Peters, L. M., Bluvstein, D., Wang, T. T., Greiner, M., Vuletić, V. & Lukin, M. D. *Continuous operation of a coherent 3,000-qubit system* 2025. arXiv.2506.20660 (↑ 8 sq., 130).

47. Lin, R., Zhong, H.-S., Li, Y., Zhao, Z.-R., Zheng, L.-T., Hu, T.-R., Wu, H.-M., Wu, Z., Ma, W.-J., Gao, Y., Zhu, Y.-K., Su, Z.-F., Ouyang, W.-L., Zhang, Y.-C., Rui, J., Chen, M.-C., Lu, C.-Y. & Pan, J.-W. AI-Enabled Parallel Assembly of Thousands of Defect-Free Neutral Atom Arrays. *Physical review letters* **135,** 060602 (2025) (↑ 8 sq.).

48. Ott, R., González-Cuadra, D., Zache, T. V., Zoller, P., Kaufman, A. M. & Pichler, H. Error-Corrected Fermionic Quantum Processors with Neutral Atoms. *Physical review letters* **135** (2025) (↑ 8).

49. Bloch, I., Dalibard, J. & Nascimbène, S. Quantum simulations with ultracold quantum gases. *Nature Physics* **8,** 267–276 (2012) (↑ 8).

50. Adams, A., Carr, L. D., Schäfer, T., Steinberg, P. & Thomas, J. E. Strongly correlated quantum fluids: ultracold quantum gases, quantum chromodynamic plasmas and holographic duality. *New Journal of Physics* **14,** 115009 (2012) (↑ 8).

51. Holten, M., Bayha, L., Subramanian, K., Brandstetter, S., Heintze, C., Lunt, P., Preiss, P. M. & Jochim, S. Observation of Cooper pairs in a mesoscopic two-dimensional Fermi gas. *Nature* **606,** 287–291 (2022) (↑ 8, 114, 131).

52. Zwierlein, M. W., Abo-Shaeer, J. R., Schirotzek, A., Schunck, C. H. & Ketterle, W. Vortices and superfluidity in a strongly interacting Fermi gas. *Nature* **435,** 1047–1051 (2005) (↑ 8).

53. Steinhauer, J. Observation of quantum Hawking radiation and its entanglement in an analogue black hole. *Nature Physics* **12,** 959–965 (2016) (↑ 8).

54. Viermann, C., Sparn, M., Liebster, N., Hans, M., Kath, E., Parra-López, Á., Tolosa-Simeón, M., Sánchez-Kuntz, N., Haas, T., Strobel, H., Floerchinger, S. & Oberthaler, M. K. Quantum field simulator for dynamics in curved spacetime. *Nature* **611,** 260–264 (2022) (↑ 8).

55. Gross, C. & Bloch, I. Quantum simulations with ultracold atoms in optical lattices. *Science* **357,** 995–1001 (2017) (↑ 9).

56. Grimm, R., Weidemüller, M. & Ovchinnikov, Y. B. Optical dipole traps for neutral atoms. arXiv.physics/9902072 (1999) (↑ 9, 88).

58. QuEra Computing Inc. *A standardized modular quantum gas platform: LinkedIn Post* (ed LinkedIn) 2025. https://www.linkedin.com/posts/quera-computing-inc_a-modular-quantum-gas-platform-activity-7301209742612254720-ZA0h%20(13.09.2025) (↑ 11).

59. Andrea Bergschneider. *Strong correlations in few-fermion systems* Dissertation (Heidelberg University, Heidelberg, 2017) (↑ 12, 87).

60. Lorenz, N. *A Rydberg tweezer platform with potassium atoms* PhD thesis (Ludwig-Maximilians-Universität München, 2021) (↑ 16, 46).

61. Jin, S., Gao, J., Chandrashekara, K., Gölzhäuser, C., Schöner, J. & Chomaz, L. Two-dimensional magneto-optical trap of dysprosium atoms as a compact source for efficient loading of a narrow-line three-dimensional magneto-optical trap. *Physical Review A* **108** (2023) (↑ 17).

62. Klostermann, T., Cabrera, C. R., Raven, H. v., Wienand, J. F., Schweizer, C., Bloch, I. & Aidelsburger, M. Fast long-distance transport of cold cesium atoms. *Physical Review A* **105.** http://arxiv.org/pdf/2109.03804v1 (2022) (↑ 17, 92).

63. Maximilian Kaiser. *Ein Aufbau zur Untersuchung ultrakalter Quantengase mit hoher räumlicher Auflösung* Diploma thesis (TU Kaiserslautern, Kaiserslautern, 2021) (↑ 17, 19, 92).

64. Gross, C., Gan, H. C. J. & Dieckmann, K. All-optical production and transport of a large Li6 quantum gas in a crossed optical dipole trap. *Physical Review A* **93.** http://arxiv.org/pdf/1605.03298 (2016) (↑ 17, 19).

65. Jan Kilinc. *Starting a Na-K experiment for simulating quantum many-body phenomena* Master thesis (Heidelberg University, Heidelberg, 2019) (↑ 21).

66. Lilo Höcker. *Building up a modular Na-K quantum gas experiment* Master thesis (Heidelberg University, Heidelberg, 2019) (↑ 21).

67. *Inventor Professional 2023: Material Catalog* 2023 (↑ 28, 30).

68. Young, W. C. & Budynas, R. G. *Roark's formulas for stress and strain* 7. ed. (McGraw-Hill, New York, NY, 2007) (↑ 28 sq.).

69. Tipler, P. A., Mosca, G. & Kersten, P. *Tipler Physik: Für Studierende der Naturwissenschaften und Technik* 9. Aufl. 2024. https://nbn-resolving.org/urn:nbn:de:bsz:31-epflicht-3123666 (Springer Berlin Heidelberg, Berlin, Heidelberg, 2024) (↑ 28, 45).

70. MatWeb LLC. *MatWeb: Material Property Data: Titanium Ti-6Al-4V (Grade 5), Annealed* https://www.matweb.com/%20(13.09.2025) (↑ 28).

71. Senjanović, I., Tomić, M., Vladimir, N. & Hadžić, N. An Analytical Solution to Free Rectangular Plate Natural Vibrations by Beam Modes – Ordinary and Missing Plate Modes. *Transactions of FAMENA* **40,** 1–18 (2016) (↑ 30).

72. Thomas Lompe. *Efimov Physics in a three-component Fermi gas* Dissertation (Heidelberg University, Heidelberg, 2011) (↑ 35).

73. KENNY, B. & PATTERSON, E. A. Load and stress distribution in screw threads. *Experimental Mechanics* **25,** 208–213 (1985) (↑ 45).

74. KENNY, B. & PATTERSON, E. A. THE DISTRIBUTION OF LOAD AND STRESS IN THE THREADS OF FASTENERS - A REVIEW. *Journal of the Mechanical Behavior of Materials* **2,** 87–106 (1989) (↑ 45).

75. Hollenbeck. Analysis of the stress and load distribution of an assembled screw including a threaded contact. *Comsol Whitepaper.* https://www.comsol.com/paper/analysis-of-the-stress-and-load-distribution-of-an-assembled-screw-including-threaded-contact-121661%20(13.09.2025) (2023) (↑ 45).

76. Eugene Hecht. *Optik* 5th ed., revised (Oldenburg Verlag München, München, 2009) (↑ 60, 74 sq.).

77. Niu, K. & Tian, C. Zernike polynomials and their applications. *Journal of Optics* **24,** 123001 (2022) (↑ 66 sq.).

78. Prashant Prabhat & Turan Erdogan. *Flatness of Dichroic Beamsplitters Affects Focus and Image Quality: IDEX Health and Science - Whitepaper* (ed IDEX Health and Science) https://www.idex-hs.com/resources/resources-detail/dichroic-beamsplitters-white-paper%20(13.09.2025) (↑ 71 sq.).

79. Norland, E. A. *Techniques in using UV adhesives for optomechanical designs* in *Optomechanical and Precision Instrument Design* (ed Hatheway, A. E.) (SPIE, 1995), 278–281 (↑ 72 sq.).

80. Arne Jakob Geipel. *Spatially Incoheren Laser Light for Homogeneous DMD-Projected Light Fields* Bachelor Thesis (Ludwig-Maximilians-Universität München, Munich, 2023) (↑ 78).

81. Kramida, A. & Ralchenko, Y. *NIST Atomic Spectra Database, NIST Standard Reference Database 78* 1999 (↑ 78).

82. Gehm, M. E. *Properties of 6Li* https://alquze.co.jp/wp-content/uploads/2023/11/reference_lithium.pdf (2003) (↑ 81 sq.).

83. Bushaw, B. A., Nörtershäuser, W., Ewald, G., Dax, A. & Drake, G. W. F. Hyperfine splitting, isotope shift, and level energy of the 3S states of (6,7)Li. *Physical review letters* **91,** 043004 (2003) (↑ 82).

84. Šibalić, N., Pritchard, J. D., Adams, C. S. & Weatherill, K. J. ARC: An open-source library for calculating properties of alkali Rydberg atoms. *Computer Physics Communications* **220,** 319–331 (2017) (↑ 83).

85. Bergschneider, A., Klinkhamer, V. M., Becher, J. H., Klemt, R., Zürn, G., Preiss, P. M. & Jochim, S. Spin-resolved single-atom imaging of Li6 in free space. *Physical Review A* **97.** http://arxiv.org/pdf/1804.04871v2 (2018) (↑ 86 sq., 130 sq.).

86. Lamporesi, G., Donadello, S., Serafini, S. & Ferrari, G. Compact high-flux source of cold sodium atoms. *The Review of scientific instruments* **84,** 063102. https://pubs.aip.org/aip/rsi/article/84/6/063102/355365 (2013) (↑ 94).

87. Tiecke, T. G., Gensemer, S. D., Ludewig, A. & Walraven, J. T. M. High-flux two-dimensional magneto-optical-trap source for cold lithium atoms. *Physical Review A* **80** (2009) (↑ 94, 97 sqq.).

88. Demtröder, W. *Mechanik und Wärme* 9. Auflage (Springer, Berlin, 2021) (↑ 99).

89. Linstrom, P. *NIST Chemistry WebBook, NIST Standard Reference Database 69* 1997 (↑ 99).

90. Hicks, W. T. Evaluation of Vapor-Pressure Data for Mercury, Lithium, Sodium, and Potassium. *The Journal of Chemical Physics* **38,** 1873–1880 (1963) (↑ 99).

91. Ketterle, W. & Zwierlein, M. W. *Making, probing and understanding ultracold Fermi gases* http://arxiv.org/pdf/0801.2500 (↑ 101).

92. Chin, C., Grimm, R., Julienne, P. & Tiesinga, E. Feshbach resonances in ultracold gases. *Reviews of Modern Physics* **82,** 1225–1286 (2010) (↑ 101).

93. Zürn, G., Lompe, T., Wenz, A. N., Jochim, S., Julienne, P. S. & Hutson, J. M. Precise characterization of 6Li Feshbach resonances using trap-sideband-resolved RF spectroscopy of weakly bound molecules. *Physical review letters* **110,** 135301 (2013) (↑ 102).

94. Setiawan, W. *Fermi Gas Microscope* Dissertation (Harvard University, 2012) (↑ 103).

95. Murthy, P. A., Kedar, D., Lompe, T., Neidig, M., Ries, M. G., Wenz, A. N., Zürn, G. & Jochim, S. Matter-wave Fourier optics with a strongly interacting two-dimensional Fermi gas. *Physical Review A* **90** (2014) (↑ 104).

96. Brandstetter, S., Heintze, C., Hill, P., Preiss, P. M., Gałka, M. & Jochim, S. Magnifying the wave function of interacting fermionic atoms. *Physical review letters* (2025) (↑ 104, 122).

97. Scazza, F., Del Pace, G., Pieri, L., Concas, R., Kwon, W. J. & Roati, G. *An efficient high-current circuit for fast radio-frequency spectroscopy in cold atomic gases* 2021 (↑ 106).

98. Watter, H. *Hydraulik und Pneumatik: Grundlagen und Übungen - Anwendungen und Simulation* 5., überarbeitete und erweiterte Auflage (Springer Vieweg, Wiesbaden and Heidelberg, 2017) (↑ 107).

99. Sigloch, H. *Technische Fluidmechanik* 11. Auflage (Springer Vieweg, Berlin and Heidelberg, 2022) (↑ 107).

100. Brown, G. O. *The History of the Darcy-Weisbach Equation for Pipe Flow Resistance* in *Environmental and Water Resources History* (eds Rogers, J. R. & Fredrich, A. J.) (American Society of Civil Engineers, Reston, VA, 2002), 34–43 (↑ 107).

101. Nirschl, H. in *VDI-Wärmeatlas* (eds Stephan, P., Kabelac, S., Kind, M., Mewes, D., Schaber, K. & Wetzel, T.) 1355–1361 (Springer Berlin Heidelberg, Berlin, Heidelberg, 2019) (↑ 107).

102. Mitra, D. *Exploring attractively interacting Fermions in 2D using a quantum gas microscope* Dissertation (Princeton University, 2018) (↑ 107 sqq.).

103. Pitt, R. & Clark, S. *Comparison of Pipe Flow Equations and Head Losses in Fittings* 2008. https://web.archive.org/web/20220121124350/http://rpitt.eng.ua.edu/Class/Water%20Resources%20Engineering/M3e%20Comparison%20of%20methods.pdf%20(13.09.2025) (↑ 107).

104. The Engineering ToolBox. *Hazen-Williams Friction Loss Coefficients: Data & Reference Guide* 2004. https://www.engineeringtoolbox.com/hazen-williams-coefficients-d_798.html%20(13.09.2025) (↑ 108).

105. Ottenstein, T. *Few-body physics in ultracold Fermi gases* Dissertation (Heidelberg University, 2010) (↑ 109).

106. Blevins, R. D. *Flow-induced vibration* 2. ed., repr (Krieger, Malabar, Fla., 1994) (↑ 110).

107. Holten, M. *From Pauli Blocking to Cooper Pairs: Emergence in a Mesoscopic 2D Fermi Gas* Dissertation (Heidelberg University, 2022) (↑ 114, 122, 130 sq.).

108. Wigley, P. B., Everitt, P. J., van den Hengel, A., Bastian, J. W., Sooriyabandara, M. A., McDonald, G. D., Hardman, K. S., Quinlivan, C. D., Manju, P., Kuhn, C. C. N., Petersen, I. R., Luiten, A. N., Hope, J. J., Robins, N. P. & Hush, M. R. Fast machine-learning online optimization of ultra-cold-atom experiments. *Scientific Reports* **6,** 25890 (2016) (↑ 114).

109. Serwane, F., Zürn, G., Lompe, T., Ottenstein, T. B., Wenz, A. N. & Jochim, S. Deterministic Preparation of a Tunable Few-Fermion System. *Science* **332,** 336–338 (2011) (↑ 119, 122 sq.).

110. Hume, D. B., Stroescu, I., Joos, M., Muessel, W., Strobel, H. & Oberthaler, M. K. Accurate atom counting in mesoscopic ensembles. *Physical review letters* **111,** 253001 (2013) (↑ 119).

111. Lunt, P. M. *Rotating few-fermion systems* Dissertation (Heidelberg University, 2024) (↑ 122).

112. Pinkse, P. W. H., Mosk, A., Weidemüller, M., Reynolds, M. W., Hijmans, T. W. & Walraven, J. T. M. Adiabatically Changing the Phase-Space Density of a Trapped Bose Gas. *Physical review letters* **78,** 990–993 (1997) (↑ 122).

113. Grimm, R. *Ultracold Fermi gases in the BEC-BCS crossover: a review from the Innsbruck perspective* 2007. https://arxiv.org/pdf/cond-mat/0703091 (↑ 123).

114. Urech, A., Knottnerus, I. H. A., Spreeuw, R. J. C. & Schreck, F. Narrow-line imaging of single strontium atoms in shallow optical tweezers. *Physical Review Research* **4** (2022) (↑ 129).

115. Brantut, J. P., Clément, J. F., de Saint Vincent, M. R., Varoquaux, G., Nyman, R. A., Aspect, A., Bourdel, T. & Bouyer, P. Light-shift tomography in an optical-dipole trap for neutral atoms. *Physical Review A* **78** (2008) (↑ 130).

116. Culemann, M. *Construction and Control of a Dark Spot Optical Tweezer Array for a Quantum Gas Microscope* Master Thesis (Ludwig-Maximilians-Universität München, Munich, 2024) (↑ 130).

117. Hebert, A. *A dipolar erbium quantum gas microscope* Dissertation (Harvard University, 2021) (↑ 131).

118. Heintze, C. *Projection of repulsive potentials in ultracold quantum gases with a Digital Micromirror Device* Master Thesis (Heidelberg University, 2020) (↑ 131).

119. Franzen, A. *GWOptics Component Library* https://www.gwoptics.org/ComponentLibrary/%20(13.09.2025) (↑ 135).

List of publications

57. Hammel, T., Kaiser, M., Dux, D., Preiss, P. M., Weidemüller, M. & Jochim, S. Modular quantum gas platform. *Physical Review A* **111** (2025) (↑ 11 sqq., 24, 41, 50 sqq., 55 sqq., 85, 92, 95 sqq., 100, 104, 120, 127).

List of Acronyms and Abbreviations

1D one-dimensional.

2D two-dimensional.

3D three-dimensional.

ADC analog-to-digital converter.

AI artificial intelligence.

AOI angle of incidence.

AOM acusto-optical modulator.

AR anti-reflection.

cMOT compressed magneto-otical trap.

CNC computer numerical control.

COTS commercial off the shelf.

DAC digital-to-analog converter.

DDS direct digital synthesis.

DMD digital micromirror device.

DoF degree of freedom.

DPS differential pumping stage.

FEA finite element analysis.

FOR frame of reference.

FOV field of view.

hODT horizontal optical dipole trap.

HQA Heidelberg Quantum Architecture.

HQA-ONE Heidelberg Quantum Architecture based experiment described in this thesis.

HV high vacuum.

IoT internet-of-things.

M-LOOP machine-learning online optimization package.

MOT magneto-otical trap.

mPoC Microscopy Piece of Cake.

MW microwave.

NA numerical aperture.

NPBS non-polarizing beam splitter.

NUV near ultraviolet.

ODT optical dipole trap.

OPLL optical phase-locked loop.

OR operative region.

PBS polarizing beam splitter.

PCB printed circuit board.

PEEK polyetheretherketone.

PID proportional-integral-derivative.

PoC Piece of Cake.

PTFE polytetrafluoroethylene.

RAR random anti-reflection.

RF radiofrequency.

RMS root mean square.

RoC radius of curvature.

ROI region of interest.

SBODT single beam optical dipole trap.

SLM spatial light modulator.

SQUIDs superconducting quantum interference devices.

SWIR short wavelength infrared.

TA tapered amplifier.

TRL technology readiness level.

UHV ultra-high vacuum.

UV ultraviolett.

vODT vertical optical dipole trap.

Acknowledgments

"To those whom it may concern..."

— Valtteri Bottas

Here we are, at the last step of writing a dissertation. I want to take a moment to reflect on the past few years that culminated in this thesis and express my gratitude to all those people who contributed directly or indirectly, without whom this project would not have been possible.

To begin with, I would like to thank the PIs of this project under whose supervision the development of HQA and the construction of HQA-ONE have been carried out.

Selim, thank you for giving me the opportunity to join the group and to pursue my PhD under your supervision. I genuinely admire your technological creativity and intuitive understanding of physics. Discussions with you about potential technological developments have been equally intellectually challenging and inspiring at the same time. Beyond that, I want to thank you for always including us PhD students in discussions with peers. Ranging from opportunities to give talks on your behalf at a PASQuanS meeting or chatting with world-class physicists, I always had the feeling that we PhD students had a seat at the table.

Matthias, it is somewhat unique that this project has two PIs, but I believe that this is what was absolutely needed for such a technology-focused project. Your complementary viewpoints and suggestions helped to expand my thinking about HQA and HQA-ONE and were invaluable during paper writing.

Furthermore, I want to thank my Dissertation committee for taking the time to read this thesis and to discuss the results with me in the Ph.D. defense. Thank you to *Julian Schmitt*, who agreed to serve as a second referee, as well as *Richard Schmidt* and *José R. Crespo López-Urrutia*, who complete the committee.

Additionally, special thanks to *Sandra*, *Tobi*, *Daniel*, *Philipp*, and *Carl* for carefully reading parts of the thesis and providing crucial feedback.

Next, I would like to thank the HQA-Team, with whom I had the pleasure to develop the presented architecture and to build the presented apparatus.

Tobi, thank you for the past 4 1/2 years of developing this modular architecture and filling that empty lab space with an operational quantum simulator together! Your enthusiasm, together with our complementary approaches to problem-solving, was what enabled the developments described here. Beyond that, I am very happy that we not only shared time in the office and lab together, but also at the Uni-Cup, the football stadium, the Oktoberfest,... . Thank you for being my lab buddy through this entire project!

Daniel, I admire your technical understanding, especially in the IT segments, which

usually just leaves me in awe. You were a perfect match to join the HQA-Team on a personal and professional level. I am confident that the apparatus is in good hands with you as the next generation of PhD students at HQA-ONE. Besides that, now that I have to skip this year, I am very much looking forward to having a beer with you again at the Oktoberfest next year.

Gerhard, thank you for your constant technical support, especially with electronics and e-lego, as well as your help in planning how to keep the coffee machine, and therefore all the quantum gases labs, running.

As already listed in an extensive table at the beginning of the thesis, many students contributed to the construction of the apparatus. Thank you to every single one of you for helping to realize our ideas. A special thanks to our Master's students *Micha*, *Vivienne*, *Johanna*, *Suraj*, and *Finn*, who were part of the team for an extended period of time and shaped my time here both in and out of the lab.

Philipp Preiss, thank you for being our closest collaborator during the development of HQA. Unfortunately, we did not have an overlap in Heidelberg, but I have always enjoyed meeting and chatting with you either at conferences or at our more or less regular meetings.

Naturally, it was not only the HQA team that made my time in Heidelberg special, but the entire Jochim-Labs team. I want to thank *Carl*, *Sandra*, *Philipp*, *Johannes*, *Paul*, and *Maciej* for making the time in Heidelberg special. From constructive collaboration in solving problems at work to quality time outside of the lab, like having drinks or dinner together, going swimming or biking, or going to a lake together, the group spirit was special. Additional thanks to all former Bachelor and Master students as well as the former generation of PhD students in the group, *Ralf*, *Marvin*, and *Keerthan*, with whom I unfortunately had only brief overlap.

Credit is also due to the people outside the group, who are essential to keep things running efficiently. I want to thank the administrative staff, especially Ferman Alkasari and Claudia Krämer. Additionally, the development of this project largely benefited from the support and exchange with the teams of our mechanical and electrical workshop, as well as our IT department. I want to thank specifically *Denis Hoffmann*, *Alexander Worsch*, and *Simon Rabenecker*.

I want to thank my dear friends *Basti* and *Niki*, who I met ten years ago when I started studying physics in Kaiserslautern and who to this day are very close friends. Time spent with you on skiing trips, when having a beer together, or at a BBQ is always amazing. You can relate to the PhD struggles, such that we can spiral if things do not work, but we can as well just have a good time, completely forgetting about the lab. To be fair, I also think that our spouses' occasional rule of not being allowed to use words like 'laser' at times is, in the end, quite healthy.

Den letzten und üblicherweise wichtigsten Absatz meiner Thesis möchte ich nutzen, um meiner Familie und den anderen mir am nächsten stehenden Menschen zu danken. Vielen Dank an meine Lieblingsschwägerin *Sarah* für deine Unterstützung, egal ob beim gemeinsamen Sport, als Edelfan beim Triathlon oder einfach auch im Alltag. Vielen Dank an meinen besten Freund *Johannes*, deine stete Unterstützung bei allem was ich tue und die gemeinsam verbrachte Zeit sind unbezahlbar. Ich hoffe sehr, dass nachdem diese Arbeit

nun vollendet ist, wir nun endlich wieder mehr Zeit für gemeinsame Kaffeepäuschen oder Läufe finden.

Ein ganz besonderer Dank geht an meine Familie! Danke *Mama*, danke *Papa*, danke *Sarah*, dass ihr immer für mich da seid, stets an mich glaubt und mich immer bedingungslos unterstützt! Ohne euch wäre dieser Weg nicht möglich gewesen!

Laura, mit den letzten Zeilen dieser Danksagung und dieser Arbeit möchte ich dir von ganzem Herzen danken, dass es dich in meinem Leben gibt und ich dich zu jeder Zeit an meiner Seite weiß!